Dipl.-Ing. Jonathan Flesch

LBE-cooled tube receiver performance – Design aspects and high-flux experiments in a solar furnace

LBE-cooled tube receiver performance – Design aspects and high-flux experiments in a solar furnace

Zur Erlangung des akademischen Grades
Doktor der Ingenieurwissenschaften (Dr.-Ing.)
von der KIT-Fakultät für Chemieingenieurwesen und Verfahrenstechnik
Karlsruher Institut für Technologie (KIT)

genehmigte
Dissertation

von
Dipl.-Ing. Jonathan Flesch
aus Berlin

Tag der mündlichen Prüfung:	12. Juni 2020
Referent:	Prof. Dr. Thomas Wetzel
Korreferent:	Prof. Dr. Robert Stieglitz

Acknowledgement

This thesis is based on project work during my employment at the KIT's liquid metal laboratory KALLA of the Institute for Nuclear and Energy technology (IKET) between March 2014 and December 2018. It was finalized throughout the years 2019 and 2020.

Prof. Wetzel, I am grateful to you for the initiation of this project and selecting me for the team. I thank you for your charismatic, constructive and motivating guidance and at times your patience.

Prof. Stieglitz, thank you for your review of this thesis and your constructive, very valuable criticism.

Luca Marocco, thank you for sharing your vast knowledge of fluid dynamics and experience in scientific practice. Thank you also for your enlightening, pleasant and also funny company at KIT.

Klarissa Niedermeier, thank you for very many insightful conversations and for your company throughout these years. Thank you also for your proof-reading several sections of this work.

Frank Fellmoser and Julio Pacio, thank you for contributing a lot of experience and sharp attention to detail to this project. I thank both of you for support, advice and the recording of first operation data before the finalization of this work.

Kurt Wittemann, thank you for contributing your technical skills and your positive thinking and especially your industry during the physical setup of the loop. Andreas Jekel, thank you for your sound designs and technical solutions which you contributed to the setting up of the SOMMER facility. Viktor Krieger and Peter Miodek, thank you for being such capable and

humorous support for the matters of electric installation and loop control implementation.

Dear team of the KALLA, dear colleagues at IKET and TVT, thank you all for a pleasant time and your support.

Dear students, thank you who have assisted significantly in several regards of the project by your work and input in the context of preparing your theses.

Many thanks to Gerd Dibowski at DLR's solar furnace in Cologne and among his team especially to Christian Willsch. Your support made the calibration of our sensor possible and at the same time fun. I am impressed by the technical level of your solar furnace and versatility down to the small mechanical equipment pieces you keep in stock.

Thomas Keck at sbp solar: Thank you for your assistance in establishing a contact with Forbes Solar and for sharing your knowledge on concentrating mirrors.

Dear Katharina, thank you for your wonderful support, for your and and our little ones' patience and also your sacrifices to allow me the completion of this work. Many thanks also to my parents and my sister for their efforts in proof-reading and for your constant support ever since and in all regards.

Berlin, December 2020 *Jonathan Flesch*

Kurzfassung

Diese Arbeit untersucht die Eignung von flüssigem Blei-Bismut (Pb-Bi) als Wärmetransport-Medium in zentralen Rohr-Receivern von konzentrierenden solarthermischen Kraftwerken. Dazu werden zwei Ansätze verfolgt: a) auf theoretischer Ebene werden anhand existierender Literatur die Materialeigenschaften von Pb-Bi und existierende Auslegungswerkzeuge für Flüssigmetall-Anwendungen betrachtet und b) anhand eines Praxisbeispiels wird die Auslegung, der Bau, die Inbetriebnahme sowie erste Betriebserfahrung eines Pb-Bi-gekühlten Modellkreislaufs in einem eigens errichteten Solar-Ofen im Technikumsmaßstab erprobt.

Der Pb-Bi-gekühlte Solarreceiver dieses Kreislaufs besitzt eine thermische Leistung von 10 kW. Pb-Bi besitzt einige hervorragende und einige ungünstige Stoffeigenschaften für seine Anwendung in Solarreceivern im kommerziellen Groß-Maßstab: eine hohe thermische Leitfähigkeit und eine geringe Viskosität stehen einer durchschnittlichen Wärmekapazität und einer sehr hohen Dichte gegenüber. Diese führen für Pb-Bi im Vergleich mit Alternativ-Wärmetransportmedien Solarsalz und Natrium beim Einsatz in Receiver-Rohren zu den höchsten Entropie-Erzeugungsraten. Pb-Bi ist darüber hinaus teuer.

Im Pb-Bi muss eine definierte Sauerstoffkonzentration eingestellt werden, um die Korrosion der Edelstahl-Rohrwerkstoffe zu begrenzen. Dadurch wird allerdings der Bereich der Einsatztemperaturen eingeschränkt: Infolge dessen kann entweder der Vorteil einer geringen Schmelztemperatur von Pb-Bi nicht ausgenutzt werden, oder aber eine Betriebstemperatur oberhalb der Temperaturgrenze von Solarsalz kann nicht erreicht werden. Nach dem aktuellen Stand der Technik dient Solarsalz als Wärmetransportmedium.

Die Literaturrecherche dieser Arbeit gibt deutliche Hinweise darauf, dass Fluide mit niedrigen Prandtl-Zahlen und insbesondere Pb-Bi empfindlicher als "konven-tionelle" Medien auf Randbedingungen mit inhomogener Wärmestromdichteverteilung reagieren. Tatsächlich werden die Rohrströmungen in konventionellen Solarreceivern nur einseitig beheizt. Unter dieser Randbedingung führen klassische Nusselt-Korrelationen, die für homogen beheizte, voll-turbulente Rohrströmung entwickelt wurden, bei Medien geringer Prandtl-Zahl zu einer deutlichen Unterschätzung der Wandtemperatur und damit einhergehend zu einer Unterschätzung der thermischen Spannungen in der Rohrwand. Daher werden alternative Auslegungsmethoden präsentiert.

Erste Messungen am Pb-Bi-Kreislauf zeigen tatsächlich äußere Wandtemperaturen der Receiver-Rohre, die höher sind als von klassischen Nusselt-Korrelationen vorhergesagt. Trotz dieses Befundes hat Pb-Bi für seinen Einsatz in einem Modell-System seine Berechtigung, da es im Vergleich zu bspw. Natrium inhärent deutlich sicherer ist und kann für Receiver-Betrieb und die Untersuchung von Phänomenen, die spezifisch für Flüssigmetalle sind, verwendet werden.

Diese Arbeit beschreibt die Auslegung der wichtigsten Teile des Pb-Bi-Kreislaufs und die ersten experimentellen Ergebnisse, darunter auch solche bei einer Wärmestromdichte von etwa $4\,\mathrm{MW\,m^{-2}}$.

Zur Messung derart hoher Wärmestromdichten wurde im Rahmen der Arbeit ein passiv-gekühlter Wärmestrom-Scanner entwickelt, dessen Funktion auf einem einzigen Heat-Flux-Mocro-Sensor basiert. Dieser Sensor bewegt sich während des Scannens auf einer Spiral-Bahn durch die Messebene. Dieses Messgerät wurde vor Messbeginn im Solarofen des DLR in Köln für den Betrieb kalibriert.

Abstract

The potential of molten lead bismuth eutectic (LBE) as heat-transfer fluid in tubular thermal central receivers in concentrating solar power plants is assessed in this thesis. Two approaches are taken: a) the theoretical review of LBE's properties and existing design tools and b) the design, construction, commissioning and early operation of a solar furnace and a small scale LBE-cooled receiver therein with a thermal solar power of 10 kW.

LBE has several advantageous as well as some unfavorable properties for its application in large-scale, commercial application in thermal receivers: a high thermal conductivity and low viscosity, however, its average mass specific heat capacity and very high density lead to higher minimum entropy generation of LBE during convective heat transfer compared to two alternative heat transfer fluids, solar salt and sodium. LBE is also expensive.

The requirement of a controlled oxygen content for corrosion protection in stainless steel tubes limits the operation temperature range: Either LBE's low melting temperature or its potential for operation at a higher upper temperature limit compared to solar salt cannot be utilized.

A literature review indicates furthermore that fluids with low Prandtl numbers, and LBE in particular, show a high sensitivity with regard to non-uniform heat flux boundary conditions. In conventional thermal tubular receivers the coolant flow is subject to heat flux along only half of the tubes' circumference. For low-Prandtl number fluids, and in case of LBE quite significanty, the application of Nusselt number correlations for uniform heat flux and fully turbulent flow will lead under such condition to a significant under-estimation of the maximum wall temperature and the resulting

thermo-mechanical stresses in the steel wall. Alternative design methods are presented.

The experimental operation of the LBE loop indeed shows higher-than-expected outer wall temperatures of the receiver tubes for operation with LBE. However, LBE is also inherently safer than for example sodium and therefore well suited as a model fluid for the investigation of liquid metal heat transfer characteristics and model receiver operation.

The design of key LBE-loop components is described and first-hand experimental results presented. During commissioning of the loop, heat fluxes of $4\,\mathrm{MW\,m^{-2}}$ have been successfully applied to the thermal receiver.

Furthermore, a flux scanner was developed which utilizes an un-cooled heat flux micro sensor (HFM) to scan the solar flux distribution by means of a circular and superimposed linear motion pattern. It was designed, build and finally calibrated in the solar simulator of the German Aerospace Center (DLR) in Cologne, Germany.

Contents

Symbols and Abbrevations

Roman Symbols

A	[m^2] surface area
a	[arbitrary] half-width of rectangular probability distribution
b	[arbitrary] correction function for heat flux measurement
c	[m] heat capacity
D	[arbitrary] nominator in least squares system of equations
F	[–] view factor
f	function
G	transfer function in frequency domain
h	[$W\,m^{-2}\,K^{-1}$] convective heat transfer coefficient
I''	[$W\,m^{-2}$] incident solar heat flux.
K	[arbitrary] constant factor
L	[m] length
m	[kg] mass
$\dot{P}$	[W] power
P	[m] pitch between hexagnoally arranged rods
Q	[J] enthalpy
q_k	[arbitrary] the k^{th} of n observations of a randomly varying quantity q
s	[s^{-1}] variable in LaPlace transformed diff. equation
s	[arbitrary] experimental standard deviation, best estimate of σ
s^2	[arbitrary] experimental variance
T	[s] time constant
t	[s] time

U	[V] voltage
U	[m] perimeter
U	[arbirary] acting variable
u	[arbitrary] standard uncertainty
u^2	[arbitrary] Type A variance, variance of the mean of an input quantity estimated from n repeated observations
v	[$\mathrm{m\,s^{-1}}$] velocity (of a flow or an object)
W	[arbirary] set point
X	[m] Cartesian coordinate in x direction
x	[m] measured sample of length in X-direction
x_i	[arbitrary] estimate of an input quantity X_i
Y	[m] Cartesian coordinate in y direction
Y	[arbirary] controlled variable
y_1	[arbitrary] fitting parameter in correction function for heat flux measurement
y_2	[arbitrary] fitting parameter in correction function for heat flux measurement
Z	[m] Cartesian coordinate in z direction
Z	[arbirary] disturbance

Abbreviations

D	differentiating gain
I	integrating gain
LBE	free crosssection
P	proportional gain
T	gain delay

Dimensionless Numbers

d	[–] differental operator
N	[–] number of measured samples
n_i	[–] sample index
r	[–] coefficient of correlation

Greek Symbols

α	[K^{-1}] coefficient of thermal expansion
α	[m] measured sample of length in X-direction
δ	[-] partial derivative operator
ζ	[arbitrary] independent variable in linearized equation, denoting deviation from design condition
ε	[–] black body light absorptance
μ	[Pa s] dynamic viscosity
μ_q	[arbitrary] expected value of quantity q
ρ	[$kg\,m^{-3}$] density
σ	[$5.67 \times 10^{-8}\,W\,m^{-2}\,K^{-4}$] Stefan-Boltzmann constant
σ	[arbitrary] standard deviation of a normal probability distribution
τ	[s] response time constant as in $e^{-\frac{t}{\tau}}$
ω	[$rad\,s^{-1}$] rotational speed

Subscripts

0	initial condition at t=0
A	compensation
amb	ambient
avg	average
C	convective
c	combined uncertainty
Cu	copper
el	electric
H	heater
h	hydraulic (e.g. diameter)
HFM	Heat Flux Micro Sensor
HFS	Heat Flux Sensor
I	incident solar heat flux
k	[–] sample index
k	index
LBE	lead bismuth eutectic alloy

M	molten metal in heater
p	constant pressure
R	controller
R	heater rod
R	receiver
ref	reference value
res	residence time
RTS	Resistance Thermal Sensor
S	process, system
s	steady state condition, i. e. at $\frac{d}{dt} = 0$
T	irradiated tube section
U	ambient
V	vessel
w	wetted
x	X-direction
y	Y-direction
z	Z-direction

All units are metric units unless otherwise specified. Currencies are given in USD or in EUR. The symbol $ refers to USD unless stated differently.

1 Liquid metal as heat transfer fluid in solar thermal electricity generation plants

1.1 Liquid metals technology

Metals are not only used in their solid state but also in their liquid state. depending on their melting temperature they are applied throughout a range from significntly below 0 °C up to significantly more than 1000 °C.

At the lower end of this temperature range, for example, the widely known mercury is used. This element melts at −38 °C and does not boil below 357 °C. It is therefore used as temperature indication material in glass thermometers but also as electric conductor in switches, batteries or thermostats fand even as liquid mirrors in telescopes. Due to its toxicity, a transition to less toxic technical solutions is attempted internationally.

Gallium based alloys, for example, are liquid at room temperature, too, but not toxic and can therefore additionally serve as conductors in stretchable hoses, soft electrodes and for renewable surfaces [1]. A liquid drop of a gallium indium tin alloy on a stainless steel surface is shown in Figure 1.1.

Although it is liquid, the 'tip' shape is maintained and stabilized by a thin oxide layer, which is immediately formed by this alloy in contact with air. At higher temperatures, for example, molten tin is applied above its melting temperature of 232 °C in the float glass production where in a continuous process glass melt is allowed to solidify floating on a pool of liquid tin which has a density higher than glass. Due to tin's high surface tension, a very smooth glass surface is thus obtained [2].

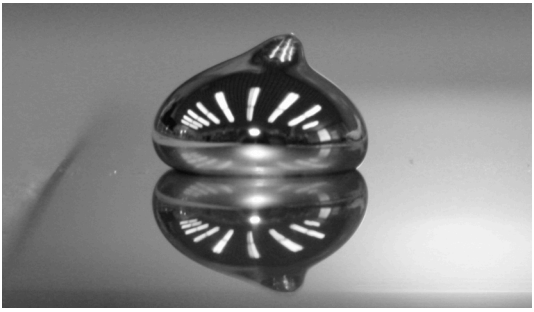

Figure 1.1: Liquid drop of InGaSn on steel plate at room temperature. Photographed by Ulli Hammann @KIT 2015

Besides their uses due to their electric, hydraulic and physical properties, which are taken advantage of by the previous applications, liquid metals have thermo-physical properties that make them very attractive in heat management and cooling systems. For example, gallium based alloys are used in CPU cooling systems [3] or, at higher temperatures, sodium is used for the cooling of pistons in combustion engines [4]. But liquid metals are also applied in the cooling of nuclear fission and fusion reactors.

Sodium cooled fast breeder reactors have among many other countries also been developed in Germany: Between 1957 and 1991 extensive experience in large scale liquid metal handling was also obtained in fast breeder reactor projects. The development of a 'Kompakte Natriumgekühlte Kernkraftanlage' (compact sodium-cooled nuclear power facility) KNK with an electric power output of 20 MW using 89 tons of sodium for cooling was initiated in 1960 by Interatom, later to be executed at the former 'Kernforschungszentrum Karlsruhe' (nuclear research center Karlsruhe) which finally merged into today's KIT. Broad research was executed in order to later contribute to the development of a much more powerful 'SNR 300' sodium-cooled fast reactor with an electric power of 300 MW. The KNK reactor started full load operation in 1974. It was later re-configured for

operation of fuel rods with length specific thermal loads of 435 $\mathrm{W\,cm^{-1}}$[5]. Under those changing settings, much practical experience with sodium was therefore obtained. While German development activities in sodium cooled fast breeder technology were stopped in 1991, such reactors are continued to be built and operated: the Russian BN-800 with a thermal power of 2.1 GW in Belojarsk started full load operation in 2016. At KIT sodium was continued to be used for different applications till today, with thermal hydraulic experiments for nuclear safety in ALINA and KASOLA loops.

Lead-bismuth eutectic (LBE) has been used as coolant in Russian nuclear submarines during cold war and is today intended for use in small modular breeder reactors SVBR [6]. It is attractive for these purposes since it does not boil up to a temperature of more than 1600 °C, thus maintaining single-phase conditions even in off-design conditions and contributing to operation safety.

In a different nuclear application, LBE can serve as a so-called spallation target: When exposed to accelerated protons it generates neutrons that can sustain nuclear fission in sub-critical nuclear cores. These kinds of nuclear reactors are called 'accelerator driven systems' (ADS) and have the inherent safety feature of shutting down when the proton beam is switched off. They may be part of a new generation of nuclear power sources with passive safety characteristics. Thermal-hydraulic experiments with LBE are continuously being executed at KIT as well, for example in the THEADES loop.

Due to these decades of practical experience, liquid metal technology is mature in the field of nuclear power generation and research.

Their benefits in the cooling of thermally highly loaded surfaces make liquid metals also beneficial in thermal receivers of concentrating solar power plants. These receivers convert radiation energy from concentrated sun light at very high flux densities to thermal energy. Liquid metals can serve in these receivers as fluids that remove the absorbed thermal energy from irradiated surfaces and transfer it to electric power generation cycles. The feasibility of using liquid metals for this purpose has been demonstrated in

the 1980s with sodium as heat-transfer fluid (HTF) in a demonstration plant with an electric power of 500 kW.

Unfortunately, upon successful demonstration of the technology, a sodium leak led to a severe fire that destroyed the demonstration facility, showed the risk inherent in sodium and brought the interest of the solar community in this coolant fluid to a hold. Since then, the solar thermal technology has instead focused on steam, air and – commercially most successfully – molten salt as coolants. However, it appears that these alternative fluids have reached their inherent techno-economical limitations compared with competing renewables such as wind power and photovoltaics.

Therefore, renewed interest in the application of liquid metals can be observed in the scientific and industrial community: Several research articles on the use of liquid metal in solar thermal electricity generation (STE) have been published only recently, often being reviews on heat-transfer fluids and numerical system studies[1].

As an addition to these mostly theoretical works, in this thesis LBE's potential as a coolant under the conditions present in such solar thermal receivers is assessed experimentally. A critical discussion of the applicability of the available tools required for thermal receiver design precedes the efforts of putting these tools to a test by also designing, constructing and operating an LBE loop with an experimental model thermal receiver of a thermal power of 10 kW.

This work seems to be executed at the right time: only very recently, commercial activities in using sodium in solar power generation have been resumed. The public results from this thesis – although using LBE instead of sodium – may complement well the results from these privately executed projects.

[1] For example, references Pacio et al. [7], [8], [9], Wetzel et al. [10],Heinzel et al. [11], Hering et al. [12], Lorenzin et al. [13], Kotze et al. [14], Boerema et al. [15] and [16], Logie [17], Pye et al. [18], Wilk [19], Ho [20], Benoit [21], Coventry et al. [22].

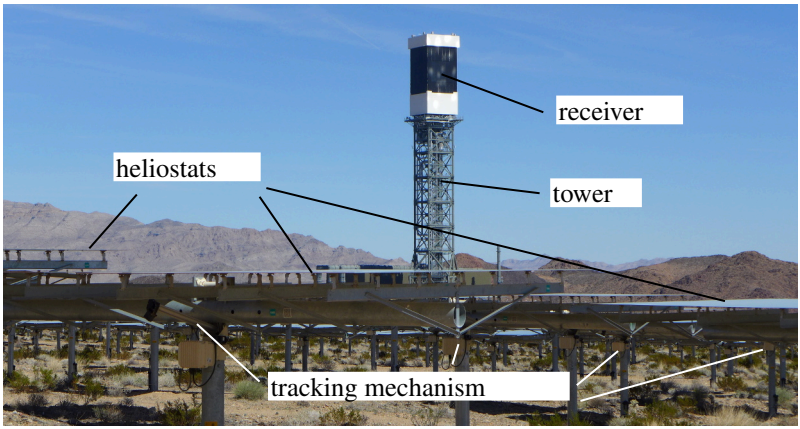

Figure 1.2: Ivanpah solar thermal power plant near Las Vegas, USA. The heliostats in the foreground are currently de-focussed from the black direct steam receiver on the tower. Photographed by Jonathan Flesch Sep. 2016.

1.2 Solar thermal electricity generation (STE)

In solar thermal electricity generation, radiation energy from the sun is collected, transformed to heat and delivered to a steam power cycle for electricity generation. The sun light thus replaces the combustion of fossil fuels or the fission of nuclear fuels in conventional steam power plants.

In one particular kind of solar thermal power plants, so-called central receivers are used as absorbers. Many mirrors located on the ground re-direct the incident sunlight to this kind of central absorber mounted on a tower tip such as shown in Figure 1.2. The one shown in the figure represents one of three central receivers of the Ivanpah solar thermal power plant near Las Vegas in the US.

In the receiver shown in Figure 1.2 steam is directly generated. Alternatively, and more commonly, a primary, non-evaporating coolant fluid other than water/steam flows in the absorber and delivers the generated heat to an evaporator of a steam power cycle.

The stat-of-the-art fluid is solar salt. It is a binary nitrate salt mixture with a melting temperature of 238 °C, consisting of mass specific 40 % KNO_3 and 60 % $NaNO_3$ [23].

Besides serving as a coolant and heat-transfer fluid, its low cost and high volumetric heat capacity also enable its direct use for thermal storage. For this purpose, solar salt is heated up in the thermal receiver and then stored it in a thermally well insulated tank for later use. It can be taken from this tank during periods without sunshine, either during cloud passages or after nightfall. Furthermore, solar salt's liquid temperature range above its melting point is well suitable for operation and the receiver can thus be operated at moderate pressure. Water, on the other hand, evaporates and forms high pressure steam which requires thick-walled, expensive and heavy tubes in the thermal receiver.

Therefore, only when no thermal storage is required water is directly evaporated in the receiver, rendering the solar power plant shown in Figure 1.2, where direct steam generation in the receiver is applied, an exception.

Generally, in central receiver power plants the solar absorber is the target for the reflected sunlight of all mirrors. All these mirror tracking mechanisms allow them to reflect the incoming light at a fixed position of the receiver in spite of the apparent motion of the sun – they are therefore called heliostat mirrors. Horizontally oriented and thus in-active heliostat mirrors are shown in the foreground of Figure 1.2. When directed to illuminate the receiver in state-of-the-art plants, all of them together generate an average flux on the absorber of about $0.5\,\mathrm{MW\,m^{-2}}$ and peak fluxes of slightly more than $1\,\mathrm{MW\,m^{-2}}$, the latter of which is about three orders of magnitude higher than the natural intensity of the sun light.

Large arrays of such mirrors are required for commercial solar power plants of more than 100 MW. In one very recently built solar power plant with solar salt as HTF, Crescent Dunes, Nevada, USA, 10 347 heliostats with a reflective area of $115.7\,\mathrm{m^2}$ each have been installed. These incredible numbers contribute significantly to these plants' investment costs which are

in total much higher per electric power output than for conventional power plants. However, since no fuel costs arise throughout those plant's lifetime the power costs are competitive even with fossil plants in some locations in the world. The large number of heliostats covers large areas where the outermost ones have a distance to the receiver of one kilometer and more. Even small aiming inaccuracies of the tracking mechanisms of these far-away mirrors lead to ''spillage' that is, the reflected light misses the absorber area of the receiver and is lost for the purpose of power conversion.

The absorber is typically made of tubes which are arranged in flat receiver panels. Several of these flat panels can be arranged in a plane ('billboard receivers'), or they can cover the rear walls of a chamber which has an open wall facing the heliostats ('cavity receiver') or they can be arranged to surround the tower tip, facing outwards ('central receivers'). For example, the Solar Two receiver consisted of 24 such panels. A single one of these panels is schematically shown in Figure 1.3. Such panel typically consists of a flow diverter on one end and a flow collector on the opposite end. The flow is evenly distributed to many parallel tubes which ideally form a plane without gaps between individual tubes. The tubes individual thermal expansion is compensated by bends in the top and bottom parts. The receiver surfaces attain high temperatures from the incident solar flux. All thermal loss mechanisms are directly related to the surface temperature and to the surface area. Therefore, a reduction of these losses and simultaneously of construction costs can in principle be obtained by reduction of the receiver aperture size. The same solar power would then be projected onto that reduced area, leading to increased heat fluxes. An additional cost reduction potential would result from higher receiver outlet temperatures which could lead to increased Carnot efficiency in the steam power cycle. This is where liquid metals can be applied.

While sodium has already been used in solar plants in the past and present, for example, LBE and tin have been discussed as potential candidates. These

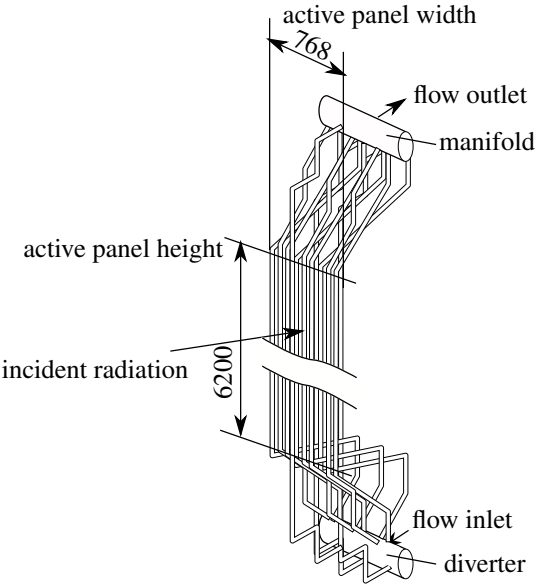

Figure 1.3: Schematic of a single panel of tubes of a central receiver, including example dimensions (in mm) of the Solar Two receiver, adapted from [24]

three coolants are liquid and chemically stable over a wider range of temperatures than the state-of-the-art conventional coolant solar salt.

Solar salt de-composes at temperatures above 600 °C and thus, local peak temperatures must be avoided during operation. Therefore, due to a safety margin, the receiver outlet temperature is typically limited to about 560 °C. Also, the maximum allowable light concentration factor that prevents local tube wall temperatures to exceed the upper temperature limit is already applied in modern facilities so that no size reduction potential of the receiver remains.

The mentioned liquid metals do not de-compose at 600 °C. Using higher heat fluxes and reduced receiver sizes with decreased losses and potentially increased outlet temperatures should be possible.

Electricity generated in solar thermal power plants has to compete with electricity form other sources, both conventional and renewable. Today, wind and photovoltaic power have very low generation costs, thus putting pressure on the generation costs of solar thermal power. Substituting the state-of-the art heat-transfer fluids has to be justified by cost reduction. A low market price of the coolant is therefore beneficial. However, not only purchasing costs are relevant. Different fluids' thermo-physical and chemical properties will lead to individual installation and operating costs:

- Melting and boiling points are constraints for the operating temperature range. A large operating temperature range may allow for higher heat fluxes, a reduced receiver size and higher thermal efficiency. Also, in the power block, the Carnot efficiency grows with the maximum operating temperature, potentially leading to increased economical benefit.
- The generation of entropy and thus loss of 'available work' caused by heat transfer and irreversibilities from flow friction is influenced by the physical properties. A desired high convective heat transfer coefficient comes with the trade-off of the cost of the required pumping power.
- A high volumetric heat capacity of the fluid enables thermal storage in small volume. Small storage tanks are desirable from an economic point of view.
- The density influences the required pumping power. A large fluid mass requires strong and potentially expensive support structures.
- Chemical compatibility with structural material enables long plant life.
- Chemical reactivity with the environment has influence on the cost for safety measures.

Besides these parameters the technology required for operating the coolant must be available.

In the past, liquid metals have demonstrated successfully some of these requirements for solar thermal power generation. Also, a detailed system study has recently indicated a significant cost reduction to be obtained from switching to liquid metal as heat-transfer fluid in central receivers. These demonstration projects and the system study are presented in the following sections:

1.3 Liquid metal-cooled solar facilities: promising results

The following sections briefly summarize three key solar thermal projects, both historic and recent where liquid metals have been applied as heat-transfer fluids. A review on the historic application of liquid sodium in additional STE projects is given by Coventry et al. [22].

1.3.1 The Small Solar Power Systems project in Almería

Scientists and engineers from nine countries participated in the Small Solar Power Systems (SSPS) demonstration project initiated by the International Energy Agency IEA worth a budget of approximately 90 million Deutsche Mark. Within that project, two power plants with an electric power output of 500 kW each were built in Almería, Spain and operated from 1981 on. An areal shot of the facility is shown in the left photograph of Figure 1.4. One of the plants built was a central receiver power plant, the other a 'distributed collector system' with parabolic trough concentrators with thermal oil as heat-transfer fluid [25], which will not be further discussed here. The DFVLR (Deutsche Forschungs- und Versuchsanstalt für Luft- und Raumfahrt e.V), the predecessor of today's German Aerospace Center (DLR) supervised the execution of the project. During the testing and op-

eration phase, the economics of the plants, the operational behavior and the viability of the selected technical solutions have been carefully assessed.

The central receiver system was operated with sodium as the heat-transfer fluid and featured a two-tank direct sodium storage system (thermal capacity of 5.5 MW h). The sodium-cooled receiver was installed at a height of 43 m and a set of 93 heliostats with a total reflective area of 3360 m^2 redirected incident sun light onto a 7.8 m^2 flat panel receiver (as shown on the right photograph of Figure 1.4), designed for a peak heat flux of 1.4 MW m^{-2} and an average heat flux of 350 kW m^{-2}. A design thermal power of 2.75 MW could be delivered by the heliostat field.

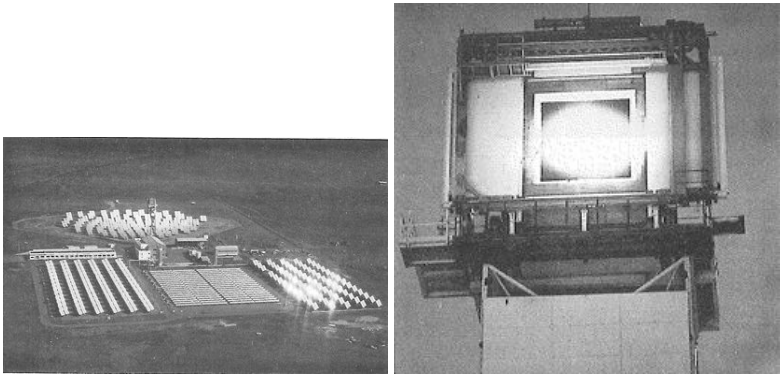

Figure 1.4: Left: Plataforma Solar de Almería with the sodium cooled receiver, which is presented enlarged at the right [26]

A 6-piston steam motor was used to convert the collected thermal power into electric power with steam at 510 °C and 100 bar and with a net efficiency of 23.5 %. Two different receiver designs were tested during the project: First, a cavity receiver where absorber tubes are mounted within a casing that limits thermal losses to the environment and which has a window through which the light is projected. Later, a flat billboard receiver was tested where the absorber tubes are arranged in a square plane and are exposed to the ambient conditions unprotected. In the latter receiver, the flow

of sodium was directed through five serial panels, which consisted of 39 parallel tubes each, the tubes being of an inner diameter of 12 mm and a wall thickness of 1 mm. Liquid sodium entered the receiver at 270 °C and was heated to 530 °C at design conditions. Between April of 1983 and August of 1984 that receiver was operational for 880 hours.

After this testing period under design conditions was completed, a 'high flux experiment' was started in early 1985 in order to test the receiver's capabilities of operating under increased heat flux of 2.5 $MW\,m^{-2}$ and increased flux gradients [27] – much higher fluxes compared to the capabilities of today's state-of-the art molten salt receivers, where peak fluxes only slightly above 1 $MW\,m^{-2}$ are applied. A good performance under these conditions would show the potential of further size reduction. This would generate the benefits of reduced receiver weight, construction and material costs and reduced thermal losses during operation for future receivers. Therefore, a one aiming point strategy was applied instead of the three point strategy that had been used previously and which had distributed the flux more evenly across the receiver.

The peak flux values were slowly increased throughout test phase I in 1985. In the spring of 1986, additional heliostats had been installed so that during test phase II shortly before August the maximum peak flux of more than 2.5 $MW\,m^{-2}$ was obtained.

On August 18th, 1986 a sodium fire destroyed the facility which occurred during maintenance work on a valve that required opening its seal weld and which was located on the pipe between receiver and hot storage tank.

Due to sodium's violent chemical reaction with water, it generates thick white caustic NaOH smoke when in contact with air oxygen and humidity inhibiting access to the fire.

This incident brought the project to an end, demonstrated visibly the risk that is inherent in liquid sodium. It resulted in a period of about 25 years with no further attempts globally of using sodium as coolant in solar thermal tower plants.

Nevertheless, with all plant components working well, successful receiver operation was demonstrated during the high flux experiment before the accident.

1.3.2 The Jemalong Solar Thermal Station

Since 2009 the Vast Solar company in Jemalong, New South Wales in Australia has conducted research and development for solar thermal power plants with sodium as the heat-transfer fluid. In 2017, the company commissioned a pilot plant with an electric power of 1.1 MW.

That pilot plant[2] has five separate modules which are connected together, each consisting of one tower billboard receiver mounted at a height of 27 m and with one individual heliostat field. Each of these modules delivers heated sodium coolant to a central thermal storage tank from which a single steam power cycle is fed. The plant has a total thermal power of 6 MW.

The construction of this plant was delayed by a sodium fire on June 14, 2015 due to a leaking flange beneath the sodium storage tank. The leakage could, however, be stopped, the fire extinguished and the construction continued.

A 50 MW hybrid plant is in the planning with 30 MW contributed from a solar thermal plant and the balance by a PV plant [3].

1.3.3 The LBE thermal storage test at CSIRO

At Australia's Commonwealth Scientific and Industrial Research Organisation CSIRO, LBE was assessed prior to 2015 as a heat transfer and storage medium in an experimental concentrated solar power plant with a pressurized air receiver and a solar air turbine [28]. LBE's performance was

[2] `https://vastsolar.com/portfolio-items/jemalong-solar-station-pilot-1-1mwe/` last accessed: Sep. 20, 2020
[3] `https://vastsolar.com/portfolio-items/mount-isa/`last accessed: Sep. 20, 2020

tested at storage temperatures of up to 770 °C, a much higher temperature compared to conventional concentrating solar power plants.

The test loop featured the solar pressurized air receiver, an air cooler and the air-to-LBE heat exchanger. It could be put into different modes of operation, namely a heat storage test mode during which the collected heat was transferred to LBE and secondly, a heat release mode where that heat was passed to the air flow and removed in the air-to-air cooler. Thirdly, in the receiver test mode, collected heat from the receiver was directly removed in the cooler, by-passing the storage system.

A tube-in-tube counter-current flow heat exchanger, made of Sandvik's 253MA steel was used to transfer heat from the pressurized air to the LBE. Stagnant tests in LBE had in a different project identified more corrosion at 860 °C compared to Kanthal – nevertheless, in spite of 185 µm corrosion depth vs. 7 µm in Kanthal APMT under not specified oxygen concentration values, 253MA was selected for the intended short term operation due to cost constraints and available welding personnel and equipment. The heat exchanger consisted of two five meter long straight sections connected by an U-bend with LBE flowing in the resulting annulus and air flowing in the inner tube. Controlled LBE flow from the cold tank to the hot tank at the required high temperatures was successfully generated by differential argon hydrogen cover gas pressure. The tank levels were monitored with a laser distance meter and ceramic coated thermal couples. LBE was pre-hated with resistive electric heaters in SiC-C crucibles to 490 °C and further heated in the heat exchanger to 770 °C.

The test system was mounted on top of CSIRO's solar tower with a LBE volume of 0.190 m^3. It was tested at 70 % part load condition with the air at an inlet temperature of 824 °C was cooled to 605 °C while LBE was heated from 490 °C to 770 °C. Unfortunately, no experimental but only design mass flow rates are reported, being 0.728 $kg\,s^{-1}$ for LBE and 0.105 $kg\,s^{-1}$ for air.

The authors of the report on this system's performance were satisfied to have successfully demonstrated the integration of a liquid metal-based ther-

mal storage system into the air receiver and air turbine system, indicating that indeed liquid LBE systems can be designed and operated with available design tools.

1.4 A Liquid metal-cooled solar tower system study (DLR)

Between 2012 and 2017, the German Helmholtz Association funded the LIMTECH research alliance worth 20 million Euros in order to amplify synergies among German research centers seeking improvements in liquid metal technology. Beside applications such as continuous steel casting, separation technologies and measurement techniques also the application of liquid metals as heat-transfer fluids in concentrating solar thermal power plants was one major research field in this program.

This was motivated by the fact that in many industries liquid metal technology development had been continued since the receiver tests in Almería. This should in principle have improved design methods and operation of liquid metal cooled solar power plants compared to the past.

The German Aerospace Center DLR participated with a strong background in STE research and the task of conducting a detailed techno-economical system study in collaboration with the Karlsruhe Institute of Technology with its strong background in liquid metal technology. KIT was supposed to contribute advice and experimental results for the validation of the simulation results.

At DLR, A. Fritsch performed detailed numerical simulations of solar tower concepts operated with the state-of-the-art heat-transfer fluid solar salt compared with liquid sodium and LBE [29]. For the comparison, annual simulations of power plants with an electric power of 125 MW in the location of Postmasburg, South Africa were performed.

Fritsch assessed plants with a single tower central receiver with a thermal power of 700 MW but also a multi-tower system with five individual receivers instead of one. Several towers distributed among the same sized

heliostat field reduce the maximum distance between the available heliostats and the receivers. This improves the heliostat field's efficiency, however, at the cost of increased piping length and potentially increased tower costs.

All cases consisted of complete plants, including a thermal storage and power cycle.

For comparability with a reference salt system, the operating temperature range of the liquid metals was limited to that of the salt system, thus penalizing the metals which could in principle operate at lower and higher temperatures than solar salt.

Currently, no state-of-the-art commercial thermal storage system exists that uses liquid metal as heat storage fluid. A. Fritsch therefore assumed two-tank molten salt thermal storage for all concepts assessed in the study at the disadvantage of additional heat exchangers in the liquid metal plants required to transfer heat to the salt thermal storage system.

Fritsch found a cost reduction potential in his sodium operated single-tower concepts of up to 16 % compared to state-of-the-art solar salt systems. This reduction is achieved due to reduced parasitic losses from pumping and trace heating and due to reduced manufacturing costs of the receiver, which can be built much smaller and lighter than for the use with molten salt.

For multi-tower arrangements, cost reduction potential of more than 8 % is obtained for sodium. This results again from strongly reduced receiver costs.

For LBE, Fritsch found a cost reduction potential of up to 6 %.

General advantages identified in these studies include that during design operation, sodium's Reynolds number is approximately ten times larger than that of solar salt. That Reynolds number is linear with the power input so that turbulent heat transfer is maintained even at operating conditions where solar salt attains laminar flow already. The use of sodium allows furthermore a receiver design with fewer serial panels. This results in significantly reduced flow transit times which leads to benefits in the receiver control.

2 The SOMMER project: Re-evaluation of liquid metal solar technology

After excellent results had been generated in Almería and before the catastrophic failure had occurred, a report on the experiments at design conditions was published [26, p1.-3]. It states that at the start of the plant design process, everyone had expected to be able to demonstrate a power plant in commercial scale. During the process, everyone had then realized that this could not be achieved. Rather, 'prototype plants' had been tested instead in the view of the authors. After the completion of these tests, they had expected that, with the lessons learned throughout the project, commercial plants could now be developed.

Is this still true today, a quarter of a century later?

By now the practical experience collected by individuals in these experiments has probably been dismissed to retirement. The state of knowledge once established is most likely lost except for what was written in reports. On the other hand, knowledge in liquid metal technology has improved in other technical fields since then, making new efforts in applying liquid metals to solar thermal power generation very promising. The successful implementation of the experiments at CSIRO and the demonstration plant by Vast Solar may support the latter statement.

The fact that the promising nature of liquid metals in STE once seen in Almería has a theoretical cost reduction potential today, as identified in the system simulation by A. Fritsch, justifies more efforts.

But could we actually build commercial metal-cooled plants today, as it is intended by Vast Solar, or will we have to recognize, too, that more prototype plants are first required to re-learn the skills?

It is the intention of this work to provide answers to this question. An experimental solar powered liquid metal loop is therefore designed, build and operated.

Small model testing is convenient when critical effects during operation can only be predicted with difficulty or uncertainty with the available design tools. Furthermore, it provides great operational flexibility. Finally, only through testing, unexpected operation difficulties can be revealed.

One example of difficult-to-predict effects that arise in the model receiver are those from the non-uniform heat flux boundary condition, both in axial and circumferential direction present in solar thermal receivers. Forced and natural convection losses as well as thermal radiation losses super-impose these effects and make them difficult to distinguish in large-scale receivers. These losses can be suppressed in the experimental model setup in order reveal the impacts of the different simultaneously present boundary conditions. Since there is no significant negative impact of freezing coolant on the project success, the model receiver can be operated at low temperatures thus reducing natural convection losses and thermal radiation losses.

In contrast to the CSIRO project, which aimed at solar air turbine technology, in this work design tools, the process technology and the liquid metals' performance under direct solar irradiance in tubular, liquid cooled central receivers are re-assessed.

In spite of the fact that commercial activities applying sodium as heat-transfer fluid have been picked up recently, the need for public experimental work persists: the details on the technology applied and the operation experience from those privately conducted facilities is likely to be kept secret as the company's intellectual property.

Vast Solar, interested in commercial operation is furthermore not likely to apply extreme operating conditions such as flux density and outlet tem-

perature to their equipment. Only in laboratory conditions such conditions' impact can be assessed safely.

More public information on the design process and the operation is required, as even public works often don't provide a complete picture. For example, the ASME conference publication on CSIRO's LBE storage system test [28] does, unfortunately, not contain detailed thermal-hydraulic design targets as, for example, heat transfer coefficient values. The conclusions are not based on a clear figure-of-merit success or failure criteria which enable to scientifically judge LBE's performance.

It is therefore necessary to conduct experimental work in order to regain lost experience in liquid metal technology for solar thermal power generation, to validate the findings reported in the earlier demonstration systems and the predictions based on numerical simulations, to complement public experimental findings, to demonstrate technological advancement that has occurred in the mean time and, finally, to identify potential further demand for research.

This task was given to KIT's liquid metal laboratory within the LIMTECH framework. Its execution is described within this thesis.

The main focus is on the coolant performance in the thermal receiver, as this component must operate under the most critical conditions in the coolant cycle of solar power plants. This performance is theoretically assessed in terms of thermal-hydraulic behavior, operation limits and cost-contribution factors associated with the coolant operation.

The experimental loop's scope is slightly broader: Three receiver operation targets are specified: Operation at average heat flux of more than $1\,\mathrm{MW\,m^{-2}}$ at an outlet temperature of 600 °C and at a Reynolds number in a range which will be present in commercial-scale receivers. Its value is to be determined in this thesis. All three targets shall simultaneously be obtained during the loops' operation.

Besides this general demonstration of a working principle, the receiver's thermal efficiency and the liquid metal's heat transfer performance in straight

receiver tubes is studied as careful and as detailed as possible within the constraints of the experimental setting.

Also, the receiver outlet temperature shall be kept constant under the fluctuating nature of the solar power source. It must be demonstrated that knowledge in liquid metal technology enables to design the remaining LBE loop's components, namely the pump, the heater and the cooler appropriately in order for this difficult control task to be achieved.

The limitation of the scope on the thermal receiver's performance is justified by the parallel works executed within the LIMTECH alliance: DLR's simulation system studies cover all conventional plant components which can be maintained if liquid metal replaces solar salt in the coolant loop.

One major plant component which is directly influenced by the selection of the primary coolant is the thermal storage. In spite of the fact that direct two-tank storage solutions have been applied in the Almería experiments and that two-tank storage is today applied by Vast Solar, these have an economical disadvantage compared with direct molten salt storage systems. Therefore, such a direct thermal storage system has not been introduced into the experimental loop.

At KIT, in parallel to the work presented here, instead Klarissa Niedermeier numerically assessed additional storage options for plants using liquid metal in the primary coolant loop. She identified the economic competitiveness for direct liquid metal based storage systems in solid particle packed beds [30], [31]. If these particles are cheap, the costs for using sodium are reduced to the same level as when salt is used in these packed beds.

3 LBE: dense, hot and brilliant?

In spite of sodium having already proven its outstanding performance in central receivers, there has also been demonstrated its inherent operational risk, making the identification of alternative HTFs, beyond solar salt's limits, a requirement. Consequently, the following sections discuss several criteria for heat-transfer fluids and specifically for the case of LBE, which has had limited application in STE systems. Wherever suitable, the properties of LBE are compared to those of sodium and solar salt, which is currently the state-of-the-art heat transfer and direct storage fluid.

Lead and bismuth exhibit a melting point of 125 °C if mixed in the eutectiic composition, i.e. at mass specific 44.5 % Pb and 55.5 % Bi. This eutectic mixture is then liquid in a very large temperature interval up to 1638 °C [32] and has a high thermal conductivity and low viscosity. It can be pumped and be used as coolant in heat transfer devices while being chemically stable throughout this range.

LBE has been selected for this demonstration for the following reasons:

- LBE has attracted only little scientific interest for the application in STE in the past. A systematic assessment of its suitability including theoretical and practical experience is missing in literature.

- Sodium's inherent operational risk was clearly demonstrated in the Almería fire. Therefore, strong concerns exist in the solar thermal community against taking it into consideration for commercial operation again. LBE is free of this risk.

- Experimental work benefits from this passive nature of LBE as well. For example, re-configuration of a once-established LBE loop for new experiments is facilitated.

- LBE has the heat transfer characteristics typical for liquid metals that result from their very high thermal conductivity. Experience obtained with LBE provides a strong basis for the application of other liquid metals.

This selection was made in spite of several indicators that predict inferior performance of LBE compared to sodium and even to solar salt in many aspects. For example, the authors in the CSIRO report on LBE test, Kim et al. [28] note that LBE's density and costs make an application in high capacity storage systems unlikely, although the expected good heat transfer characteristics were validated in the tests. The following sections of this thesis will add further limitations of LBE in the context of STE.

Nevertheless, in spite of these constraints and the material cost A. Fritsch found a cost reduction potential for LBE compared to solar salt. This justifies the selection of LBE for demonstration purposes even if LBE will be used only in the receiver in combination with molten salt storage systems.

3.1 LBE's thermo-physical properties and their impact on its cooling performance

The physical properties of LBE, sodium and solar salt which are most important for the thermal-hydraulic design of central receivers are shown in Figure 3.1, plotted over the temperature.

These properties are the density, the heat capacity at constant pressure, the thermal conductivity and the dynamic viscosity. The properties of solar salt and sodium are plotted approximately within their operating temperature ranges, thus, where they are liquid. LBE's liquid temperature range is larger

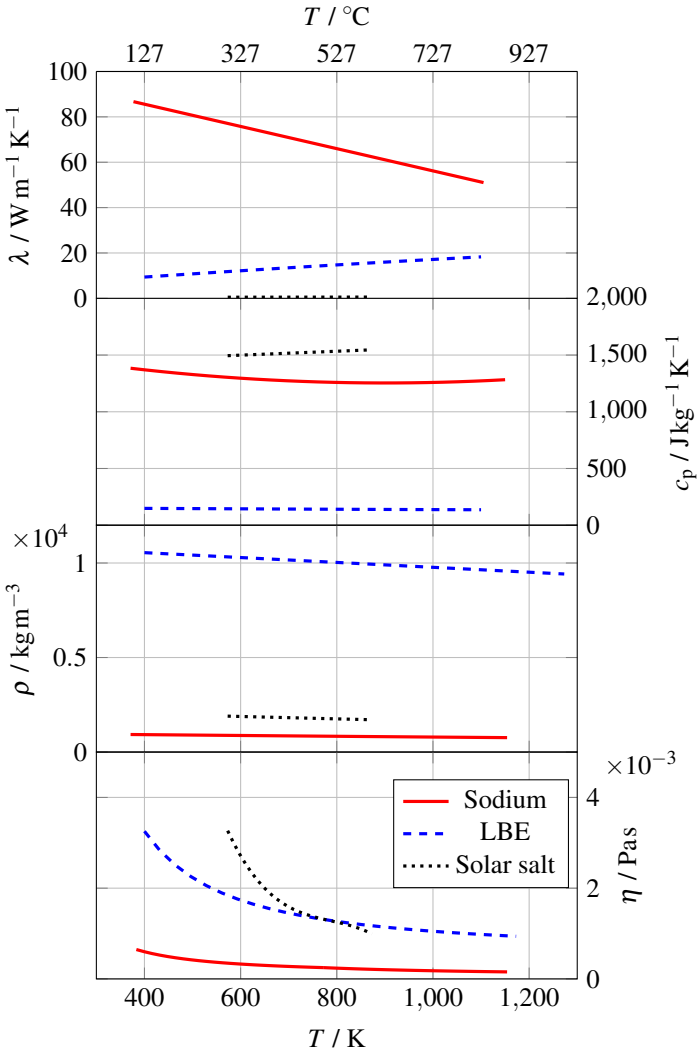

Figure 3.1: Thermo-physical properties of solar salt, LBE and sodium in the applicable temperature ranges of the property correlations within the liquid state temperature ranges. Correlations for sodium are obtained from Ref. [33], for LBE from Ref. [32], and for solar salt from Ref. [23].

than shown, it is of the three coolants thus the fluid with the highest boiling point.

Average values of these and additional properties are listed in Table 3.1. They are averaged in the temperature range of 301.85 °C to 596.85 °C which can be viewed as a potential range of operation in a solar thermal power plant.

Of all three fluids sodium has the highest thermal conductivity, being more than 100 times that of solar salt. LBE ranges in-between with values more than 20 times that of solar salt. Due to generally low dynamic viscosity values of LBE and salt and a very low value of sodium the liquid metals differ significantly from solar salt in their value of the Prandtl number which is for both metals much lower than 1. This fact strongly impacts the metals' heat transfer behavior and makes their special treatment during the design of heat transfer devices a requirement.

In flows of the same Nusselt number and the same diameter the liquid metals' convective heat transfer coefficient is much larger than that of solar salt. On the other hand, at identical values of convective heat transfer coefficient the conductive heat transfer is dominant in liquid metals.

LBE's density is significantly higher and its mass specific heat capacity is significantly lower compared to solar salt and sodium. Both properties are more or less constant with the temperature for all fluids. The volume specific heat capacities of LBE, sodium and solar salt are, respectively and at $T = 700\,\mathrm{K}$: $1.088 \times 10^6\,\mathrm{J\,m^{-3}\,K^{-1}}$, $1.45 \times 10^6\,\mathrm{J\,m^{-3}\,K^{-1}}$ and $2.76 \times 10^6\,\mathrm{J\,m^{-3}\,K^{-1}}$. Thus, beneficial effects from LBE's high density are diminished by the low mass specific heat capacity and sodium's high heat capacity cannot make up for the negative effects of its low density. Both are consequently less suitable for direct thermal storage than solar salt.

LBE's high density further leads to several mechanical issues in large-scale receivers: Its high static pressure leads to a large thickness of the tube wall. Under thermo-mechanical stress and strain due to the fluctuating high solar flux this wall thickness reduces the lifetime compared to salt or sodium

Table 3.1: Physical properties of solar salt, liquid sodium and liquid LBE averaged in the temperature range of 575 K to 870 K (301.85 °C to 596.85 °C). Correlations for sodium are obtained from Ref. [33], for LBE from Ref. [32], and for solar salt from Ref. [23].

physical property	solar salt	liquid sodium	liquid LBE
lower temperature limit, K (°C)	457.15 (220)	371.5 (98.35)	397.7 (124.55)
upper temperature limit, K (°C)	873,15 (600)	1156.15 (883)	1943.15 (1670)
heat capacity, c_p, $\mathrm{J\,kg^{-1}\,K^{-1}}$	1520.3	1278.7	142.1397
thermal conductivity k, $\mathrm{W\,m^{-1}\,K^{-1}}$	0.5284	69.7818	13.7135
density ρ, $\mathrm{kg\,m^{-3}}$	1804.2	850.7998	10131
dynamic viscosity, μ, Pa s	0.0021	0.0002759	0.0015
Prandtl number, Pr, –	6.2126	0.005	0.0165

receivers [29]. The receivers are installed on top of towers, in the case considered by Fritsch [29] with a height of more than 200 m. On the tower base static pressures of more than 200 bar result. The respective riser and downcomer tubes require significantly large wall thickness, deemed to be too unlikely to be applied by Fritsch to further consider such a case. Instead the case of a small LBE loop with a metal to salt heat exchanger on the top of the tower has been assessed.

This case resulted in a reduction potential for the levelized cost of electricity generation (LCOE) of up to 6% compared to the reference case with salt, mainly due to the possibility to reduce the aperture area (cheaper construction cost) and to operate at increased heat fluxes. Despite the reduction of the receiver size by almost the factor of two the coolant-filled LBE receiver is nearly four times heavier than the salt receiver. Such a significant weight addition may result in increased cost of the tower structure itself. This impact is not assessed by Fritsch and is thus not included in the result of 6% reduction of LCOE.

Does the metals' high thermal conductivity make them superior coolants? Heat transfer to a coolant flow is an irreversible process and thus associated with the generation of entropy. That generation of entropy is proportional to the destruction of exergy and thus the destruction of the potential to perform work. A good coolant should therefore allow heat to be transferred with low generation of entropy.

This property was assessed under conditions typical for concentrating solar thermal central receivers for the three coolants solar salt, sodium and LBE. The approach of an entropy generation minimization study as proposed by Bejan [34, pp.78–82] and the results of that study are described in more detail in Ref. [35]. It is based on an algebraic minimization of the two additive contributions to entropy generation, namely the dissipation of pumping power on one hand and the temperature mixing along the radial temperature gradient between inner tube wall and bulk flow. By increasing the rate of turbulence in the flow i.e., by increasing Reynolds number, the

radial temperature difference is decreased, however, at the cost of increased pressure drop and increased requirement for pumping power. There exists one unique Reynolds number for such problem where the sum of entropy generation from both contributions is minimized.

Heat transfer devices have to be designed to operate at this optimum Reynolds number. Then, they operate then at their highest efficiency. At this condition different coolants' efficiency can be compared.

The pumping power requirement is in fact a significant individual cost factor of different coolants. Fritsch [29] found that the annual financing costs of the receiver coolants are much lower than the annual operating costs, dominated by the pumping. In case of LBE the former make up for 1.1 % due to LBE's high price and the latter make up for about 1.3 % of the total annual financing costs due to its high density, viscosity and low heat capacity. In comparison, the financing costs of solar salt make up for way less than 0.1 %.

Figure 3.2 shows the dimensionless entropy generation number[1] N_S of solar salt, sodium and LBE for the case of turbulent tube flow with uniform heat flux at a thermal power of 660 kW and an axial temperature increase of 275 K over a range of Reynolds numbers. When looking closely at the optimum Reynolds numbers, that is, where the entropy generation is minimized, LBE shows a slightly higher generation of entropy than solar salt. At these conditions LBE is therefore not better suited as a coolant than solar salt. More detailed explanation of N_S and the applied methodology are given in Ref. [35].

The fact that LBE is comparably efficient in spite of its high pumping effort is due to its high thermal conductivity which compensates the entropy generation from pumping. This concludes that the high value of thermal conductivity alone is not a sufficient indicator of great performance as heat-transfer fluid. LBE's high density and low heat capacity nearly eliminate

[1] That is the rate of entropy generation $\dot{S}_{\mathrm{gen}}$ normalized by the transferred thermal power $\dot{Q}$ and the average tube temperature T_{m}

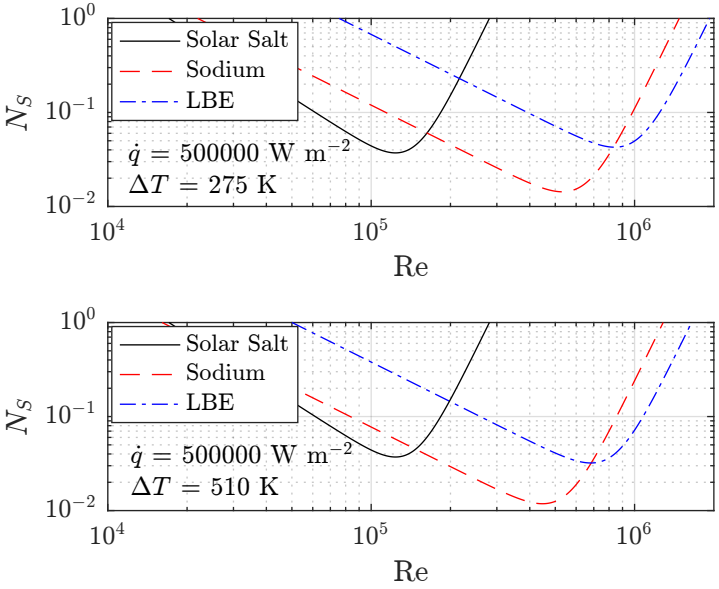

Figure 3.2: Calculated entropy generation numbers of solar salt, sodium and LBE. Top: all fluids operating in the same temperature range. Bottom: outlet temperature of LMs raised to 800 °C, whils salt is still working in previous range.[35]

the benefits arising from a high thermal conductivity while sodium features property values which enhance the good performance.

In case the outlet temperature is raised for the liquid metals under otherwise identical conditions the liquid metals operate optimally at reduced Reynolds number and reduced entropy generation. LBE is then in principle able to operate at slightly lower entropy generation than solar salt.

Sodium is able to operate at much lower generation of entropy than the remaining two coolants in both cases.

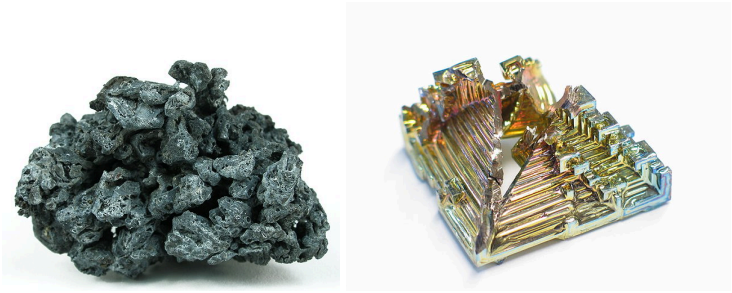

Figure 3.3: Left: Naturally occuring lead in rare form of hoppered growth crystal found in the Langban Mine in Sweden (5 cm length). By Rob Lavinsky[2]; Right: Bismuth crystal with iridescent thin oxide layer, (about 3.5 cm length). By Dschwen[3].

3.2 LBE's availability

While LBE was easily obtained in the required amounts and at reasonable costs for the SOMMER facility with a thermal power of 10 kW (it was taken from an existing loop), this must not be the case for an intended use in large scale applications. Current conventional tower plants typically have an electric power output of 100 MW to 150 MW [29].

Boungiorno [36] compared the cost of LBE with those of pure lead, sodium and heavy water to be used in a LBE cooled fast nuclear reactor. He found that LBE has costs higher than sodium and pure lead and lower than heavy water. He expected that the advantages inherent in LBE would lead to simplifications in the plant design which would compensate the additional cost of LBE. However, it is not certain that LBE will lead to simplifications in the design of a solar tower.

[3] Image by Lavinsky: SiRocks.com, https://de.wikipedia.org/wiki/Datei:Lead-288819.jpg – CC-BY-SA-3.0, https://creativecommons.org/licenses/by-sa/3.0/deed.deLast accessed: Sep. 20,2020

[3] Image by Dschwen:https://commons.wikimedia.org/wiki/File:Bismuth_crystal_macro.jpg, CC BY-SA 3.0, https://creativecommons.org/licenses/by-sa/3.0/deed.enLast accessed: Sep. 20,2020

The following example shall provide a reference case to help determine whether there is a sufficient availability of lead-bismuth eutectic with a mass specific composition 44.5 % of lead and 55.5 % of bismuth:

A six hour two-tank direct storage system for the delivery of a thermal power of 700 MW to the power block would require a mass flow rate of LBE[4] of 19 094 kg s^{-1}. The storage would have to contain 412 439 tons of LBE at 550 °C to be cooled down to 290 °C in the steam generator. This amounts to 183 535 tons of lead and 228 903 tons of bismuth. Is this too much with respect to the global resources and markets and is it commercially feasible?

Lead concentrations in the earth's crust high enough to economically extract pure lead from them exist in association with zinc, silver and copper deposits in Australia and China and other countries and amount to more than 2 billion tons globally [37]. The reserves[5] are 89 million tons. The global mine production in 2015 was 4.7 million tons while the global *refined* lead production of that year was expected to be 10.9 million tons by the International Lead and Zinc Study Group [39]. China and Australia have the largest mine productions with 2.3 million tons and 0.6 million tons respectively annually [37]. The global production rate equaled the global consumption rate in 2015. For example in the United States, lead is used mainly in the lead-acid battery industry for the automotive industry and for stationary standby power sources [37]. In 2015 the U.S. consumed 1.62 million tons of lead apparently, 69 % of which was secondary lead, meaning it was recovered from old scrap. That year the average price of lead was 1.83 \$ kg^{-1} while in October 2014 it had been 2.04 \$ kg^{-1} [37]. In Germany, according to the

[4] LBE has a heat capacity of 141 J kg^{-1} K^{-1} at 873.15 K (600 °C). Properties of LBE can be found in Table 3.1 on page 25 and in Figure 3.1 on page 23.

[5] 'Reserves' are defined as the part of identified resources which are available at a minimum required grade, quality, thickness, and depth in terms of mining practices and the extraction of which is economically feasible at the time of the resources' discovery [38].

Genesis database of the German 'Statistisches Bundesamt[6]', for the year 2015 the lead imports of 56347 tons in Germany happened at an average price of $1.82\,\$\,\mathrm{kg}^{-1}$.

Bismuth is approximately twice as abundant as gold in the earth's crust and much rarer than lead. Bismuth is often contained in lead ore and therefore a by-product of lead production. In other countries it is also a by-product of tungsten production and other metal ore processing. In 2015 the estimated world wide mine production of bismuth was 13600 tons. There are reserves of 370 thousand tons [40], thus two orders of magnitude smaller than those of lead. 1504 tons of bismuth worth 23 million USD were apparently consumed in the U.S. in 2014, two thirds of which used in chemicals for cosmetics, industrial laboratory and pharmaceutical applications [40]. Lead consumption is therefore one thousand times higher than bismuth consumption in the U.S. Bismuth is also applied in ceramic glazes, crystal ware and pearlescent pigments and can serve as replacement of lead in metallurgical applications, such as in brass, steels solders and other applications. Since lead was banned from drinking water fixtures and pipes, bismuth has gained market share in lead-free components of water pipe networks. Other applications include bismuth as triggering mechanism in fire sprinklers, optical lens manufacturing and semi-conductor production. According to Ref. [40] at the end of 2014 the price of Bismuth was $13.66\,\$\,\mathrm{kg}^{-1}$ after it had been $24.03\,\$\,\mathrm{kg}^{-1}$ at the beginning of 2014. This was due to two factors: the first one being a financial crisis of a metal exchange company that froze traders' accounts and the second one a suspended investment product that was unable to deliver the guaranteed annual returns to holders.

The German 'Statistisches Bundesamt' states a German import in 2015 of bismuth and bismuth products of 839 tons at an average price of $14.95\,\$\,\mathrm{kg}^{-1}$.

[6] which can be publicly accessed here: `https://www-genesis.destatis.de/genesis/online/logon?language=en,`, last accessed: Sep. 20, 2020. The commodity classification ID for raw lead is 7801, for bismuth and bismuth products it is 8106

The resulting price of LBE, based on the values of the end of 2014 from Ref. [37] and Ref. [40] is approximately 8.5 $\$\,kg^{-1}$.

The amount of 183 535 tons of lead and 228 903 tons of bismuth for a six hour storage of a single power plant would represent 15 % of the annual U.S. secondary refinery production of 2014 of lead and 62% [37] of the world's known reserves of bismuth! Bismuth is clearly not available in sufficient amounts to make storage in LBE possible. Even if it was, the costs under a cost assumption of the above mentioned 8.5 $\$\,kg^{-1}$ (2014) result in storage fluid costs of 3.5 billion U.S. Dollars!

To put this value in perspective with regard to alternative heat-transfer fluids: under identical assumptions for the storage capacity and temperature range, the cost for the fluid alone in a two-tank direct storage for sodium are 91.4 million U.S. Dollars and 50 million U.S. Dollars for solar salt. (At 2 $\$\,kg^{-1}$ for sodium [41] (Prices vary; according to Genesis between 2015 and 2018 sodium's average import price to Germany increased from 2.4 $\$\,kg^{-1}$ to 2.87 $\$\,kg^{-1}$)[7] and at 1.3 $\$\,kg^{-1}$ for salt [42].)

Clearly, the cost for using LBE in that storage concept would lead to a value much too high to be economically feasible.

Even in packed bed direct storage systems as assessed by Niedermeier LBE is too expensive to be used. Niedermeier [43] assumed mass specific costs of LBE to be 12 times higher than of salt and four times higher than of sodium identified for a storage working in the range between 290 and 565 °C that this storage is 21 times more expensive than with solar salt and 17 times more expensive than with sodium.

Due to the high price of the fluid it is more likely that only the receiver can be operated with LBE. Thermal storage will be done with other media. The tubes in a thermal receiver with a thermal power of 700 MW power[8] contain about 34 m^3 of LBE which, at costs of 8.5 $\$\,kg^{-1}$, amounts to 2.86 million

[7] The commodity code for sodium in the German Genesis database is 280511

[8] Assumed here are tubes with 60 mm outer diameter and an average flux on the receiver of 1 $MW\,m^{-2}$ Mw/m^2

U.S. Dollars. While that amount represents an insignificant share of the annual mine production of lead, such receiver would consume about 1.4 % of the annual mine production of bismuth. For the riser and downcomer tubes, the heat exchanger/steam generator as well as for the pump sumps and drainage tanks additional fluid will be required. Sufficiently long-term planning of the bismuth purchase is likely to be required, especially in case a larger number of plants shall be installed. This is even more important as there have been strong fluctuations observed in the bismuth price in the near past due to actions of some of the few actors in the bismuth market.

3.3 LBE's safety

The historic severe accidents have demonstrated the significant damage potential of liquid sodium in contact with air and moisture. Solar salt bears small operation risk due to its being a nitrate mixture and nitrates being oxidizing agents. Thus, when in contact to organic material, such as mineral oil ignition, combustion and even explosion may result [44]. This makes the integration of molten salt storage systems in parabolic trough plants with thermal oil as HTF problematic if an oil-to-salt heat exchanger is required, but this is not problematic for central receiver systems.

LBE in contact with the ambient atmosphere shows a low reaction-enthalpy oxidation. Its main risk for humans is due to its potentially harmful temperature when leaking. This risk can largely be mitigated by collecting grooves in which leaked fluid can be detected automatically.

Furthermore, bismuth is no serious health risk but lead is highly toxic. Therefore its inhalation, ingestion and absorption into the body must be prevented. Airborne lead, for example as dust, bears the threat of being inhaled and then absorbed to the blood stream in the lungs.

During plant operation in STE application the LBE is contained in the loop and no exposure to lead and lead vapor occurs on a regular basis. Only during initial filling and during regular maintenance works contact is possi-

ble and special attention has to be paid to safety. An overview on existing labour regulations for lead work is compiled in [32, p.910].

An exceptional event in LBE loops with potential formation of lead-containing dust and fumes is that of a spray leakage in tubes, fittings or instruments uncovered from insulating material.

Overall LBE is considered to be much safer for experimental works and therefore selected as the heat-transfer fluid for the SOMMER loop.

3.4 LBE's corrosion behavior

Typical structural steels may suffer from corrosion in LBE [11]. The alloying elements of steel have different solubilities in LBE, are susceptible to react with non-metallic impurities in the flow and can be removed from the steel matrix by forces that result from high flow velocities and mechanical impact. Respectively, corrosion therefore can simultaneously occur controlled by dissolution, oxidation, erosion corrosion and fretting corrosion.

By superficial and intergranular dissolution alloying elements are removed from the structural steel. The potential for dissolution is high at high temperatures where a higher solubility for the alloying elements occurs. The dissolved elements may then be deposited on surfaces with low temperatures in the system.

Oxidation can prevent the dissolution attack on structural steel. It is an important strategy to prevent corrosion in LBE to control the oxygen content.

The structural material can be eroded from high-velocity flow of LBE. High shear stresses can strip a protective oxide layer away. And the renewal of the oxide layer on the underlying steel can accelerate the degradation.

Vibrations of the surfaces in contact with LBE can destabilize the corrosion barriers as well. Erosion and fretting corrosion can both enhance the dissolution attack.

Oxides of the coolant form when the oxygen content is higher than the solubility. The upper solubility limit of oxygen in LBE is given by the saturated oxygen concentration C^*_O

$$\log C^*_{O,(wt.\%)} = 2.25 - \frac{4125}{T_{(K)}}, \tag{3.1}$$

for the temperature range $400\,°C < T < 740\,°C$ [32],[45],[46]. The main oxide formed in LBE is lead monoxide PbO.

As long as the oxygen content is below this maximum value no coolant oxide is formed. On the other hand a stable oxide film is desired on the inner tube wall formed with elements of the steel structure. Such a film inhibits the dissolution of elements, primarily nickel and iron from the steel matrix into LBE. This requires a minimum oxygen concentration in the flow, if stainless steels are used. At oxygen concentrations too high, however, an oxide layer on the wall grows rapidly and causes degradation of the structure. The element first to release oxygen to lead at low oxygen concentrations in the coolant is iron. The oxygen concentration at which this occurs is

$$\log C_{O,\min\,(wt.\%)} = -\frac{3}{4}\log C_{Fe,(wt.\%)} + 2.28 - \frac{10465}{T_{(K)}}, \tag{3.2}$$

with,

$$\log C_{Fe^S,\min\,(wt.\%)} = 2.01 - \frac{4380}{T_{(K)}}, \tag{3.3}$$

in a temperature range $550\,°C < T < 780\,°C$ [32].

In a system where the hottest surface has a temperature of $T = 650\,°C$ as in the SOMMER receiver the lowest weight specific oxygen concentration is $C_{O,\min} = 1 \times 10^{-7}\,\%$.

Because of these limits LBE can be operated only within a constrained temperature and oxygen concentration window. With an increasing maximum operation temperature the oxygen content must increase to prevent

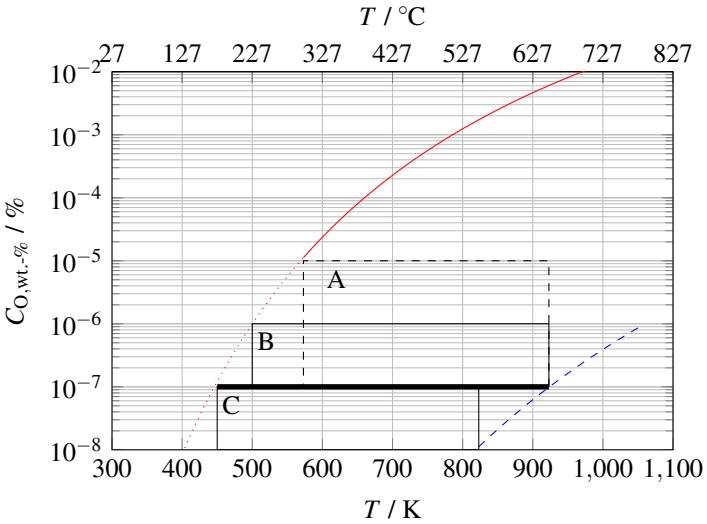

Figure 3.4: Oxygen concentration limits in LBE as a function of the liquid solid interface temperature. The upper concentration limit (red solid line) indicates the oxygen concentration at which lead oxide is formed because the saturation concentration is reached [45]. (The dotted red line extends the plot to temperatures outside the applicable range of the correlation.) The blue dashed line indicates the lower limit of oxygen, just enough to prevent iron oxide to release the oxygen ion to the lead-bismuth [32]. Frames A,B and C indicate operation windows at different temperature levels and oxygen concentration levels known with varying uncertainty.

the removal of the protective oxide film on hot surfaces. That oxygen concentration, however, prohibits low temperatures where lead oxide is formed. Of the temperature range throughout which LBE is liquid therefore only a reduced portion can be utilized during operation. Figure 3.4 shows such windows for operation between 570 K and 920 K in a black dashed frame (A) and between 500 K and 920 K in a solid black frame (B). The wider the window is defined the less tolerance exists for the oxygen concentration in order to prevent corrosion.

For operation in the SOMMER facility the LBE should be saturated with oxygen before start-up by adding lead- and bismuth oxide pellets to the sump tank. After sufficient time equilibrium can be achieved. The temperature at which this saturation must be attained depends on the desired highest temperature during operation: When LBE is saturated at 450 K with $C_{O,min} = 1 \times 10^{-7}$ % it could be heated to 920 K under the assumption that the oxygen is exactly at equilibrium. (This operation 'window' is indicated in Figure 3.4 with a black thick solid line.) If one assumes uncertainty in the concentration value of about one order of magnitude the maximum temperature is 800 K (indicated by frame C). In order to allow for a peak temperature of 920 K the saturation would have to be performed at 570 K (frame B). If the uncertainty in the concentration value is assumed to be two orders of magnitude the black dashed frame A indicates the operational window and saturation would have to be performed at 570 K. With this safety margin applied, LBE's theoretical asset of a large operational temperature range is lost at the lower temperature end: No benefit exists to solar salt, which has a melting point of 560 K because both fluids require trace heating at at least 560 K. Maximum process temperatures above 920 °C will require an even higher minimum temperature.

3.5 Heat transfer: Nusselt number calculation

While the liquid metal technology is quite mature regarding its application in nuclear power generation, the same does not automatically hold for its application in solar thermal power generation. Different thermal conditions arise, most prominently the fluctuating and cyclic nature of solar power input.

Also the intended magnitude of local heat flux and the non-uniform exposure of cooled elements to this flux make significant differences to state-of-the-art liquid metal operation. Therefore, existing design tools are assessed for their applicability in solar receiver design in the following section.

The scope of this assessment is limited to engineering correlations for basic design. Available numerical methods such as CFD for detail engineering are not considered. Existing methods that account for the low Prandtl number fluid dynamics are, however, described in Ref. [32] and have been applied in the context of this project, for example in Ref. [47].

Numerical methods for the assessment of mechanical stability are as well beyond this work's scope as their application is not specific for liquid metal heat-transfer fluids. These methods, such as finite element analysis use thermal boundary conditions as an input. These conditions again result from liquid metal thermal-hydraulics, which are therefore carefully considered.

Liquid metal's thermal-hydraulic behavior is different from 'conventional' fluids because of their Prandtl numbers, which are much smaller than unity.

In the nuclear industry, research has therefore been conducted in the past and generated broad knowledge of the liquid metals' thermo-hydraulic behavior in a variety of flow scenarios, for example, laminar and turbulent, wall-confined, free-surface or two-phase flows under forced, mixed or natural convection, fully developed or developing [32]. Much of the existing experience and knowledge can be found in the OECD/NEA's[9] Handbook on Lead-bismuth Eutectic Alloy and Lead Properties, Materials Compatibility, Thermal-hydraulics and Technologies [32]. It will be called 'LBE handbook' in the following.

For the design of solar receivers mainly mixed- and forced-convective, single-phase flow in circular tubes under a developing and fully developed velocity profile and developing temperature profile are required. Most of these conditions are also met in additional components of the HTF cycle in a solar power plant such as heat exchangers or steam generators.

Their small Prandtl numbers cause a scale separation of the flow's boundary layers of velocity and temperature and the assumption of a constant tur-

[9] Organisation for Economic Co-operation and Development / Nuclear Energy Agency, `oecd-nea.org`

bulent Prandlt number close to unity (Reynolds analogy) does not hold. On the contrary, the thermal boundary layer is of greater thickness than the viscous layer and molecular conduction remains significant in relation to eddy conduction of heat in turbulent flow up to high Reynolds numbers. Liquid metals therefore require correlations for the prediction of the average turbulent Nusselt numbers for uniform heat flux different from those for constant wall temperature boundary conditions.

For laminar flow, on the other hand, the classical Nusselt number values for uniform heat flux ($\mathrm{Nu} = 4.364$) or uniform wall temperature ($\mathrm{Nu} = 3.6568$) can be applied, as they are independent of the Prandtl number [32, p.657f].

3.5.1 Forced turbulent convection in fully developed flows

Some of the existing correlations for constant heat flux can be applied for all liquid metals, including for example, mercury or alkali metals such as sodium and sodium potassium alloy. However, some correlations are particularly suited for specific liquid metals [48]. In a comparitive study of correlations and experimental data conducted by Pacio et al. [48] 93.3% of the data of lead and lead-bimuth eutectic resided within $\pm 20\,\%$ of the predicted values by the correlation of Lubarsky and Kaufman [49]:

$$\mathrm{Nu} = 0.625 \cdot (\mathrm{Re}\,\mathrm{Pr})^{0.4}. \tag{3.4}$$

For sodium, 83.3 % of the samples reside within $\pm 20\,\%$ of a correlation by Chen and Chiou [50]. However, only 67% of the samples of all metals considered resided within $\pm 20\,\%$ of a correlation by Skupinski et al. [51] which is best suited for all liquid metals.

The correlations were tested only for data with Reynolds numbers above 10×10^4 to account for the fully turbulent regime. For LBE this corresponds approximately to Peclét numbers above 160. Within the data base used in

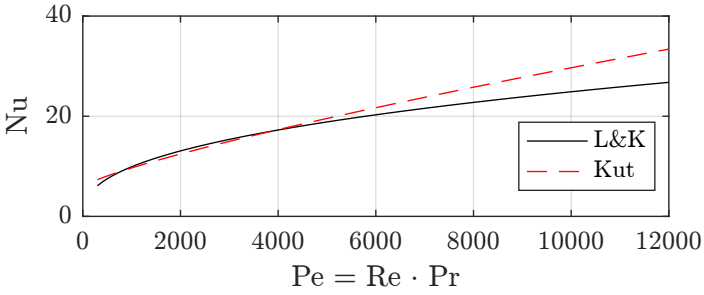

Figure 3.5: Nusselt values according to the correlation by Lubasky and Kaufman (solid black line) and Kutateladze [52](dashed red).

the assessment by Pacio et al. the five available data sets for LBE showed less scatter among each other compared to other groups of metals, indicating potentially good data quality. However, while the presented correlation represents the data of LBE well within that assessment it includes no data set of LBE at Reynolds numbers higher than 1.92×10^5 and Peclét numbers above 5×10^3. In contrast, for sodium data of up to $\mathrm{Re} = 2 \times 10^5$ and for NaK even up to $\mathrm{Re} = 8.79 \times 10^5$ have been used.

The LBE Handbook on the other hand suggests a different correlation for LBE, namely one developed originally for sodium by Kutateladze [52] :

$$\mathrm{Nu} = 5.9 + 0.0015 \cdot (\mathrm{Re}\,\mathrm{Pr})^{0.8} \tag{3.5}$$

These two correlations of Kutateladze and Lubarsky and Kaufmann agree well in the range of underlying LBE data, however, at higher Reynolds numbers they strongly deviate. This is relevant since it is expected that Reynolds number even higher than 5×10^5 will be obtained in solar thermal receivers. The deviation is shown in Figure 3.5 where the Nusselt number according to both correlations is plotted over a range of Peclét numbers that correspond to Reynolds numbers between 1.2×10^4 up to 7.3×10^5 for LBE at 400 °C, approximately.

Which one to use at high values of Reynolds? Among all correlations assessed by Pacio et al. [48] and the LBE Handbook [32] the one by Lubarski & Kaufman [49] is one of only two with a power of 0.4 applied to the Peclét number. In contrast, the vast majority applies a power of 0.8 and greater to the Peclét number. Since that power dominates at high Peclét number values and can even be found in correlations for common fluids as well (e.g. in the Dittus-Boelter correlation [53] (3.27)) and since turbulent heat transfer is increasingly dominant at higher Reynolds numbers making the flow increasingly 'common' the correlation by Kutateladze [52] may be the more appropriate choice.

The cause for the general deviations of correlations for different liquid metals – even in the lower ranges of the Peclét number – is believed to be related to differences in the experimental setups and experimental difficulties:

For example, the establishment of the intended heat flux boundary conditions and the uncertainty in the measurement of small temperature differences in literature is not of consistent quality and reliability. Indeed, different liquid metals show individual partial or no-wetting characteristics that inhibit the heat transfer at individual degrees. It may also lead to the trapping of gas in non-wetted wall cavities that can locally reduce heat transfer rates by up to 40 % [32]. Also the development of growing oxide layers and deposition of impurities on the wall can individually influence the heat transfer.

3.5.2 Mixed convection

It is generally assumed that buoyancy affects heat transfer in liquid metals 'over a wider range of flow parameters than in other fluids '[32].

Due to the relatively thick temperature boundary layer in liquid metal flows buoyant effects occur in a greater distance than in higher-Prandtl number flows [32]. Consequently, buoyancy effects have been observed in LBE

flows up to Reynolds numbers of 1.1×10^5 in upward flow for uniform heat flux.

The Richardson number:

$$\mathrm{Ri} = \frac{\mathrm{Gr}}{\mathrm{Re}^2}, \tag{3.6}$$

can be used as an indicator whether or not natural convection plays a significant role in the heat transfer process. For $\mathrm{Ri} \geq 0.002$ natural convection influences heat transfer in vertical and horizontal liquid metal pipe flow [32].

According to experimental data for upward flow in an annulus by Marocco et al. [54] the velocity profiles are influenced by the heat flux density at low Reynolds numbers of $\mathrm{Re} \approx 6.67 \times 10^4$ and lower, indicating mixed convection. For example, when heated the Nusselt number was up to two times greater compared to the case without significant heating. This observation of enhancement of heat transfer through buoyancy is backed by experiments by Jackson et al. [55], [56]. The experiments indicated differences to fluids with Prandtl numbers near unity, for example regarding the transition between forced and mixed convection and the impact on the Nusselt number when buoyancy dominates.

Other work has been done, for example by Sviridov et al. [57] and Belyaev et al. [58], who investigated mixed-convection mercury flow in uniformly heated horizontal tubes, finding increased values of perimeter-averaged Nusselt number when buoyancy is present versus the prediction of correlations for forced convection but also locally much higher wall temperatures than the average. Belyaev et al. [59] also investigated downward flow under uniform heating at $\mathrm{Re} = 20\,000$ at $55\,\mathrm{kW\,m^{-2}}$ with no significant deviation from correlations for uniformly heated fully tubulent flow. Also, mixed-convection flow under non-uniform heat flux was investigated by Melninkow et al. [60] in downward flow at $\mathrm{Re} = 35\,000$ with only half of the tube' circumference heated, showing lower average Nusselt numbers compared to predicted for forced convection (according to Lyon's correlation [61] $\mathrm{Nu_t} = 7 + 0.025\,\mathrm{Pe}^{0.8}$) at low Peclét numbers. Better agreement was

observed at higher Peclét numbers – potentially indicating that downward flow heat transfer is reduced by buoyancy.

However, neither by these works nor in the LBE handbook exist design tools to easily be applied the for engineering purposes to take buoancy into account. In principle, for geometries other than pipes existing correlations for higher Prandtl number fluids must be applied for liquid metals, too, however, the resulting error is not yet satisfactorily quantified in literature.

3.5.3 Developing flow

The LBE handbook provides a theoretically determined thermal development length of up to $L/D = 35$ for hydrodynamically developed flow and constant wall heat flux, however, without experimental validation. Only for constant wall temperature correlations for the local Nusselt number exist and they are independent of the Reynolds number. Also for simultaneously developing flow a correlation for the local Nusselt number is provided under constant wall heat flux.

The prediction of the thermal development region in hydraulically devloped flow for liquid metals is therefore subject of uncertainty.

3.5.4 Non-uniform heat flux in fully turbulent tube flow

In solar receivers the heat transfer to pipe flow is characterized by the heat flux imposed upon the outer wall of one side of the tube and the resulting radial temperature profile between bulk fluid and the outer tube wall. This profile is of interest because the outer wall temperature influences thermal losses and the axial and circumferential temperature variation impacts thermal stress and structural stability of the tube material.

As presented in the previous section, state-of-the-art correlations for the Nusselt number in turbulent liquid metal flow exist but they are valid only for the case of thermally and hydraulically developed flow and for uniform

circumferential heat flux along the circumference. The respective two conditions are not fulfilled in a thermal receiver; its tubes are heated from only one side with axially varying heat flux and a deviation from the predicted behavior according to the Nusselt number correlations is expected.

How can they be predicted? Special attention must be paid to these special boundary conditions. One is depicted in the left image in Figure 3.6 where the flux varies cosinusoidally along half of the tube perimeter while the non-heated half can be considered adiabatic. This bondary condition results geometrically from the parallel rays of light imposed upon the curved tube wall and the individual tubes being arranged in banks without gaps in-between individual tubes.

The right image shows an artificial boundary condition type where the tube is heated with a constant heat flux along only half of the perimeter. This theoretical situation is better suited for the following discussion on the effect of such a non-uniform distribution on the heat transfer characteristics of liquid metals.

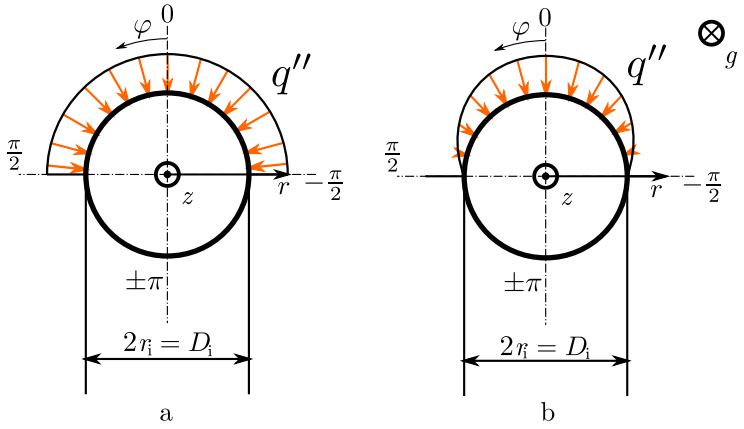

Figure 3.6: Sketch of a real (a) and an artificial (b) surface heat flux distribution on an absorber tube of a solar tube receiver

Figure 3.7 shows two longitudinal cross-sections of tube flows under fully developed forced convective flow that are heated from the outside. Gravity is neglected. In both graphs the resulting temperature profile of a fluid with a Prandtl number of unity is shown as solid line and that of a Prandtl number much smaller than unity (such as liquid metals) as a dashed line. Note, that in order to illustrate the difference in those two fluids' behavior the profiles are plotted over a common axis along a non-dimensional diameter, or $2r^*$, where, however, the absolute diameters under otherwise equal boundary conditions are different for both fluids. Both cases shall have the same velocity profile, bulk temperature and average wall temperature. For each fluid, however, the diameter is constant for the left and the right case. Suppose that in the left graph the flow is heated with constant heat flux along the entire perimeter. In the right graph that tube is heated with constant heat flux along half of the perimeter, however, with twice the flux density compared to the case depicted at the left. This way the powers added to fluids of the same Prandtl number are identical in both graphs.

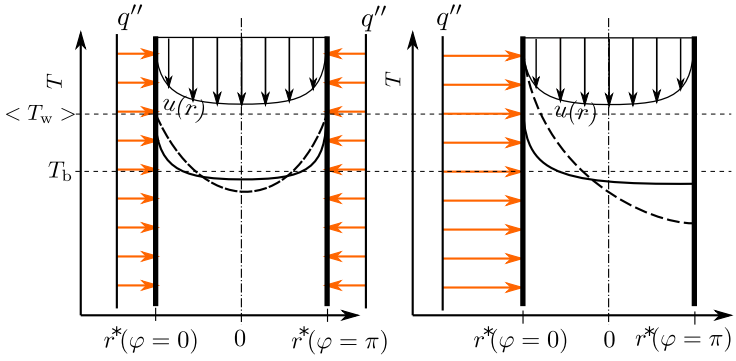

Figure 3.7: Qualitative temperature profile along the longitudinal cross section from $\varphi = 0$ to π of the tube. Left: The case of the fully heated tube. Right: The case of the tube heated along only half of the circumference. Solid line: Fluid with $\mathrm{Pr} = 1$, dashed line: Fluid with $\mathrm{Pr} \ll 1$.

Flesch et al. [62] found that for fluids of a Prandtl number much below unity average Nusselt numbers defined according to,

$$\mathrm{Nu} = \frac{< q'' >}{(< T_\mathrm{w} > - T_\mathrm{b}) \frac{k}{2r}}, \tag{3.7}$$

that have been calculated with state-of-the-art correlations for the situation on the left are valid for the boundary condition shown in the right graph, as well. The brackets <> indicate variables averaged along the complete circumference of the tube.

In that definition of the Nusselt number the adiabatic equilibrium mixing temperature, T_b, of that cross section is defined:

$$T_\mathrm{b}(x) = \frac{\int_{A(x)} \rho c_p v T(x,r) dA}{\int_{A(x)} \rho c_p v dA}. \tag{3.8}$$

This temperature is in the following called the bulk temperature of the flow.

This result form a CFD simulation agrees with experimental findings by Melnikov et al. [60] who found that for non-uniform heat flux in a mercury flow the averaged Nusselt number asymptotically approximates the one predicted by a Nusselt correlation by Lyon [61],

$$\mathrm{Nu_t} = 7 + 0.025\,\mathrm{Pe}^{0.8}, \tag{3.9}$$

at increasing Peclét numbers, while being lower than the prediction at low Peclét numbers.

From these findings follows that in both cases shown in Figure 3.7 the average wall-bulk temperature difference for low-Prandtl number flows is the same. (The average wall temperature is indicated in Figure 3.7 with $< T_\mathrm{w} >$ on the temperature axis). For fluids of Prandtl number of unity and greater this is the generally expected behavior.

As mentioned before, low-Prandtl number fluids have a larger thickness of the thermal boundary layer than the viscous boundary layer. In the fully heated case on the left the following can be deduced: At identical velocity profile and identical bulk temperatures according to the previously stated definition and secondly at identical average wall temperature, low-Prandtl number fluids can only have a greater thickness of the thermal boundary layer if the temperature in the center of the tube at $r = 0$ is lower than that of the fluid with $\mathrm{Pr} = 1$.

On the right the case of heating only along half of the perimeter is shown. In order to comply again with the definition of the bulk temperature the wall temperature on the adiabatic side must be lower than T_b for both fluids. Then, in order for both to have the same average wall temperature as on the left, according to the finding by Flesch et al. [62], the local wall temperature at $\varphi = 0$ must be higher than average.

Fluids of $\mathrm{Pr} = 1$ with a thin thermal boundary layer can comply with the bulk temperature definition by assuming temperatures near the adiabatic wall that are only slightly lower than bulk temperature.

However, fluids with $\mathrm{Pr} \ll 1$ require

- a much lower temperature than bulk temperature near the adiabatic wall to compensate for their thicker thermal boundary layer in order to maintain the same bulk temperature and as a consequence
- require a much higher temperature on the heated side in order to comply with the average wall temperature value to compensate the low value on the adiabatic side!

A much wider spread of front and back wall temperature is to be expected in flows with $\mathrm{Pr} \ll 1$ when wall and bulk temperature are identical in the left and right case.

Local temperatures on the irradiated side may therefore be much higher than the average wall temperature which would be obtained by the application of local Nusselt number values according to:

$$T_w(\varphi) - T_\mathrm{b} = \frac{q''(\varphi) 2 r_i}{k\,\mathrm{Nu}}. \tag{3.10}$$

These considerations are backed by numerical simulations by Marocco et al. [47] for a cosinusoidal heat flux distribution along the entire perimeter of a tube in forced-convective flow of Re = 1×10^5, finding as well that existing correlations for average nusselt numbers can be applied, however, local Nusselt numbers vary more significantly than in higher-Prandtl number flows.

Also, Melnikov et al. [60] found this behavior experimentally under the boundary condition of constant heat flux along half of the circumference. The local temperatures observed under turbulent flow are generally much higher than predicted by the Lyon equation [61] and at low Peclét numbers even higher than what would have been predicted when a Nusselt number for laminar flow is applied. The experimental local dimensionless temperature as obtained from Melnikov et al.,

$$\Theta_\mathrm{w} = \frac{1}{\mathrm{Nu}(\varphi)} = k \frac{T_\mathrm{w}(\varphi) - T_\mathrm{b}}{q_\mathrm{w} D}, \tag{3.11}$$

with $D = 2r$, is shown in Figure 3.8 with black dots, which correspond to a case without the influence of a strong superimposed magnetic field, whereas the remaining data show that such a magnetic field further strongly impacts the heat transfer behavior. (Note, that in that graph the definition of φ is such that the heat flux is applied between 90° and 270°.)

In the heated part of the tube's perimeter much higher than expected local wall temperatures are measured while lower than expected temperatures are obtained in the non-heated section. It is therefore an important effect that has to be considered during the design of solar thermal receivers using liquid metal as coolant.

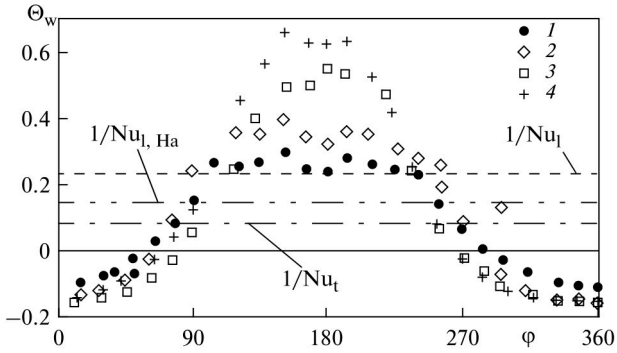

Figure 3.8: Experimental results of Melnikov et al. [60] for a heat flux of $55\,\mathrm{kW\,m^{-2}}$ along the heated half of the perimeter (between 90° and 270°) at an heated entry length of $z/d = 37$ and $\mathrm{Re} = 35000$ in mercury. 1: Data without superimposed magnetic field, 2-4: data with superimposed magnetic field of Hatta numbers between 130 and 410. The top dashed line indicates the expected dimensionless temperature in fully developed laminar flow at $\mathrm{Nu} = 4.36$. The dashed line marked with $1/\mathrm{Nu_t}$ indicates the expected dimensionless wall temperature calculated using the Lyon correlation [61].

In the design of the sodium receivers in Almería, however, such an effect was probably not considered . Neither in [26] nor in [27] special treatment of this boundary condition is mentioned:

In Almería two different receivers were tested. Initially, tests with a cavity receiver have been performed. In [26, pp 5.3.-5.8] briefly the stress analysis was described. In order to determine the wall to bulk temperature difference a correlation of unknown source for average Nusselt numbers was applied:

$$\mathrm{Nu} = 4.48 + 0.0238\,\mathrm{Pe}^{0.8}\,. \tag{3.12}$$

For the flat panel advanced sodium receiver (ASR), a simulation code using the correlation of Lubarsky and Kaufman [49] was developed and used and also most likely used in the thermal stress analysis.

Interestingly, the report of the high flux experiment [27] indicated that the measured tube wall temperatures were higher than expected during operation. As a consequence, for example, a new code for thermal-hydraulic simulation of the receiver (TheresaN) was written once operation data had been obtained since its first version had under-predicted the temperatures of the tubes. In part this deviation was attributed to the effect of the Pyromark 2500 coating on the tube which has a very low thermal conductivity. The report [27, p.169] states that a 100 K drop might have occured in the Pyromark coating of 45 micro meter thickness during the high flux experiment. When higher than expected temperatures were observed probably a high value of the potential range of the conductivity value was implemented in the code. The new code then showed better agreement with measured data. In Ref. [27] it is unfortunately not explained in detail how the code was altered.

An infrared camera was available during the high flux experiment in order to monitor the tube surface temperatures during operation. In spite of a stated measurement error of just a few Kelvin the locally measured surface temperatures are not discussed in the report. Results from calculations with a so-called 'Hotrec' code are compared to only one set of measured temperatures where good agreement for a Pyromark coating temperature of up to 770 °C is obtained. In the appendix of the report, however, further camera readings for maximum local receiver temperatures are listed. Maximum temperatures much above 800 °C have accordingly been measured in test case D.9.1 [27, p.113] under full load and coolant temperature rise of 280 to 560 °C during the high flux campaign. These high values are not discussed in the report.

Based on these observations from the report, likely the wall temperatures have been under-predicted for the high flux experiment because average Nusselt numbers have been used for the design. Consequently, it may for the future be important to apply alternative methods to correctly predict local Nusselt number values.

The results found by Marocco et al. [47] – locally much higher than average wall temperatures – were compared to those obtained by a method by W.C. Reynolds for the calculation of local wall temperatures under non-uniform heat flux along the circumference of a circular tube with fully turbulent flow. Reynolds' approach is better suited to predict local wall temperatures under non-uniform heat flux than Equation 3.10.

In his 1962 paper [63], Reynolds gives a general solution for the function of the wall temperature for arbitrary cases of periodic functions of the heat flux density that have a Fourier expansion.

$$q''_{\mathrm{w}}(\varphi) = q''_0 + F(\varphi), \tag{3.13}$$

and

$$F(\varphi) = \sum_{n=1}^{\infty} \left(a_n \sin n\varphi + b_n \cos n\varphi\right), \tag{3.14}$$

assumed to be constant along the tube axis. The index 0 denotes the average value along the circumferential coordinate to which the periodically varying property is added.

The solution by Reynolds then provides a temperature distribution on the wall, also consisting of a constant value and a periodic deviation from this average value:

$$\Delta T(r,\varphi) = \Delta T_0(r) + g(r,\varphi), \tag{3.15}$$

with

$$g(r,\varphi) = \frac{r_0}{k} \sum_{n=1}^{\infty} R_n(r) \left(a_n \sin n\varphi + b_n \cos n\varphi\right). \tag{3.16}$$

Solutions for $R_n(r/r_o)$ on the wall ($r = r_0$) are denoted by Reynolds as $S_n = R_n(1)$. With the definition of the Nusselt number the function for ΔT_0 at the wall is

$$\Delta T_{0,\mathrm{w}} = \frac{2 r_0 q''_0}{k\,\mathrm{Nu}_0}, \tag{3.17}$$

where

$$\frac{2}{\mathrm{Nu}_0} = S_0. \tag{3.18}$$

Then, with the solutions for S_n assumed to be at hand, in a cross section of the heated tube

$$T_w(\varphi) - T_m = \frac{r_0}{k}\left[S_0 q_0'' + \sum_{n=1}^{\infty} S_n \left(a_n \sin n\varphi + b_n \cos n\varphi\right)\right]. \tag{3.19}$$

In Reynolds' paper T_m denotes the adiabatic mixing temperature at the cross section which is called bulk temperature T_b in this thesis.

Reynolds also provides the solutions for S_n listed for specific Reynolds numbers and Prandtl numbers. For the calculation of these parameters the flow is assumed to be hydrodynamically fully developed and constant properties are assumed, using a radial function for the eddy diffusivity of momentum and very simple friction factor correlations. Reynolds explains that the temperature distribution is independent of the velocity field in the flow but dependent of the diffusivity distribution. These diffusivities are assumed to be identical in radial and circumferential direction. The eddy diffusivity of heat is obtained by multiplying the eddy diffusivity of momentum with factors by Jenkins [64], however, corrected by an additional factor of 1.15 in order to match experimental results by Kays and Leung [65] in a flow of Prandtl number $\mathrm{Pr} = 0.7$. This factor is applied also for $\mathrm{Pr} \leq 0.7$ for the calculation of S_n. Therefore a the values of S_n are potentially less reliable for much smaller Prandtl numbers.

Accordingly this leads to higher thermal eddy diffusivity compared to the model used by Marocco et al. [47] for a CFD analysis of a cosinusoidally varying heat flux distribution. In Reynolds' case energy mixing is higher and resulting wall temperatures in the heated zone are about 15% lower than in Marocco's case at $\mathrm{Pe} = 3000$ and $\mathrm{Pr} = 0.03$. This is taken as a sufficiently good agreement for illustrating the special behavior of low Prandtl number fluids.

According to the previously stated hypothesis, the effect of increased local temperatures was not considered in the design of former sodium receivers. However, probably by coincidence, during operation of the ASR this effect did not show prominently – due to the use of rather narrow tubes in the ASR. Therefore the project team was not convinced to conduct more detailed analyses on this effect. The over-temperature probably remained within a threshold of potential over-temperature of the Pyromark 2500 coating layer.

In order to check validity of the hypothesis the conditions of test case A3 of the high flux experiment [27] shall be applied to Reynolds' solution with a very simple cosinusoidal heat flux distribution,

$$q''(\varphi) = hq''_0(1+\cos(\varphi)), \tag{3.20}$$

with $h = 0.5$ applied. In that test case A3 a Reynolds number of 83 094 was obtained in the flow in the individual tubes. More conditions of that test case A3 are further specified in Table 4.1 in Section 4.3 on page 103. Note that a cosinoidal flux distribution as in the previous equation is not precisely the boundary condition to be found in receivers as depicted in Figure 3.6 on the left. That real flux distribution cannot be expressed by a Fourier series, therefore, the cosinusoidal distribution along the entire perimeter is used as an approximation of the real flux. The resulting wall temperature distribution according to,

$$T - T_b = \frac{r_o q''_0 h}{k}\left(S_0 + S_1 \cos\varphi\right) \tag{3.21}$$

is shown as solid line in Figure 3.10.

Table 3.2 provides a selection of Reynolds' parameters S_n for specific Reynolds and Prandtl numbers. Parameters have been interpolated logarithmically to match the actual Reynolds of $\mathrm{Re} = 83\,094$ and Prandtl numbers of $\mathrm{Pr} = 0.005$ present at test case A3.

The interpolation for the unknown value of $y = f(x_1 + a)$, which is located in-between the known values $y_1 = f(x_1)$ and $y_2 = f(x_2) = f(x_1 + a + b)$ was performed according to ,

$$y = y_2^f y_1^{1-f}, \tag{3.22}$$

with

$$f = \frac{a}{a+b}. \tag{3.23}$$

These interpolated values are shown in the middle and bottom section of the table.

Table 3.2: Parameters S_n as listed in Reynolds [63] and interpolated.

Pr	Re	S_0	S_1	S_2	S_3	S_4	S_5
			listed parameters				
0.003	3×10^4	0.302	0.994	0.498	0.332	0.249	0.200
0.003	1×10^5	0.282	0.957	0.484	0.325	0.245	0.197
0.003	3×10^5	0.246	0.831	0.435	0.299	0.229	0.186
0.003	1×10^6	0.156	0.473	0.279	0.203	0.170	0.145
0.01	3×10^4	0.286	0.952	0.483	0.325	0.245	0.197
0.01	1×10^5	0.224	0.733	0.397	0.279	0.217	0.178
0.01	3×10^5	0.141	0.409	0.246	0.186	0.153	0.132
0.01	1×10^6	0.0655	0.161	0.109	0.0894	0.0784	0.071
0.03	3×10^5	0.0618	0.145	0.0986	0.0816	0.0720	0.0654
0.03	1×10^6	0.0248	0.0535	0.0402	0.0353	0.0326	0.0307

(... to be continued on the next page ...)

Table 3.2: Continued: Parameters of the SSPS receiver operated with molten sodium and LBE. Values indicated with * are based on assumptions.

Pr	Re	S_0	S_1	S_2	S_3	S_4	S_5
			(... continued from the previous page ...)				
3	1×10^5	0.00495	0.00629	0.00540	0.00508	0.00490	0.00479
3	3×10^5	0.00194	0.00246	0.00213	0.00201	0.00194	0.00190
10	1×10^5	0.00290	0.00322	0.00296	0.00286	0.00281	0.00277
10	3×10^5	0.00111	0.00123	0.00113	0.00110	0.00108	0.00107
			interpolated parameters				
0.003	83094	0.2867	0.9658	0.4873	0.3267	0.2460	0.1977
0.003	539946	0.2104	0.6850	0.3736	0.2618	0.2067	0.1708
0.001	83094	0.2376	0.7808	0.4163	0.2895	0.2235	0.1824
0.01	539946	0.1084	0.2971	0.1861	0.1447	0.1217	0.1067
0.01	477272	0.1161	0.3230	0.2002	0.1545	0.1292	0.1128
0.03	477272	0.049	0.1127	0.0786	0.066	0.0589	0.054
3	144062	0.004027	0.005115	0.004399	0.004141	0.003995	0.003907
10	144062	0.002347	0.002605	0.0023942	0.002317	0.002276	0.002246
0.0049	83094	0.2724	0.9116	0.4669	0.3162	0.2397	0.1934
0.0049	539946	0.17578	0.5461	0.3092	0.2229	0.1790	0.1503
0.0153	477272	0.09237	0.2444	0.1563	0.1233	0.1049	0.09279

(... to be continued on the next page ...)

Table 3.2: Continued: Parameters of the SSPS receiver operated with molten sodium and LBE. Values indicated with * are based on assumptions.

Pr	Re	S_0	S_1	S_2	S_3	S_4	S_5
			(... continued from the previous page ...)				
4.6	144062	0.003562	0.0043879	0.003831	0.00363	0.003516	0.003446

An additional second approximate boundary condition shall be applied to the same case: a circumferential square function which can roughly be approximated with a 5th order Fourier expansion:

$$q''(\varphi) = < q'' > \cdot (h + \frac{4h}{\pi}\cos(\varphi) + \frac{4h}{3\pi}\cos(3\varphi) + \frac{4h}{5\pi}\cos(5\varphi)). \quad (3.24)$$

This better approximates the left situation in Figure 3.6 and is shown in Figure 3.9.

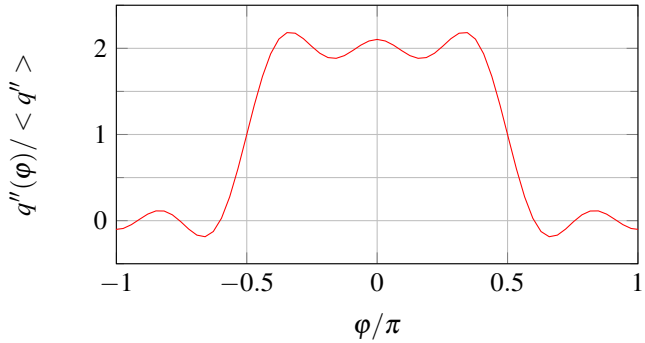

Figure 3.9: Heat flux boundary condition approximated with a 5th order Fourier expansion.

It can also be seen as an average between both cases shown in Figure 3.6. The resulting (reduced) wall temperature is, according to Reynolds:

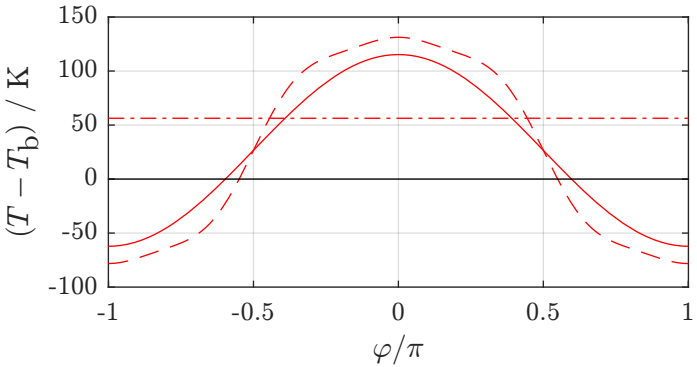

Figure 3.10: Computed temperatunre difference between wall and fluid bulk for different assumed heat fluxes on a tube. Solid red: inner wall temperature distribution under cosinusoidal heat flux distribution. Dashed line: approximated square function flux distribution. Dash-dotted line: predicted average wall temperature under uniform heat flux.

$$\frac{T_w(\varphi) - T}{q'' \frac{r}{k}} = S_0 h + S_1 \frac{4h}{\pi} \cos(\varphi) - S_3 \frac{4h}{3\pi} \cos(3\varphi) + S_5 \frac{4h}{5\pi} \cos(5\varphi). \quad (3.25)$$

The average temperature along the circumference is obtained according to:

$$\begin{aligned} \frac{\overline{T_w - T}}{< q'' > \frac{r}{k}} &= \frac{1}{2\pi} \int_{-\pi}^{\pi} \frac{T_w(\varphi) - T}{< q'' > \frac{r}{k}} d\varphi \\ &= \frac{1}{2\pi} \left[\left(hS_0 \cdot \varphi + S_1 \frac{4h}{\pi} \sin(\varphi) \right. \right. \\ &\quad \left. \left. - S_3 \frac{4h}{9\pi} \sin(3\varphi) + S_5 \frac{4h}{25\pi} \sin(5\varphi) \right) \right]_{-\pi}^{\pi}. \end{aligned} \quad (3.26)$$

The local wall-to-bulk temperature difference resulting from this boundary condition is shown in Figure 3.10 as dashed line.

During case A3 of the high flux experiment at a bulk temperature of 500 °C a wall *outside* temperature of 690 °C was measured and 590 °C assumed as inner wall temperature, which corresponds to a radial flow temperature difference of 90K [27]. According to the Reynolds solution rather 115 K would have to be attributed to the radial flow temperature difference.

According to the average Nusselt number correlations, however, only about 60 K would have to be expected, so that this 30 K deviation would have had to be explained as well in the report – which it was not. Nevertheless, the differences probably resided within the limits of uncertainty in the measurement of the surface and flow temperatures, flux distribution etc. and have mainly been attributed to the impact of the Pyromark coating by the authors. Coincidentally, the flow conditions and the tube geometry limited the extent to which the over-temperature due to non-uniform heat flux occurred.

The effect, however, may be very dramatic in large-scale receivers:

An example with flow parameters and tube geometries of the optimized receiver parameters by Fritsch [29] shall be provided to illustrate the dramatic impact.

The parameters by Fritsch are optimized for least LCOE generation of a 140 MW thermal receiver during a multi-variable optimization. Therefore the fluids are compared at a condition of optimized economy. This represents a fair basis for their comparison. Fritsch applied the value of the average Nusselt number in the same fashion as the designers of the Almería receivers in order to predict local wall temperatures, as in Equation 3.10. The respective parameters are listed in Table 3.3. The LBE and sodium cases assume peak heat flux values of more than 2.472 $\mathrm{MW\,m^{-2}}$ – and result in maximum local tube wall temperatures of 938 °C for LBE and 673 °C for sodium according to Fritsch. Reynolds' parameters S_n for Reynolds and Prandtl numbers of these cases are as well listed in Table 3.2. Wall temperature distributions for tubes with parameters in Table 3.3 are shown in Figure 3.11 for cosiunusoidal varying heat flux along the circumference. With an

Table 3.3: Flow parameters of optimized tube geometries for a 140 MW thermal receivers with solar salt, sodium and LBE as HTFs.

parameter	solar salt	sodium	LBE
case	reference	V.2.16	V.2.26
design heat flux, $\mathrm{kW\,m^{-2}}$	1125	2472	2472
inner diameter, mm	32.8	59	35.4
Reynolds number, –	144062	539946	477272
Prandtl number, –	4.6	0.0049	0.0153
bulk temperature, K	700	700	700

approximated square flux profile the temperature distributions of Fritsch's cases result as depicted in Figure 3.12. For comparison, the predicted wall temperature of solar salt at the same peak heat flux as the liquid metals is included as dotted black line. Horizontal lines indicate the average wall temperatures when Equation 3.10 is applied with the peak heat flux value and state-of-the-art average Nusselt number correlations. For both liquid metals the correlation by Lubarsky and Kaufman [49], Equation 3.4 was used and for salt that of Dittus and Boelter [53]:

$$\mathrm{Nu} = 0.023\,\mathrm{Re}^{0.8}\,\mathrm{Pr}^{0.4}\,. \tag{3.27}$$

Slightly higher local wall temperatures are obtained with the approximated square heat flux distribution boundary condition.

When for solar salt the peak temperature is calculated according to the solution by Reynolds for a peak flux value of $q''_0 = 1.125\,\mathrm{MW\,m^{-2}}$ it only very slightly exceeds the average value predicted by the correlation for the average Nusselt number. This is true for both boundary conditions applied. Also, in sections of the tube wall where no heat input is present the wall temperature is only slightly lower than bulk temperature. Under approx-

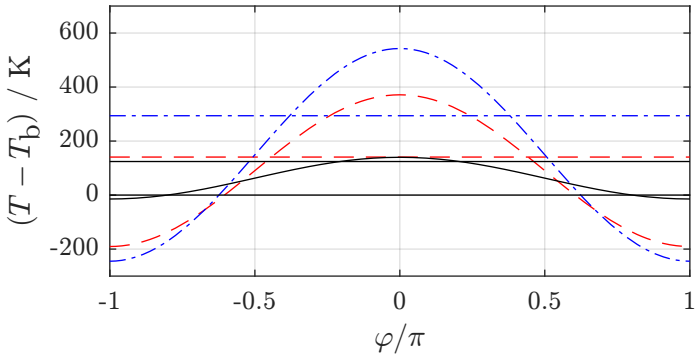

Figure 3.11: Local wall temperature difference distribution of cosinusoidal flux profile in three different coolants from top to bottom at $\varphi = 0$: LBE (dashed-dotted, blue line) at Re $= 477\,272$, sodium (dashed, red line) Re $= 539\,946$ and solar salt (solid, black line) at Re $= 144\,062$. The horizontal lines show the average wall temperatures predicted by state-of-the-art Nusselt number correlations (from top to bottom of LBE, sodium and salt). The cosinusoidal heat flux peaks at 2.3 MW m^{-2} and is zero at $\varphi = \pi$.

imated square heat flux distribution and low heat flux a maximum radial wall-to-bulk temperature difference of 150 °C is obtained in the irradiated section. The average Nusselt number correlation predicts a difference of 125 °C. The correlation for uniform heat flux is able to predict the temperatures quite well, although a very non-uniform heat flux distribution is present. For solar salt, when exposed to 2.3 MW m^{-2} about 310 °C are predicted as wall-to-buk temperature difference by Reynolds and 260 °C by the average correlation; thus, the average correlations under-estimate the local temperatures slightly for solar salt and dramatically for lower-Prandtl number fluids.

The predicted average temperature for sodium at twice the heat flux nearly equals that of salt – implying the conclusion that sodium is an excellent heat-transfer fluid which can easily handle twice the peak heat flux. However, this

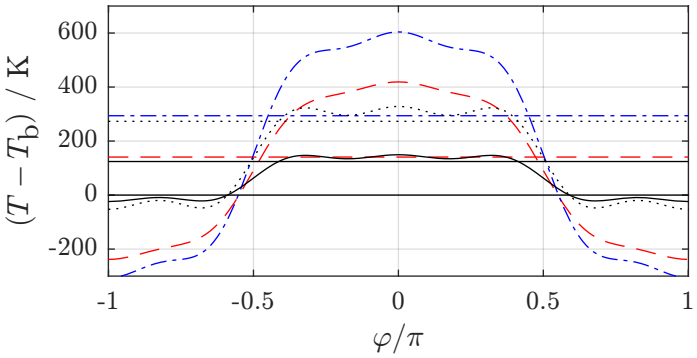

Figure 3.12: Temperature difference distributions along the wall for an approximated square flux profile. In solid black: Solar salt at a peak flux of 1.125 MW m^{-2}. The remaining curves are for a peak flux of 2.3 MW m^{-2}: dash-dotted blue: LBE, dashed red: sodium and dotted black: solar salt. The horizontal lines show the average wall temperature as calculated with state-of-the-art average Nusselt number correlations. Bulk temperature is marked by a horizontal black line.Black, dotted line: Temperature difference distribution of Solar Salt at the peak flux value applied to the metal flows.

is only true for the prediction based on the average Nusselt number. In fact, the observed local peak temperature is more than twice the predicted value. Also, on the non-heated side the temperature is much below bulk temperature. A front-to-back gradient of nearly 600 K results which is intolerably large, given the intended temperature rise of the coolant of 'only' 275 K.

For LBE the matters are even more extreme. Up to 600 K difference between the wall and bulk must be expected although the average Nusselt number correlation predicts only 270 K.

Figure 3.13 shows the difference in the predicted wall temperature if it is either calculated with the average Nu value locally, according to Equation 3.10,

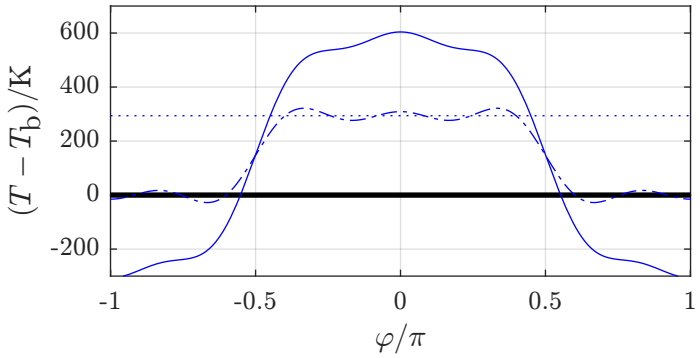

Figure 3.13: Solid blue: local wall temperature differences of LBE calculated with Reynold's solution; dash-dotted: calculated with the average Nusselt value applied locally. Dotted line: average predicted wall temperature. An error of more than 300 K will be obtained.

$$\begin{aligned} T_w(\varphi) - T_b &= \frac{q''(\varphi) 2 r_i}{k\,\mathrm{Nu}} \\ &= \frac{< q'' > 2 r_i}{k\,\mathrm{Nu}} \left(h + \frac{4h}{\pi}\cos(\varphi) + \frac{4h}{3\pi}\cos(3\varphi) \right. \\ &\quad \left. + \frac{4h}{5\pi}\cos(5\varphi) \right), \end{aligned} \tag{3.28}$$

or when computed according to Reynolds' method in Equation 3.25.

About the factor of two resides between both peak temperature values and a much larger resulting front-to-back gradient is obtained by Reynolds' method.

Based on these observation it is not recommended for liquid metals to optimize receiver tube flow conditions and geometries with the help of correlations for average Nusselt numbers and applying these to the heated fraction of the circumference. This approach is likely to result in designs with much higher than estimated peak temperatures. As a consequence, more

than expected turbulence is required for liquid metal flows and accordingly, more than expected pumping power is required – reducing the liquid metal's efficiency as heat-transfer fluids.

Obviously, the significant discrepancy found in the discussed example may have a significant effect upon the thermal stresses in the receiver tube's wall. This will be discussed in the following section 3.6.

In that section, the circumferentially averaged temperature value of the distribution as calculated with an average Nusselt number value is required, which is obtained according to

$$\overline{T_w - T} = \frac{< q'' > 2 r_i h}{k\,\mathrm{Nu}} \frac{1}{2\pi} \left[\left(\varphi + \frac{4}{\pi} \sin(\varphi) - \frac{4}{9\pi} \sin(3\varphi) + \frac{4}{25\pi} \sin(5\varphi) \right) \right]_{-\pi}^{\pi}. \tag{3.29}$$

3.6 Thermal tube stress calculation

The previous findings impact the magnitude of thermal stress in the tube wall. Although thermal stress is not of primary interest in this thesis the findings of the previous section require a brief demonstration of the effects of non-uniform heat flux on the thermal stress in the tube wall. As summarized by Logie et al. [17] analytic methods exist in order to calculate the thermal radial, circumferential and axial stress components in a tube induced through an non-uniform temperature distribution.

These methods can be applied if a plane harmonic Fourier series exists that describes the temperature field:

$$T_\varphi = \sum_{n=1}^{\infty} \left((A_n r^n + B_n r^{-1}) \cos n\varphi + (C_n r^n + D_n r^{-1}) \sin n\varphi \right). \tag{3.30}$$

According to Logie et al., all linear terms $r\cos\varphi$ and $r\sin\varphi$ do not generate stress and thus only terms of the B_n and D_n coefficients are required to calculate the stress components. Also, terms with $n > 1$ result in stresses of

zero. Thus, only the terms with $n = 1$ contribute to the non-uniform stress. Logie et al. validate the analytic approach with a finite element simulation, which agree well.

Solutions for the calculation of stress components exist based on the coefficients determined in the inner and outer wall surface. Thus, if the inner and outer temperature distributions are known, stresses can be calculated.

$$T_i = \bar{T}_i + \sum_{n=1}^{\infty} \left(B'_n \cos n\varphi + D'_n \sin n\varphi \right), \tag{3.31}$$

$$T_o = \bar{T}_o + \sum_{n=1}^{\infty} \left(B''_n \cos n\varphi + D''_n \sin n\varphi \right). \tag{3.32}$$

The variables $\bar{T}_i$ and $\bar{T}_o$ denote the inner and outer circumferentially averaged mean temperatures at that cross-section. These equations can easily be compared to the solutions obtained by Reynolds in order to obtain the coefficients for the inner tube wall temperature distribution.

It shall be assumed that only radial conduction occurs in the tube wall. Then from the inner temperature distribution and the applied heat flux profile the outer distribution can be obtained according to:

$$T_o(\varphi) = T_i(\varphi) + \frac{q''_0(\varphi) r_o}{k} \ln \frac{r_o}{r_i}. \tag{3.33}$$

The temperature field $K'(r, \varphi)$ based on B_1 and D_1 is:

$$K'(r, \varphi) = \frac{r r_i r_o}{r_o^2 - r_i^2} \left[\left(\frac{B'_1 r_o - B''_1 r_i}{r_i^2 + r_o^2} \right) \cos\varphi + \left(\frac{D'_1 r_o - D''_1 r_i}{r_i^2 + r_o^2} \sin\varphi \right) \right]. \tag{3.34}$$

With this temperature field and the steel's properties the radial and circumferential stress can be calculated, both as functions of φ and r:

$$\sigma_r = K' \frac{\lambda E}{2(1-\nu)} \left(1 - \frac{r_i^2}{r^2}\right) \left(\frac{r_o^2}{r^2} - 1\right), \tag{3.35}$$

$$\sigma_\varphi = K' \frac{\lambda E}{2(1-\nu)} \left(\frac{r_i^2 r_o^2}{r^4} + \frac{r_i^2 + r_o^2}{r^2} - 3\right). \tag{3.36}$$

Under the assumption of un-constrained tube ends, the axial stress can be calculated according to,

$$\begin{aligned} \sigma_z = & K \frac{\lambda E}{2(1-\nu)} \left[1 - 2\ln\frac{r_o}{r} - \frac{2r_i^2}{r_o^2 - r_i^2} \ln\frac{r_o}{r_i}\right] \\ & + K' \frac{\lambda E \nu}{1-\nu} \left(2 - \frac{r_i^2 + r_o^2}{r^2}\right) - \lambda E T_\varphi, \end{aligned} \tag{3.37}$$

with,

$$K = \frac{(\bar{T}_i - \bar{T}_o)}{\ln \frac{r_o}{r_i}}, \tag{3.38}$$

and,

$$T_\varphi = T - K \ln\frac{r_o}{r} - \bar{T}_o. \tag{3.39}$$

where T_0 is the stress free temperature. If only the effect of non-uniform heat flux distribution is investigated, the stress free temperature can be set as T_b, that is the case without heat flux imposed upon the tube.

All stress components can be summarized in van Mises stress σ_{vM}:

$$\sigma_{vM} = \sqrt{\frac{1}{2}[(\sigma_r - \sigma_\varphi)^2 + (\sigma_\varphi - \sigma_z)^2 + (\sigma_z - \sigma_r)^2]}, \tag{3.40}$$

which provides a single, total value to compare different load cases.

For the boundary conditions applied to receiver tubes only the cosine terms occur. Therefore, only the coefficients B_1' and B_1'' have to be identified by comparing Reynolds solution with equations (3.31) and (3.32).

For the simple cosinusoidal profile these are:

$$B_1' = S_1 \frac{h q_0'' r}{k}, \tag{3.41}$$

$$B_1'' = (S_1 + \ln \frac{r_o}{r_i}) \frac{h q_0'' r}{k}, \tag{3.42}$$

and for the approximated square flux distribution:

$$B_1' = S_1 \frac{4 h q_0'' r}{\pi k}, \tag{3.43}$$

$$B_1'' = (S_1 + \ln \frac{r_o}{r_i}) \frac{4 h q_0'' r}{\pi k}. \tag{3.44}$$

For the case of the receiver tube of the ASR in Almería, Figure 3.14 shows the differences of van Mises stresses between a cosinusoidally varying heat flux distribution and an approximated square function heat flux distribution. Some of the operating parameters of this receiver are listed in Table 3.4.

The two curves on top of Figure 3.14 represent Reynolds' solution and the two curves on the bottom result from the calculation of wall temperatures with an average Nusselt number. The stresses are plotted along the radial coordinate at $\varphi = 0$, where van Mises stresses are the highest.

Apparently, the approximated square function boundary condition generates slightly higher temperatures in the irradiated part of the tube than the cosinusoidal varying distribution. This consequently results in higher stresses, too. Also, using the average Nusselt number for the determination of local wall temperatures leads to a significant under-estimation of the thermal stress in the tube.

For the LBE case of Fritsch under approximated square heat flux profile the van Mises stresses of the cases shown in Figure 3.13 are shown in Figure 3.15. The stresses are due to the very large temperature gradients by one order of magnitude higher than what could be accepted for both cases.

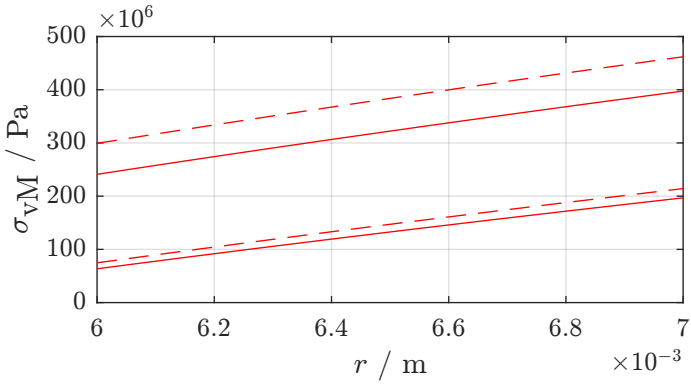

Figure 3.14: Van Mises stresses in the receiver tube of the SSPS ASR [27]: solid line: cosinusoidal heat flux profile, dashed line: approximated square function flux profile. Upper two lines according to Reynolds' solution, lower two lines with average Nusselt number.

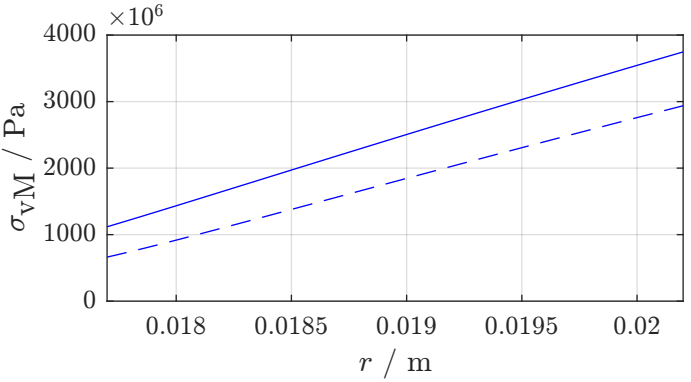

Figure 3.15: Solid blue: van Mises stress calculated with Reynold's solution, dash-dotted line: stresses when calculated with average Nusselt number correlation along the radial coordinate at $\varphi = 0$ where the highest stresses occur at 2.3 MW m^{-2}.

Table 3.4: Operation parameters of the SSPS receiver in Almería during the high-flux experiment.

property/unit	symbol	value sodium
absorbed thermal power / W	P_{th}	3 058 000
inlet temperature / °C	T_{in}	270
outlet temperature / °C	T_{out}	560
average flux / $\mathrm{W\,m^{-2}}$	q''_{mean}	435 880
peak flux / $\mathrm{W\,m^{-2}}$	q''_{max}	2 500 000
tube inner diameter / m	d_{i}	0.012
wall thickness / m	l	0.001
tube outer diameter / m	d_{o}	0.014
Reynolds number / –	Re	83 094
conv. heat transfer coefficient / $\mathrm{W\,m^{-2}\,K^{-1}}$	h	39 971

Again the stresses resulting from Reynolds' solution are twice as large as those predicted when the average Nusselt number is applied.

Although these results are based on approximations of the actual boundary conditions and on model assumptions in the solutions of Reynolds they are so significant that further experimental research should be performed to test their validity.

3.7 Pressure loss calculation

For liquid metal flows in rough pipes friction factor correlations for non-metal flows can be used when wetting of the walls is provided. The LBE Handbook [32] specifically suggests the use of Churchill's formula for the calculation of the friction factor over the full turbulent range. However, experience at the KALLA laboratory shows that also alternative correlations

suggested in for example, the VDI Heat Atlas [66] allow to correctly estimate pressure losses in liquid metal flows.

3.8 LBE as a 'model fluid'

This section discusses LBE's ability to show behavior typical for liquid metals and the option that based on the observed behavior, the behavior of other liquid metals is predicted. LBE could thus serve as a model fluid in a model geometry, such as the thermal receiver of the SOMMER loop.

Operation parameters observed in a model only lead to quantitative conclusions for a larger scale reference geometry if technical similarity between the model and the reference is respected. That is, as long as the relevant dimensionless numbers are maintained.

The size of the model receiver had to be adapted to the small available zone of concentrated flux and the resulting maximum power of 10 kW, which is very small in comparison to commercial-scale receivers. Therefore, scaling considerations have been made during its design phase:

Let us first consider the relevant dimensionless numbers required to express similarity in the flow and pipe wall: The average Nusselt number of the liquid metal flow is defined as:

$$\mathrm{Nu} = \frac{h \cdot D_i}{k}. \tag{3.45}$$

Under the assumption that the receiver tube in SOMMER and a potential reference receiver operate at a similar temperature, the values of physical properties do not change in the scaling process. At a constant Nusselt number, during scaling the proportionality of $d_i \propto h^{-1}$ is given, so an increased convective heat transfer coefficient must be achieved at a decreased diameter in order to maintain similarity. The Nusselt number can usually be correlated as a function of the Reynolds and Prandtl number, the latter of which is constant if the temperatures are kept the same. In that case at the same di-

mensionless radial distance from the tube axis $r^* = r/r_\infty$ the dimensionless temperature is in both cases:

$$T^* = \frac{T - T_\mathrm{o}}{T_\mathrm{b} - T_\mathrm{o}}. \tag{3.46}$$

At constant temperatures the Nusselt number is then only a function of the Reynolds number. The heat transfer in the reference and in the model is therefore similar if the Nusselt number and the Reynolds number are kept constant during scale-up.

The Prandtl number is defined by the fluid's thermo-physical properties and thus different for each fluid at the identical temperature. Therefore, experimental results from one fluid cannot be imposed upon different fluids without violating Reynolds similarity. For strict scaling, however, all relevant dimensionless numbers have to be kept similar.

The radial temperature difference in a heated tube flow is given by:

$$\Delta T_\mathrm{rad} = \frac{q_\mathrm{i}'' d_\mathrm{i}}{\underbrace{d_\mathrm{i} h}_{=\text{const.}}}, \tag{3.47}$$

with $d_\mathrm{i}h$ constant during scaling at a constant Nusselt number. If, in addition, the radial temperature difference is kept constant to satisfy identical model and reference temperatures, $q_\mathrm{i}'' \propto d_\mathrm{i}^{-1}$ must be adhered to during scaling.

The radial temperature difference between inner and outer tube wall is:

$$\Delta T_\mathrm{wall} = \frac{q_\mathrm{i}'' d_\mathrm{i}}{2k} \ln \frac{d_\mathrm{o}}{d_\mathrm{i}}. \tag{3.48}$$

Since the material properties of the tube's steel affect the temperature gradient, tube materials with identical thermal conductivity have to be used for model and reference.

It is required that:

$$d_{\mathrm{o}} \propto d_{\mathrm{i}}, \tag{3.49}$$

$$d_{\mathrm{i}} \propto q_{\mathrm{i}}''^{-1}, \tag{3.50}$$

in order to maintain a constant temperature difference in the tube wall at constant Nusselt number, a constant Reynolds and Prandtl number, and at a constant radial temperature.

These are the required scaling laws for the thermal-hydraulic behavior inside of the receiver tube: With these boundary conditions in place, the radial temperature profile of the tube in the model receiver is identical to the radial profile of a tube in a large scale receiver. At such conditions the tube face temperature is identical in both cases. This generates radiation losses of the same relative magnitude in both geometries.

Loss mechanisms to the ambient of external panel receivers are independent from the heat-transfer fluid applied and in principle not of primary interest of this work. Nevertheless, their impact on the experiment must be considered.

The impact of forced convection, which plays an important role in commercial receivers, can be suppressed by the protected environment when examining the model receiver. Radiation losses and those due to natural convection can be kept at a low level by application of low receiver temperature, but will unavoidably be present.

Losses due to natural convection are a function of the Prandtl number of air and the Grashof number,

$$\mathrm{Gr} = \frac{g\beta(T_{\mathrm{o}} - T_{\infty})L^3}{\nu^2}. \tag{3.51}$$

In that definition, T_{∞} equals the ambient temperature This number contains the geometry parameter L, that is the receiver's height, to the power of three. This high power will make it impossible to compensate a significant scaling

of the aperture height through the remaining parameters appearing in the definition of this dimensionless number.

Therefore, the model receiver will not feature Grashof-similarity with commercial systems and thermal losses of the reference cannot be predicted quantitatively.

Partial similarity between LBE and sodium is obtained in a small temperature range: The LBE flow at 600 °C has the same Prandtl number as sodium at 390 °C: $\mathrm{Pr} = 0.01$. Accordingly, the same Nusselt number can be obtained for both flows at the same Reynolds number. Scalable results for the wall-to-bulk temperature difference can then be obtained. However, due to those fundamentally different temperature levels the resulting losses on the outside are not similar at all. Also, thermal conductivity values in the tube wall will differ and would require adaptation of the wall thickness. These factors make it impossible to draw general conclusions for the same receiver which is operated with sodium.

Nevertheless, the receiver in SOMMER can serve as a model for a reference LBE receiver and at least indicateive results can be obtained and extrapolated to receiver operation with other fluids, for example, sodium.

4 Solar test loop and receiver design with LBE: SOMMER

The following sections provide an overview of the design and construction of the experimental facility SOMMER. Explanations are continued in the appendix where appropriate in order to achieve brevity in the following sections. However, the design of the heat flux measurement device and the thermal receiver are presented more thoroughly to account for these component's important role in the experiment.

4.1 The solar furnace

For the solar furnace a location close to the KALLA's office building and workshops has been selected to facilitate maintenance, logistics, integration in the available control and data-logging infrastructure. The KALLA operates a centralized, in-house data management system, ZEUS, for measurement data logging of all experimental loops. The SOMMER project's data are as well managed by ZEUS and, therefore, a nearby installation was convenient. The previously built laboratory hall pre-defined the available area for the solar furnace, the operator's room and the liquid metal loop, which is required to supply the receiver with cold coolant and remove the collected thermal energy from the heated coolant. A bird's view image of the assembly, an outside view with the heliostat frame, an inside view of the hall and the respective area plot are shown in Figures 4.1 and 4.2, respectively. The hall's roll-up gate is located south-east of the base of the heliostat. This heliostat is required to re-direct the sunlight into the hall upon a stationary concentrating mirror while compensating the earth's rotation and

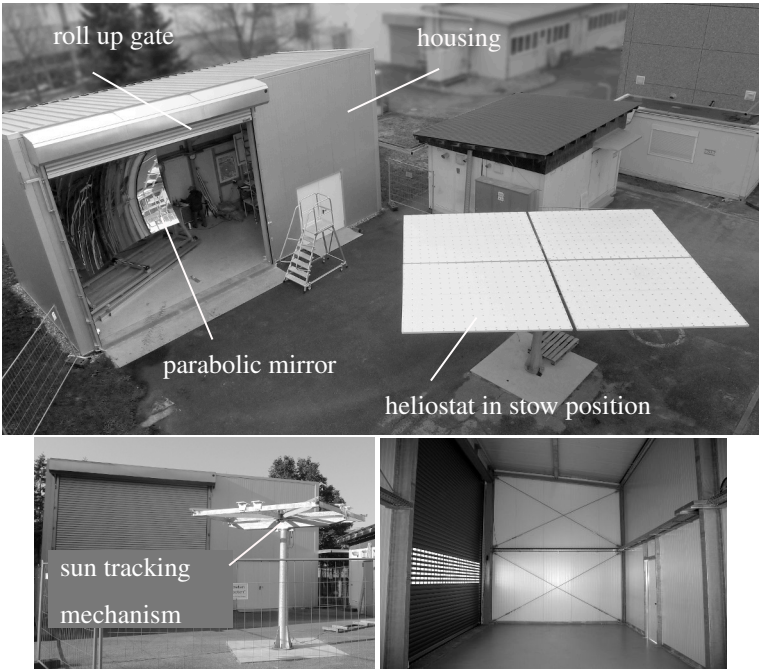

Figure 4.1: Top: Bird view of solar furnace assembly during winter (with frosted mirror surface and reflective tags for mirror qualification campaign) prior to the erection of the liquid metal loop.Bottom left: Heliostat frame (without mirrors) as of Dec. 2013. Bottom right: Empty hall with shut roll-up gate as of Oct. 2013.

the apparent motion of the sun throughout the day. The concentrating mirror generates high-flux conditions required for the experiments in its focal point.

The location of this facility on KIT's Campus North in Eggenstein-Leopoldshafen[1] has good irradiance values in comparions with other regions

[1] 49.0932N, 8.435 96E

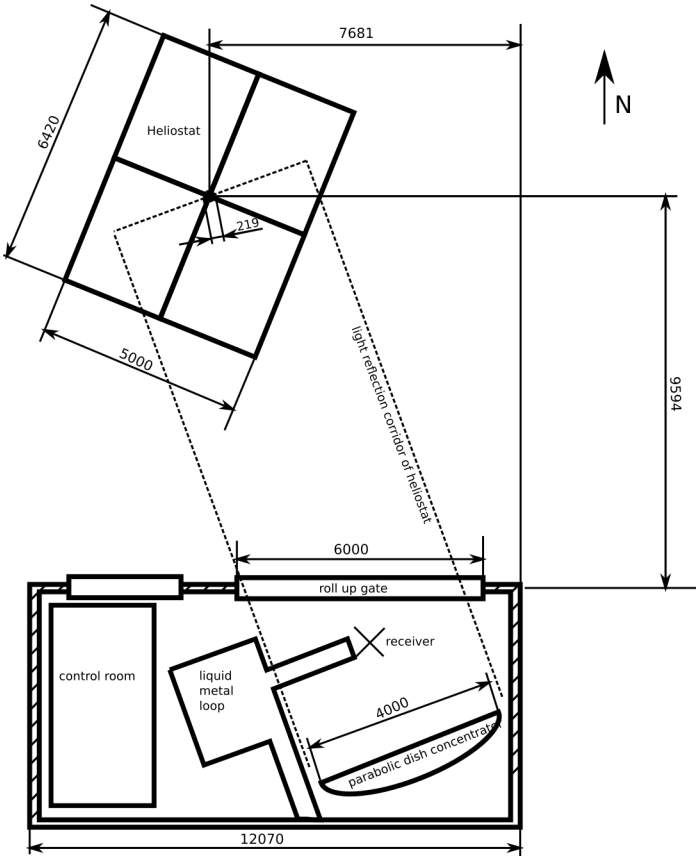

Figure 4.2: Area plot of the SOMMER facility including the parabolic concentrating mirror in the hall and the approximate location of the focal point.Dimensions in millimeter.

in Germany: Between 2007 and 2016 in average, annually a cummulated direct normal irradiance (DNI) of 1043 kW h m^{-2} had been available[2].

In Figure 4.3 the annual direct normal irradiance in Germany is shown. It can be observed, that the location in Eggenstein-Leopldshafen near Karlsruhe this value above the country's average.

4.1.1 The heliostat

The heliostat, required to continuously transfer sunlight to the stationary solar thermal receiver of the liquid metal loop, consists of four sandwich mirror panels by ToughTrough, with an AGC Thin Mirror Glass as front layer and a polyurethane core contained in a weather sealed housing. The mirrors have a 1 mm thickness and use silver as reflective layer, at a claimed 95 % to 96 % hemispherical reflectivity. Each panel is subdivided along the long, horizontal axis in two flat facets that are slightly canted with a focal length of 500 m. It was expected that due to the small distance between receiver and heliostat of approximately 10 meters the projected images of these canted facets would overlap only slightly. Each panel has a width of 3220 mm and a height of 2510 mm including the 5 mm frame thickness surrounding the reflective area. The heliostat's total reflective area is therefore 32.1 m^2. The pole, drive unit and mounting are made by former Cirris[4] with hydraulic azimutal and elevation tracking. Based on a serial bus protocol the tracking control algorithm for the drive unit was manually implemented by the KALLA-team in Labview[5].

[2] according to PVGIS data from `https://re.jrc.ec.europa.eu/pvg_tools/en/tools.html#MR`, Last accessed Nov 15, 2020.

[3] Source: Solar resource map © 2019 Solargis (`https://solargis.com/maps-and-gis-data/download/germany` , published under CC BY-SA 4.0 license, `https://creativecommons.org/licenses/by-sa/4.0/`) Last accessed Nov 15, 2020, edited to include Karlsruhe.

[4] CIRRIS Solutions GmbH, Steinung 3/1 Jettingen, Germany. In 2015 Cirris was aquired by Schleuniger Group, Bierigutstrasse 9 CH-3608 Thun, +49 74 52 740 62 80 `schleuniger.com`

[5] Acquisition, installation of the base frame and programming of the heliostat mainly conducted by F. Fellmoser and J. Pacio

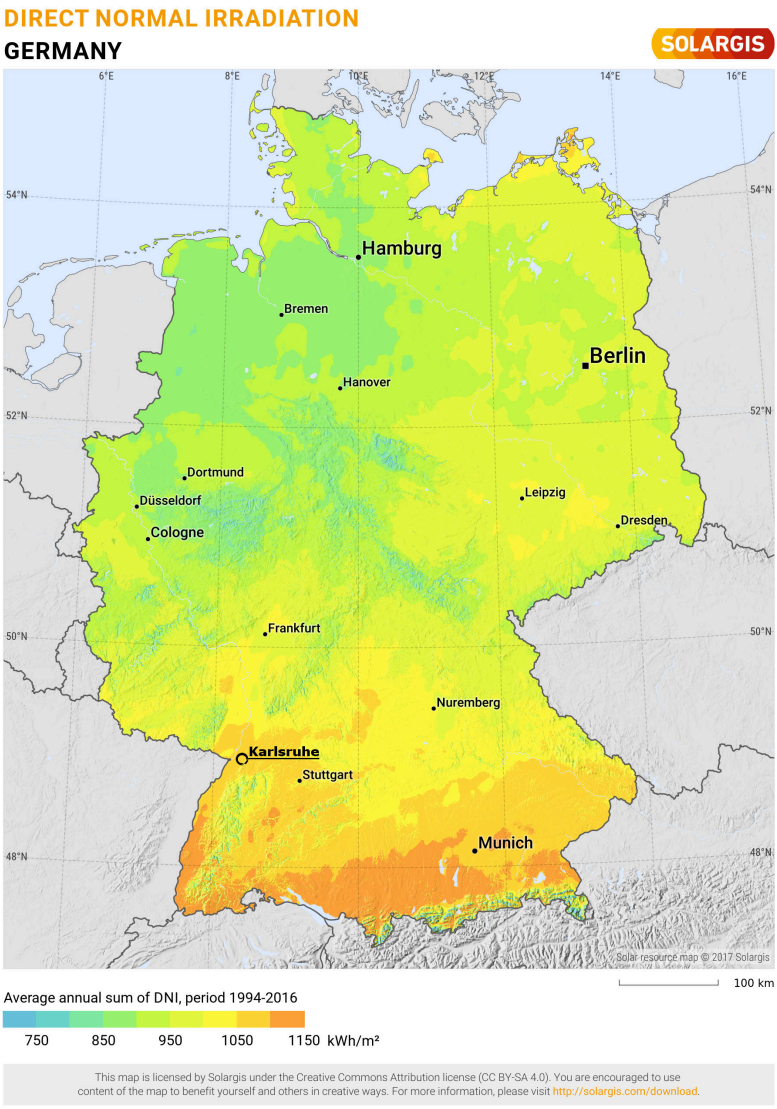

Figure 4.3: Annual direct normal irradiance in Germany[3]

The heliostat's support frame allows individual alignment configurations of each of the four mirror panels. Therefore, the optimum alignment of all facets has been determined in a mirror qualification campaign conducted between November 23 and 26, 2015 with support of CSP Services[6] who applied a photogrammetry analysis in order to quantify the present misalignment and to define corrections for all mounting points. After correction of the alignment it has been possible to state a residual maximum angle deviation of all surfaces of -0.7 mrad in horizontal direction and 0.8 mrad in vertical direction. The effect of the present canting of the indiidual facets in each of the four panels the surfaces has been quantified to equal 2 mrad.

4.1.2 The parabolic mirror

A stationary parabolic concentrator mirror in the laboratory hall is used to focus the incoming light from the heliostat on the test receiver. A frontal photograph of the mirror is shown in Figure 4.4 Figure 4.5 shows several stages of the mirror assembly. This configuration provides solar flux to a fixed point in the laboratory hall independent of the continuous apparent advancement of the sun along its path across the sky and thus allows for a permanent, fixed experimental setup to be exposed to that flux.

On the market only very few designers and supplyers of parabolic mirrors exist and in general no off-the-shelf products can be found in the required quality and size.

Fortunately, sbp solar[7] provided a contact to Forbes Solar[8], an Inida-based company that at that time offered a twin-mirror concentrating photovoltaic co-generation system. These units featured two dishes mounted on

[6] CSP Services GmbH, Friedrich-Ebert-Ufer 30, 51143 Köln (Cologne), Germany, `http://www.cspservices.de/`

[7] Schwabstraße 43, 70197 Stuttgart, Germany, +49 711 64871-0, `https://www.sbp.de/en/solar-energy/`

[8] FORBES SOLAR PVT LTD. A-34/35, MIDC Estate, H Block, Pimpri, Pune – 411 018. Or: PB #29, Mumbai-Pune Rd., Kasarwadi, Pune 411 034, Tel : +91-20-39858555, `www.forbesmarshall.com`

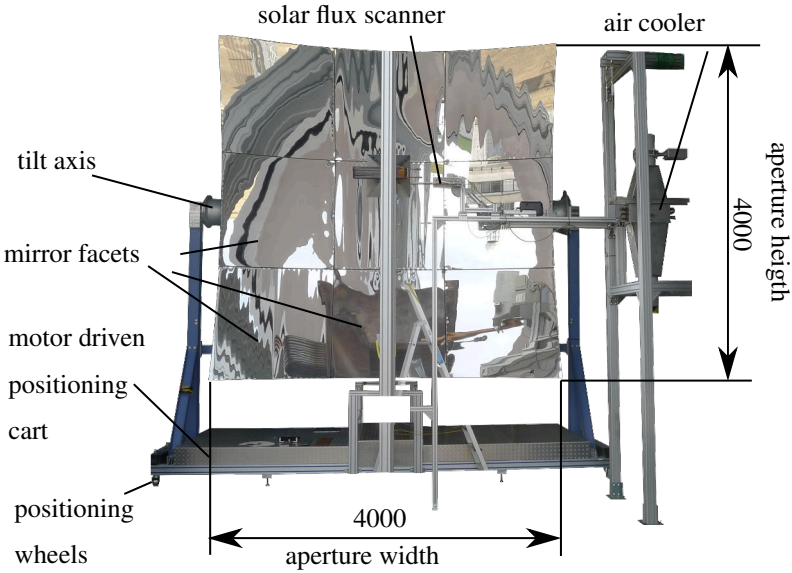

Figure 4.4: Frontal photograph of the parabolic mirror during the construction of the liquid metal loop.

Figure 4.5: Parabolic mirror prior to (left image) and after mounting (right image) on support frame.

a common and two-axis tracking unit. Each of these twin parabolic shaped mirror sets had a square $16\,m^2$ aperture area and consists of nine mirror facets of three different shapes. In the intended application a water-cooled concentrating photovoltaic solar cell by Azur Space would generate electricity and warm water for use in remote applications, for example, in laundry services. As the mirror support structure and the mirror facets of this system matched the requirments of the SOMMER' solar furnace it has been negotiated with Forbes Solar to purchase a single one of the twin sets of the rigid support structure for the mirror mounting and two sets of nine glass segments, each.

These are 3D-shaped glass segments made by Flabeg[9] with typically a total slope error of equal or less than 3 mrad. The focal length of 2400 mm of the complete assembly made the setup within the hall possible.

A custom mounting for the mirror has been designed and built[10] with the ability to drive the parabolic mirror a distance of 525 mm along the axis between the heliostat's center of rotation and the parabola's center. This option allowes to focus and de-focus the focal point on the receiver's absorber plane. The linear motion has later been constrained to 450 mm due to the space required for shutter, emergency curtain and receiver. The support structure is furthermore equipped with wheels that allow the positioning in the laoratory hall for alignment with the heliostat. A drawing of the support structure is shown in Figure 4.6[11]. During the mirror qualification campaign with CSP Services also the alignment of the concentrator's mirror facets has been assessed by deflectometric measurements and the identified offsets corrected. The individual facets have a very slight stripe pattern – a typical residue from the production process, which is human-eye visible and has

[9] FLABEG Deutschland GmbH, Waldaustrasse 13, 90441 Nuremberg, +49-911-964560, `http://www.flabeg.com/`

[10] Design and acquisition of this support structure was mainly conducted by A. Jekel according to the required specifications.

[11] Simplified mirror parabola with exaggerated curvature, with 9 original individual facets replaced by a single one and without the cover of the linear drive unit.

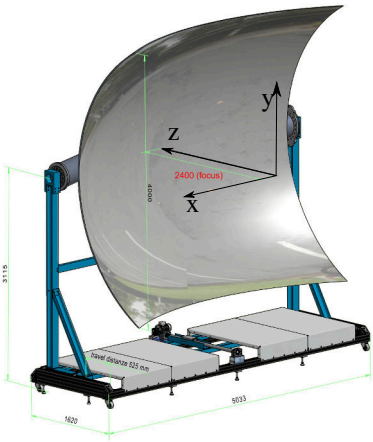

Figure 4.6: Parabolic mirror; design and drawing by A. Jekel. Dimensions in millimeter.

been revealed by defectometry as well as slight canting of individual faces. After the correction of alignment the average slope standard deviation error in horizontal direction has been reduced from 2.51 mrad to 1.94 mrad mrad and in vertical direction from 2.31 mrad to 2.14 mrad. The mean deviation of all panels has been reduced to less than 1 mrad in both directions. It has also been tested and approved that the forward- and backward drive applies no stress or strain onto the facets which could have reduced the alignment accuracy or have introduced flexing of the facets and a distortion of the projected flux.

The parabolic mirror has been simulated by CSP Services via ray-tracing under assumption of a 90% reflectivity of the mirrors at circum-solar ratio of 3.5 %. A concentration ratio[12] of more than 17 000 was found versus 12 400 prior to the alignment correction.

[12] That is the ratio of concentrated solar flux density in the focal point and the solar flux density entering the concentrator's aperture.

SolTrace has been used throughout the selection process to assess the suitability of the offered mirror geometries. Based on a 3D model of the solar furnace the flux distribution has been estimated. Since the flux measurement system has become operational[13], the predicted and measured flux can be compared. On September 13, 2016 at 15:13 o' clock and DNI of $770\,\mathrm{W\,m^{-2}}$, the distribution as shown in Figure 4.7 in the bottom graph has been measured. The top graph shows the simulation. There is a horizontal offset between bot recordings visible which is a result of the aim point of the heliostat, which was not perfectly aligned with the center of the absorber in the bottom graph.

The distributions both agree in containing two separate vertically aligned maxima of flux. The origin of a two maxima instead of only one expected maximum is the canting of the heliostat mirror's facets.

The 3D model is simplified and estimated values for reflectance and surface quality have been applied. This has been sufficient for the estimation of the expected orders of magnitude for power and peak flux. Therefore the observable differences between simulation and measurement arise from irregular imperfections of the heliostat and from the shutter (Section 4.1.4), which was in a lowered position during this measurement with its lamellae in horizontal orientation. The shutter was not accounted for in the simulation.

4.1.3 The DNI measurement

The direct normal on site is measured by a Hukseflux DR02-05 Pyrheliometer mounted on an EKO STR-21G sun tracker with GPS receiver.

More than $960\,\mathrm{W\,m^{-2}}$ are frequently measured on clear days.

[13] At this stage the first of three generations of HFM sensors was used. At that point of time no precise calibration was available. Therefore a high uncertainty must be assumed in the resulting images.

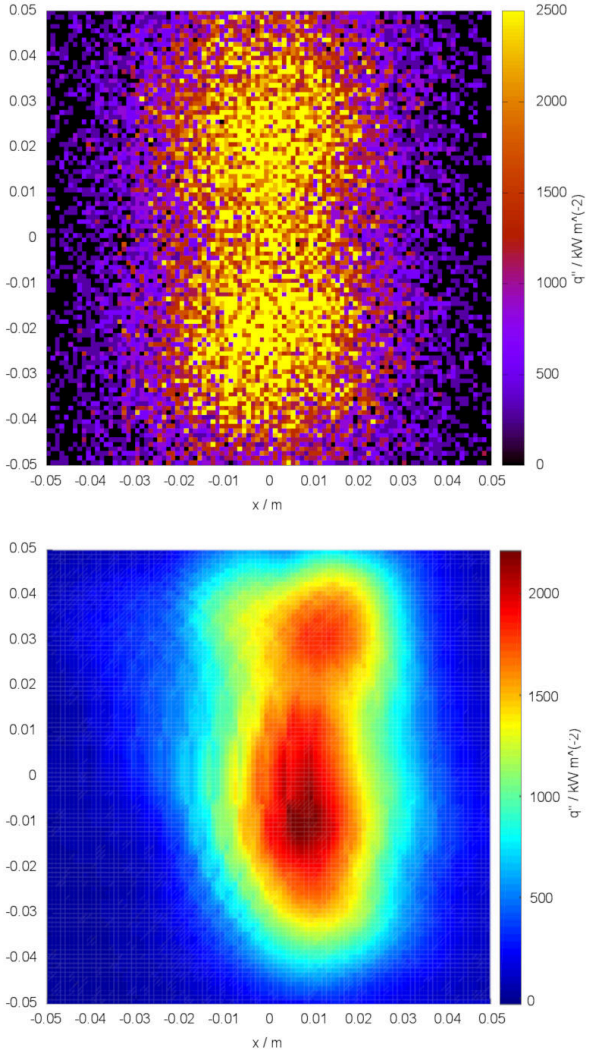

Figure 4.7: Heat flux distribution $q''/\mathrm{kW\,m^{-2}}$ on the focal plane. Top graph: simulated; bottom graph: measured.

4.1.4 The shutter and emergency flux shutoff

Three different means exist to block the light passage between heliostat and the parabolic mirror: A weather-proof roll-up gate, variable-angle shutter blinds and an opaque curtain that can be dropped within seconds in emergency situations and which is gravity driven.

The gate serves the purpose of protecting the hall's innards from ambient conditions during down-time and stand-by. Due to small windows contained in the blades it cannot serve as a light shut-off.

Horizontal lamellae impose only a small effect on the flux distribution when used for regulating the amount of light passing through to the parabolic mirror. Therefore shutter blinds by Warema[14] are installed in the plane behind the gate. These can be controlled via a SMI PC interface from the control room and set to pre-defined angular positions in order to set the transmitted solar power.

The white aluminum lamellae are 95 mm wide and shut tight in vertical orientation. They are arranged in two vertical columns of 2330 mm by 4582 mm each with a vertical center rail.

This shutter is closed as a safety precaution prior start of daily loop operation. Once coolant flow is established, the blinds can be opened. With the lamellae in horizontal position roughly 80 % of maximum solar power can pass the shutter. For more power the blinds are raised via an electric drive.

The closed shutter is shown in Figure 4.8 with light from the heliostat projected upon it.

In emergency situations, such as power outage, however, this shutter cannot serve as shut-off mechanism. Also the slow speed of its drive makes an additional, instantaneous emergency shut-off a requirement.

Therefore, a gravity driven curtain, actively held in place by electromagnetic spring loaded actuator has been installed in the second plane behind

[14] WAREMA Renkhoff SE, Hans-Wilhelm-Renkhoff-Straße 2, D-97828 Marktheidenfeld, `https://www.warema.com`, phone: 9391 / 20-0

Figure 4.8: Closed shutter with sunlight reflected upon it by the heliostat on a morning at 10:45 o'clock near autumn equinox. The neighboring building casts its shadow onto the heliostat which is visible in the projection's bottom left edge.

the gate. Upon power outage or upon release signal the actuator's spring triggers the release of the curtain which then drops to the floor within less than three seconds and closes the passage of light. This prevents overheating of the receiver and its surroundings in inexpected events, such as a power outage causing the pump to stop. The curtain is guided and held in place by steel wires and is pulled to the floor by weights so that it cannot be pulled aside by wind.

4.2 The liquid metal loop

The lead-bismuth loop provides a continuous liquid metal coolant flow at constant temperature to the thermal receiver and removes the thermal power absorbed by the receiver. Besides the thermal receiver it consists of a pump, a heater, an air cooler, a storage vessel with 300 L of volume and a gas supply system. The loop's PID is shown in Figure 4.9. These components

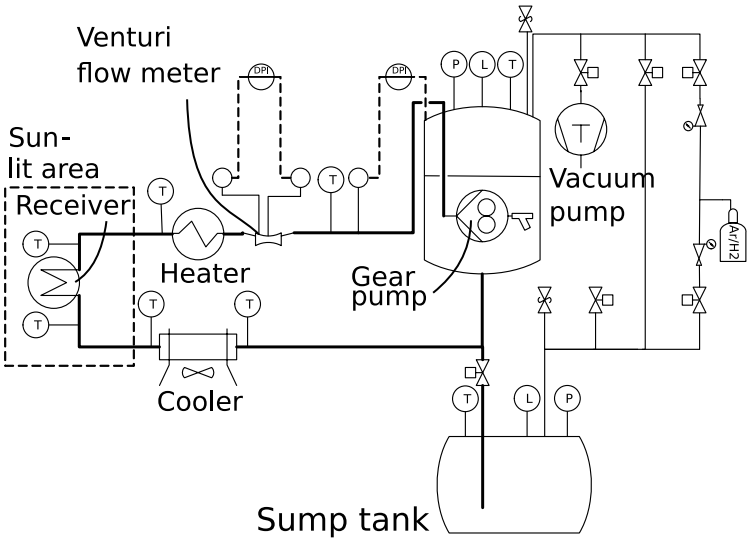

Figure 4.9: Slightly simplified PID of the SOMMER loop.

are vertically arranged as shown in Figure 4.10 with the receiver located in the focal point at an elevation of approximately 3 m above ground. This sump vessel contains all the loops LBE volume during down time. The loop is equipped with a vacuum pump in order to remove all gas prior to the filling process and a argon hydrogen gas supply in order to apply a gas cover to the pump vessel after the filling procedure is completed.

Several temperature sensors are distributed along the LBE flow, as shown in Figure 4.11. The LBE's mass flow rate is determined from measured differential pressure in a venturi orifice.

Highly precise pressure measurement is possible in LBE. Due to the risk that sensitive pressure indicators are damaged from freezing LBE during down time, these indicators can be separated from the direct LBE contact by hydraulic oil. This requires a remote pressure coupling and fluid separa-

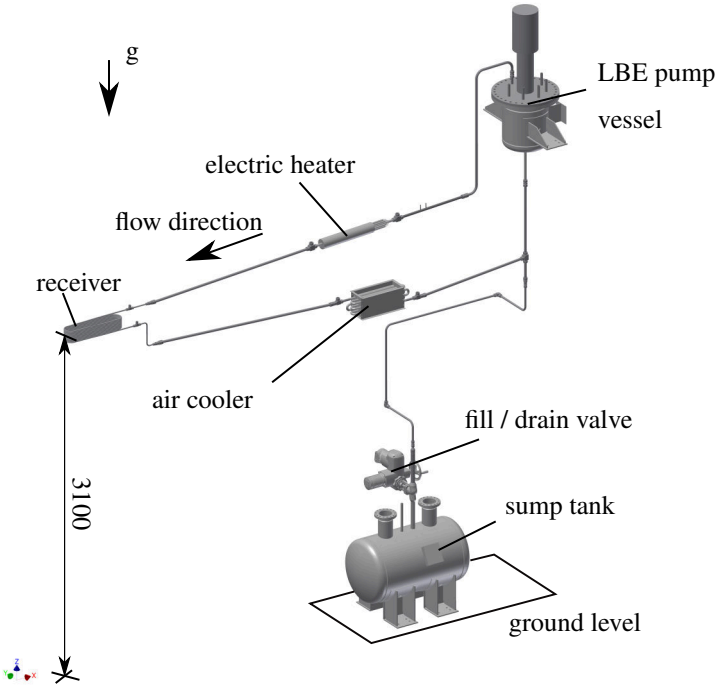

Figure 4.10: CAD drawing of the LBE loop's main components.
(F.Fellmoser/Flesch)

tion by stainless steel diaphragm seals which are commercially offered by instrument manufacturers.

During operation, gas residuals can interfere with the pressure measurement. The amounts of gas are reduced significantly beforehand by evacuation of the entire loop prior to each filling. Once the loop is evacuated, LBE is pushed up the filling/draining line by a argon hydrogen pressure applied to the free surface in the storage vessel. Once the LBE level has risen to the pump vessel it is detected by level indicators which signal the detection of LBE by having an electric circuit closed by the electrically conducting liquid metal itself. Once this level is reached the drain valve is closed and the pump vessel is filled with an argon hydrogen mixture until atmospheric pressure is obtained. This pressure increase pushes the LBE level up into the pressure line behind the pump to completely fill the loop.

Due to the periodic draining and filling of the loop sludge and particles can precitipate on the diaphragms and impact the measurement. Even though the loop is evacuated during filling, compressible gas can still be trapped on the diaphragms.

Therefore purge lines are required for each diaphragm hydraulic coupling. These lines are collected and re-directed to the pump vessel. Purging requires a running pump: With extra purge valves open, the diaphragms are purged upon the establishment of mass flow through pumping. They are then closed and the loop is ready for operation. Successful removal of trapped air or debris would be detected by a measured change in the pressure value after purging.

For draining of the loop the automatic drain valve is opened and argon hydrogen allowed to fill the volume freed from LBE. Driven by gravity LBE flows then back into the storage vessel. All tubes in the loop are sloped towards the drainage line to ensure complete draining of the loop.

All pipes and instruments in contact to LBE must be trace heated and temperature monitored to prevent the freezing of LBE. Tubular heaters made by Eichenauer and flexible heating cables by Horst are used.

The storage vessel is designed and protected by a safety relieve valve for pressure up to 6 bar required in the gas cover in order to push fluid against the static pressure of LBE when the level resides in the pump vessel of about 5 bar.

All connecting pipes are of 1.4571 stainless steel and have an inner diameter of 16 mm and a wall thickness of 2 mm. As an exception the drainage pipe has an outer diameter of 16 mm and wall thickness of only 1 mm in order to provide a larger cross section for emergency drainage. All components are connected with Swagelok fittings.

Mineral wool is used in the cold part and ceramic wool in the hot part for thermal insulation.

The desing of the loop, including its operation parameters and configuration as shown in Figure 4.11, and its geometry was stronlgy influenced by design decisions of the thermal receiver and by the availablility of equipment, such as pumps. Therefore the final design presented here is a result of several iterations including the receiver design. This process is briefly outlined in the Appendix section A.3.

4.2.1 The pump

A mechanical gear pump has been used for the final design of the loop. The gear pump model CHEM 10,2-2, has been obtained from the German manufacturer Witte. The pump has been delivered pre-mounted in a custom top flange for the respective pump vessel. The final assembly of that vessel with the pump mounted on top is shown in Figure 4.12 The predicted, differntial pumping pressure of more than 6 bar has been much higher and design LBE flow rate of $1\,\mathrm{kg\,s^{-1}}$ has been much lower than what had been applied in present laboratory loops at KALA in the past and thereofre constituted a novelty. The existing loops use centrifugal pumps that are specially selected to cope with LBE's very high density.

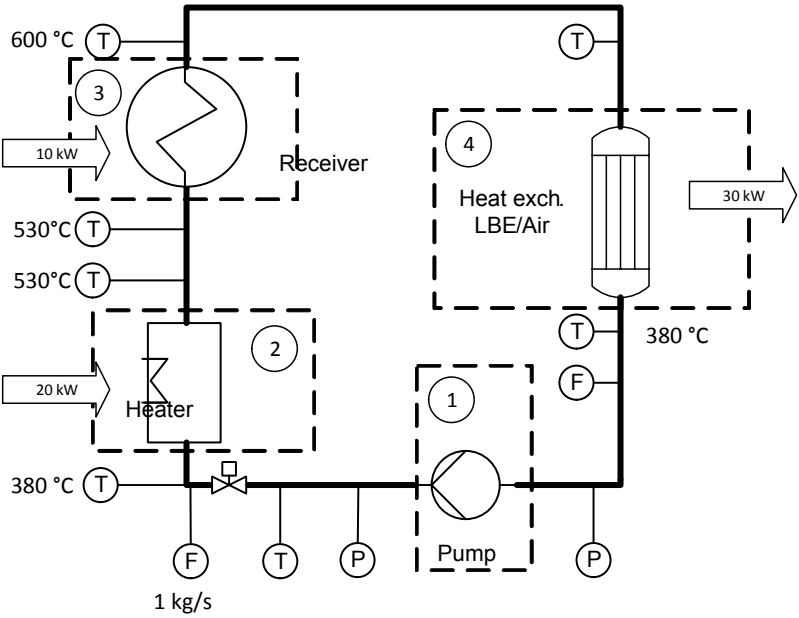

Figure 4.11: Flow diagram of final loop configuration excluding gas and vacuum supply and other peripheral pieces of equipment.

The high density generates high axial forces in centrifugal pumps, which act on the axial bearings. They are problematic as these are proportional to the liquid's density.

As a general rule the pump head H is quadratic proportional to the pump's rotational speed n:

$$\Delta H \propto n^2, \tag{4.1}$$

and the differential pressure is related to the pump head according to,

$$\Delta p = \rho g H. \tag{4.2}$$

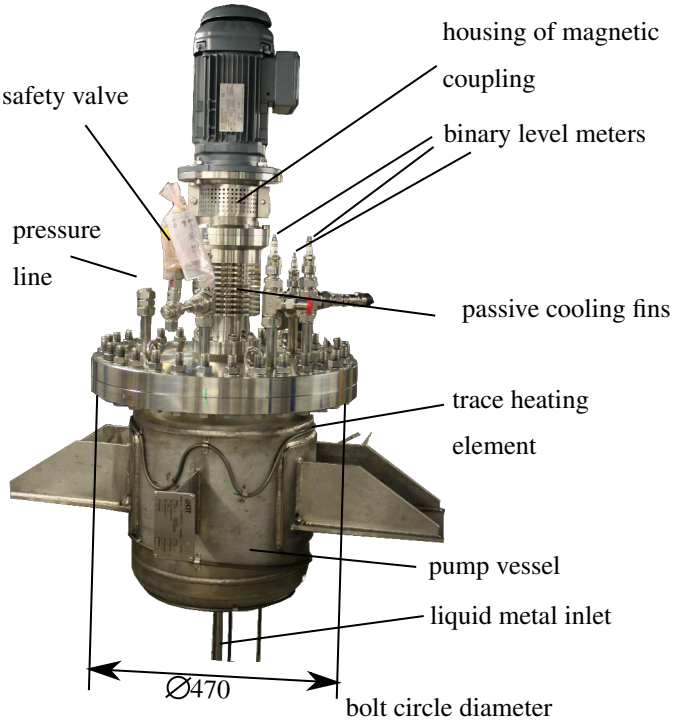

Figure 4.12: Complete pump assembly without thermal insulation.

At the same pressure difference, for example, water can be pumped ten times higher than LBE.

The axial force on the shaft is approximately equivalent to,

$$F_{\mathrm{ax}} \approx \Delta p A = \rho g H A, \tag{4.3}$$

with A being the free cross section between the pump blades. In order to keep the axial forces constant at the ten times higher density and one tenth

of pumping head the rotation speed of the pump in a LBE flow has to be reduced to $\sqrt{1/10}$, which equals approximately one third.

The volume flow is directly proportional to the rotational speed so that in LBE service the pump delivers only one third of its nominal water volume flow.

Thus, if a pump specified for the use with water shall be selected for LBE service its design water pump head has to be ten times of that intended for the LBE application, three times the intended volume flow rate and that pump has then to be operated at one third of the design rotational speed.

However, no centrifugal pump could be found on the market to operate in the intended operation window due to the small required volume flow rate. and therefore a gear pump has been selected.

Straight tooth gears of 1.4112 stainless steel with 28 mm axis distance and a tip diameter of 32 mm are applied. They are hardened with a CrN-mod coating in order to improve wear resistance. A silicon carbide shaft bearing in contact with LBE is used. The casing in made of 1.4313 steel. A 400 V SEW 0.75 kW electric motor drives the pump. The pump operates in a range of 588 min^{-1} to 1118 min^{-1} for mass flow rates of 0.1 $\mathrm{kg\,s}^{-1}$ and 1 $\mathrm{kg\,s}^{-1}$, The nominal operation differential pressure is 11 bar, and in order to protect the loop the pressure line is equipped with a safety valve with nominal 17 bar release pressure.

Due to the small gaps between the gear teeth' outer edges and the inner wall of the casing these pumps are sensitive to particles in low-viscosity fluids. Accordingly, the LBE flow is filtered prior to entering the pump with a mesh filter with 0.2 mm thread thickness and square pores with 0.3 mm edge length. This stainless steel mesh is applied onto a cylindrical frame in order to provide 183 cm^2 mesh area with 66 cm^2 free cross section; an area ten times that of the pump's suction inlet in order to obtain a minimal pressure loss of this filter. The pump head with the filter installed is shown in Figure 4.13.

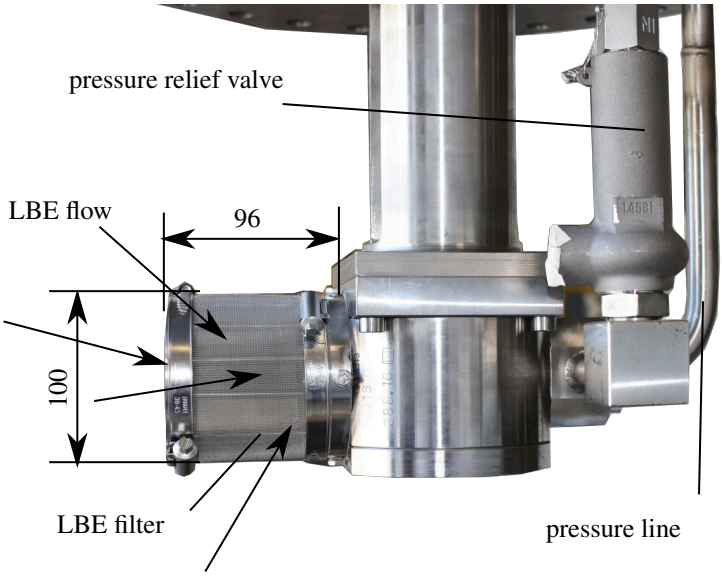

Figure 4.13: Pump head with particle filter on the left and safety valve in the pressure line on the right. To be submerged in LBE in the pump vessel.

Shaft sealings are potentially incompatible with LBE. This makes pump heads submerged in a free-surface pool of LBE a convenient solution. The free surface is conveniently contained in a vessel where the shaft sealings can be located outside the liquid volume, for example near the vessel's lid. The selings they are then in contact only with a cover gas above the open surface. As cover gas, argon-hydrogen is applied in the SOMMER facility. In order to obtain the free surface, the pump vessel is installed in the highest

position at the filling level of the loop. This allows to apply the cover gas at a low pressure difference to the ambient pressure.

A magnetic coupling of the shaft is used, sealed with a borosilicate glass can. The magnets in the coupling are sensitive to heat and therefore installed in a distance away from the vessel. The support is equipped with cooling fins in order to keep the coupling's operating temperature low when the maximum allowable LBE temperature of 380 °C is attained.

The vessel lid, which is derived from a DN350 blind flange geometry with 520 mm of diameter and 39 mm thickness is attached to the vessel and sealed with a Heliocoflex spring energized seal with armco coating. Experience in the laboratory shows that the number of screws as defined for DN flanges is not sufficient to apply enough and sufficiently evenly distributed force onto this kind of sealing to make it completely tight. The standard for DN350 flanges requires 16 M24 metric screws for tightening. For this application, however, 32 M16 screws are used instead.

The flange has been specified to be pierced by the pressure line outlet and five pipes. These pipes are used to permanently mount level indicators, a temperature measurement probe and to connect the argon hydrogen supply, the vacuum system and the safety relieve valve, as well as the purge fluid return flow.

The LBE level during operation resides approximately 5 cm above to suction inlet of the pump in order to generate sufficient static pressure for cavitation suppression.

The allowable over-pressure of the pump vessel is one bar and ensured by the safety relieve valve.

4.2.2 The heater

In the SOMMER loop a flow of 1 kg/s of liquid lead-bismuth eutectic alloy shall be heated under reference conditions as listed in Table 4.2 on page 111. The flow leaves the pump vessel at a temperature of 380 °C and shall be

heated up to 530 °C, which is the required temperature at the receiver inlet in order to achieve a receiver outlet temperature of 600 °C. Were there a higher thermal power available from the associated solar furnace such heater would become obsolete and the liquid could be heated with sunlight, exclusively. The heat capacity of LBE at 530 °C is approximately $142\,\mathrm{J\,kg^{-1}\,K^{-1}}$ and nearly constant throuthgout the loop's operational temperature range. The required steady-state deliverable design thermal power equals therefore:

$$\dot{Q} = \dot{m} \cdot c_p \cdot \Delta T = 1\mathrm{kg/s} \cdot 140\,\mathrm{J\,kg^{-1}\,K^{-1}} \cdot (530\,^{\circ}\mathrm{C} - 380\,^{\circ}\mathrm{C}) = 21\,000\,\mathrm{W}. \tag{4.4}$$

In the loop the heater is acting as control element for its own outlet temperature. Therefore heating rates higher than the required steady-state power are required to counteract temperature fluctuations or disturbances in the mass flow rate. These can occur, for example, when the sun is fully exposed after having been partially covered by a cloud and the mass flow is suddenly increased for compensation. Higher than nominal heating power is then required to quickly restore the heaters outlet temperature to its set point value. For that purpose the heater is designed to deliver a thermal power of up to $\dot{P}_{th} = 30\,\mathrm{kW}$.

The temperature response of that heater shall be as quick as possible, therefore the design should present a minimum fluid volume for minimum residence time and a lightweight construction while at the same resist the design pressure of 17 bar.

The heater as depicted in Figure 4.14 has therefore been specially designed for the loop. The design process is described in detail in the Appendix section A.5.

4.2.3 The air cooler

A cross-flow air heat exchanger with continuously finned tubes is used as a cooler, shown in Figure 4.15.

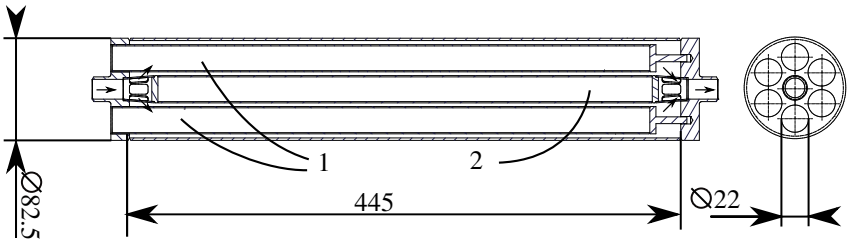

Figure 4.14: Final design of the heater. The protective shells for the heater rods are indicated with '1', the central, non-heated tube is indicated by '2'.

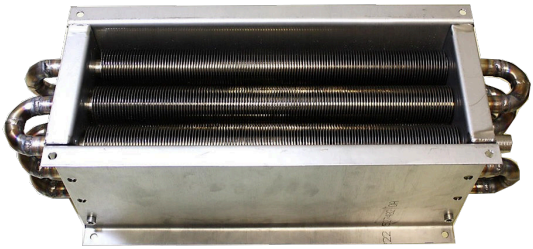

Figure 4.15: Finned tubes heat exchanger.

The liquid metal flow in the tubes passes the air stream in serial fashion nine times. The respective nine straight tubes are arranged in a rectangular pattern in three rows and columns with the hot LBE flow entering first the three serial tubes in cross-flow with the entering cold air. This cooler has been designed by Michael Kant according to the cell method presented in [67, p.258], build and tested during his Master's thesis [68] under Julio Pacio's supervision. The requirements for this cooler have changed for the present design. Its design process and the positive assessment for the application under these changed parameters are described in the Appendix section A.6

4.3 The thermal receiver

An iterative process has been required for the design of the thermal receiver of the SOMMER experiment and the attached liquid metal loop. Ambitious operation targets and at the same time existing constraints in size and power rating initially posed a great challenge for the attached liquid metal loop and vice versa. This design process is summarized in the following sections.

The size for the receiver is a result from the available solar power as delivered by the solar furnace and the design target of an average flux density of $1\,\mathrm{MW\,m^{-2}}$. On days with high irradiation the solar flux is sufficient for generating a thermal power of 10 kW. This results in a receiver aperture area of $0.01\,\mathrm{m^2}$.

Additionally, the receiver was designed for maximum dimensionless similarity of heat transfer to the liquid metal flow in comparison with a larger-scale receiver, resulting in requirements for the flow conditions.

The following section therefore discusses the process of generating a larger-scale reference system, obtaining the thermal-hydraulic flow conditions of that system and implementing these with dimensionless similarity in the experimental receiver of the SOMMER experiment. The receiver applied in the SOMMER loop shall therefore be called ‘model receiver’ throughout the following section.

4.3.1 A hypothetical reference receiver

The dimensionless numbers of the flow, which are likely to occur during the operation of a commercial-scale thermal Receiver, must be obtained as well during the small-scale, model receiver’s operation. Otherwise, no similarity between both systems is provided and an extrapolation of measured performance to the large-scale case is not possible. Such commercial-scale receiver will be called ‘reference receiver’. However, what are typi-

cal thermal-hydraulic conditions and the respective values of dimensionless numbers of such a reference receiver?

A well-documented project with a thermal receiver operated with a liquid metal is that of the SPSS advanced sodium receiver as introduced in Section 1.3.1. During its operation until 1986 the receiver was tested up to its very limits when imposing a peak heat flux density of $2.5\,\mathrm{MW\,m^{-2}}$ to it at a thermal power of 3.4 MW. The design of this receiver as well as operational experience is documented in a couple of publications (e.g. Ref. [26, 27]). The latter report provides enough data to derive a reference for the model receiver of the SOMMER loop.

However, this receiver was operated with sodium, not with LBE and both fluids have different fluid properties and consequently, they have different Prandtl numbers except for a very small range of temperatures. Only in this interval their Reynolds and Nusselt numbers can be identical simultaneously:

$$\mathrm{Nu} = f(\mathrm{Re}, \mathrm{Pr}). \tag{4.5}$$

Due to this difference in properties a reference case operated with LBE instead of sodium must be obtained; then identical Prandtl numbers allow for scaling in a wide range of temperatures. Since LBE has not been used in commercial receivers such a commercial-scale reference must be theoretically determined. This reference's geometry, operated with LBE, can then be scaled to experimental proportions in a second step while maintaining both, the reference's Reynolds and Nusselt numbers.

One way to obtain a commercial-scale reference geometry for an LBE receiver is a detailed numerical system design and optimization including all components of a solar power plant simultaneously. This approach has been adopted during the LIMTECH alliance by the German Aerospace Center DLR, however, it has not yet been completed at the time when reference parameters were required. The execution of such an approach would therefore have exceeded the scope of this work. Therefore, only a simple model

of the receiver has been derived and optimized for operation with LBE, as described in the following:

A sodium-operated demonstration-scale reference has been used although some paragraphs ago a commercial-scale power reference has been demanded. However, currently only existing receivers operated with solar salt or water steam, both not being liquid metals, fulfill the criterion of having commercial scale. These fluids have a fundamentally different heat transfer behavior compared to liquid metals. Therefore, using a salt or steam system as reference would introduce uncertainty in whether their respective hydraulic configuration would be suitable for LBE at all. It shall be assumed that there is more similarity between the two liquid metals sodium and LBE and the transformation of a sodium receiver into an LBE receiver is more legitimate than using a salt or steam receiver as a basis. The resulting compromise in power rating has therefore been accepted and the SSPS receiver has been used as a basis for the identification of an LBE reference system, as presented next. Nevertheless, for comparison the same approach was applied to the case of the solar salt-cooled receiver of the Solar Two thermal power plant and the differences between both references discussed.

In a first step the sodium of the SSPS project's receiver has been hypothetically replaced by LBE. In a second step the receiver's geometry has then been optimized under a set of constraints and simplifications. The parameters resulting from that calculation could then serve as a reference for the SOMMER model receiver. During the fluid replacement operation the reference receiver was required to maintain the same overall thermal power output, the same temperature increase of the fluid and the same pumping power of the receiver flow as in the original case. The only parameters to be changed are the number and diameters of the tubes. Under these presumptions the effect of the fluid replacement imposed onto the remaining parts of the power plant are considered to be small: the original heliostat field size and the original power block configurations could be maintained.

This simple model used strong assumptions: it has been assumed that an equally efficient and economical storage option exists for LBE and sodium that allows to keep the plants' energy storage capacity. Also additional costs or savings of using LBE on the plant's economic balance have been neglected as well as mechanical stresses in the tubes of the newly obtained reference.

The resulting tube geometry and thermal-hydraulic behavior of the LBE flow in the reference then presented a case to which the small scale SOMMER receiver could relate.

For this approach at first the required receiver aperture area has been determined. The SSPS sodium receiver had a thermal power rating of 3.4 MW at approximately 90% thermal efficiency. In order to obtain that thermal power,

$$P_{\mathrm{rad}} = \frac{P_{\mathrm{th}}}{\eta_{\mathrm{th}}} = 3.4\,\mathrm{MW} \tag{4.6}$$

of radiation power is required incident onto the receiver.

An additional assumption was made: For the LBE reference receiver and the original operated with sodium the same thermal efficiency was assumed. With this assumption the same receiver aperture resulted and no impact on the required configuration of the heliostat field was generated. This assumption neglected that LBE will in fact not be able to cool the tubes as efficiently as sodium when the same pumping power is invested, as discussed in Section 3.1. The tube wall temperatures and the thermal losses would therefore in reality be higher at the same power output and the LBE receiver's thermal efficiency would be lower than that of a receiver operated with sodium. However, in order to precisely determine the actual LBE receiver's thermal efficiency, very detailed and iterative modeling of the thermal losses would be required. For our purpose of obtaining a first-approximation reference geometry the application of such a detailed method was out of scope. Alternatively, the LBE receiver's efficiency could have manually been set to

some lower value, which, however, would not have yielded a result being 'more right' as neither had resulted from a detailed simulation.

In order to obtain a thermal power of $P_{\mathrm{th}} = 3.1\,\mathrm{MW}$, a radiation power of $P_{\mathrm{rad}} = 3.4\,\mathrm{MW}$ is required. The SSPS receiver was operated with an average flux of $0.43\,\mathrm{MW\,m^{-2}}$ so the LBE receiver required an aperture area of $7.91\,\mathrm{m^2}$ in order to collect the required radiation power. The total mass flow of the receiver was calculated according to:

$$\dot{Q} = \dot{m} \cdot c_{\mathrm{p}} \cdot (T_{\mathrm{out}} - T_{\mathrm{in}}), \tag{4.7}$$

with $T_{\mathrm{out}} = 560\,^{\circ}\mathrm{C}$ and $T_{\mathrm{in}} = 270\,^{\circ}\mathrm{C}$ and c_p evaluated at the arithmetic mean of inlet and outlet temperature , that is in the considered case $415\,^{\circ}\mathrm{C}$.

The resulting mass flow rate is $\dot{m} = 74.1\,\mathrm{kg\,s^{-1}}$. This mass flow now has to be delivered across the receiver area to absorb the thermal power through receiver panels with their parallel tubes as shown in Figure 1.3. This has to be accomplished in such a way as to obtain the highest possible convective heat transfer coefficient but at the same time a pressure drop that results in a pumping power equal to that of the reference sodium receiver by allowing the number of tubes per panel and the tubes' diameters to be adjusted.

For the present case, the reference's nearly square receiver aperture area $A = W \cdot H$ is maintained which leads to a width W and height H of the receiver of $H = A/W \approx 2.73\,\mathrm{m}$. The reference's geometry is such that all tubes stretch vertically along the full receiver height as shown in Figure 1.3where one of several panels is schematically shown. The number of panels n_{p} horizontally divide the receiver in sections. The tube diameter d then determines how many parallel tubes ($n_{\mathrm{t,p}}$) can be fit into one panel, which results in each tube's mass flow rate and each tube's flow velocity. Then, the Reynolds numbers and Nusselt numbers of the tubes, as well as receiver's pressure drop can be calculated. A small number of serial panels leads to low pressure drop because of short, parallel receiver passage.

For this study it was decided not to vary the number of panels from the sodium case. This number is the result from minimized entropy generation from mixing of flows from the panel's tubes before advancing to the next panel. Also the differences in the outlet temperatures of individual tubes within the same panel are influenced by the flux distribution onto the receiver panels. These differences are in the original receiver also optimized for minimum thermal stress.

Additionally, construction constraints play a role. The panel design is optimized for manufacturing and installation on the tower top. Only detail engineering of the receiver will justify a reduction in the number of panels which was out of this work's scope. Also, since the flux distribution is assumed to remain unchanged in this study the number of panels was maintained.

Then the inner tube diameter and the number of tubes per panel has been varied to obtain the highest possible convective heat transfer coefficient while not exceeding the required pumping power of the SSPS receiver. A Monte-Carlo optimization algorithm in Microsoft Excel has been used for this task. The pumping power took into account only the pressure losses of the straight tubes. Pressure losses in collectors and diverters have been neglected.

The fluid properties of LBE were taken from Ref. [32] and for sodium from Ref. [69] and are evaluated at the arithmetic mean temperature of the receivers. The pressure drop has been calculated for smooth tubes of the length of five times the receiver height (five serial panels) and the friction factor correlation by Nikuradse, Prandtl, v. Kármán etc. [66, p.Lab 2]. For LBE, the Nusselt number has been calculated with the correlation by Lubarsky and Kaufman, which at the present Peclét numbers of about $Pe = 1300$ is an appropriate choice.

The results from the calculations are presented in Table 4.1.

Table 4.1: Parameters of the SSPS receiver operated with molten sodium and LBE. Values indicated with * are based on assumptions.

Property	Symbol	Value Sodium	Value LBE
Absorbed thermal power / W	$\dot{Q}$	3 058 000	3 058 000*
Inlet temperature / °C	T_{in}	270	270*
Outlet temperature / °C	T_{out}	560	560*
Average flux / W m^{-2}	q''	435 880	435 880*
Peak flux / W m^{-2}	q''_{max}	2 500 000	2 500 000*
Receiver efficiency / –	η_{R}	0.9017	0.9017*
Receiver radiation incidence / W	$\dot{Q}_{\mathrm{sol}}$	3 391 371*	3 391 371*
Receiver aperture area / m^2	A_{R}	7.78	7.78*
Arith. mean temperature / °C	T_{m}	415	415*
Mass flow rate / kg s^{-1}	$\dot{m}_{\mathrm{tot}}$	8.25	73.9*
Volume flow rate / m^3 s^{-1}	$\dot{V}$	0.01	0.0073*
Tube inner diameter / m	D_{i}	0.012	0.019*
Wall thickness / m	t_{w}	0.001	0.001*
Tube outer diameter / m	D_{o}	0.014	0.021*
Panels / –	n_{p}	5	5*
Parallel tubes per panel / –	n_{t}	39	27*

(... to be continued on the next page ...)

Table 4.1: Parameters of the SSPS receiver operated with molten sodium and LBE. Values indicated with * are based on assumptions.

Property	Symbol	Value Sodium	Value LBE
(... continued from the previous page ...)			
Panel height / m	H_p	2.75	2.75*
Single tube fluid velocity / $\mathrm{m\,s^{-1}}$	v	2.19	0.95*
Reynolds number / –	Re	83 094	124 148*
Nusselt number / –	Nu	6.99	12.98*
Peclét number / –	Pe	417*	1965*
Prandtl nummber / –	Pr	0.005*	0.016*
Conv. heat transfer coefficient / $\mathrm{W\,m^{-2}\,K^{-1}}$	h	39 971*	9098*
Tube pressure drop / bar	Δp	0.86*	1.01*
Pumping power / W	$\dot{P}_\mathrm{pump}$	827*	737*

When operated with LBE, the SSPS receiver would require 5 panels with 27 parallel tubes each of an inner diameter of 19 mm. This set of parameters serves as the reference for the design of the SOMMER receiver.

The comparison of the original sodium receiver and the similar receiver, but operated with LBE reveals the following observations: While the Reynolds number in the LBE receiver is increased, the convective heat transfer coefficient is only one fourth of that of the sodium-cooled receiver. In comparison, the LBE receiver's pressure drop is higher but due to the smaller flow velocity the hydraulic pumping power is similar compared to the pump-

ing power of the sodium receiver. As predicted, the lower convective heat transfer coefficient will result in higher outer tube wall temperatures and in increased thermal losses to the ambient. As mentioned before these are not considered in this design process for the experimental receiver but they reduce the measured thermal efficiency. The LBE-cooled reference receiver has a Reynolds number of more than 10^5. This number is used as a design target for the SOMMER receiver.

In LBE large-scale receivers also larger tube diameter will be required. For a single tower plant with a thermal power of 140 MW A. Fritsch [29, p210] identified, for example, an optimum diameter of nearly 38 mm for the case with the highest flux density considered in his study when the flow is divided in two with only 3 panels each and 78 parallel tubes per panel. Also Reynolds numbers of nearly 10^5 are obtained.

Also for the receiver-only single tower concepts with sodium as heat-transfer fluid Reynolds numbers significantly above 5×10^5 have been found.

For comparison, the same procedure has been applied using the molten salt receiver of the Solar Two project as a reference. That receiver had a thermal power of 42 MW. For the resulting LBE reference system as obtained by the same procedure as describe above, tube diameters for LBE of 50 mm and a Reynolds number of even more than 7×10^5 result.

Note that according to the LBE Handbook and Pacio et al. [48] currently no Nusselt number correlations exist that have a data basis covering for LBE the range of Reynolds numbers above 1.92×10^5.

Based on the findings of the previous section the following operating conditions have been defined as operation targets for the model receiver:

- a receiver outlet temperature of 600 °C,
- a Reynolds number of more than 10^5.

A flat panel receiver design is intended for the use in the SOMMER facility.

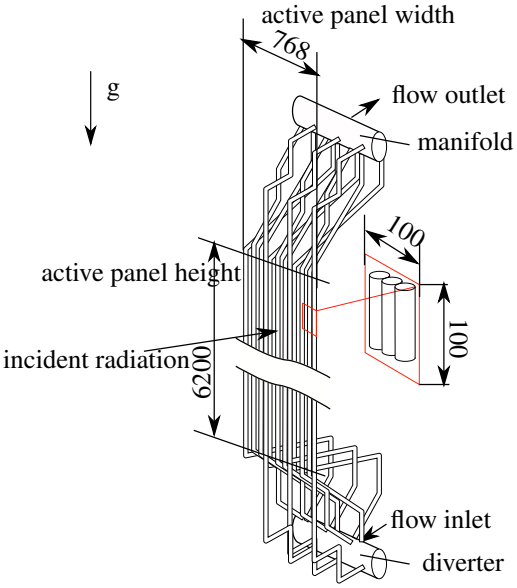

Figure 4.16: Life-scale receiver panel with a 10 by 10 cm section taken out to be placed in the SOMMER solar furnace arrangement.

Now that a reference case is obtained, in principle two approaches can be used to conduct small-scale experiments with results that are applicable in large scale power plants:

- the investigation of a life-scale representative part of the reference
- the investigation of a down-scaled element of the reference.

The model receiver should in both cases resemble an element of the reference receiver's geometry as shown in Figure 4.16, however, with tube dimensions according to the LBE-cooled reference receiver from the previous Section 4.3.1 as listed in Table 4.1.

However, it will be limited to an aperture area of approximately 10 cm by 10 cm in order to achieve sufficiently high flux values at the available solar power. This introduces a dissimilarity in flux distribution compared to

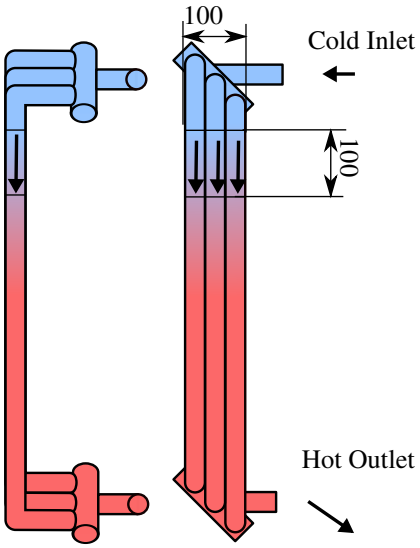

Figure 4.17: Draft of a three-tube life-scale receiver. The black square represents the same area as the square at the left image while the total number of parallel tubes is reduced.

a section of the reference receiver where the flux distribution would be very homogeneous.

The receiver must consist of at least three parallel tubes, schematically shown in Figure 4.17 Only with three tubes the center tube is exposed to the same conditions as any central tube in a large scale receiver. The remaining two tubes would then resemble edge tubes.

The experiment in SOMMER should furthermore simulate patches from all possible positions of the reference receiver. For example, at the tube inlets of each reference panel non-developed turbulent flow will be present while hydraulically developed flow will be present after an development region of the length of 30 to $40 \cdot D_i$. Therefore, such SOMMER receiver

requires a hydraulically developing entrance section. The black square, as shown at the right image in Figure 4.17, which indicates the region of the receiver that is exposed to solar radiation, can be shifted along the model receiver. This allows the investigation of the heat transfer under different flow conditions. An increase of the operation temperature of the model receiver simulates a 'hotter' patch of the original receiver.

Also the resulting temperature increase between in- and outlet should be at least $\Delta T = 10\,\mathrm{K}$ in order to sufficiently reduce the uncertainty of temperature difference measurement. It is desired to determine the efficiency of the receiver which requires good knowledge of the temperature increase.

The discussion of the options of designing the thermal receiver as an unscaled or scaled section of the large-scale reference in the Appendix sections A.3.1 and A.3.2 results in the conclusion that the application of parallel flow in the model receiver tubes eliminates the option to achieve the operation targets of a temperature increase of more than 10 K and the Renolds number of more than 10×10^5 simultaneously at the given maximum solar power.Also the fabrication of such parallel tubes in the required compact volume was expected to be very difficult. This makes the approach of testing a patch of the reference, either in 1:1 scale or scaled down, impractical.

As a compromise a single tube can be bent to form a coil as shown in Figure 4.18 in order to pass through the receiver aperture along its flat section several times. This way a single flow absorbs all the power projected onto the receiver which reduces the required mass flow rate and a temperature increase much larger than 10 K at a Reynolds number of $\mathrm{Re} > 1 \times 10^5$ is obtained.

4.3.2 The down-scaled tube coil design

In such a tube coil the flow re-enters the absorber area several times. The tubes outside the abrober area are thermally insulated so that the flow maintains the temperature it had at the end of the preceding pass. The coiled

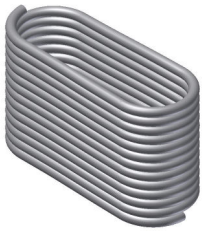

Figure 4.18: Simple spiral-design receiver concept where the tubes located in the front plane will be exposed to the concentrated solar radiation. The back side will be insulated.

design can therefore be interpreted as a single tube of the reference, scaled as a representative part of a full receiver, but cut in pieces several times in order to fill out the full available space around the focal point provided by the SOMMER solar furnace. The bending of the tubes and the applied flux distribution, however, introduce a remarkable dissimilarity to the reference because in a coil the flow obtains a swirl component.

In order to make the flow hydraulically developed before entering the absorber zone, a flow development section was foreseen before each pass by means of an elongated design of the coil. The top view of the resulting design is shown in Figure 4.19, with the flow moving in clockwise direction. A market investigation revealed that only tubes with internal diameter of 9 mm and 0.5 mm wall thickness could be supplied in the desired kind of steel. The resulting operating parameters at design conditions as shown in the right column of Table 4.2.

While being the simplest possible layout for the SOMMER project both, the high temperature and the high Reynolds numbers could be obtained while the fluid temperature in the receiver rised significantly so the desired outlet temperature of 600 °C could be achieved. It was therefore selected for execution. The coiled tube design equires significantly less mass flow and therefore relaxes the electrical and recuperating augmentation which

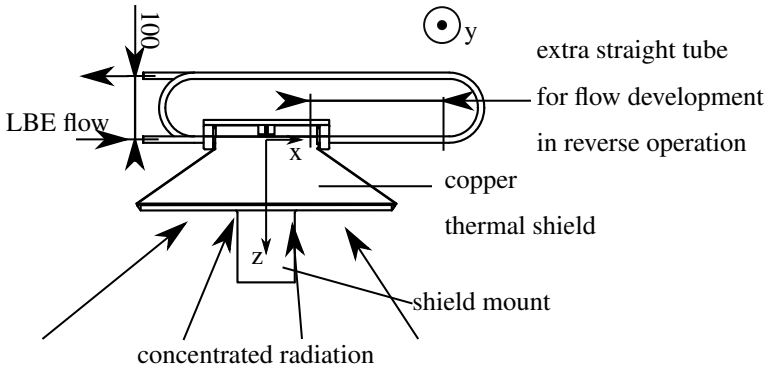

Figure 4.19: Top view receiver drawing

would have been required for parallel flow model receivers as indicated in the Appendix in Figure A.15.

The final design of the receiver with its thermally insulated tube coil is shown in Figure 4.26.

Details regarding the receiver's construction can be found in the appendix section A.3.3.

4.3.3 Down-scaling effects

The selected tube geometry of an inner diameter of 9 mm and a wall thickness of 0.5 mm and the heat flux density that can be varied between 0 and 1 MW m^{-2} correspond to geometries according to the scaling laws on page 71.

Such model conditions represent, for example, the case of a tube of the hypothetical reference of 19 mm (a scaling factor of 2.1) at an average heat flux density between 0 and 473 684 W m^{-2}. Then, the wall thickness is 1.055 mm. The available peak flux in the SOMMER facility of up to 3 MW m^{-2} corresponds to a peak heat flux in the reference of up to 1.4 MW m^{-2}.

Table 4.2: Resulting parameters from a scaled receiver

parameter / unit	value
tube internal diameter D_i / mm	9
tube wall thickness / mm	0.5
number of windings / –	10
tube length / m	10.4
temperature rise / K	70
mass flow rate $\dot{m}$ / $kg\,s^{-1}$	1
thermal power / W	10 000
flux density q'' / $W\,m^{-2}$	1 000 000
radial temperature difference ΔT / K	54
approximated pressure drop Δp / bar	6
Reynolds number Re / –	118 000
convective heat transfer coefficient h / $W\,m^{-2}\,K^{-1}$	18 675

Can similarity between model and reference be obtained regarding natural convection? A difficulty arises from the copper shield, as shown in Figure 4.19 which will impact the natural convection, especially when heated from strong solar spillage, that is, concentrated solar flux that misses the receiver aperture due to improper aiming of the heliostat or due to mirror imperfections. If this impact is neglected, the characteristic length of the receiver aperture window in SOMMER is 10 cm versus a characteristic length of 2.8 m in the reference. That is a ratio of 28. For the Grashof number to obtain the same value in the model the temperature difference would have to be increased by this ratio to the power of three while maintaining the Prandtl number of the surrounding fluid identical – probably impossible in a solar furnace.

For the case of a flat surface of 600 °C and an ambient temperature of 0 °C natural convection will have the following effect on the model receiver:

The Grashof number for $L = 0.1\,\mathrm{m}$ is $\mathrm{Gr} = 8.98 \times 10^6$ and the corresponding Rayleigh number $\mathrm{Ra} = 6.29 \times 10^6$. The resulting Nusselt number for a vertical flat plate

$$\mathrm{Nu} = \left(0.825 + 0.387(\mathrm{Ra} \cdot 0.345)^{(1/6)}\right)^2 = 27.3, \tag{4.8}$$

according to Ref. [66], $h = 12.02\,\mathrm{W\,K^{-1}\,m^{-2}}$ and the resulting lost thermal power $\dot{Q} = 72.1\,\mathrm{W}$ or $q'' = 7215\,\mathrm{W\,m^{-2}}$; that is 0.7 % of the absorbed thermal power. The reference with $L = 2.7\,\mathrm{m}$ would at the same surface temperature result in $q'' = 5490\,\mathrm{W\,m^{-2}}$, which, however, make up for 1.3 % of the total thermal power, because in average a lower heat flux density of $435\,880\,\mathrm{W\,m^{-2}}$ is applied.

If the entire cavity is assumed to be a 'flat plate' at a temperature of 400 °C (cool copper plates), an average heat flux density of $q'' = 9330\,\mathrm{W\,m^{-2}}$ is obtained, thus, nearly 1 % of the incident flux is lost.

Note though that the flow conditions of this receiver deviate strongly from a flat plate, due to the 'roughness' of the vertically stacked tubes and due to the copper shield which forms a cavity around the absorber plane. Therefore, the calculated value is likely to be wrong and serves merely for an assessment of an order of magnitude.

Forced convection is suppressed by the fact that the receiver is tested in a protected environment.

The specific radiation losses of the model are smaller than in a large scale receiver at identical surface temperature. This results from the solar furnace arrangement, where the parabolic mirror covers a very large portion of the model receiver's field of view. From the receiver point of view the net positive thermal radiation heat transfer with the sun image occurs through the mirror face. Losses occur only with the surroundings of the mirror that have ambient temperature. A real tower receiver on the other hand sees in its en-

vironment a large portion of the sky which is a sink for radiation. According to Duffy et al. [70, p148], the clear-sky temperature can be up to 30 K lower than the ambient air temperature in cold, dry climate.

Due to the present arrangement of parabolic mirror and receiver the receiver's view factor of the parabolic mirror is $f = 0.55$ and with its surroundings less than $f_s = 1 - f = 0.45$ due to the copper cavity. For the radiation exchange with the surroundings the emitted power can be calculated according

$$q''_{\mathrm{rad}} = \sigma f_s (T_{\mathrm{R}}^4 - T_{\mathrm{amb}}^4) = 14.6\,\mathrm{kW\,m^{-2}} \tag{4.9}$$

for $T_{\mathrm{rec}} = 873\,\mathrm{K}$ and $T_{\mathrm{amb}} = 300\,\mathrm{K}$. That amounts to 1.5 % of the radiation input . Both effects added together cause losses of 2.5 % of the power input which superimpose effects from internal heat transfer.

The real magnitude of losses can approximately be determined by operation without sunlight projected onto the receiver at inlet temperatures of up to 530 °C and extrapolated to higher temperatures. Such test conditions will, however, differ from sun-on operation in the reversal of the temperature gradients from bulk flow to outer tube wall which has to be taken into account during this extrapolation. The receiver is for this purpose monitored by an infrared camera which provides high-resolution data of the surface temperature both, with and without solar flux on the absorber.

Losses can furthermore be reduced in the experiment by working at reduced temperatures. For example,

$q''_{\mathrm{rad}} = 1383\,\mathrm{W\,m^{-2}}$ and $q_{\mathrm{conv}} = 2227\,\mathrm{W\,m^{-2}}$ at a mean receiver temperature of 226 °C which together make up for 0.36 % of incident heat flux. Under these conditions losses can be neglected.

However, due to the fact that physical properties vary differently with temperature, the results at low experimental temperatures cannot simply be transferred to operation at high temperature. The Prandtl number at 226 °C is 0.03 for LBE versus 0.01 at 600 °C. Accordingly, it is not possible to

obtain both, an identical Nusselt number and Reynolds number when scaling the geometry and changing the temperature simultaneously.

Also the thermal conductivity of the tube steel changes and a different temperature difference is obtained between outside and inside of the tube wall. It increases from $17\,\mathrm{W\,m^{-1}\,K^{-1}}$ at 200 °C to $23\,\mathrm{W\,m^{-1}\,K^{-1}}$ at 600 °C.

This has to be taken into account when wall and bulk temperatures are measured under these conditions.

Alongside the overall shape of the tube (a coil) additional differences remain to the reference: The tubes of the coil are coated with a layer Pyromark 2500 paint at a thickness of 21 µm which has a very low thermal conductivity about one hundred times smaller than that of steel [41], which translate to $0.17\,\mathrm{W\,m^{-1}\,K}$ to $0.23\,\mathrm{W\,m^{-1}\,K}$ for steel in the temperature range of 200 °C to 600 °C. Pyromark consists of silicone resin forming silica once it has undergone thermal treatment. The thermal conductivity of silica ranges between $0.6\,\mathrm{W\,m^{-1}\,K}$ to $1.8\,\mathrm{W\,m^{-1}\,K}$ [27, p81]. This layer's thickness cannot be scaled under the assumption that it is applied via the identical spray painting procedure in the reference. This layer in its un-scaled thickness could, according to Equation (3.48), generate a temperature difference just within the coating of 11 °C up to 34 °C at a flux density of $1\,\mathrm{MW\,m^{-2}}$ in the model and the reference alike. This is valid under the assumption that the high values of Pyromark's thermal conductivity apply. On the SSPS receiver an average paint thickness of 45 µm has been measured, leading to significantly higher temperature differences.

And finally: In the small scale SOMMER receiver the flux distribution on a tube section is much different compared to a large scale reference plant. Accordingly, the flow temperature profile is undeveloped to a higher yet unquantifiable degree in the model receiver.

In conclusion, the boundaries of this thermal model receivers require numerous simplifications and compromises during the receiver design process. These result in a situation that not all important effects and performance in-

dicators can be measured and used for the prediction of the behavior of larger-scale reference systems.

Note also that no numerical stress analysis has been performed of the current prototype receiver. Therefore, the quality of its design will be tested during operation.

Nevertheless, the receiver is operated under absolute conditions that exceed the limits currently present in commercial thermal receivers and provide valuable experience.

4.3.4 The thermal efficiency of the model receiver

The receiver's thermal efficiency η_{th} is defined as the ratio of thermal power absorbed by the coolant $\dot{P}_{\mathrm{abs}}$ and the solar power applied to the receiver aperture $\dot{P}_{\mathrm{S}}$. It is of economic importance and efforts are ongoing internationally to increase this value even by a few percentage points in commercial receivers. Because of the significance of even small improvements, the uncertainty in the measured value of thermal efficiency must be reasonably low.

For example, a stated efficiency of 92 % should not be associated with an uncertainty of more than 5 %, given that at the limits of this range of uncertainty the efficiency could be 87.4 % (quite bad) or 96.6 % (very good).

However, the reduction of uncertainty in its measurement requires significant effort, so that an uncertainty of 5 % should be considered to be an acceptable value.

The solar power absorbed in the SOMMER receiver is measured according to the temperature increase of the coolant between in- and outlet of the receiver and the current mass flow rate and heat capacity:

$$\eta_{\mathrm{th}} = \frac{\dot{P}_{\mathrm{abs}}}{\dot{P}_{\mathrm{S}}} = \frac{\dot{m} \cdot c_p \cdot \Delta T}{\dot{P}_{\mathrm{S}}}. \tag{4.10}$$

The uncertainty of measured thermal efficiency η_{th} shall be assessed for the case of the SOMMER facility. It is propagated from the uncertainties in the variables existent in Equation 4.10 according to

$$u^2(\eta_{\mathrm{th}}) = \sum_i \left(\left(\frac{\partial \eta_{\mathrm{th}}}{\partial x_i} \right)^2 \cdot u^2(x_i) \right) \tag{4.11}$$

with the following terms:

$$\frac{\partial \eta_{\mathrm{th}}}{\partial \dot{P}_{\mathrm{S}}} = - \frac{\dot{m} c_p \Delta T}{\dot{P}_{\mathrm{S}}^2}, \tag{4.12}$$

$$\frac{\partial \eta_{\mathrm{th}}}{\partial \Delta T} = \frac{\dot{m} c_p}{\dot{P}_{\mathrm{S}}}, \tag{4.13}$$

$$\frac{\partial \eta_{\mathrm{th}}}{\partial \dot{m}} = \frac{c_p \Delta T}{\dot{P}_{\mathrm{S}}}, \tag{4.14}$$

$$\frac{\partial \eta_{\mathrm{th}}}{\partial c_p} = \frac{\dot{m} \Delta T}{\dot{P}_{\mathrm{S}}}. \tag{4.15}$$

The variance values to each partial derivative are picked as follows: Type B relative uncertainties which are according to [71] based on scientific judgement as opposed to a statistical analysis are used for the variance of $\dot{m}, c_p$ and ΔT, and are taken from own characterization measurements, the LBE handbook [32] and from operational experience, respectively. These uncertainties are stated as the bounds of a rectangular uncertainty distribution, such as: 'Any value around the expected value within the range of a can occur with the same likelihood while the measured value will never lie outside this range'. (With a being an uncertainty interval.) These relative uncertainties are converted to absolute uncertainties for this assessment. The absolute standard uncertainty of the measurement of $\dot{P}_{\mathrm{S}}$ can be directly provided as a variance as function of the measured value, $u^2(\dot{P}_{\mathrm{S}})$.

The uncertainty in the thermal efficiency of the receiver depends on the mass flow rate, the magnitude of temperature rise in the receiver and the solar power. Furthermore, the heat capacity depends on the temperature;

Table 4.3: Measurement uncertainty of variables used to determine the uncertainty of the thermal receiver's thermal efficiency. The uncertainty interval of the solar power measurement is currently undetermined (marked with *).

variable	range	variance
x_i	a	$u^2(x_i)$
mass flow rate $\dot{m}$	$0.01 \cdot \dot{m}$	$\frac{a^2}{3}$
heat capacity c_p	$0.05 \cdot c_p$	$\frac{a^2}{3}$
temperature difference ΔT	$0.02 \cdot \Delta T$	$\frac{a^2}{3}$
solar power $\dot{P}_\mathrm{S}$	–*	$u^2\left[\dot{P}_\mathrm{S}\right]$

Table 4.4: Reference conditions in the SOMMER loop.

parameter / unit	reference value
mass flow rate $\dot{m}$ / $\mathrm{kg\,s^{-1}}$	1
temperature difference ΔT /K	70
heat capacity c_p / $\mathrm{J\,kg^{-1}\,K^{-1}}$	143
solar power $\dot{P}_\mathrm{S}$ / W	10 800

compared to the previously mentioned variables the influence of the temperature on the value of c_p is, however, negligible.

In the following step the effect of an estimated uncertainty in the measurement of the solar power on the combined uncertainty of the thermal efficiency shall be investigated under reference conditions, as shown in Table 4.4.

With these parameters fixed the uncertainty of the measurement of the solar power is varied in the range of $u(\dot{P}_\mathrm{S})/\dot{P}_\mathrm{S} = [0.005...0.06]$ in terms of relative standard deviation. The resulting standard deviation in the value of the thermal efficiency is shown in Figure 4.20.

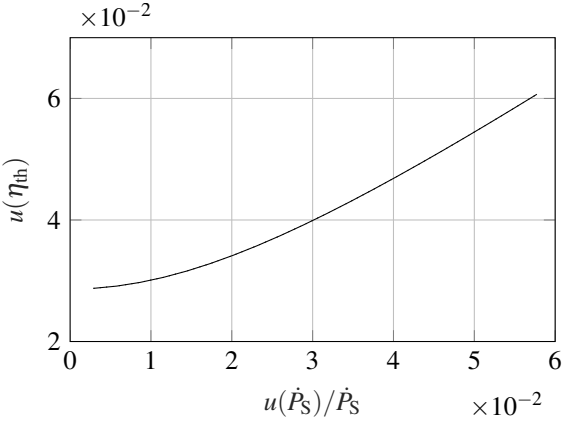

Figure 4.20: Standard deviation in the value of thermal efficiency of the receiver as a function of the relative standard deviation of the measured solar power under reference conditions (solid line).

According to this analysis, it is required that the solar power can be measured with a relative uncertainty below 4.5% in order to keep the standard deviation of the thermal efficiency value below 5%.

. For a '95.5%' level of confidence of 5% for the thermal efficiency the allowable standard deviation is 2.5%. As can be seen in the diagram, even with zero uncertainty in the measurement in solar power such high confidence cannot be reached. This is the case because the uncertainty is most sensitive to the uncertainty in the solar power and in the heat capacity, the latter of which is obtained from literature and can therefore not be reduced with reasonable effort.

Therefore, high accuracy in the measurement of the solar power is required in order to be able to determine an accurate value of the thermal efficiency. For the SOMMER facility a measurement device has been specially developed with this condition in mind. This device is explained in Section A.2.

That device has been calibrated against the FMAS flux measurement system of DLR, Cologne. During that campaign an uncertainty for a power prediction by the flux measurement system in SOMMER was determined for reference conditions of $s_c(\dot{P}) = 3.14\,\%$ in forward direction and $s_c(\dot{P}) = 2.86\,\%$ in backward direction.

These values allow the determination of the relative standard uncertainty of the thermal efficiency of the receiver with a combined absolute standard uncertainty of $u(\eta_{\mathrm{th}}) = 4.08\,\%$ and $u(\eta_{\mathrm{th}}) = 3.9\,\%$, for extending and retracing measurement direction, respectively[15].

4.3.5 Measurable quantities and equipment

The temperature distribution of the receiver front shall be observed and measured. For this purpose an InfraTec VarioCam (R) HD head 800 infrared camera was installed. Its 1024x768 image resolution and tele lense allow for temperature monitoring of a 580x435 mm field-of-view image of the receiver aperture including a large portion of the surrounding copper shield.

Any structure that's temperature shall reliably be determined from the IR camera must cover four of the camera sensor's pixels arranged in a square. The corresponding minimum area on the receiver plane equals 1.13 by 1.13 mm. The temperature distribution across the absorber area can therefore be resolved with roughly 90 by 90 pixels. The vertical temperature distribution on a single horizontal tube with an outer diameter of 10 mm, projected on the IR camera's plane of view is resolved by approximately 8.8 pixels and therefore just sufficiently well in order to derive a circumferential temperature distribution of each tube.

The receiver is designed such that prior to each pass through the aperture window the flow passes an adiabatic hydraulic development flow section of a length $D_{\mathrm{d}} \approx 250\,\mathrm{mm} = 27.78 \cdot D_{\mathrm{i}}$. The flow's velocity profile should thus

[15] Note, these are percentage points.

be almost developed and a homogeneous temperature across the diameter should be obtained before the heated absorber area is entered.

Once experiments with this configuration are completed the in- and outlet connectors can be reversed leading to a reversed flow direction. The flow will then enter the absorber area without passing a hydraulic development section after the passage of the bend and the velocity profile will not be developed. Under equal flux input the measurable surface temperatures for each flow direction should differ and provide an indication of the impact of the flow conditions on the receiver's thermal conditions. These could then be compared with the scarce literature existing on this topic. Unfortunately, the condition of thermally developed flow at the receiver inlet cannot be obtained. Such condition is, however, rarely ever to be found in solar central receivers since solar flux constantly varies locally.

In five locations on the absorber area thermocouples are installed, as indicated in Figure 4.21. Thermal couples number 13 and 14 are attached to the outer tube surface on top of the most central tubes, while # 15 is installed in the gap between them. Thermocouples # 11 and # 12 are installed in spots with low intensity flux. All thermal couples have been applied to the tubes prior to the application of the Pyromark 2500 coating.

They have the purpose of providing reference temperature values in order to validate the readings of the infrared camera, the absolute accuracy of which depends on the correct knowledge of the thermal emissivity value of the paint coating. That paint's emissivity is, however, temperature dependent. Also the sunlight projected onto the receiver aperture potentially reflects solar radiation in the camera's sensitive IR band. This kind of radiation would superimpose the thermal radiation of the tube resulting exclusively from its temperature. The local temperature readings from the thermocouples will enable the identification of such effect. While during preliminary tests this contribution was not observed the thermal couples would also help to detect gradual changes of the paint's spectral properties during extended exposition to high power flux. The placement of the central thermocou-

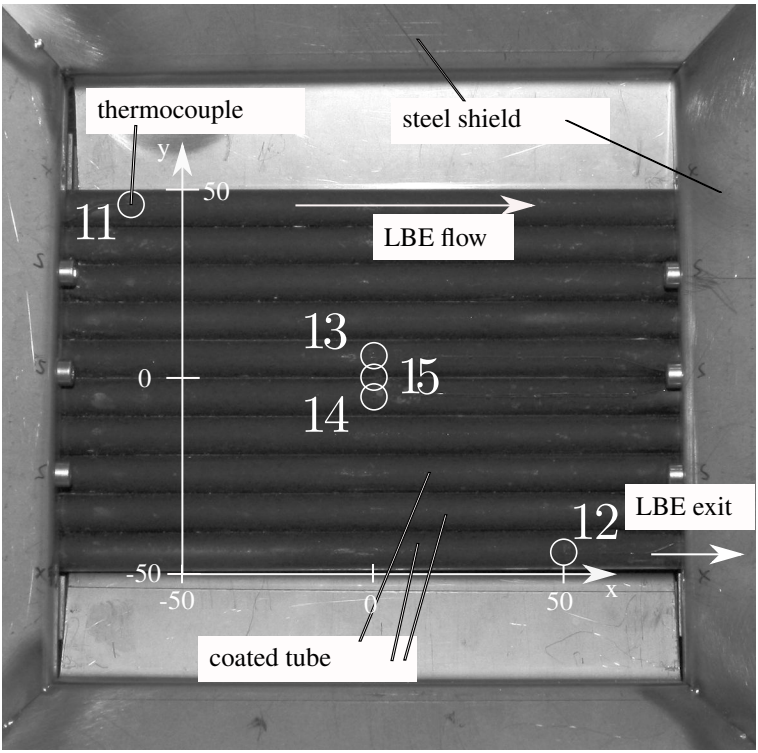

Figure 4.21: Absorber front with thermocouples without the protection copper shield which protects lateral screw heads during operation.Dimensions in millimeter

ples is furthermore rather experimental: Under full load flux the cooling provided by the LBE flow in the tube is most likely not sufficient in order to prevent them from a 'thermal death'. However, during commissioning under part-load conditions they enable the infrared camera's image quality assessment.

The infrared camera furthermore assists the plant operator by automatically detecting critical local temperature values. Upon detection of a critical temperature the solar furnace's emergency light shut-off can be triggered by the camera's operating software IRBIS 3.1 plus.

Another safety feature is provided by the individual sheets of the copper shield, as shown in 4.19, each of which is equipped with two thermocouples. In case the focal point leaves the absorber area a significant temperature increase will be detected by these plates which will trigger the emergency light shut-off. On the rear of the tube coil, that is, on the side not exposed to solar flux and completely thermally insulated each individual tube's outer wall temperature is measured. It is expected that during steady-state conditions at that location flow and wall temperatures are equal. This allows for calculating the energy gain of each pass through the absorber plane. Thermal conduction between individual tubes will occur, however, the rate is estimated to be low since only a line contact between the tubes is present, conduction through the air is low and the temperature differences between individual tubes is less than 10 K under design conditions at the maximum power input.

Also the inlet and outlet temperatures of the heat-transfer fluid are measured via thermocouples immersed in the fluid. These are required to calculate the overall energy gain and to assess the receiver's energy balance.

This value takes into account only the net gain. In order to account for the various thermal losses, such as reflection and thermal radiation and convection, and in order to calculate the receiver's thermal efficiency it is required to also measure the power of the light projected onto the receiver.

For this purpose the facility is equipped with a specially developed solar flux scanner which is able to locally measure the incident local flux. This fundamental device is described in detail in Section A.2.

4.4 The heat flux measurement

The measurement of the total power of the incoming solar light is required for the determination of the thermal efficiency of the thermal receiver of the SOMMER facility. Also the information on the distribution of flux on the receiver aperture and the local peak flux is important to characterize the condition under which the receiver is operated.

Most existing practical approaches for the determination of these parameters as described in the Appendix section A.2 are , however, not applicable in SOMMER due to the special the setting and the required precision. Also, while reviewing existing methods, an apparently simpler approach has been proposed, which, after some initial considerations has been decided to be executed: a flux scanner using a single heat flux micro sensor (HFM) with rotational and superimposed linear scanning motion.

4.4.1 The measurement problem

At the SOMMER facility's receiver the absorber face is surrounded by copper heat shields that protect the insulation of the receiver tubes from highly concentrated light. These shields form a pyramidal cavity and the flux distribution on the absorber plane is therefore not easily accessible for measurement devices. Also the dimensions of the receiver aperture at the bottom of the cavity with a height of only slightly more than 100 mm and a width of about 120 mm impact the selection of a measurement devices. In order for the receiver to absorb a maximum amount of solar power it is required that the available space on the bottom of this cavity is completely filled with absorber tubes. This leaves no space for the potential installation of sensors

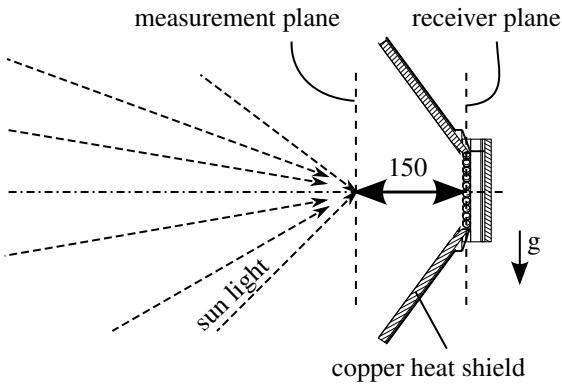

Figure 4.22: The measurement plane and receiver plane in the SOMMER setup. Flux measurement occurs in the measurement plane 150 mm in front of the receiver plane.

in the absorber plane which could otherwise provide a local reference flux value.

The receiver is fixed in its place. It is not allowed to move in any direction in order to maintain a defined location at the focal point during all operating conditions. Accordingly, it cannot be moved during operation out of the focal point in order to create space for flux measurement. Therefore, the loop thermal expansion during warm-up is compensated by a movable support of the loop components other than the receiver: they hang loose in the structural aluminum frame like a pendulum. This allows an expansion of the tubes connected to the receiver only along their axis away from the receiver.

Since the receiver is fixed, measurements have to occur in a plane parallel to the absorber plane but shifted in positive Z direction, as shown in Figure 4.22

The coordinate system applied for the absorber in this text is shown in Figure 4.23: The absorber's surface normal vector points in positive Z-

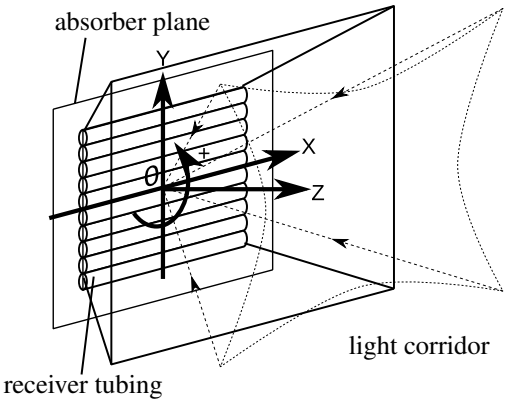

Figure 4.23: Coordinate system for the thermal receiver and the flux density measurement system

direction (towards the source of the concentrated light), the Y-axis points up (opposite to gravity) and the X-axis points in horizontal direction.

For this reason the parabolic concentrator of the SOMMER facility is designed to move the focal point along the optical axis of the solar furnace by driving back and forth. With this mechanism the flux distribution on the absorber plane can be moved during operation to a measurement plane outside of the copper cavity where there is enough space for flux measurement approaches.

A literature survey has been conducted by Mr. Giokchan Moumin during his master's thesis [72] in order to identify the best approach of flux measurement under these circumstances. The identified, existing approaches are summarized in the appendix section A.2.1.

4.4.2 Discussion of existing concepts

Moumin found that an indirect measuring approach (using a diffusely reflective target (Lambertian target) and a camera) is only applicable with a water-cooled target that is mechanically moved in front of the receiver into

the measurement plane for measurement and removed again for the continuation of operation. This target requires to have one direct-reference sensor included in its surface and a mechanical mechanism to quickly move in front of the receiver for measurements as well as with flexible piping. Additionally, a camera and lens with available information on image distortion of the lens, non-linearities of the sensitivity of brightness of the camera, transmissive spectra of applied grey filters is required. Such approach is further sensitive with respect to the placement of reference coordinates of a Lambertian target and the thermal absorber. The properties of the Lambertian target, which is in principle a diffuse reflector, and the calibration of the reference flux gauge should be monitored as maintenance activities. Alternatively, an un-cooled Lambertian bar with one directly mounted fast flux gauge could be moved across the measurement plane. Because the image is then produced from several single images of a moving bar and the sensor requires calibration prior to its service, the implementation effort grows even further.

Provided that the required property data of the target and the camera sensors and lenses are available, quite a good result can be obtained with high spatial resolution. The effort for the implementation has, however, to be considered quite high.

Existing direct approaches using several fast flux gauges mounted on a traversing rod are also be applicable. However, this approach's resolution depends on the number of sensors installed on that rod, thus, high resolution is expensive and potentially requires calibration of several sensors.

These considerations for a 'fixed' indirect, moved indirect and moved direct approach are summarized in Table 4.5. None of these options appeared to be very attractive regarding their precision (summarizing resolution and accuracy) and implementation effort. These existing methods inspired to an alternative method, as is described in the following section.

Table 4.5: Advantages and disadvantages of existing methods for flux measurement. High rating: '+'; low rating: '-'; average rating: 'o'.

method:	direct	indirect	
implementation:	moved	fixed	moved
precision	o	+	+
implementation effort	+	o	-
maintenance effort	o	-	-

4.4.3 Mechanical implementation of a spiral-path scanning motion

Instead of using multiple fast flux gauges mounted on a single traversing bar with a fixed pivoting point (one circular motion component), instead, in this approach, a single sensor is moved across the entire measurement plane at high speed using two, a rotational and a linear motion component: a flux scanner. In effect the single sensor thus scans the flux distribution on a finely spaced spiral path.

This special motion pattern was selected over the alternative of two linear motion components for the following reasons: Line scans require motion in X- and Y-direction which at the high required measurement speed generate very large inertial forces whenever the linear motion is reversed. This is difficult to mechanically compensate, e. g. through a stiff structure to avoid swinging from deceleration and acceleration. Such swinging causes an uncertainty in the determination of the sensor's position. At the same time the high fluxes within in the irradiated region impose a damage risk to exposed parts. These therefore require active cooling or a mechanical solutions that transposes the motion to the sensor so that flux-sensitive parts can always remain in the safe region.

Instead, a circular motion with a superimposed linear motion is applied. This, combined with a fast flux gauge, allows to obtain high image resolution. The scanning paths across a flux distribution (indicated as contour plot) resulting from this motion are shown in Figure 4.30 on page 134 as thick, black lines.

A photographic image acquisition on a mechanically moved Lambertian target, potentially actively cooled, and the post-processing of photographs are not required.

From an initial literature research it was furthermore expected that the factory calibration of the fast flux gauge would be sufficient for the accuracy needs within the SOMMER project.

What are the mechanics of this concept? A horizontal, balanced rod is connected to two rotors, the first of which is attached to one of the rod's ends and the second one is attached to the rod's center of gravity. On the opposite end of the rod the flux sensor is installed. The first rotor (at the rear of the rod) is driven by an electric motor. Its continuous circular motion is transferred to the second rotor by a belt drive so that both rotors' rotation is synchronized. The rod maintains its horizontal orientation throughout a full motor's rotation and transposes that circular motion to the sensor. Due to the rod's length the sensor rotates through the flux distribution while the rest of the device remains outside of it. This principle is shown in Figure 4.24 and schematically, illustrating the mechanics in Figure 4.25. In the latter image the belt drive is indicated by a simplified straight connection between both rotors. The sensor is represented by a black dot.

A counter weight that generates the same momentum of rotation as the rod is mounted to the opposite end of the first rotor (not illustrated in Figure 4.25) to compensate the eccentricity due to the rod's weight. It is also visible in Figure 4.26, where on the left the flux scanner is shown and on the right the thermal receiver. The counter weight, pointing diagonally up in that photograph, generates a very smooth and continuous rotational motion.

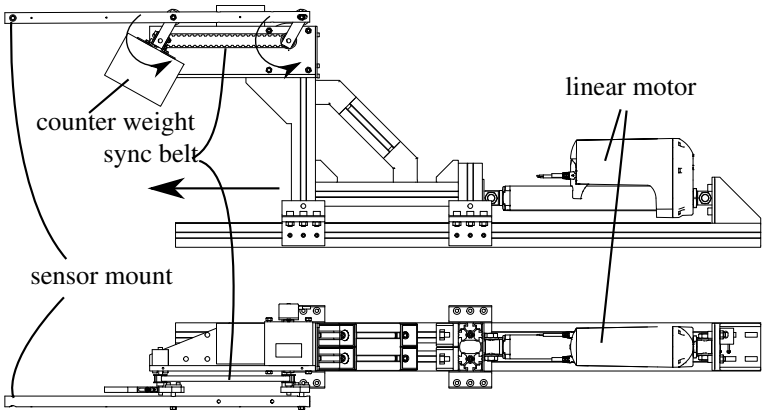

Figure 4.24: Flux scanner as seen from the heliostat (top) and top view (bottom).

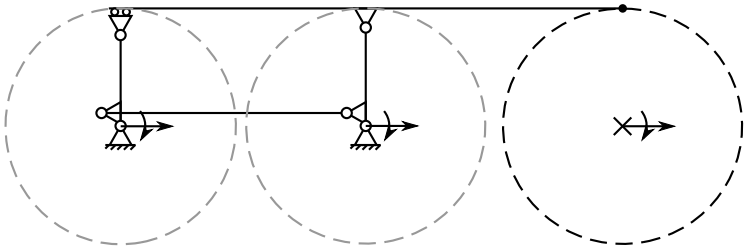

Figure 4.25: Illustration of the device's mechanics in front view.

The sensor wires are safely attached to the side opposite to the concentrated solar flux. Although the sensor moves on a circular path due to the mechanism this motion is translated into a repeated downward-upward and forward-backward motion pattern that does not lead to twisting in the cable.

This circular motion is superimposed by a motion resulting from a linear motor that shifts the rotating mechanism forward on a aluminum bar. These to motion components combined result in a spiraling scanning pattern.

A HFM-6D/H heat flux micro sensor by Vatell as shown in figure 4.27, is used as the flux sensor as it has a very small response time constant of

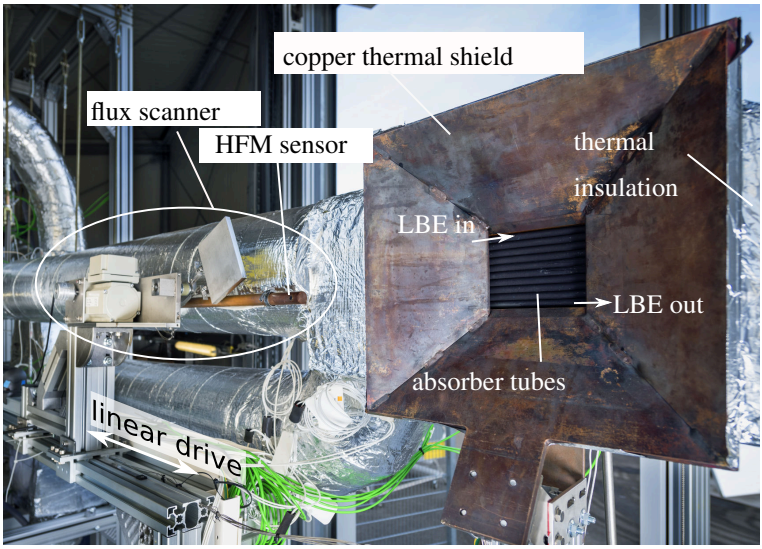

Figure 4.26: Assembly of the thermally insulated receiver on the right. On the left: the flux scanner in retraced position.

300 µs. The sensor used is specially coated with a highly light absorptive and heat resistant black paint: Pyromark 2500 by Tempil. The upper operating temperature limit of the HFM is specified by the vendor to be 800 °C, although this value equals the temperature limit of Pyromark 1200 paint typically used as coating material. With the specially applied Pyromark 2500 coating the sensor is potentially resistant to even higher temperatures. Due to the unsteady conditions to which the sensor is exposed during operation, however, an upper limit of 500 °C was defined (and never reached during operation).

This tolerance to high temperatures allows for the system to operate without active cooling. Copper has been selected as material for the rod carrying the sensor after a thermal analysis had predicted superior tolerance to the high fluxes in the focal point compared to stainless steel. Copper can, due

Figure 4.27: Vatell HFM sensor with pyromark 2500 coating.

to its high thermal conductivity, quickly distribute thermal energy in its volume, avoiding deformation from local overheating and keeping the sensor temperature below critical values. After a measurement run the energy collected at the rod's tip is evenly distributed in the entire rod's volume through conduction, leading to thermal expansion in its rear section. The rear support is therefore movable along the rod's axis, as shown in Figure 4.25 to prevent strain on the rotating mechanism.

The sensor body has a length of 24.5 mm. A rod shape with a circular cross section[16] and a diameter of 20 mm was selected for the copper rod in order to bear most of the sensor's body whilst minimizing the rod weight. This way the sensor body is protected against solar irradiation in places other than its face. The copper rod's geometry is shown in Figure 4.28.

The large distance a-b is required to keep enough distance between the drive section and the sensor which is the only part to enter the region of concentrated sunlight for the measurement. In order to keep the drive block small, distance b-c is configured to be smaller than distance a-b. For smooth rotation, however, the rod must be balanced around b where the driving rotor is attached in order to prevent the generation of a rotational momentum

[16] Rod shapes with rectangular cross section and smaller volume would in principle be possible, too. Hollow tubes, on the other hand, were expected to heat up much faster, leading to thermal bending and were thus excluded. Details can be found in Moumin's thesis [72].

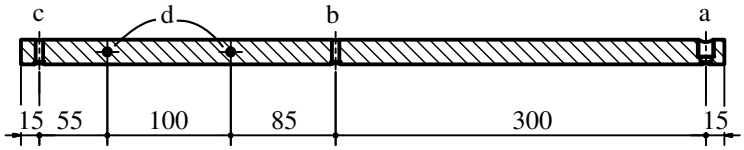

Figure 4.28: Top view on the geometry of the cylindrical copper rod (diameter of 20 mm). The HFM sensor is placed in drilling *a*, the rotors are attached with axles in drillings *b* and *c*. Drillings *d* are used to attach additional weight required to shift the center of gravity exactly to drilling *b* and to fix signal cables.

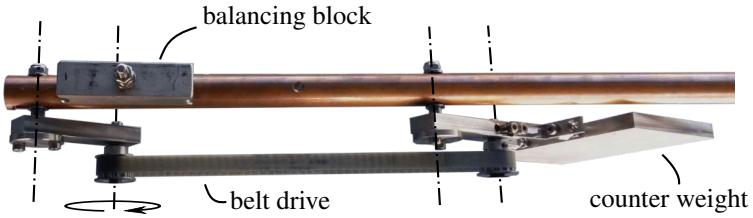

Figure 4.29: Photograph: Top view of the rod mechanics section including the copper rod and the rotational axes (dash dotted lines)

in b when the system starts to move vertically. This is accomplished by mounting a weight to drillings d that compensates the 'too short' rod length b-c and balances the rod in b. In Figure 4.29 a section of the rod with balancing weight, the rotors, the belt drive and the main counter weight are shown.

The assembly of the flux scanner shifts effort to the mechanical system, which is more complex than that of a state-of-the-art moving bar direct measurement approach with several sensors: Both systems require a bar, a rotational motor and a device for the measurement of the angle. In addition, the scanner requires: a linear motor, a sensor for linear distance measurement, minor parts such as bearings, a counter weight, a belt drive with corresponding gears and a more complex support structure.

Alternatively, for indirect measurement, an actively cooled Lambertian target for the entire distribution would likely be the best option. This must be actively moved into the distribution while being connected to cooling water. A water-cooled, calibrated flux gauge would have to be mounted somewhere in the face of that target.

The approach of the flux scanner, however, generates a higher spacial image resolution than the direct measurement approach and avoids at the same time the entire camera system required for indirect measurement.

This concept therefore promised to feature higher precision than existing direct measurement approaches at the benefit of requiring only a single, factory-calibrated sensor.

4.4.4 Scanner operation

Three operation parameters influence the measurement: the sample rate, the rotational velocity and the linear velocities. The sensor's velocities are a trade-off between image resolution, measurement duration and motion blur and forced thermal convection on the sensor-air interface: A low linear motion velocity leads to high horizontal resolution of the image at the expense of long measurement times. A higher linear motion velocity requires a higher rotational velocity in order to maintain the image resolution. Due to the finite response time of the sensor, however, higher rotational velocity causes a reduced capability of the sensor to measure fine, high frequency changes in the flux distribution. Also forced thermal convection losses to the ambient are increased at higher velocity.

The operation parameters have been narrowed down to find a good compromise. For the rotational speed for the present design 1.8 revolutions per second have been defined, where a full revolution equals a 2π rotation of the sensor on a circular path around position 'x' in Figure 4.25. In order to keep the measurement duration low a linear speed in horizontal direction of about $0.024\,\mathrm{m\,s^{-1}}$ is applied. This speed leads to a one-way passage

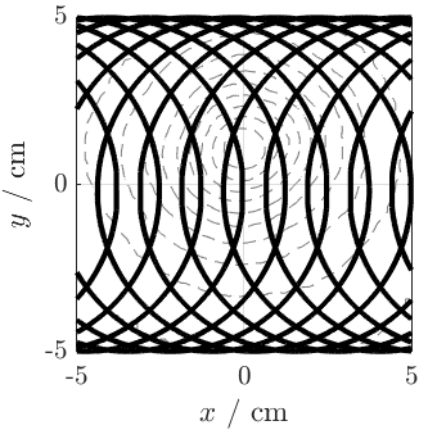

Figure 4.30: Sensor scanning path (solid black) across a flux distribution (contours in light grey).

time across a typical solar flux distribution of a horizontal width of 100 mm slightly above 8 s during which nearly 15 revolutions of the sensor occur and a linear distance of 20 cm is covered by the device's center of rotation. During operation the scanner's center of rotation will horizontally travel across the flux distribution (forward motion) and then reverse its direction and cross the distribution again (backwards motion). The measured values during each pass are evaluated to result in two individual images of the flux distribution. At the before-mentioned speed applied, during each revolution the center of rotation progresses by about 12 mm in X direction.

This value is the name-plate resolution of the image acquisition in X direction. Due to the nature of the circular scanning motion in fact in most places of the acquired image the resolution in X direction is higher because the individual circular paths overlap in a favorable manner. This is shown in Figure 4.30, where the sensor's scan path is shown on the countour plot of a flux distribution. The resolution in Y direction is defined by the sample rate of the data acquisition system and the rotational speed. During the

calibration of the device (Section A.2.5) a sample rate of about 6 kHz has been applied, which leads to roughly 1000 values in Y direction in the image center and, due to the circular shape of the path even higher sample density toward to lower and upper boundary of the distribution. Such high sample rate allows to filter out random noise during the post-processing. The post-processing is described in the Appendix Section A.2.5.

4.4.5 Device calibration

When focusing more on the system's uncertainty analysis (as described in more detail in the Appendix Section A.2.4) it was found that the HFM manufacturer's sensor calibration is not valid for the high fluxes as obtained in SOMMER and that it introduced systematic errors when the sensor is used in the solar spectrum. It also turned out that many sources of uncertainty resulting from the mechanics and dynamics of the system are difficult to quantify and to attribute to the measurand, that is, the power delivered to the receiver and the maximum local heat flux value in the distribution.

Therefore, in order to account for all sources uncertainty of the device simultaneously, a calibration under conditions similar to those expected to occur in SOMMER has been required. This has been conducted in the solar simulator of the DLR in Cologne, to where the complete device has been shipped to and calibrated for fluxes up to 2.16 MW m^{-2} and radiation powers delivered to the measurement plane of up to 6.3 kW.

During this calibration campaign, the relative uncertainty of the predicted power at design conditions of 10 kW of the calibrated sensor was in terms of standard deviation found to be $s_c(\dot{P}) = 3.14\,\%$ in forward motion and $s_c(\dot{P}) = 2.8\,\%$ in backwards motion. Details on the treatment of uncertainty throughout this work are explained in the Appendix Section A.1.

The relative uncertainty of total power measurement and the local peak flux value is shown in Figures 4.31 and 4.32 individually for both, forward and backward direction. According to GUM this is the uncertainty of a

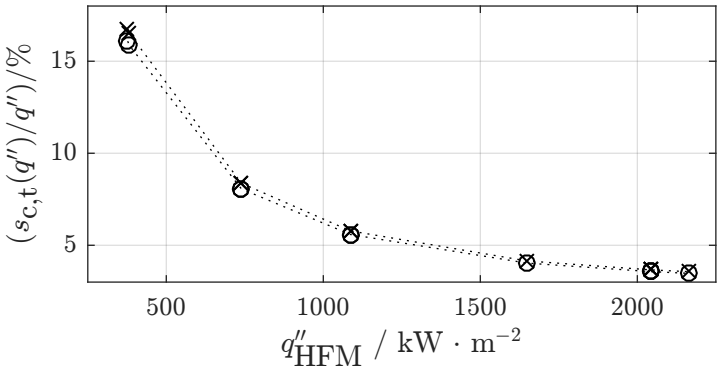

Figure 4.31: Relative combined standard deviation of the peak flux density value q'' in forward measuring direction (x) and in backward direction (o).

single measured sample (and not the average uncertainty of a large number of samples).

Under reference conditions of the SOMMER-facility, that is at a power of 10 800 W, a relative uncertainty below 4.5% is required. From the previous

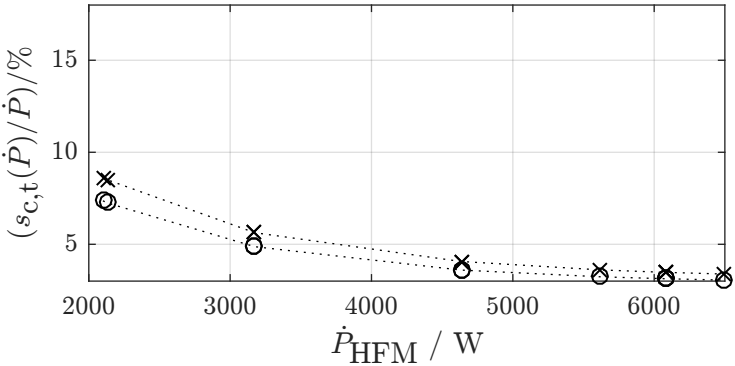

Figure 4.32: Relative combined standard deviation of the total solar power value $\dot{P}_S$ in forward measuring direction (x) and in backward direction (o).

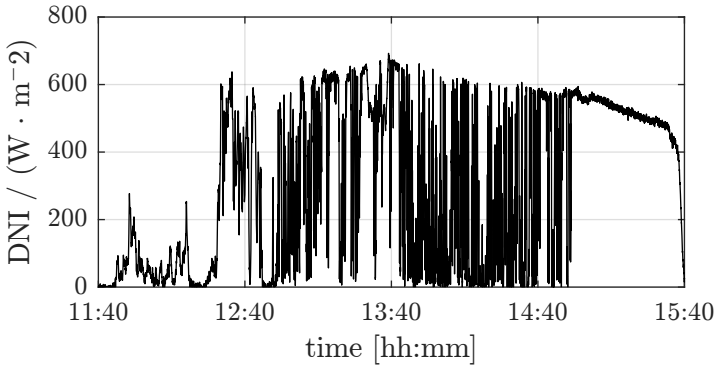

Figure 4.33: Direct normal irradiance measured on Jan 22, 2016 at KALLA

diagrams it can be observed that already at 6000 W the relative uncertainty is below 4% and maintains a decreasing trend toward higher powers.

This value is therefore sufficiently low in order to calculate meaningfully the receiver's thermal efficiency.

More detailed descriptions regarding the devices data acquisition equipment, the operation user interface, sources of uncertainty and the sensor calibration in DLR's solar simulator in Cologne are provided in the appendix section A.2.2.

4.5 Loop control

Solar irradiation strongly fluctuates throughout a day and very fast transients result for the solar power transferred to the solar receiver of the SOMMER facility. Figure 4.33 shows the DNI values throughout January 22, 2016. In the morning frequent cloud passages are observed and in the afternoon clear-sky conditions lead to a smooth decay while the sun approaches the horizon. The fluctuation during a short time frame of the same day is shown in Figure 4.34.

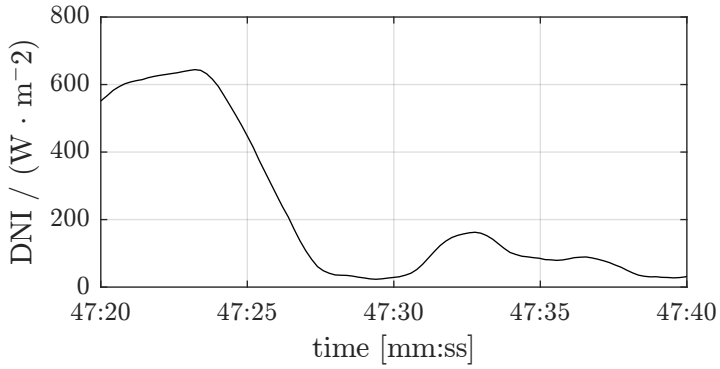

Figure 4.34: Direct normal irradiance measured on Jan 22, 2016 at KALLA, from 13:47:20 on.

The DNI can drop by nearly 100% in about five seconds, as is the case shortly after 12:47:20.

In spite of changes of input power it is a demand imposed upon the SOMMER facility , that the outlet temperature of the receiver shall remain constant in order to demonstrate liquid metal operation under transient conditions which are similar to those of a commercial, large-scale solar power plant. In such a facility the transients are, less abrupt: The shadow cast by a cloud front does not instantaneously cover all heliostats in the field. The shadow will rather gradually travel across the field at the speed of the cloud. Given the dimensions of heliostat fields this results in a ramp with smaller slope compared to what is shown in the graph. In the case of SOMMER there is only one single heliostat which is covered by a cloud at that speed nearly instantaneously. Clouds often have a semi-transparent border at their edges surrounding the opaque zone in the center. In the sample of recorded DNI values this causes the observed gradual but nevertheless quick decrease. Therefore, in comparison with larger systems the control system of SOMMER faces increased difficulty in this respect. Also, as explained before, the outlet temperature is not obtained by the receiver alone but additional

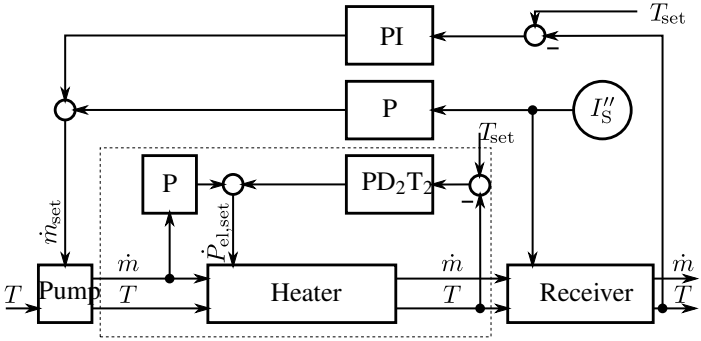

Figure 4.35: Control scheme of SOMMER receiver and heater.

thermal power is provided by a heater. The control system has therefore not only to manage the transient response by the receiver but simultaneously the dynamic effects of the heater in order to maintain a constant outlet temperature. A dynamic 1D simulation model of the loop has therefore been implemented in order to design a control algorithm and also to identify the range in which a disturbance of the input power can still be handled. It was proposed to record step responses of system components during operation in order to validate the applicability of existing design tools also under dynamic conditions.

Based on the control algorithms applied in the Solar Two and SSPS projects a control algorithm has been developed for the SOMMER loop. It's block diagram is shown in Figure 4.35 and its derivation is presented in detail in Section A.4.

At the time of writing recorded temperature responses of step inputs to the heater have been available. These could habe been used to validate the dynamic models of the heater. No data were yet available for the receiver, for which the modeled, un-validated dynamics were used during the design of the control algorithm. Due to the not entirely validated state of analysis this discussion has been moved to the appendix sections.

DNI changes of up to 30 % of its nominal value have been assessed. The dynamic responses of the receiver outlet temperature to power input are presented in Figure 4.36 with and without the designed control algorithm activated.

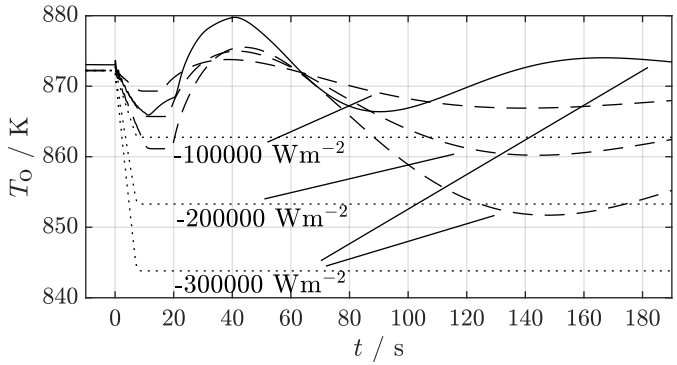

Figure 4.36: Response of the receiver's outlet temperature for negative steps of 100 000, 200 000 and 300 000 W m^{-2} in flux density. Dotted lines: all controllers switched off. Dashed lines: compensations active, solid line: compensations and PI controller active (for the case of a negative step of 300 000 W m^{-2}.

The dotted lines show the response of the system when no action is taken to maintain the desired outlet temperature. The dashed lines show the effect of adjusting the mass flow rate in a feed-forward fashion upon a change in the measured insolation value for three different steps. The solid line, finally, for a step in 300 000 W m^{-2}, shows the active feed-forward compensation and the effect of a slow PID controller combined. Both are in combination able to limit the fluctuations in the response, even though an overshoot up to nearly 880 K occurs. This is, however, tolerable.

5 Results of LBE solar loop operation

Shortly before finishing the work on writing this thesis, the commissioning of the experimental facility have been started and first experimental results obtained.

For the implementation of a control algorithm, several steps in mass flow rate and electric heating power have been imposed upon the heater. The resulting temporal responses are presented in section A.4.3 and compared with the simulated response from a simple dynamic model of the heater.

In the following sections first operation data of the pump and loop, the heater, the receiver and the flux measurement device are presented.

5.1 Overall loop operation

The following results have been obtained for receiver operation under full sun power and a receiver inlet temperature of 250 °C. The diagram in Figure 5.1 shows the power absorbed by the receiver P_{abs} based on its temperature increase and mass flow rate in blue, as well as the solar power on the receiver as measured by the heat flux scanner P_{HFM}(blank circles). The measurements shown have been performed throughout the day with increasing DNI values in the morning and decreasing DNI values in the afternoon. The red markers indicate the losses that are estimated based on the losses calibration of the receiver without incident sunlight as discussed in Section 5.4. The reference values from the heat flux scanner's outward and inward drive are arithmetically averaged in this graph.

The sensor showed during the calibration campaign only a slight difference between inward and outward drive. During operation in the SOMMER

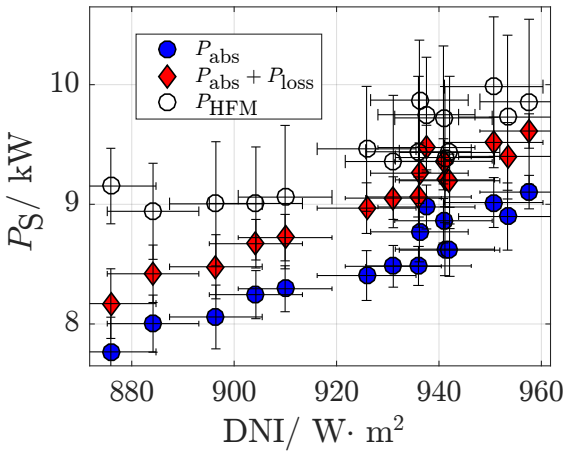

Figure 5.1: Power over a range of DNI values.Source: Pacio [73]

facility these deviations have increased. The differences in outward and inward measurement runs are shown in Figure 5.2. The top graph shows the measured peak heat flux values found somewhere in the distribution. The bottom graph shows the efficiency $\eta = P_{\mathrm{abs}}/P_{\mathrm{HFM}}$ for both runs. During calibration the inward drive showed lower values and slightly better agreement with the reference. Now, in operation, the inward peak heat flux and total power values are as well systematically lower than the outward values, however, with more significant deviation. Consequently, systematically higher thermal efficiency values are measured during inward drive, as indicated in the bottom graph. The increased offset between inward and outward drive has several possible reasons. As can be seen the measured peak flux values are close to $4\,\mathrm{MW\,m^{-2}}$. This is much higher than expected during the design phase of the solar furnace and what was observed prior to the calibration campaign. For this reason, during calibration flux values up to only $2.1\,\mathrm{MW\,m^{-2}}$ have been applied. Therefore, the present flux values are outside the scanner's valid flux range and the influence of the temperature

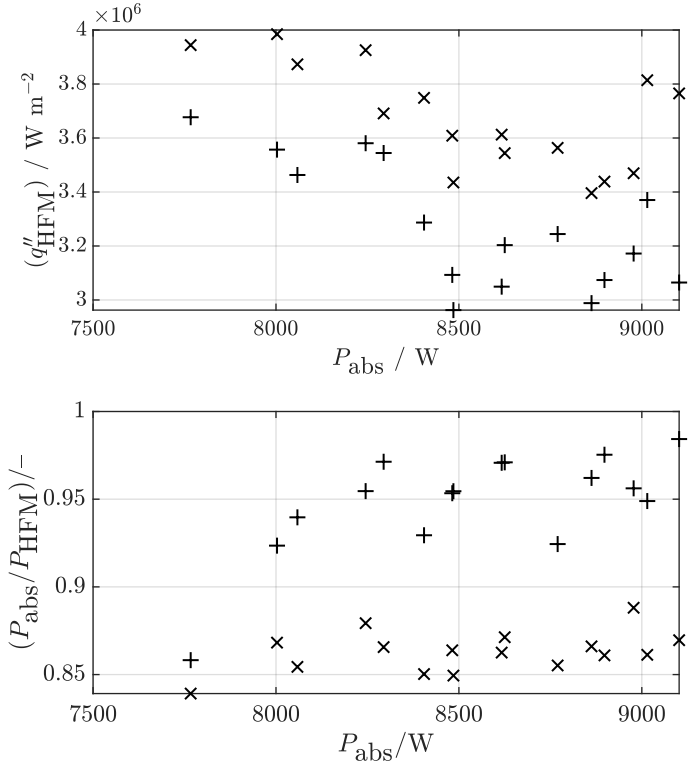

Figure 5.2: Thermal efficiency and peak heat flux values as determined from outward (x) and inward (+) sensor runs.

increase during a measurement run may not be converted to precise flux values and lead to an increased offet between inward and outward drive.

Secondly, the tracking of the heliostat mirror was paused during flux measurements as it can cause the focal point to swing, introducing error to the scan. Although pausing the tracking reduces swinging, during the pause, the focal point travels a few milimeters across the measurement plane due to the continuous rotation of the earth. Also, wind can introduce slight swing-

ing which remains unnoticed for the operators until above a certain threshold the measured distribution becomes visibily distorted.

The reason why the peak flux is much higher than expected results from the fact, that instead of two separate peaks in the distribution, now only one, central peak is observed. Indeed, the heliostat panels have aged significantly during the few years since their installation, which caused the facets' canting to disappear. In horizontal stow position, apparently, gravity pulled the canted facets into a more planar shape, which persists even in vertical position during operation. The planar shape of the heliostat now causes the initially separate focal points to unite in a single one with significantly higher peak flux. It is therefore required to repeat the calibration in cologne after the measuerments are completed and to then extend the range of peak flux values up to $4\,\mathrm{MW\,m^{-2}}$.

Figure 5.3 shows on top the temperature distribution during a measurement run with an inlet temperature of 250 °C and an exit temperature of 407 °C. On the bottom the respective flux distribution measurement of the flux scanner during outward drive is shown.

In the images, the flow enters from the bottom left corner and exits after the last pass in the top right corner.

The fluid's temperature increase along the ten passes through the receiver's absorber plane is shown in Figure 5.4. The temperatures indicate the outlet temperature of each pass so that in the sixth tube from the bottom the fluid is heated up from 344 °C to 369 °C.

In the infrared camera's image shown in the top graph in Figure 5.3 the respective temperatures of the outer tube walls are shown. The wires of the three thermal couples installed on top of the tubes are visible as bright lines. As they are not effectivly cooled they gain very high temperatures and have in fact ceased operating after fluxes as present in the shown case have been applied for a few times.

At fluxes of locally more than $3.5\,\mathrm{MW\,m^{-2}}$ the steel attains at a mass flow rate of $0.38\,\mathrm{kg\,s^{-1}}$ an outer temperatures of nearly 630 °C in the sixth

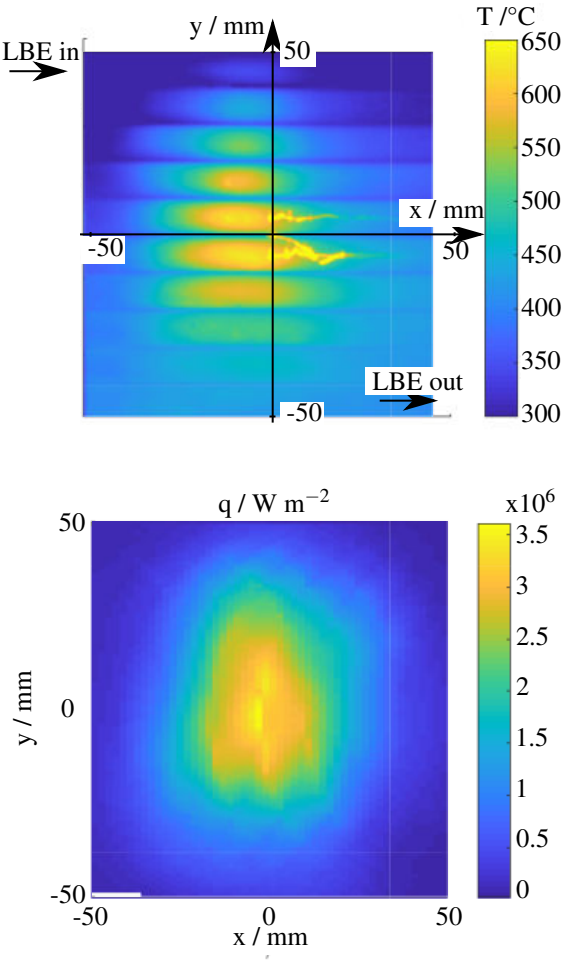

Figure 5.3: Top: Temperature distribution as measured with IR camera with assumed absorptance of 95%. at 11:42 am. LBE inlet temperature: 250 °C, LBE outlet temperature: 407 °C. Mass flow rate: 0.38 kg s^{-1}. Bottom: The corresponding flux distribution as measured by the flux scanner during outward drive.

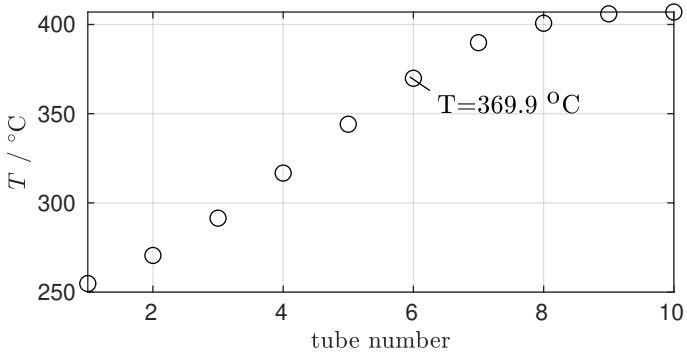

Figure 5.4: Fluid temperature after each pass through the absorber plane, as measured at the receiver coil's rear tube walls after each turn.

tube, when counted from top to bottom. After the passage of that tube the fluid has attained a temperature of 369 °C. The difference between bulk temperature and maximum wall temperature in that tube is therefore higher than 260 K.

At the given mass flow rate a Reyolds number of approximately $\mathrm{Re} = 31\,000$ is present. According to Lubarsky and Kaufman's correlation a Nusselt number of 8.3 corresponds to that Reynolds number. It allows to predict a radial temperature difference between bulk and inner tube wall of 90 K. At the maximum heat flux measured in Figure 5.3 a temperature difference across the tube wall of 66 K is estimated if the steel's thermal conductivity is assumed to equal $16\,\mathrm{W\,m^{-1}\,K^{-1}}$, according to Equation (3.33). In total therefore a bulk-to-outer-wall temperature difference of only 156 K would be expected if the correlation by Lubarsky and Kaufman were to be applied. The observed temperature difference is, however, 260 K.

Since the validity of these measurements has to be assessed more thoroughly and more experience is required to draw final conclusions the difference between expected and observed temperature is nevertheless significant

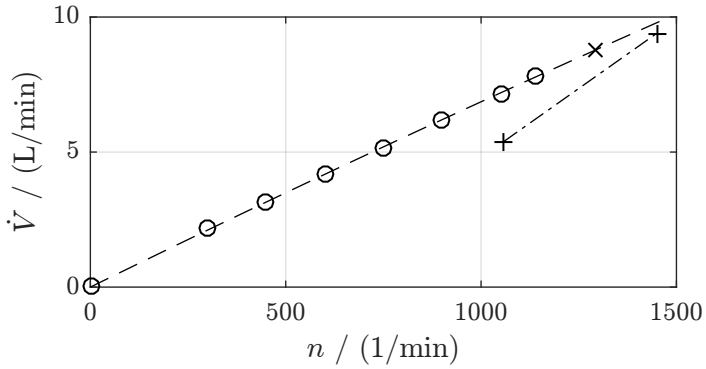

Figure 5.5: Volume flow rate over pump speed. Circles: measurements, dashed line: quadratic fit through measurements, x: volume flow and pump speed which result in a differential pressure of 11 bar at 200 °C, +: two points on pump curve at 11 bar and 380 °C as estimated by manufacturer, dash-dotted-line: linear interpolation between these two points.

enough to suggest that correlations for uniform heat flux have to be applied with care.

5.2 The loop and the pump

The volume flow curve of the loop was evaluated as a function of the pump speed at 200 °C . It is shown in Figure 5.5. The manufacturer of the pump estimated points for constant differential design pressure of 11 bar at different pump speeds. Two of these points are shown in Figure 5.5, indicated by + symbols and connected by a dash-dotted line indicating a linear interpolation between these two points. The measured volume flow rates resulting in the loop at different pump speeds are indicated with circles. A quadratic function in the form:

$$\dot{V} = 0.007106 \cdot n - 2.439 \times 10^{-7} \cdot n^2, \tag{5.1}$$

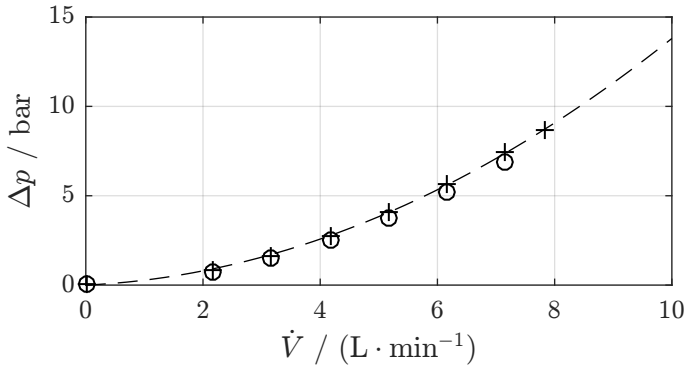

Figure 5.6: Loop pressure drop as a function of the loop flow rate at 200 °C (+), at 250 °C (o).

represents these data with an R^2 value of 0.9998. The combination of pump speed and flow rate, at which a differential pressure of 11 bar is achieved, is indicated with an x.

Ideally, at the same temperatures, the dashed and dash-dotted lines should cross at that location. However, due to strong decrease in viscosity of LBE with increasing temperature, the pumping efficiency at 380 °C is lower than at 200 °C and, therefore, the predicted flow rate at the same differential pressure is lower than at 200 °C

Measured volume flows at a differential pressure of 11 bar and higher temperatures are lower than the data shown in the present graph and then better agree with the manufacturer's prediction.

The manufacturer's performance prediction (first time designing a LBE pump) works apparently well for gear pumps for operation with LBE, in spite of its special physical properties.

The plant pressure drop curve (data and fit) at 200 °C and at 250 °C is shown in Figure 5.6 with a + and o symbol, respectively.

The pressure drop in the loop is dominated by the receiver with its small tube cross section and its overall length of 10 m. The predicted pressure

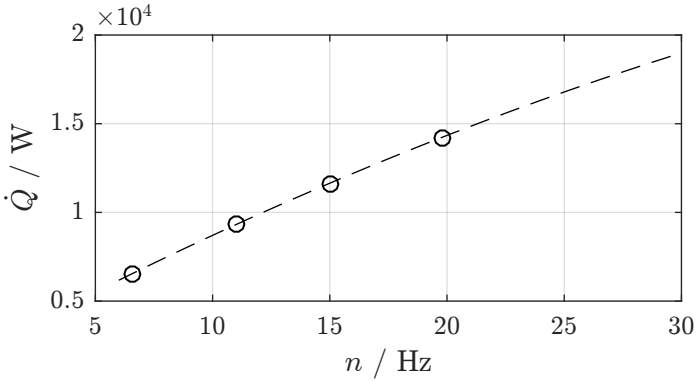

Figure 5.7: Cooler power at respective rotational blower speed. Circles: measured data, dashed line: 2nd order polynomial fit and extrapolation.

drop under nominal conditions is approximately 6 bar at a flow of 6 L min^{-1} and 600 °C. The offset from the design pressure drop is due to a conservative absolute tube roughness estimation of $K = 0.09$ mm applied during design. When $K = 0.05$ mm is used and applied for a temperature of 250 °C the calculated value equals $\Delta p = 5.27$ bar and agrees well with the measured pressure drop. For a temperature of 600°C only $\Delta p = 4.97$ bar are then predicted. Although the dynamic viscosity drops significantly in the temperature range between 250 °C and 600 °C this affects the pressure drop only by 5 % because the density changes, too.

5.3 The cooler

The cooler was tested for various inlet temperatures and a constant outlet temperature value of 232 °C prior to finishing this thesis. During design operation an outlet temperature of 380 °C is intended.

The cooling power as calculated from the LBE temperature difference between cooler in- and outlet and the applied mass flow is plotted for the respective blower speeds in Figure 5.7.

The extrapolation indicates that at this LBE outlet temperature level blower speeds higher than 30 Hz are required to obtain a cooling power of 20 kW. While the blower can operate up to much higher speeds an extrapolation up to those speeds based on the limited number of data points is unreliable and therefore limited to 30 Hz on the x-axis. However, due to the asymptotic shape of the fit under steady-state full power input of 30 kW, that is from the sun and from the electric heater simultaneously, significantly higher blower speeds will have to be applied. The heater is designed for peak power of even 30 kW for control operation – this cooling demand will then be met by at nominally higher LBE outlet temperatures. The cooler therefore seems to be appropriately chosen to meet the demand of that large operation window.

5.4 The receiver

Also the thermal losses of the receiver without solar input have been measured. This evaluation has been executed by J. Pacio and F. Fellmoser. The following function was fit to the data:

$$Q(T_{\mathrm{ref}}) = A\left(\frac{T_{\mathrm{ref}}}{300\,\mathrm{K}} - 1\right) + B\left(\left[\frac{T_{\mathrm{ref}}}{300\,\mathrm{K}}\right]^4 - 1\right) + C, \qquad (5.2)$$

with T_{ref} being the value of the receiver surface temperature at which the respective heat loss occurs. Under solar irradiance T_{ref} is a hypothetical value: due to the non-uniform heat flux distribution and strong increase of the fluid flow the local surface temperatures will vary significantly throughout the receiver's aperture. Furthermore, thermal losses increase non-linearly with the surface temperature (in case of radiation with the power of four). The reference temperature is therefore not simply the arithmetic mean of all local temperature values. During the measurement of losses without solar power input, however, at large mass flow rates the surface temperature was nearly isothermal and thus equaled sufficiently well T_{ref}.

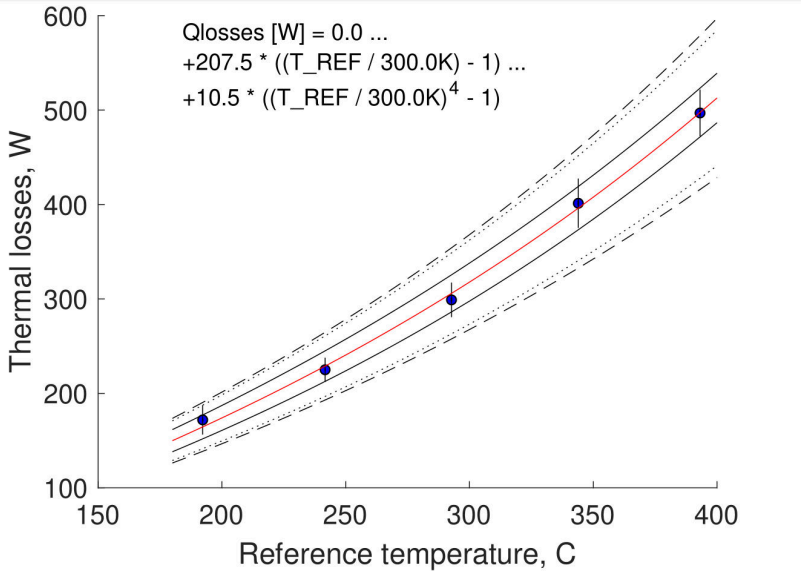

Figure 5.8: Thermal losses of the receiver of the SOMMER loop. Source: Pacio [73] Best fit: red line, fit shifted to data points with highest and lowest offset to best fit – resulting in RMS deviation to the red line of 6.5%: black, solid lines, fit shifted to capture all data points and their uncertainty, RMS 14% vs. best fit: black, dotted line; RMS 16.8% boundary: black, dashed line.

The best fit to measured data was obtained for

$$Q(T_{\mathrm{ref}}) = 207.5\,\mathrm{W}\left(\frac{T_{\mathrm{ref}}}{300\,\mathrm{K}} - 1\right) + 10.5\,\mathrm{W}\left(\left[\frac{T_{\mathrm{ref}}}{300\,\mathrm{K}}\right]^4 - 1\right) + 0. \quad (5.3)$$

and is plotted in Figure 5.8.

Thermal radiation dominates the simple physics behind the thermal losses above 400 °C. Therefore, an extrapolation to higher temperatures should result in reasonably accurate values. Accordingly, at 600 °C losses in the order of 1 kW and thus of 10 % must be expected. This is a significant figure

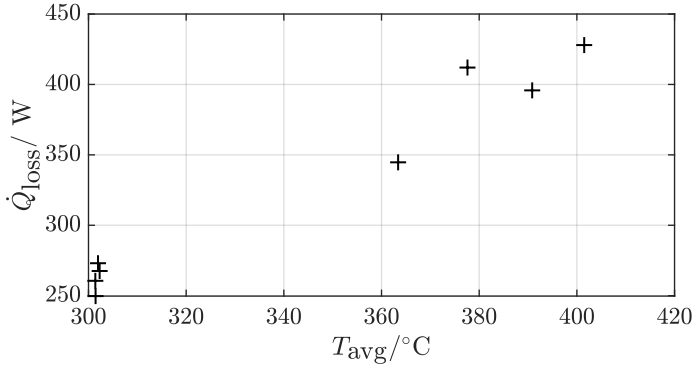

Figure 5.9: Receiver losses measured with lid on.

when taking into consideration that the receiver resides well-protected in a laboratory hall.

As presented in Section 4.3.3, based on a theoretical prediction, thermal losses of the absorber plane of only 2.5 % of the nominal power were predicted.

Indeed, the measured loss values also include thermal insulation losses. These losses have to be subtracted from the total losses for the evaluation of the losses generated by the absorber aperture alone.

The insulation losses were measured during the commissioning of the electric heater, when the receiver's aperture was covered with a thermally insulated lid. These are shown in Figure 5.9. For example, at a value of the reference temperature $T_{\mathrm{ref}} = 300\,^{\circ}\mathrm{C}$ the losses of the completely insulated receiver were found to be approximately between 250 W and 270 W. Without the lid the losses were higher by only about 30 W. The losses with the lid on can therefore be significant, if not dominant, compared to the additional losses of an open receiver aperture.

There are, however, a number of reasons why insulation losses could currently indeed dominate the total losses:

- The receiver aperture of $0.01\,m^2$ is small in comparison to the total surface area of the receiver of about $1.7\,m^2$ (including the closed lid). In spite of the insulation layer significant losses may occur across the insulation in comparison to those from the open receiver aperture.

- stainless steel (low thermal conductivity) and copper parts that either hold the receiver spiral or the copper shield (high thermal conductivity) protrude out of the insulated body and may serve as cooler fins.

- The lid covers up the front surfaces of the copper shield but not their outer edges. These may thermally conduct heat to the outer regions of the insulating layer and increase the losses locally.

A more detailed assessment of the losses, both with and without lid must take the temperature of the copper plates, the temperature of the outer insulation and of the protruding metal parts into account. The initially applied thermal insulation may then turn out not be sufficient and may have to be improved.

Loop components in front of the parabolic mirror, such as the receiver, its vertical support beam and the horizontal, and thermally insulated liquid metal tubes cast shadows that reduce the available power value. With assumed reflectivities of 90 % for the mirrors and an absorptance of 90 % of the absorber, on days with a DNI value of $960\,W\,m^{-2}$ a solar power of more than 11 kW is theoretically delivered to the receiver. The measured powers achieved values of slightly below 10 kW, instead.

5.5 The heater

Although the heater is well designed regarding its dynamics, during design the effect of buoyancy was insufficiently taken into account. The horizontal orientation at the given design causes a fluid stagnation near the hot outlet when reaching a threshold temperature. Above it, hot fluid cannot exit the

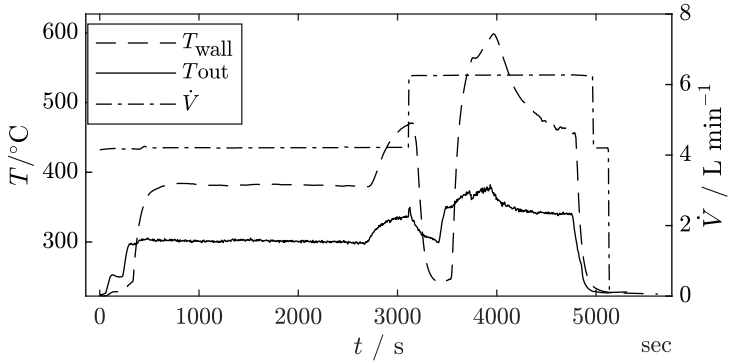

Figure 5.10: Temperatures of the LBE at the outlet (solid line) and of the top vessel wall near the outlet (dashed line) and the LBE's volume flow rate (dash-dotted line).

device – it floats on the cooler, flowing fluid – and is heated up to temperatures much higher than the outlet temperature would suggest. This behavior was detected thanks to a wall-attached thermocouple used for the trace heating element at the heater's outlet. The temperatures reach values above the heater's allowable operation temperature.

This behavior is shown in Figure 5.10.

The stagnation limits the operation range of the loop in the followint way: After applying 6.5 kW of heater power at the given flow rate steady-state conditions at the heater outlet are obtained with a outlet temperature of 300 °C. The wall temperature is already significantly higher than the temperature of the fluid exiting. After less than 3000 s the operator increased the heater power to 10 kW. As a result the wall temperature rises quickly. The operator tried successfully to remove the stagnant fluid by raising the volume flow rate to nominal 6 L min^{-1}, causing the wall temperature to drop below that of the fluid. After steady-state conditions were obtained the operator increased the heater power to 20 kW, causing the formation of a new stagnation zone which quickly increased the local wall temperature

to nearly 600 °C, at which moment the operator reduced the heater power to 15 kW and then, after the wall temperature still remained at too high values, switched the power off.

This design flaw unfortunately limits the outlet temperature to around 250 °C, in contrast to 530 °C which had been intended.

Buoyancy effects

With existing design tools the potential of this problem could have been predicted. With the wall-to-bulk temperature difference known, the Grashof number for a single heater rod is calculated with a diameter used of 22 mm. Additionally, the Richardson number defined as:

$$\mathrm{Ri} = \frac{\mathrm{Gr}}{\mathrm{Re}^2}, \tag{5.4}$$

can be considered as a ratio of potential forces and initial forces. It serves thus as an indicator whether or not natural convection plays a significant role in the heat transfer process. In the present case it has a value of $\mathrm{Ri} = 2.86$. For $\mathrm{Ri} \geq 0.02$ natural convection was shown in the past to influence heat transfer in upward sodium tube flow [32]. In principle, existing correlations for higher Prandtl number fluids are applicable for liquid metals, too, however, whether bouyancy impedes or enhances heat transfer for example in upward flow is not answered in literature on liquid metals, yet. In general, bouyant effects are viewed to affect heat transfer in liquid metals ‘over a wider range of flow parameters than in other fluids ’[32] and are therefore of concern for the designer of devices such as the heater discussed. However, very few works exist that correlate the buoyancy effect under mixed convection with the Nusselt number for engineering purposes.

A vertical installation of the heater will remove this problem. However, at the limited available space in the SOMMER loop such re-orientation will

come at the costs of an U-shaped loop extension requiring an additional draining line and valve – it is thus a significant effort.

5.6 General operation experience

A few months of operation have allowed to commission the LBE loop and collect initial data providing a picture of the achievements. Apparently, the existing design tools are generally sufficient in designing and operating a solar-powerd LBE loop.

6 Summary

Due to inherent techno-economical limitations of state-of-the-art coolant fluids compared with competing renewables such as wind power and photovoltaics renewed interest in the application of liquid metals can be observed in the scientific and industrial community and the design, construction and operation of a solar-powered liquid metal loop SOMMER has been executed, as is presented in this work.

Lead-bismuth eutectic (LBE) is applied as liquid metal heat-transfer fluid.

LBE's physical properties a liquid metal design tools

The physical properties of LBE have to be taken into account for commercial application :

Compared to solar salt and sodium, LBE is very dense on the one hand and lacks a high mass specific heat capacity on the other. Therefore, its high density generates no advantage in heat transfer, but high pressure losses instead. It thus diminishes the benefits from its high thermal conductivity and reasonably low viscosity. These properties result in an optimum heat transfer performance of LBE at slightly higher exergy destruction than solar salt under uniform heat flux boundary conditions when operated in the same temperature interval – and thus slightly lower heat transfer performance.

Many Nusselt number correlations for fully turbulent liquid metal flow and uniform heat flux have been developed in the past. The ones recommended by the LBE Handbook [32] agree well with those recommended by Pacio [48] in the range of Reynolds and Peclét numbers up to approximately

5000 However, very likely hypothetical large-scale receivers operated with LBE will operate at Peclét numbers of more than 10 000 where existing Nusselt correlations deviate .

Also, different correlations exist for different groups of metals, probably due to experimental differences and difficulties. If LBE is further assessed as primary heat transfer fluid in solar central receivers, the upper regions of the required Peclét number range should be validated experimentally, in order to unify existing correlations.

The existing correlations for uniform heat flux and forced convective flow under-predict local wall temperatures at non-uniform boundary conditions as present in solar thermal receivers. This effect has not been adequately recognized in the community, although predicted by W. C. Reynolds [63] in 1963. The observation of unusually high local wall temperatures during experiments with sodium receivers decades later in the SSPS Almería projects, under non-uniform heat flux present on receiver tubes may be explained by this effect.

Since existing engineering Nusselt number correlations for turbulent flow and uniform heat flux are capable only of predicting an average wall temperature for liquid metal flows, basic design should instead be executed by applying W. C. Reynolds' [63] approach.

Alternatively, numerical simulations can be applied if the liquid metals' low Prandtl numbers are correctly accounted for as computations by Marocco et al. [47] demonstrate. These, as well as experimental results by Melnikov et al. [60] indicate this behavior (high local temperatures) as well.

LBE has a particularly strong local deviation from the average wall temperature under non-uniform heat flux compared to the case of uniform heat flux – stronger than for sodium and much stronger than with solar salt where the local temperatures do not deviate much. In terms of exergy destruction rates (Section 3.1) it is therefore inferior to solar salt when a non-uniform heat flux boundary conditions are applied.

While these findings correspond to the case of forced convective and fully developed flow, more work should also be invested in the development and testing of engineering correlations for the case of heat transfer under *mixed* convection conditions in a variety of geometries in order to enable engineers to quickly and confidently design heat transfer devices.

LBE operation at temperatures above 600 °C has limitations. For stainless steels the corrosion potential by LBE, that is the dissolution attack of alloying elements, is enhanced. Special materials that are very resistant the the corrosion attack of LBE up to temperatures of 750 °C, such as Kanthal [32, p.637] are expensive alternatives as receiver construction tube materials. When applying oxygen control to the system for steel corrosion prevention, the upper and lower oxygen concentration bounds require an increasing lower equilibrium temperature when the upper process temperature is increased. While the remaining temperature range may be sufficiently large for operation in solar receivers, the required increase of the lower temperature level will potentially compensate the benefit of a higher outlet temperature, because it makes increasingly powerful trace heating a costly requirement.

LBE is expected to show better performance than sodium in terms of storage efficiency and thermocline degradation in single-tank packed bed storage systems, as found by Niedermeier [43].

Due to the lack of chemical de-composition LBE can be re-used even after long term operation. This could potentially in part compensate for the initially high investment costs. It is uncertain whether this property will make LBE an attractive candidate in thermal storage systems: At the same time Niedermeier's assessment shows satisfactory storage efficiency for sodium at competitive costs.

LBE is, however, also expensive, subject to price fluctuations and may have limited availability with bismuth as the expensive component.

In summary, LBE's benefits are:

1. The operation at increased heat flux densities in receivers of reduced aperture area, however, under careful monitoring of its oxygen concentration for corrosion protection.

2. Lower safety requirements when applied to experimental model systems compared to sodium.

Indeed, the selection of LBE facilitated building a liquid metal loop however, lacking the dimensionless similarity of the SOMMER receiver with a reference receiver operated with sodium.

The use of LBE will, according to the previous findings and according to those by Fritsch [29], likely be limited to the solar receiver exclusively. In his study, Fritsch identified a cost reduction potential for this scenario compared to the current state-of-the-art with solar salt as HTF, however, he did not consider the impact of the non-uniform boundary condition on the wall temperature distribution of the liquid metal flows. These impacts should be re-assessed in order to investigate the requirement of a design adaptation for higher heat transfer coefficients and smaller tube diameters and the impact on the receiver operation and construction costs.

Solar loop and solar furnace

The thermal receiver has been operated at solar flux densities up to nearly $4\,\mathrm{MW\,m^{-2}}$. An available thermal power of $\dot{Q} = 10\,\mathrm{kW}$ has been transferred by the coolant in the thermal receiver while exposed to this flux.

The flux has been measured using a specially developed flux scanner and a single heat flux micro sensor with a measurement accuracy of below 4% for the overall design solar power on the absorber plane at $\dot{P}_\mathrm{S} = 10\,800\,\mathrm{W}$. This device operates with a linear and superimposed rotational motion pattern. An offset in the power and peak flux values of the two available scanning directions is observed, likely due to its operation outside the cal-

ibration flux range (A much lower peak flux had been expected during the design phase.)

Liquid metal receiver operation

The operation experience has been limited to a few months of commissioning and operation. and the resulting data provide at this stage a limited picture. Nevertheless, some interesting findings have been obtained in this facility.

The experimental operation data of the thermal receiver at local heat flux values of nearly 4MW/m2 suggest that local wall temperatures of the receiver tubes are higher than when predicted with Nusselt correlations for uniform heat flux and fully turbulent flow, in agreement with the predictions of W. C. Reynolds. The local wall temperatures in low-Prandtl number fluid flows may deviate more significantly from the average wall temperatures than in regular Prandtl-number fluid flows. Future designs of liquid metal cooled solar thermal receivers should take this into consideration.

The receiver's absorber paint shows no signs of ageing upon human-eye inspection.

Thermal losses have been recorded without solar flux imposed upon the absorber plane. These turn out higher than predicted, probably due to insufficient thermal insulation, a large ratio of overall receiver's casing area to absorber area and the copper radiation protection shield surrounding the receiver aperture acting like cooling fins.

The hydraulic behavior of the gear pump agrees well with the predictions of the manufacturer within the operation range presented, in spite of the special wetting properties of LBE which could potentially have led to an improper selection of gap widths. However, for unknown reasons the pump ceases operating at liquid temperatures in the pump vessel above 250 °C. Whether or not this problem is due to LBE in particular could not be answered prior to completion of this thesis.

Buoyancy in the horizontally oriented electric heater led to hot fluid stagnation and over-heating. It should be installed vertically in order to continue operation at heater powers above 6.5 kW.

Overall work

The assessment of LBE's thermo-physical properties and of state-of-the-art liquid metal design-tools led to the identification of benefits, however, also of limitations of LBE as heat transfer fluid for concentrating solar thermal power receivers. The importance of some liquid metals' high sensitivity to non-uniform heat flux boundary conditions has in the past potentially been neglected in the design of solar thermal receiver components. It is shown in this work, that these should rather not be neglected and further studied. Design-tools which take this behavior into account are presented. A complete solar furnace including a liquid LBE-loop for the cooling of the solar thermal receiver has been designed, build, commissioned and operated. Therefore, the SOMMER project demonstrates generally the applicability of the required design tools for many loop components operated with liquid metal for short-term solar operation. Further operation may show whether long-term solar operation is feasible with the current design, as well.

Bibliography

[1] M. D. Dickey, "Emerging applications of liquid metals featuring surface oxides," ACS Applied Materials & Interfaces, vol. 6, no. 21, pp. 18 369–18 379, Oct. 2014. https://doi.org/10.1021/am5043017

[2] L. A. B. Pilkington, "Review lecture. the float glass process," Proceedings of the Royal Society A: Mathematical, Physical and Engineering Sciences, vol. 314, no. 1516, pp. 1–25, Dec. 1969. https://doi.org/10.1098/rspa.1969.0212

[3] K. Ma and J. Liu, "Liquid metal cooling in thermal management of computer chips," Frontiers of Energy and Power Engineering in China, vol. 1, no. 4, pp. 384–402, Oct. 2007. https://doi.org/10.1007/s11708-007-0057-3

[4] W. B. Lineton, "Piston with a cooling gallery partially filled with a thermally conductive metal-containting composition," 2012. https://patents.google.com/patent/US9127619B2/en

[5] W. Marth, "Die geschichte von bau und betrieb des deutschen schnellbrueter-kernkraftwerks knk ii," Kernforschungszentrum Karlsruhe, Tech. Rep., 1993, 90; LK 01; KfK-5155 (August 93). https://publikationen.bibliothek.kit.edu/270034572

[6] A. Zrodnikov, G. Toshinsky, O. Komlev, Y. Dragunov, V. Stepanov, N. Klimov, V. Generalov, I. Kopytov, and V. Krushelnitsky, "Innovative nuclear technology based on modular multi-purpose lead–bismuth cooled fast reactors," Progress in Nuclear Energy,

vol. 50, no. 2-6, pp. 170–178, Mar. 2008. https://doi.org/10.1016/j.pnucene.2007.10.025

[7] J. Pacio, A. Fritsch, C. Singer, and R. Uhlig, "Liquid metals as efficient coolants for high-intensity point-focus receivers: implications to the design and performance of next-generation CSP systems," Energy Procedia, vol. 49, pp. 647 – 655, 2014, proceedings of the SolarPACES 2013 International Conference. http://www.sciencedirect.com/science/article/pii/S1876610214005244

[8] J. Pacio, C. Singer, T. Wetzel, and R. Uhlig, "Thermodynamic evaluation of liquid metals as heat transfer fluids in concentrated solar power plants," Applied Thermal Engineering, vol. 60, no. 1-2, pp. 295–302, 2013. http://www.sciencedirect.com/science/article/pii/S1359431113004985

[9] J. Pacio and T. Wetzel, "Assessment of liquid metal technology status and research paths for their use as efficient heat transfer fluids in solar central receiver systems," Solar Energy, vol. 93, pp. 11 – 22, 2013. http://www.sciencedirect.com/science/article/pii/S0038092X13001357

[10] T. Wetzel, J. Pacio, L. Marocco, A. Weisenburger, A. Heinzel, W. Hering, C. Schroer, G. Müller, J. Konys, R. Stieglitz, J. Fuchs, J. Knebel, C. Fazio, M. Daubner, and F. Fellmoser, "Liquid metal technology for concentrated solar power systems: contributions by the German research program," AIMS Energy, vol. 2, no. 1, pp. 89–98, 2014. http://www.aimspress.com/aimse/ch/reader/create_pdf.aspx?file_no=20140103&year_id=2014&quarter_id=1&falg=1

[11] A. Heinzel, W. Hering, J. Konys, L. Marocco, K. Litfin, G. Mueller, J. Pacio, C. Schroer, R. Stieglitz, L. Stoppel, A. Weisenburger, and T. Wetzel, "Liquid metals as efficient high temperature heat transport fluids," Energy Technology, vol. 5, pp. 1026–1036, 2017. http://onlinelibrary.wiley.com/doi/10.1002/ente.201600721/abstract

[12] Hering, W., Stieglitz, R., and Wetzel, Th., "Application of liquid metals for solar energy systems," EPJ Web of Conferences, vol. 33, p. 03003, 2012. http://dx.doi.org/10.1051/epjconf/20123303003

[13] N. Lorenzin and A. Abánades, "A review on the application of liquid metals as heat transfer fluid in concentrated solar power technologies," International Journal of Hydrogen Energy, vol. 41, pp. 6990–6995, 2016. http://www.sciencedirect.com/science/article/pii/S0360319915311654

[14] Kotzé, "High temperature thermal energy storage utilizing metallic phase change materials and metallic heat transfer fluids," Journal of Solar Energy Engineering, vol. 135, p. 6, 2013. http://solarenergyengineering.asmedigitalcollection.asme.org/article.aspx?articleid=1692818

[15] N. Boerema, G. Morrison, R. Taylor, and G. Rosengarten, "Liquid sodium versus Hitec as a heat transfer fluid in solar thermal central receiver systems," Solar Energy, vol. 86, no. 9, pp. 2293 – 2305, 2012. http://www.sciencedirect.com/science/article/pii/S0038092X12001703

[16] N. Boerema, G. Morrison, R. Taylor, and G. Rosengarten, "High temperature solar thermal central-receiver billboard design," Solar Energy, vol. 97, pp. 356 – 368, 2013. http://www.sciencedirect.com/science/article/pii/S0038092X1300368X

[17] W. R. Logie, J. D. Pye, and J. Coventry, "Thermoelastic stress in concentrating solar receiver tubes: A retrospect on stress analysis methodology, and comparison of salt and sodium," Solar Energy, vol. 160, pp. 368–379, Jan. 2018. https://doi.org/10.1016/j.solener.2017.12.003

[18] J. Pye, C.-A. Zheng, M.and Asselineau, and J. Coventry, "An exergy analysis of tubular solar-thermal receivers with different working

fluids," Energy Procedia, 2014. http://stg.anu.edu.au/publications/assets/inproc/pye-solarpaces-2014.pdf

[19] G. Wilk, A. DeAngelis, and A. Henry, "Estimating the cost of high temperature liquid metal based concentrated solar power," Journal of Renewable and Sustainable Energy, vol. 10, no. 2, p. 023705, 2018. https://doi.org/10.1063/1.5014054

[20] C. K. Ho and B. D. Iverson, "Review of high-temperature central receiver designs for concentrating solar power," Renewable and Sustainable Energy Reviews, vol. 29, no. Supplement C, pp. 835 – 846, 2014. http://www.sciencedirect.com/science/article/pii/S1364032113006394

[21] H. Benoit, L. Spreafico, D. Gauthier, and G. Flamant, "Review of heat transfer fluids in tube-receivers used in concentrating solar thermal systems: Properties and heat transfer coefficients," Renewable and Sustainable Energy Reviews, vol. 55, pp. 298–315, Mar. 2016. http://dx.doi.org/10.1016/j.rser.2015.10.059

[22] J. Coventry, C. Andraka, J. Pye, M. Blanco, and J. Fisher, "A review of sodium receiver technologies for central receiver solar power plants," Solar Energy, vol. 122, pp. 749–762, Dec. 2015. http://dx.doi.org/10.1016/j.solener.2015.09.023

[23] A. B. Zavoico, "Solar power tower design basis document," Sandia National Laboratories, Tech. Rep. SAND2001-2100, 2001. http://prod.sandia.gov/techlib/access-control.cgi/2001/012100.pdf

[24] J. Flesch, "Development of a simulation model for a solar thermal central receiver system," Diploma Thesis, Technische Universtiät Berlin, Apr. 2013.

[25] P. Kesselring and C. S. Selvage, "Distributed collector system," in The IEA/SSPS Solar Thermal Power Plants — Facts and

Figures— Final Report of the International Test and Evaluation Team (ITET). Springer Berlin Heidelberg, 1986, pp. 79–84. https://doi.org/10.1007/978-3-642-82684-9_33

[26] P. Kesselring, Ed., The IEA/SSPS Solar Thermal Power Plants - Facts and Figures - Final Report of the International Test and Evaluation Team (ITET): Volume 1: Central Receiver System (CRS). Springer, 1986.

[27] W. Schiel, M. A. G. Geyer, and R. Carmona, Eds., International Energy Agency/Small Solar Power Systems Project: The IEA, SSPS High Flux Experiment: Testing the Advanced Sodium Receiver at Heat Fluxes up to 2.5 MW/m2. Springer, 1987. https://www.springer.com/gp/book/9783540182245

[28] J.-S. Kim, A. Dawson, R. Wilson, K. Venkatesan, and W. Stein, "High-temperature heat transport and storage using LBE alloy for concentrated solar power systems," in Proceedings of the ASME 2015 9th International Conference on Energy Sustainability, ser. Energy Sustainability, vol. Volume 1: Advances in Solar Buildings and Conservation; Climate Control and the Environment; Alternate Fuels and Infrastructure; ARPA-E; Combined Energy Cycles, CHP, CCHP, and Smart Grids; Concentrating Solar Power; Economic, Environmental, and Policy Aspects of Alternate Energy; Geothermal Energy, Harvesting, Ocean Energy and Other Emerging Technologies; Hydrogen Energy Technologies; Low/Zero Emission Power Plants and Carbon Sequestration; Micro and Nano Technology Applications and Materials, 06 2015, v001T05A025. http://proceedings.asmedigitalcollection.asme.org/proceeding.aspx?articleid=2467442

[29] A. Fritsch, "Potenzialanalyse von solarturmkraftwerken mit flüssigmetallen als wärmeträgermedium," Ph.D. dissertation, RWTH Aachen, Fakultüt für Maschinenwesen, 2018.

[30] K. Niedermeier, J. Flesch, L. Marocco, and T. Wetzel, “Assessment of thermal energy storage options in a sodium-based CSP plant,” Applied Thermal Engineering, vol. 107, pp. 386–397, Aug. 2016. http://dx.doi.org/10.1016/j.applthermaleng.2016.06.152

[31] K. Niedermeier, L. Marocco, J. Flesch, G. Mohan, J. Coventry, and T. Wetzel, “Performance of molten sodium vs. molten salts in a packed bed thermal energy storage,” Applied Thermal Engineering, vol. 141, pp. 368–377, Aug. 2018. https://doi.org/10.1016/j.applthermaleng.2018.05.080

[32] Handbook on Lead-bismuth Eutectic Alloy and Lead Properties, Materials Compatibility, Thermal-hydraulics and Technologies. OECD Nuclear Energy Agency, Nov. 2015, no. 7268. https://www.oecd-nea.org/science/pubs/2015/7268-lead-bismuth-2015.pdf

[33] O. J. Foust, Ed., Sodium-NaK engineering handbook. New York: Gordon & Breach, 1976.

[34] A. Bejan, Entropy Generation Minimization – The Method of Thermodynamic Optimization of Finite-Size Systems and Finite-Time Processes, 1st ed., ser. Mechanical and Aerospace Engineering Series (Book 2). CRC Press, Oct. 1995.

[35] J. Flesch, L. Marocco, A. Fritsch, K. Niedermeier, and T. Wetzel, “Entropy Generation Minimization Analysis of Solar Salt, Sodium, and Lead–Bismuth Eutectic as High Temperature Heat Transfer Fluids,” Journal of Heat Transfer, vol. 142, no. 4, Feb. 2020, 042103. https://doi.org/10.1115/1.4046302

[36] J. Buongiorno, “Conceptual design of a lead-bismuth cooled fast reactor with in-vessel direct-contact steam generation,” Ph.D. dissertation, Massachusetts Institute of Technology, 2001. http://dspace.mit.edu/handle/1721.1/32205

[37] D. E. Guberman, “Mineral commodity summaries: Lead,” Online factsheet by the U.S. Geological Survey National Minerals Information Center, Jan. 2016, date last accessed: Nov. 16, 2020. https://s3-us-west-2.amazonaws.com/prd-wret/assets/palladium/production/mineral-pubs/lead/mcs-2016-lead.pdf

[38] “Mineral commodity summaries: Appendix c: Reserves and resources,” Online factsheet by the U.S. Geological Survey National Minerals Information Center, 2016, date last accessed Nov. 16, 2020. https://s3-us-west-2.amazonaws.com/prd-wret/assets/palladium/production/mineral-pubs/mcs/mcs2016.pdf

[39] International lead and zink study group, “Ilzsg brochure 2016,” online, Apr. 2016, date last accessed Dec. 15, 2016. http://www.ilzsg.org/generic/pages/file.aspx?file_id=1845

[40] C. S. Anderson, “Mineral commodity summaries: Bismuth,” Online factsheet by the U.S. Geological Survey National Minerals Information Center, Jan. 2016. http://minerals.usgs.gov/minerals/pubs/commodity/bismuth/

[41] C. J. Winter, R. L. Sizmann, and L. Vant-Hull, Eds., Solar Power Plants: Fundamentals, Technology, Systems, Economics. Springer-Verlag, 1991. https://www.springer.com/gp/book/9783642647598

[42] D. C. P. Grogan, “Development of molten-salt heat transfer fluid technology for parabolic trough solar power plants - public final technical report,” Office of Scientific and Technical Information (OSTI), Tech. Rep., 2013.

[43] K. Niedermeier, “Numerical investigation of a thermal storage system using sodium as heat transfer fluid,” Ph.D. dissertation, KIT Department of Chemical and Process Engineering, 2019. https://publikationen.bibliothek.kit.edu/1000093902

[44] U. Herrmann, B. Kelly, and H. Price, "Two-tank molten salt storage for parabolic trough solar power plants," Energy, vol. 29, no. 5-6, pp. 883–893, Apr. 2004. https://doi.org/10.1016/s0360-5442(03)00193-2

[45] B. F. Gromov, Y. I. Orlov, P. N. Martynov, and V. Gulevskij, "Technological problems of the heavy liquid-metal coolants (lead-bismuth, lead)," in Heavy liquid-metal coolants in the nuclear technologies. Collection of the conference reports in two volumes., vol. 1, no. INIS-RU–473, 1999, pp. 128–135. https://inis.iaea.org/search/searchsinglerecord.aspx?recordsFor=SingleRecord&RN=34075876

[46] L. Martinelli, C. Jean-Louis, and B.-C. Fanny, "Oxidation of steels in liquid lead bismuth: Oxygen control to achieve efficient corrosion protection," Nuclear Engineering and Design, vol. 241, no. 5, pp. 1288 – 1294, 2011. http://www.sciencedirect.com/science/article/pii/S0029549310005303

[47] L. Marocco, G. Cammi, J. Flesch, and T. Wetzel, "Numerical analysis of a solar tower receiver tube operated with liquid metals," International Journal of Thermal Sciences, vol. 105, pp. 22 – 35, 2016. http://www.sciencedirect.com/science/article/pii/S1290072916000508

[48] J. Pacio, L. Marocco, and T. Wetzel, "Review of data and correlations for turbulent forced convective heat transfer of liquid metals in pipes," Heat and Mass Transfer, vol. 51, no. 2, pp. 153–164, 2015. http://dx.doi.org/10.1007/s00231-014-1392-3

[49] B. Lubarsky and S. J. Kaufman, "Review of experimental investigations of liquid-metal heat transfer," Lewis Flight Propulsion Laboratory - National Advistory Comitee for Aeronautics, Tech. Rep. Technical note 3336, 1955. https://digital.library.unt.edu/ark:/67531/metadc57490/m2/1/high_res_d/19930084144.pdf

[50] C.-J. Chen and J. S. Chiou, "Laminar and turbulent heat transfer in the pipe entrance region for liquid metals," International Journal of Heat and Mass Transfer, vol. 24, no. 7, pp. 1179 – 1189, 1981. http://www.sciencedirect.com/science/article/pii/0017931081901678

[51] E. Skupinski, J. Tortel, and L. Vautrey, "Determination des coefficients de convection d'un alliage sodium-potassium dans un tube circulaire," International Journal of Heat and Mass Transfer, vol. 8, no. 6, pp. 937 – 951, 1965, in French. English title: Determination of convection coefficient for a sodium-potassium alloy in a circular tube. http://www.sciencedirect.com/science/article/pii/0017931065900773

[52] S. Kutateladze, V. Borishanskii, and I. Novikov, "Heat transfer in liquid metals," Journal of Nuclear Energy. Part B. Reactor Technology, vol. 9, no. 14, pp. 214 – 229, 1959. https://linkinghub.elsevier.com/retrieve/pii/036832655990177X

[53] F. Dittus and L. Boelter, "Heat transfer in automobile radiators of the tubular type," International Communications in heat and mass transfer, vol. 12, pp. 3 – 22, 1985.

[54] L. Marocco, A. Loges, T. Wetzel, and R. Stieglitz, "Experimental investigation of the turbulent heavy liquid metal heat transfer in the thermal entry region of a vertical annulus with constant heat flux on the inner surface," International Journal of Heat and Mass Transfer, vol. 55, no. 23-24, pp. 6435 – 6445, 2012. http://www.sciencedirect.com/science/article/pii/S0017931012004656

[55] J. Jackson, "Turbulent mixed convection heat transfer to liquid sodium," International Journal of Heat and Fluid Flow, vol. 4, no. 2, pp. 107 – 111, 1983.

[56] J. D. Jackson, B. P. Axcell, and A. Walton, "Mixed convection heat transfer to sodium in a vertical pipe," Experimental Heat Transfer,

vol. 7, no. 1, pp. 71–90, 1994. http://www.tandfonline.com/doi/abs/10.1080/08916159408946473

[57] V. G. Sviridov, N. G. Razuvanov, Y. P. Ivotchkin, Y. I. Listratov, E. V. Sviridov, L. G. Genin, Z. V. G., and I. A. Belyaev, "Liquid metal heat transfer investigations applied to tokamak reactor," in Proceedings of the 14th International Heat Transfer Conference, 2010, pp. 287–294.

[58] I. A. Belyaev, Y. P. Ivochkin, Y. I. Listratov, N. G. Razuvanov, and V. G. Sviridov, "Temperature fluctuations in a liquid metal mhd-flow in a horizontal inhomogeneously heated tube," High Temperature, vol. 53, pp. 734–741, 2015.

[59] I. A. Belyaev, L. G. Genin, Y. I. Listratov, I. A. Melnikov, V. G. Sviridov, and E. V. Sviridov, "Liquid metal heat transfer specific in a tokamak reactor," Magnetohydrodynamics, vol. 49, pp. 177–190, 2013.

[60] I. A. Melnikov, N. G. Razuvanov, V. G. Sviridov, E. V. Sviridov, and A. A. Shestakov, "An investigation of heat exchange of liquid metal during flow in a vertical tube with non-uniform heating in the transverse magnetic field," Thermal Engineering, vol. 60, no. 5, pp. 355–362, Apr. 2013. https://doi.org/10.1134/s004060151305008x

[61] R. Lyon, "Liquid metal heat-transfer coefficients," Chemical Engineering Progress, vol. 47, no. 2, pp. 75–79, 1951.

[62] J. Flesch, A. Fritsch, G. Cammi, L. Marocco, F. Fellmoser, J. Pacio, and T. Wetzel, "Construction of a test facility for demonstration of a liquid lead-bismuth-cooled 10 kw thermal receiver in a solar furnace arrangement - sommer," Energy Procedia, vol. 69, pp. 1259 – 1268, 2015, international Conference on Concentrating Solar Power and Chemical Energy Systems, SolarPACES 2014. http://www.sciencedirect.com/science/article/pii/S1876610215004634

[63] W. Reynolds, "Turbulent heat transfer in a circular tube with variable circumferential heat flux," International Journal of Heat

and Mass Transfer, vol. 6, no. 6, pp. 445–454, Jun. 1963. http://dx.doi.org/10.1016/0017-9310(63)90119-4

[64] R. Jenkins, "Variation of the eddy conductivity with prandtl modulus and its use in prediction of turbulent heat transfer coefficients," in Heat Transfer and Fluid Mechanics Institute, vol. 147. Stanford University Press Stanford, California, 1951.

[65] W. Kays and E. Leung, "Heat transfer in annular passages—hydrodynamically developed turbulent flow with arbitrarily prescribed heat flux," International Journal of Heat and Mass Transfer, vol. 6, no. 7, pp. 537–557, 1963.

[66] Verein Deutscher Ingenieure, Ed., VDI-Wärmeatlas, 10th ed. Berlin: Springer, 2013. http://link.springer.com/book/10.1007%2F978-3-642-19981-3

[67] P. Böckh and T. Wetzel, Wärmeübertragung. Springer Berlin Heidelberg, 2017.

[68] M. Kant, "Design of heat transfer components for the liquid-metal-cooled sommer demonstration plant." Master Thesis, Mechanical Engineering Department at Karlsruhe Intitute of Technology KIT, Jul. 2013.

[69] J. Fink and L. Leibowitz, Thermodynamic and Transport Properties of Sodium Liquid and Vapor. 9700 South Cass Avenue, Argonne, Illinois 60439: Argonne National Laboratory, Jan. 1995, no. ANL/RE-95/2. http://www.ne.anl.gov/eda/ANL-RE-95-2.pdf

[70] Duffie and Beckman, Solar Engineering of Thermal Processes -. New York: John Wiley & Sons, 2013.

[71] "Evaluation of measurement data – guide to the expression of uncertainty in measurement," online, Joint Committee for Guides in Metrology (JCGM/WG 1), 2018. https://www.bipm.org/utils/common/documents/jcgm/JCGM_100_2008_E.pdf

[72] G. Moumin, “Aufbau optischer komponenten eines solarofens,” Master’s thesis, Faculty for chemical and process engineering, Karlsruher Institut für Technologie, March 2015.

[73] J. Pacio, “Calibration of thermal losses and offsets at the sommer receiver,” Mar. 2019, technical Report KALLA-INT-2019-01, unpublished.

[74] M. Röger, P. Herrmann, S. Ulmer, M. Ebert, C. Prahl, and F. Göhring, “Techniques to measure solar flux density distribution on large-scale receivers,” Journal of Solar Energy Engineering, vol. 136, no. 3, p. 031013 (10 pages), May 2014. https://doi.org/10.1115/1.4027261

[75] R. Gardon, “An instrument for the direct measurement of intense thermal radiation,” Review of Scientific Instruments, vol. 24, no. 5, pp. 366–370, May 1953. https://doi.org/10.1063/1.1770712

[76] E. Guillot, I. Alxneit, J. Ballestrin, J. L. Sans, and C. Willsh, “Comparison of 3 heat flux gauges and a water calorimeter for concentrated solar irradiance measurement,” Energy Procedia, vol. 49, pp. 2090–2099, 2014. https://doi.org/10.1016/j.egypro.2014.03.221

[77] E. Schmidt, “Device for the measurement of heat,” Munich, 03 1925. https://patents.google.com/patent/US1528383

[78] U. Groer and A. Neumann, “Development and test of a high flux calorimeter at DLR cologne,” Le Journal de Physique IV, vol. 09, no. PR3, pp. Pr3–643–Pr3–648, Mar. 1999. https://doi.org/10.1051/jp4:19993102

[79] S. Ulmer, Fortschritt-Berichte VDI: Messung der Strahlungsflussdichte-Verteilung von punktkonzentrierenden solarthermischen Kraftwerken. VDI Verlag, 2004.

[80] CNRS, “Report on flux measurement for users,” SFERA Solar Facilities for the European Research Area, Seventh Framework

Programme, Seventh Framework Programme – Project Delivarable Grant Agreement No 228296 – R12.13, 2013, date last accessed Nov. 16, 2020. http://sfera.sollab.eu/downloads/JRA/WP12/Deliverable_R12.13_Guidelines_on_flux_measurement_for_user.pdf

[81] J. J. Singh and R. R. Antcliff, Eds., The 1992 NASA Langley Measurement Technology Conference, no. NASA-CP-3161. Hampton, Virginia: NASA, April 1992. https://ntrs.nasa.gov/search.jsp?R=19930004473

[82] O. Yorgev, P. Gleckman, and M. Rozler, "High-heat solar flux scanner," Sep. 15-18, 2009, solar Paces Conference, Berlin.

[83] J. Ballestrín, S. Ulmer, A. Morales, A. Barnes, L. Langley, and M. Rodríguez, "Systematic error in the measurement of very high solar irradiance," Solar Energy Materials and Solar Cells, vol. 80, no. 3, pp. 375 – 381, 2002. http://www.sciencedirect.com/science/article/pii/S0927024803001922

[84] I. Pardoe, Applied regression modeling, 2nd ed. Hoboken, NJ: Wiley, 2012, includes bibliographical references (p. [309]-313) and index. - Description based on print version record.

[85] K. Ziouche, P. Godts, Z. Bougrioua, C. Sion, T. Lasri, and D. Leclercq, "Quasi-monolithic heat flux microsensor based on porous silicon boxes," Sensors and Actuators A: Physical, vol. 164, no. 1-2, pp. 35–40, Nov. 2010. https://doi.org/10.1016/j.sna.2010.09.015

[86] J. E. Pacheco, "Final test and evaluation results from the Solar Two project," Sandia National Laboratories, Albuquerque, New Mexico 87185 and Livermore, California 94550, Tech. Rep. SAND2002-0120, Jan. 2002.

[87] E. Camacho and C. Bordons, Model Predictive Control. Springer, 2003.

[88] D. Mayne and J. Rawlings, Model Predictive Control: Theory and Design. Nob Hill Publishing, 2013.

[89] A. Meaburn and F. Hughes, "A simple predictive controller for use on large scale arrays of parabolic trough collectors," Solar Energy, vol. 56, no. 6, pp. 583 – 595, 1996. http://www.sciencedirect.com/science/article/pii/0038092X96000035

[90] E. Camacho, M. Berenguel, and F. Rubio, Advanced control of solar plants. Springer Berlin, 1997.

[91] M. Mokhtar, "Control of solar thermal linear fresnel collector plants in single phase and direct steam generation modes," Ph.D. dissertation, KIT-Fakultät für Maschinenbau, Karlsruhe, 2018.

[92] C. M. Cirre, M. Berenguel, L. Valenzuela, and E. F. Camacho, "Feedback linearization control for a distributed solar collector field," Control Engineering Practice, vol. 15, no. 12, pp. 1533 – 1544, 2007. http://www.sciencedirect.com/science/article/pii/S096706610700055X

[93] P. Ushakov, A. Zhukov, and N. Matyukhin, "Heat transfer to liquid metals in regular arrays of fuel elements," High Temperature (USSR), vol. 15, no. 10, pp. 1027–1033, 1978. http://www.osti.gov/scitech/servlets/purl/7030158

Publications by Jonathan Flesch

FLESCH, J ; FRITSCH, A ; CAMMI, G ; MAROCCO, L ; FELLMOSER, F ; PACIO, J ; WETZEL, T: Construction of a Test Facility for Demonstration of a Liquid Lead-bismuth-cooled 10 kW Thermal Receiver in a Solar Furnace Arrangement - SOMMER. In: Energy Procedia 69 (2015), 1259 - 1268. http://dx.doi.org/http://dx.doi.org/10.1016/j.egypro.2015.03.157. – DOI http://dx.doi.org/10.1016/j.egypro.2015.03.157. – ISSN 1876–6102. – International Conference on Concentrating Solar Power and Chemical Energy Systems, SolarPACES 2014

FLESCH, J ; MAROCCO, L ; A.FRITSCH ; NIEDERMEIER, K ; WETZEL, T: Entropy generation minimization analysis of Solar Salt, sodium and lead-bismuth eutectic as high temperature heat transfer fluids. In: Asme J. Heat Transfer (sumbitted)

FLESCH, J ; NIEDERMEIER, K ; FRITSCH, A ; MUSAEVA, D ; MAROCCO, L ; UHLIG, R ; BAAKE, E ; BUCK, R ; WETZEL, T: Liquid metals for solar power systems. In: IOP Conference Series: Materials Science and Engineering 228 (2017). https://doi.org/10.1088/1757-899x/228/1/012012

FRITSCH, A ; FLESCH, J ; GEZA, V ; SINGER, C ; UHLIG, R ; HOFFSCHMIDT, B: Conceptual Study of Central Receiver Systems with Liquid Metals as Efficient Heat Transfer Fluids. In: Energy Procedia 69 (2015), Mai, 644–653. http://dx.doi.org/10.1016/j.egypro.2015.03.074. – DOI 10.1016/j.egypro.2015.03.074

MAROCCO, L ; CAMMI, G ; FLESCH, J ; WETZEL, T: Numerical analysis of a solar tower receiver tube operated with liquid metals. In: International Journal of Thermal Sciences 105 (2016), 22 - 35. http://dx.doi.org/http://dx.doi.org/10.1016/j.ijthermalsci.2016.02.002. – DOI http://dx.doi.org/10.1016/j.ijthermalsci.2016.02.002. – ISSN 1290–0729

NIEDERMEIER, K ; FLESCH, J ; MAROCCO, L ; WETZEL, T: Assessment of thermal energy storage options in a sodium-based CSP plant. In: Applied Thermal Engineering 107 (2016), Aug, 386-397. http://dx.doi.org/10.1016/j.applthermaleng.2016.06.152. – DOI 10.1016/j.applthermaleng.2016.06.152. – ISSN 1359–4311

NIEDERMEIER, K ; MAROCCO, L ; FLESCH, J ; MOHAN, G ; COVENTRY, J ; WETZEL, T: Performance of molten sodium vs. molten salts in a packed bed thermal energy storage. In: Applied Thermal Engineering 141 (2018), aug, 368–377. http://dx.doi.org/10.1016/j.applthermaleng.2018.05.080. – DOI 10.1016/j.applthermaleng.2018.05.080

SCHÖTTL, P ; BERN, G ; ROOYEN, D. W. ; FLESCH, J ; FLURI, T ; NITZ, P: Efficient modeling of variable solar flux distribution on Solar Tower receivers by interpolation of few discrete representations. In: Solar Energy 160 (2018), jan, 43–55. http://dx.doi.org/10.1016/j.solener.2017.11.028. – DOI 10.1016/j.solener.2017.11.028

Conference contributions - Talks

J. Flesch, A. Fritsch, L. Marocco, G. Cammi, F. Fellmoser, Th. Wetzel, Construction of a test facility for the demonstration of a liquid lead-bismuth-cooled 10kW thermal receiver in a solar furnace arrangement SOMMER (Talk), Solar Paces Conference 19.09.2014

Conference contributions - posters

1. J. Flesch, L. Marocco, Th. Wetzel, Design of the SOMMER Loop – LBE as fluid in concentrating solar power plants (Poster) LIMTECH PHD-Symposium 22.-23.07.2014, Dresden
2. J. Flesch, K. Niedermeier, P.Dan, G. Cammi, L. Marocco, H.Piecha, th. Wetzel, B2: The SOMMER plant – Preliminary design studies of the thermal receiver (Poster), LIMTECH Jahrestreffen, 10.11.2014, Ilmenau
3. J. Flesch, K. Niedermeier, P.Dan, G. Cammi, L. Marocco, H.Piecha, th. Wetzel, Design of the AVANTI test section – Measurement of heat transfer coefficients in Lms (Poster), LIMTECH Jahrestreffen, 10.11.2014, Ilmenau
4. J. Flesch, K. Niedermeier, L. Marocco, Th. Wetzel, Liquid metals vs. Solar Salt performance – High vs. Low Prandtl number fluids (Poster), LIMTECH PhD summerschool, 30. Juni–1. Juli 2015, Karlsruhe
5. J. Flesch, K. Niedermeier, F. Fellmoser, A. Jekel, K. Wittemann, L. Marocco and Th. Wetzel, Tdesign of a liquid metal-cooled solar thermal receiver (Poster), LIMTECH Midterm evaluation, 30. September 2015, Dresden-Rossendorf
6. L. Marocco, J. Flesch, K. Niedermeier and T. Wetzel, Numerical investigation of turbulent forced convection to liquid metal flowing inside the receiver tube of a solar tower (Poster), SolarPACES conference, 13.–16. Oktober 2015, Kapstadt, Südafrika
7. J. Flesch, K. Niedermeier L. Marocco and Th. Wetzel, Tmeasurement of the thermal efficiency of the LBE-cooled receiver in the SOMMER facility (Poster), LIMTECH PhD Summer School, 12.–13. Juli 2016, Ilmenau

8. J. Flesch, G. Moumin, J. de Geus K. Niedermeier, F. Fellmoser, A. Jekel, K. Wittemann, L. Marocco, th. Wetzel, HFM-based device for the measurement of high solar heat flux densities with superimposed linear and rotational scanning motion (Poster), SolarPACES conference, 11.–14. Oktober 2016, Abu Dhabi, UAE

9. K. Niedermeier, J. Flesch, L. Marocco and Th. Wetzel, The current state of the SOMMER project (Poster), LIMTECH Jahrestreffen, 3.–4. November 2016, Freiberg

10. J. Flesch, K. Niedermeier, A. Fritsch, D. Musaeva, L. Marocco, R. Uhlig, E. Baake, R. Buck and Th. Wetzel, Liquid metals for solar power systems (Poster), LIMTECH-Symposium, 19.–20. September 2017, Dresden-Rossendorf

Posters and talks for public interest

1. Flüssigmetalle für solarthermische Kraftwerke - Das Projekt SOMMER (SOlar furnace with Molten MEtal-cooled Receiver), KIT im Rathaus,31.01.2018, Karlsruhe

2. J. Flesch, Th. Wetzel und das KALLA-Team, Hell, heiß, effizient: Flüssigmetalle und thermische Solarkraftwerke, Nacht der Wissenschaften, 30.01.2016, Kalrsuhre, KIT

Students supervised and co-supervised (marked *) by Jonathan Flesch

ALBRECHT, K: Messung der Leistung konzentrierter Solarstrahlung in einem Sonnenofen, Master Thesis, 2016

DAN, P: Aufbau zur experimentellen Bestimmung des Wärmeüberganges in einer Rohrströmung mit niedriger Pr-Zahl bei einer inhomogenen Randbedingung, Diploma Thesis, 2015

DEGEUS, G: System zur Flussdichtemessung in einem Sonnenofen, Master Thesis, 2015

EMMENDÖRFER, F: *Bestimmung des Wärmeübergangs in einer Glattrohrmessstrecke bei Durchströmung mit Flüssigmetall, Bachelor Thesis, 2015

JIPA, A: Messung der Leistung konzentrierter Solarstrahlung in einem Sonnenofen, Diploma Thesis, 2017

MICHALAK, A, 2-month internship: Ontario-Baden-Württemberg (obw) Summer Exchange Program, 2017

MOUMIN, G: Aufbu optischer Komponenten eines Solarofens, Master Thesis, 2015

VILLARI, B: Concepts for indirect thermal energy storage systems with liquid metals as heat transfer fluids, Bachelor Thesis, 2013

A Appendix

A.1 Expression of uncertainty

Throughout this work the 'Guidelines for the Expression of Uncertainty in Measurement '(JCGM 100:2008 GUM 1995 with minor corrections) [71] are followed.

Accordingly, for a randomly varying quantity q the arithmetic mean $\bar{q}$ of n independent observations q_k can be used as best estimate of the expected value μ_q. Due to the random variations the values of the q_k differ. The variance σ^2 of the normal probability distribution of q can be approximated by the experimental variance s^2. Its positive square root is called the experimental standard deviation $s(q_k)$. The variance of the mean $\sigma^2(\bar{q}) = \sigma^2/n$ is best estimated by:

$$s^2(\bar{q}) = \frac{s^2(q_k)}{n}, \tag{A.1}$$

and called the experimental variance of the mean. Its positive square root is called the experimental standard deviation of the mean $s(\bar{q})$. This value quantifies 'how well $\bar{q}$ estimates the expectation μ_q of q'[71]. In the guide, when determined from n independent observations, for convenience this parameter is written $u(x_i) = s(\bar{X}_i)$ and called *Type A standard uncertainty*. When evaluated by scientific judgment, $u(x_i)$ is called *Type B standard uncertainty*.

Statistically about 68% of samples of a measurement with normally distributed random error reside within a range of the standard deviation above

and below the expected mean. If this range is doubled in size, about 95% of all samples will reside within this range, that is, the '95% confidence interval'.

A.2 Heat flux measurement

A.2.1 Existing concepts

There exist indirect and direct measurement methods for the determination of solar flux – and measurement augmented simulation methods [74].

Indirect Methods

The method of camera-recording the visible reflection of a flux distribution on a white target surface is called 'indirect'. The recorded variation in brightness corresponds to the variation in the local flux intensity according to a functional relationship, which depends on the reflective properties of the target and on camera properties ranging from the camera sensor's linearity in brightness detection, image distortion of the lens and spectral transmittance of grey filters to observable dark current. As a benefit of these methods, the high resolution CCD sensors in the cameras result in high resolution images of the flux distribution.

Besides a well-characterized camera, a flux gauge is typically required on the target plane in order to tie a local, directly measured reference flux reading of this sensor to the corresponding, indirectly measured local brightness value from the camera.

Radiometers or calorimeters can be used as the flux gauges. Radiometers use the generation of an electromotive force due to temperature differences in two connected junctions of two different types of metal as measurement principle, for example as described by Gardon [75].

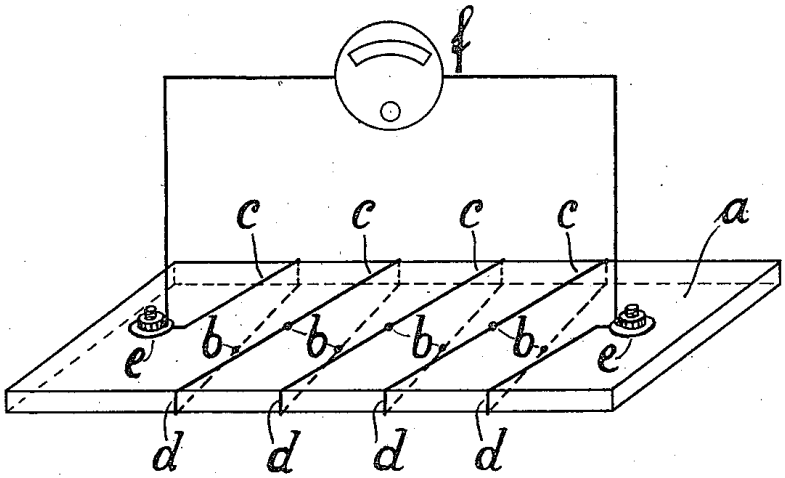

Figure A.1: Thermopile arrangement according to Schmidt's 1925 patent [77] where *a* is a thermal resistor, *b* junctions between wires of two different metals *c* and *d*, the wire ends,*e*, with a voltage proportional to heat flux along to the surface normal, measurable by a volt-meter, *f*.

Often for solar heat flux measurement, commercially available Gardon-type radiometers by Vatell are applied. These have a relatively short response time of a little less than one second [76]. They are available with water-cooling. Vatell's radiometers have a cylidrical shape with a diameter between 7.9 mm to 25.4 mm.

One particular way of utilizing the electromotive force for solar flux measurement is the thermopile arrangement, that is, several thermocouple-junctions arranged in series on opposite sides of a thermal resistor as shown in Figure A.1 [77].

The resulting temperature difference on both sides of that resistor is proportional to the heat flux passing through the thermal resistor. The resulting temperature difference causes a potential difference between all the thermocoule junctions which add up to a measureable voltage. Thermopiles by

Vatell used in their Heat Flux Microsensors (HFM), are manufactured using thin-film process technology for micro-process manufacturing such as sputtering. The resulting very thin layers for the metal junctions and the thermal resistor minimize thermal inertia and a high areal density of thermocouple junctions can be obtained. That way, although only small temperature differences along the thermal resistor occur due to its small thickness a μV signal is obtained, which can be measured with good accuracy. These sensors are very fast and have theoretical reaction time constants of as little as $\tau = 300\,\mu s$.

The second general type of flux gauges, the calorimeters, measure the temperature increase of a known coolant mass flow absorbing the radiation energy of the light. That temperature increase is proportional to the collected energy.

Calorimeters for solar flux measurement reported in literature are often specially designed for their use in specific facilities, such as the water cooled SunCatch calorimeter developed ad DLR [78]. That particular device's circular aperture has a diameter of 15.85 mm and has a response time of at least a few seconds [76]. They are therefore quite large, especially in relation to SOMMER's receiver dimensions.

The white target in indirect approaches requires Lambertian properties, that is, the reflective properties of the white surface reproduce the local brightness with negligible influence of the viewing angle of the camera. Target coatings can approximate Lambertian properties; they do, however, show a slight angular and temperature dependency in their reflectance values [79]. The latter effect must be compensated by active cooling if a target is supposed to remain in the focal point during measurement. The angular dependency is particularly relevant in the solar furnace where incidence angles of up to 52° to the absorber surface's normal are present. Also Lambertian properties deteriorate over time due to soiling [74].

While a large, actively cooled target could be applied covering the entire distribution, also, moving bar Lambertian targets are sometimes applied. These targets cover an area smaller than the flux distribution that is to be measured and are actively moved across it in a matter of seconds. During this short period the camera takes several images as the target progresses across the distribution. These single images are then stitched together to the complete distribution during post-processing.

Because of a shorter exposure to high flux of a moved target active cooling is not required. The required reference flux gauge cannot be placed on the bar if it has a long response time but has to be placed in the receiver plane and be actively cooled. This results in an offset between measurement plane (where the bar moves) and receiver plane (where the gauge is placed). The error introduced from this offset grows with their relative distance.

Ulmer [79] reports significant differences between values in the measurement plane and those actually expected on the receiver plane during a ray-tracing simulation of a large-scale receiver when that distance is large. The distance between possible measurement plane and absorber plane in the solar furnace of SOMMER is larger than the absober surface's diagonal; that is very large considering the wide angular range of incoming ray trajectories. Also the placement of an actively cooled sensor in the receiver of SOMMER is not possible due to the space limitation.

Accordingly, the moving bar approach could only work if a fast reference flux gauge is installed on the moving bar Lambertian target.

Direct Methods

Stationary direct methods use at least one flux sensor mounted in the measurement plane that directly measures the local flux value at its position with a high accuracy. In this case ideally the measurement plane equals the receiver plane in flat panel receivers (such as the SOMMER receiver) or the

aperture plane in case of cavity receivers. If more than one sensors are distributed across the measurement plane a coarse distribution of flux can be determined; however, in order to obtain highly resolved information on the flux distribution a large number of sensors is required and the corresponding investment and maintenance have to be considered.

Also reported in literature are moving direct methods where several flux sensors are mounted along a bar that is traversed through the flux distribution. Such a system was, for example, applied on the SSPS-CRS tower at the Plataforma Solar de Almería (PSA) [80]. For this approach either fast sensors are required in order to avoid overheating of the moving bar by reducing exposure to flux to a short time or active cooling is required when a slower traversing speed is applied to allow for sensors with a slower response time.

In the SSPS case eight HFM sensors were aligned on a straight rotor that traversed across the receiver with its center of rotation well below the center of the receiver (like a wind shield wiper). From the sensors' readings the distribution of flux on the aperture was interpolated. The plane in which that rotor moved was a slight distance away from the absorber plane, which in this case was a small distance relative to the receiver area.

The moved direct option obtains a reasonably good accuracy only with a rather large number of sensors (eight in case of the reference). This causes high investment costs as each sensor is expensive and multi-channel fast data acquisition technology and a precise measurement of the bar's angle is required. The mechanical setup is rather simple. A larger number of sensors requires maintenance effort in case re-calibration is frequently required. Post-processing requires interpolation and integration routines that are readily available in many data processing software packages and potentially the application of corrections from individual sensors' calibrations.

A.2.2 Data acquisition

In the SOMMER experiment data acquisition is performed by a PC with a PCI express Multifunction I/O Device NI-PCIe-6341 by National Instruments and a matching SCB-68 connector block.

This I/O device features 16 analog 16-bit input, single ended channels with 500 kilo-samples per second, two analog outputs channels with 900 kilo-samples per second, 24 digital input-output multi-function channels and 4 32-bit counter channels for linear and angular position encoders.

The stated input sample rate is not specified per-channel and accordingly, the per-channel rate depends on the number of input channels used.

The HFM device outputs differential signals for the heat flux and sensor temperature, which, when measured differentially use 4 out of 16 analogue input channels. The three thermocouples for the observation of the rod's temperature each provide differential signals as well, using up another 6 channels.

The angular position of the rotor is determined by an digital encoder with defined angular increments that are counted based on an A-B-Z pulse pattern[1] provided by the angular encoder by WayCon. Based on the coordinate system defined in Figure 4.23 on page 125 for operation a negative, clockwise direction of rotation was implemented. Zero degrees of rotation is located on the positive X-axis. A voltage $U = 5\,\mathrm{V}$ is provided by the I/O device for both, the angular and the linear encoder (manufactured by

[1] The periodic pulses A and B have a 90° phase shift where one completed period of both signals indicates a single angular increment. The device used generates 3600 increments per revolution, that is, a angular resolution of one tenth of a degree per pulse.
The NI device also allows to count each edge of the A and B pulse separately; that increases the resolution further by the factor of four. The Z pulse indicates a complete revolution. Because of this, for the determination of an absolute angular position, an initialization with the Z pulse is required. One of the NI device's digital counters is occupied by the A,B and Z pulse signal. The second counter is occupied by the linear encoder, which uses the same encoding as well as a 5 V voltage, however, with a resolution of 0.1 mm per increment. The Z pulse indicates an increment of 5 mm.

ELGO) which uses a magnetic tape for the measurement of the progress in X direction.

For each measured sample of the flux scanner besides the voltages from heat flux and temperature measurement thus also the X position of the system's center of rotation and the current angle are measured. Given the radius of rotation of 50 mm the current, k^{th}, position in a Cartesian X-Y-plane is calculated according to:

$$X_k = x_k + 0.05 \cdot \cos(\varphi_k), \tag{A.2}$$

$$Y_k = 0.05 + 0.05 \cdot -\sin(\varphi_k). \tag{A.3}$$

An AMP-10 signal amplifier by Vatell is used in this setup for the amplification of the HFM sensor voltage signals. This amplifier is readily equipped with two separate gain switches for the resistance thermal sensor (RTS) signal and the heat flux sensor (HFS) signal as well as matching two-channel (four-pin) LEMO input plug. Also, a calibration certificate is provided with precisely specified gain factors for each gain value. This amplifier readily generates the excitation current for the voltage measurement on the thermal sensor's resistor.

It also offers manual zero-offset compensation. Due to changes in room temperature and body temperature of the amplifier the HFS and RTS voltages can deviate slightly from zero even at zero heat flux at the beginning of a measurement. For this reason the manual recommends to let the case temperature stabilize for eight minutes after switch-on before using the manual compensation. With a screw on the amp casing the observed offset can be manually removed.

Table A.1: Signal amplification and scale settings. Best parameters for the present case are marked with *.

device	parameter	range/value	abs. accuracy	rel. accuracy
NI card	signal scale	± 0.2 V*	60 µV	–
	signal scale	± 1 V	240 µV	–
	signal scale	± 5 V	1130 µV	–
Vatell amp	gain setting	1*	–	± 0.6 %
	gain setting	100	–	± 1.5 %

A.2.3 User interface

The operation of the flux scanner is controlled through a LabView user interface. It is used to set measurement parameters, to run the measurement, run the extension and retraction drive of the system and to write the measured data to a data file. Also the signal amplification factors settings of the amplifier have to be specified. The recommended setting, as was used during the calibration campaign in Cologne, is a gain of 100 for both channels.

During that campaign, where maximum flux density values of about 2.4 MW m^{-2} occured, a maximum voltage of the HFS signal of 8.9 mV and of the RTS signal of 5.6 mV were generated by the sensor. Depending on the expected input signal range a scale width for the measurement can be specified in LabView with limits of 0.2 V,1 V, 5 V and 10 V, each associated with different measurement uncertainty, as listed in Table A.1.

If amplified with a gain of 100 the 5 V scale needs to be selected, where an absolute uncertainty of 1130 µV occurs from the NI device, that is 0.13 % relative uncertainty for the HFS signal, where, however, the amplifier introduces an uncertainty of 1.5 %.

The 1 V scale is too narrow at a gain of 100 in case peak flux values higher than in Cologne occur.

If un-amplified that signal can be measured with the 0.2 V signal scale width by the NI device with an absolute uncertainty of 60 µV, that is, 0.6 % relative uncertainty. An additional 0.6 % uncertainty from the amplification occurs at the corresponding gain of 1.

A gain of 1 would, therefore, generate the lowest uncertainty[2]. Nevertheless, since the calibration was performed with a gain value of 100, a gain setting of 100 both for HFS and RTS signal is applied throughout the SOMMER experiment.

The LabView program aborts if prior to the generation of the measurement file the rotating motor is not running. This is a safety precaution since a sensor passage through the focal point without rotation generates a flux exposure with a rapid temperature increase that can destroy the sensor. On the other hand, when rotating, the residence time in the maximum of the flux distribution is short and followed by a comparably long residence time at the periphery of the flux distribution where the collected heat can be conducted away from the sensor to the copper body, thus limiting the temperature increase.

Thus, the linear drive can only be started when rotation is detected.

Upon the starting command the linear motor will automatically fully extend and retrace. The raw voltage values of HFS and RTS signal are stored to a data file, with the amplification factors provided in the header.

The data evaluation including the calculation of total absorbed power and peak flux value is performed with a Matlab script.

[2] If an option is available to operate the RTS resistance thermal sensor without the amplifier its use could be avoided all together at such high fluxes, however at the expense of the manual zeroing option. Zeroing could then just as well be performed digitally.

A complete measurement with the settings used for the calibration in Cologne takes about 8 s, where half of that time the sensor's center of rotation moves outward until the entire measurement plane has been passed and the remaining time it moves inward, completely passing the distribution again.

Picturing the sensor's path as a circle that is moved forward through the distribution each point in the distribution is passed two times by the sensor during the extension of the linear motor: First when the front semi-circle passes and again, when the rear semi-circle passes it. The same occurs in reversed order during inward drive. Since the motion in reality equals a spiral and not a circle, not all points of the distribution are reached by the sensor, but instead many are passed nearby.

The evaluation script therefore allows for the user to chose the different data segments for evaluation: All data can be evaluated simultaneously. That is, the interpolation of the distribution's shape is based on four stacked data sets. This creates a single image of an 8 second time frame. This case is shown in the bottom right graph in Figure A.2. Should, however, during this time frame the focal point have moved (for example due to wind hitting the heliostat), the measured distribution will 'smear' and appear larger than the original. Therefore, data of the forward drive and data of the backward drive can be evaluated separately (= recommended default), so that only a four second time frame is visualized, where still the sensor has passed the distribution two times, each. This case is shown in the bottom left graph in Figure A.2.

Furthermore, during forward drive the scan of the distribution can be divided into the data on the semi-circular front fraction (top left graph) of each revolution and into the rear fraction (top right graph). The same applies during the inward drive of the linear motor. Thus, four individual measurements of each point of the distribution are recorded during a single run, however, each of them is based on a coarse grid of measured data.

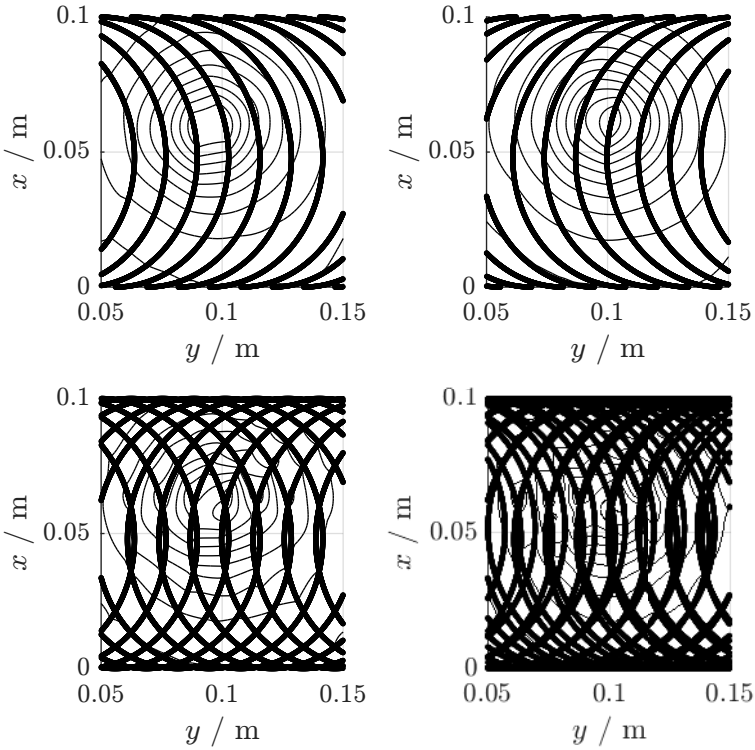

Figure A.2: Top left: forward front semi circle, top, right: forward rear semi circle, bottom left: forward full circle, bottom right: all data.

Small changes in the DNI value during a measurement can be compensated during post-processing based on the DNI values that are logged by the SOMMER's data acquisition system.

A.2.4 Sources of uncertainty

The presented system's uncertainty of measurement results from uncertainty in the determination of the sensors location, the finite response time of the sensor quickly moving across a flux distribution and from thermal effects.

Errors in the determination of the exact place of the sensor can distort the recorded shape of the actual distribution. Besides random errors, also systematic errors from the rod's thermal expansion are present. Should the recording, for example, be systematically compressed by the rod's thermal expansion, the integration over the locally sampled power values will result in an over estimation of the total power because flux outside of the defined boundaries is included.

In the following the expansion is assessed which occurs in the rod's front section away from the fixed axle that is indicated in Figure 4.28 with the letter b.

The temperature increase during the return drive of a measurement performed during the calibration campaign in Cologne is shown in Figure A.3. For the complete run (including also the outward drive) a temperature increase the sensor itself (solid black line) from initial 60 °C by about 120 K was recorded with a total power of 6400 W. The rod's temperature right by the HFM sensor increased by about 80 K (red dashed line) and by only 30 K 150 mm away from the sensor (blue, dash-dotted line).

Under theses conditions the rod's average temperature remained below 100 °C. Given, that during operation in SOMMER a total power of 10800 W is expected, assuming an averaged temperature increase of $\Delta T = 150\,\mathrm{K}$ will most likely not be exceeded. The resulting thermal expansion ΔL_{Cu} is calculated for these conditions to:

$$\Delta L_{\mathrm{Cu}} = L \cdot \alpha_L \Delta T = 300\,\mathrm{mm} \cdot 1.6 \times 10^{-5}\,\mathrm{K}^{-1} \cdot 150\,\mathrm{K} = 0.72\,\mathrm{mm}, \quad \text{(A.4)}$$

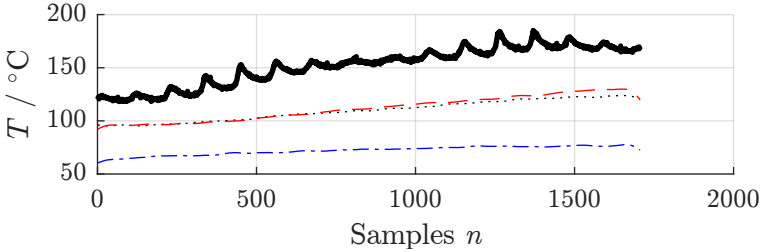

Figure A.3: Temperature increase during the return drive of a measurement at solar power of about 6400 W on the measurement plane. (filtered, every 30th value shown). Sensor face temperature: solid, black line; rod tip temperature: dashed red and black dotted line; rod temperature 10 cm away from the sensor

, where α_L is the coefficient of thermal expansion of copper.

Thermal expansion is the main source of uncertainty for the exact determination of the X coordinate (axial direction). Minor uncertainty in the measurement of the X position is introduced by the determination of the angular position from the angular encoder, the determination of the linear position from the linear encoder and very small uncertainties from the measurement of the length of the rotor and the amount of bearing clearance.

Uncertainty in the determination of the Y position stems mainly from uncertainties in the determination of angular position, rotor length measurement and bearing clearance and is thus smaller than that in X direction.

The thermal exchange of the sensor with the ambient and the copper rod by means of thermal radiation, convection and conduction introduces additional uncertainty.

Unfortunately, of the sensor only the design of the sensitive, circular sensor face is known with the thermo-pile located in its center and surrounded a platinum conductor which serves as resistance temperature sensor.

A sensor reading depends on the temperature difference between front and back of the thin thermal resistor that serves as substrate upon which the thermo couples junctions are sputtered. This temperature difference depends only on the heat flux and thermal conductivity of the resistor in axial direction. Radiation and convection losses on the sensor face influence the heat flux crossing the resistor. The capacity and conductivity of the heat sink underneath the resistor influence the temperature level at which this difference across the resistor is measured; this level is detected by the resistance thermal sensor and used to correct the resulting non-linearity between flux and ΔT.

The gradient across the thermal resistor is influenced only if a significant heat conduction in radial direction occurs. This appears in case of a poor axial thermal contact with a heat sink and a good thermal contact along the edge of the thermal resistor with the sensor body and the copper rod. However, the sensor is deposited directly upon the heat sink material during production (good thermal contact, indeed) and the thermal resistor layer with a diameter of 6.3 mm has a thickness of less than 1 µm [81]! In conclusion, axial conduction must be the dominating in the sensor face and thermal transport to the rod via conduction is very unlikely to influence the sensor reading.

The more relevant radiation losses to the ambient, which reduce the heat flux passing through the sensor, are a function of the sensor face temperature and the ambient temperature. It occurs during measurements from the hot sensor face only to the cold surroundings of the concentrating mirror, whereas from the sensor's point of view the mirror surface is filled out completely with the reflection of the sun from where it gains radiation energy.

In order to predict the lost power through radiation to the surroundings of the mirror the solid angle of its silhouette has to be subtracted from the sensor's total field of view. A view factor is then calculated which allows to estimate the lost power:

The projection of the mirror face can roughly be approximated with a square shape of height L_y and width L_x with $Lx = L_y = 4\,\mathrm{m}$, respectively in a distance from the sensor of $L_z = 1.9\,\mathrm{m}$. The sensor, although of circular shape with a diameter of $D = 0.006\,35\,\mathrm{m}$ is so small compared to the mirror that a negligible error in the calculation of a view factor results when a square shape is imposed upon it with $L_x = L_y = D$.

According to Ref. [66] with $L_y/L_z = 2.1$ and $L_x/L_z = 2.1$ the view factor from sensor (index i) to mirror (index j) is approximately $F_{i,j} = 0.6$. The remainder, $1 - F = 0.4$ is the sensor's view factor with the surroundings.

Then, the heat flux density on the sensor can be calculated according to:

$$q'' = (1-F)\sigma(T_{\mathrm{HFM}}^4 - T_{\mathrm{amb}}^4), \tag{A.5}$$

with $T_{\mathrm{amb}} = 25\,^{\circ}\mathrm{C}$ and the Stefan-Boltzmann constant σ.

For an estimated sensor face temperature of $200\,^{\circ}\mathrm{C}$ this results in a heat flux of $q'' = 957.5\,\mathrm{W\,m^{-2}}$. This loss is negligible at mean heat fluxes of more than $1\,000\,000\,\mathrm{W\,m^{-2}}$, even in case the sensor temperature is higher.

Mixed convection losses are influenced also by the rotational speed. Due to the rod's cylindrical shape, into which the sensor is smoothly embedded, convection losses will be assessed in this paragraph using a correlation for a hot cylinder in perpendicular flow is selected. An angular velocity of $\omega = 11.7\,\mathrm{s^{-1}}$ (tangential velocity $v = 0.59\,\mathrm{m\,s^{-1}}$) and linear velocity of $v = 0.0237\,\mathrm{m\,s^{-1}}$ have been applied. The copper rod, which has the sensor embedded into it, periodically moves on its circular path up and down in Y direction. In this situation the highest convective losses are expected. As mentioned, the rod's temperature is usually below that of the sensor. Nevertheless, for a conservative estimation of the convective losses it is assumed that the rod's temperature equals the sensor's temperature, which attains much higher values. Then, the Nusselt number for the rod can be calculated

by correlations for mixed convection. Finally the average heat transfer coefficient obtained from this correlation is applied to the surface area of the sensor face in order to calculate the losses.

A correlation according to [66] is applied for a horizontal cylinder in perpendicular flow. This results in a combined natural and convective heat transfer coefficient of $h = 18.9\,\mathrm{W\,m^{-2}\,K^{-1}}$. For a sensor temperature of $T = 200\,^{\circ}\mathrm{C}$ and an ambient temperature of $T_{\mathrm{amb}} = 25\,^{\circ}\mathrm{C}$ the resulting heat flux is $q'' = 3310\,\mathrm{W\,m^{-2}}$.

Although this loss mechanism is more relevant than thermal radiation it is still negligible at design conditions compared to the average incident solar heat flux and remains well below one percent.

Finally, conductive heat transfer in the rod is present whenever the sensor's temperature has been raised by exposure to heat flux. Due to its black coating its absorptance value is much higher than that of the surrounding copper volume and the sensor's temperature is raised more significantly at transit through high flux areas. Once that area is passed the sensor is periodically moved to low-flux areas where heat transfers from the sensor to the rod along the previously generated temperature gradient.

Ultimately, the heat will be conducted from the sensor face to the copper rod. The exact path of conduction is, however, unknown and will not influence the measurement. If minor effects arise, those will be accounted for during device calibration under conditions as expected during operation in the SOMMER furnace.

The original calibration of the sensor as delivered is usually performed at quasi-steady state conditions where body temperature and sensor face temperature are in equilibrium. In the target application, however, unsteady conditions are generated.

Yorgev at al. [82] report that the manufacturer's calibration, which is performed at around $350\,\mathrm{kW\,m^{-2}}$, delivers no correct readings for flux values

one order of magnitude larger as expected in SOMMER's solar furnace. Furthermore, as the manufacturer's calibration uses an electric graphite resistor at 850 °C [83] as black-body radiation source for that calibration the intensity maximum of its spectrum shifted to red compared to that of the sun.

Therefore, a correction factor, which can be calculated according to a procedure presented in Ref. [83], must be applied for the sensor to match the power in the solar spectrum. This procedure takes into account the different spectra of the sun and the graphite radiation source as well as the absorption and recflectance spectra of mirror surfaces and the Pyromark coating.

All required spectra are available in literature, each of them, however, containing some uncertainty, so that the accuracy of the correction factor is difficult to determine.

All these many sources of uncertainty and the difficulty of quantifying them separately make a calibration of the system with a good reference a requirement. That way, all accumulated uncertainty can that way be accounted for simultaneously.

A.2.5 Device calibration

The device was calibrated with reference measurements at the Xenon-High-Flux Solar Simulator of the German Aerospace Center (DLR) in Cologne. Reference measurements were taken with DLR's flux mapping acquisition system FMAS. FMAS is an indirect measurement system that uses a 8 bit grey scale CCD image of the flux on a aluminum-oxide-coated Lambertian target.

A reading of a Gardon-type calorimeter located on the target is used as reference flux gauge. This system overall acquisition uncertainty is stated by DLR to be below 3%.

For the calibration procedure flux from a varying number of Xenon lamps was directed onto a common aim point above a table with a 3-axis translation capability. DLR's water-cooled Lambertian target equipped with the radiometer and the KIT's flux scanner were mounted side-by-side on top of that table. With this table it was possible to first align the Lambertian target with the aim point of the lamps and to measure the present flux distribution and power with the FMAS system in order to obtain a reference value. Then, KIT's scanner was motioned into the aim point's vertical plane where it could measure the same distribution.

The FMAS generates measurement data in CSV files that contain the flux reading for each measured pixel in the image, as well as coordinate vectors based on a previously defined reference plane that specify each pixel's location. Flux values measured by the heat flux micro sensor at a defined set of coordinates can therefore be compared with the value obtained by FMAS at that same position. A.4 shows on the left the distribution obtained from reading a file of the FMAS measurement # 33 on a reference plane of 50 cm by 50 cm.

On the right of Figure A.4 the sensor path in forward motion (along the x-axis) of the flux sensor (orange line) across this distribution of concentrated heat flux is shown, this time the same distribution as in the left graph is indicated by a contour plot (black line).

On its path the sensor measures local values of the heat flux density. FMAS reference values along the sensor path are shown in Figure A.5. Due to the rotational motion pattern data measured by the HFM generally lie between data nodes of the regular grid of FMAS data. FMAS reference values are therefore obtained from the regular reference data nodes by creating linear interpolations[3] between data nodes of the FMAS CSV-file to locations where samples have been taken by the HFM sensor. During the calibration

[3] Matlab (R) 2016a, function `griddedInterpolant`

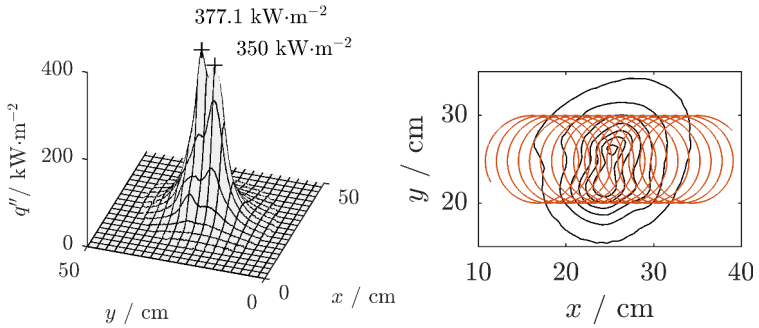

Figure A.4: Reference flux distribution.as measured by FMAS, DLR. The magnitudes of two local maxima of the distribution are indicated.

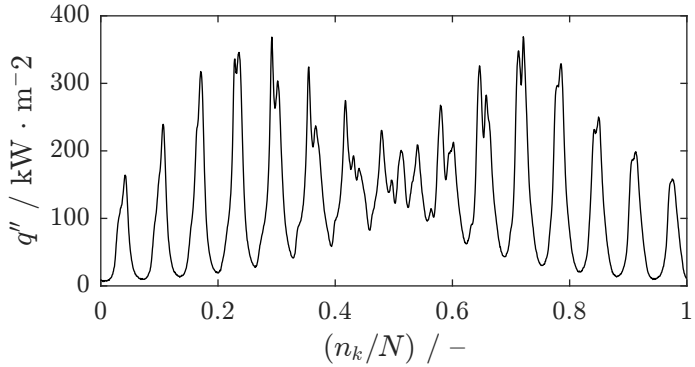

Figure A.5: Reference heat flux density values at normalized sample count (k'th sample n_k divided by the total number of samples N) for forward motion. (Every 30th data point is shown.)

fixed values for the rotational and linear speed of $\omega = 1.8642\,\mathrm{rad\,s^{-1}}$ and $v = 0.0232\,\mathrm{m\,s^{-1}}$, respectively, were applied .

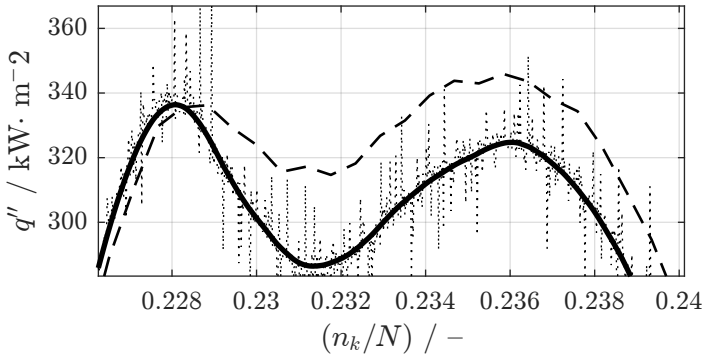

Figure A.6: Measured signal (dotted), filtered signal (thick solid) and reference signal (dashed).

Figure A.6 shows the filtered measured signal[4] of an arbitrary peak of the data set compared to the reference; there is a macroscopic difference in the shape of the measured and reference curve which results from experimental X and Y offsets between measurement plane and reference plane and from smoothing effects due to the sensor's motion velocity. This velocity generates smoothing due to the finite response time constant of the sensor and due to thermal forced convection losses. The remaining difference found in that figure is at the applied motion parameters nevertheless acceptably low, as will be shown next.

Heat flux values from the FHM are obtained by applying a calibration function which requires two different voltage values as inputs, $q''_{HFM}(U_{HFS}, U_{RTS})$. The measured data in Figure A.6 have been calculated accordingly (dotted linie). The 2D calibration function applied in this graph was determined by applying a surface fit of measured voltages (U_{HFS} and U_{RTS}) from the

[4] Compared to the reference signal the measured signal is noisy. The shown signal is therefore filtered for noise reduction using Matlab's `filtfilt` function This function can be configured to result in a zero-offset moving average filter. The Y values of 50 data points before and after the data point (x_i, y_i) are averaged to determine the value of the corresponding y_i-value in this evaluation.

Table A.2: Coefficients for calibration fit of flux density data and their 95% confidence bounds. Also shown: The coefficient of determination R^2 and the root mean square error RMSE

parameter	value	95% confidence bound	
		lower	upper
p_{00}	5.563	4.538	6.589
p_{10}	2285	2274	2295
p_{01}	-25.23	-35.67	-14.79
p_{11}	1463	1417	1510
p_{02}	-122.5	-155.5	-89.43
p_{12}	-2330	-2381	-2278
p_{03}	225.9	194.2	257.6
R^2	0.9984		
RMSE	$10.8737\,\mathrm{kW\,m^{-2}}$		

device's heat flux sensor (HFS) and resistance thermal sensor (RTS) to local heat flux data from the FMAS at DLR, q''_{ref}. The best fit fit for both, extending and retracing motion direction, was determined for a polynomial surface function of first degree of x and third degree of y of the form:

$$f(x,y) = p_{00} + p_{10}\cdot x + p_{01}\cdot y + p_{11}\cdot x\cdot y + p_{02}\cdot y^2 + p_{12}x\cdot y^2 + p_{03}\cdot y^3 \quad \text{(A.6)}$$

where x represents the HFS voltage, U_{HFS}, and y represents the RTS voltage, U_{RTS}.

The resulting coefficients as well as the coefficient of determination R^2 and the root mean square error RMSE are provided in Table A.2. The data and resulting surface are shown in Figure A.7. From the distribution it appears that the sensor's temperature sensitivity increases at growing tem-

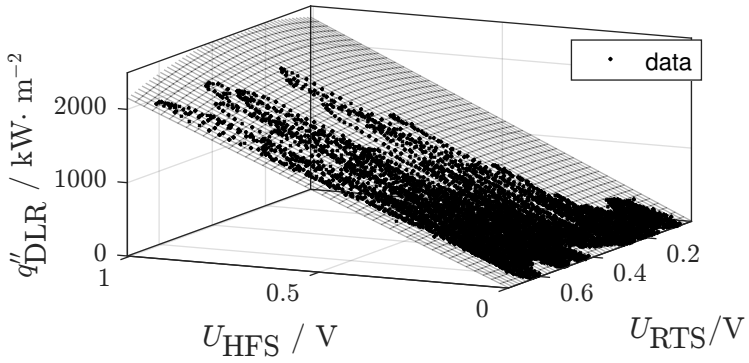

Figure A.7: Measured data (black dots) used for surface fit. Parameters of best fit are provided in Table A.2

peratures, whereas the sensitivity with respect to the heat flux remains rather constant. It it therefore advised to operate the sensor only within the temperature range obtained during this calibration. On the other hand, for higher fluxes than obtained during calibration, the prediction of the fit should be more reliable.

For the processing of data measured with the flux scanner a rectangular regular grid of the size of the measurement plane is defined with a horizontal resolution of $\Delta x = 2$ mm and a vertical resolution of $\Delta y = 1$ mm. The values at the regular nodes of the grid are interpolated using Matlab's `griddata` function from the measured values of the flux density $q''_{\mathrm{HFM},k}(x_k, y_k)$, which are irregularly distributed in this plane. In this case, interpolation is performed using the `'natural'` method; that is, a triangulation based natural neighbor interpolation. The result of this interpolation is shown in Figure A.8 in a contour plot.

Due to the grid resolution being coarser than the resolution of data points along the sensor path this interpolation has a filtering effect on the noise recorded during data acquisition.

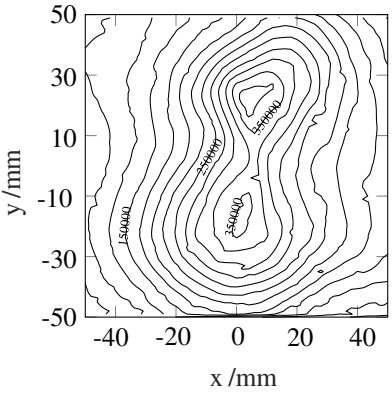

Figure A.8: Distribution of heat flux at DLR, $q''/\mathrm{W\,m^{-2}}$ as measured with the HFM sensor after post processing; Coordinates of the calibration setup at DLR, Cologne. Isoline spacing: $25\,\mathrm{kW\,m^{-2}}$; Total power: $\dot{P} = 2290.48\,\mathrm{W}$; peak flux density $q''_{\mathrm{max}} = 387.8\,\mathrm{kW\,m^{-2}}$

The total power is then obtained by numerical integration across this grid. The peak flux value is determined by a search of the maximum value on this grid.

During the calibration campaign in Cologne such distributions were recorded for seven different power levels. For different power levels, also the target coordinates for individual lamps of the solar simulator have been changed. The maximum flux value was, for example, obtained with one common aim point for all lamps used. For lower fluxes, such as in the previously shown distribution # 33 in Figures A.4 and A.8, two aim points were defined. These change of configuration were applied in order to validate the flux scanner's ability to scan differently shaped flux distributions.

On some power levels measurements were repeated. In total it was possible to obtain eleven measurements. These are summarized in Table A.3 where the reference total power and peak flux values for each successful measurement are provided. These data points are shown in Figure A.9.

Table A.3: Measured flux distributions during calibration campaign in Cologne

#	DLR reference		HFM forward drive		HFM backward drive	
	power	peak flux	power	peak flux	power	peak flux
	$\dot{P}_{\mathrm{ref}}$/W	q''_{ref}/kW m^{-2}	$\dot{P}_{\mathrm{HFM}}$/W	q''_{HFM}/kW m^{-2}	$\dot{P}_{\mathrm{HFM}}$/W	q''_{HFM}/kW m^{-2}
33	2100	377.8	2040.8	375.1	2090.5	387.8
34	2133	382.3	2040	384.4	2152.6	399.4
37	3174	739.3	2919.2	732.1	3062.2	773
38	3174	739.3	3072	721.6	3160.3	754.4
39	4633	1086.1	4593.4	1181.4	4806.5	1194
41	4633	1086.1	4709	1132.6	4786.4	1205.8
43	5622	1648.4	5600.8	1716.7	5577.9	1739.4
44	6080	2043.7	5704.7	2047.1	5946.6	2062.2
45	6080	2043.7	5952.8	2021.1	6023.7	2059.1
46	6080	2043.7	5975.2	2058.1	6031.3	2073.7
47	6493	2164.7	6322.2	2110.7	6368.3	2191

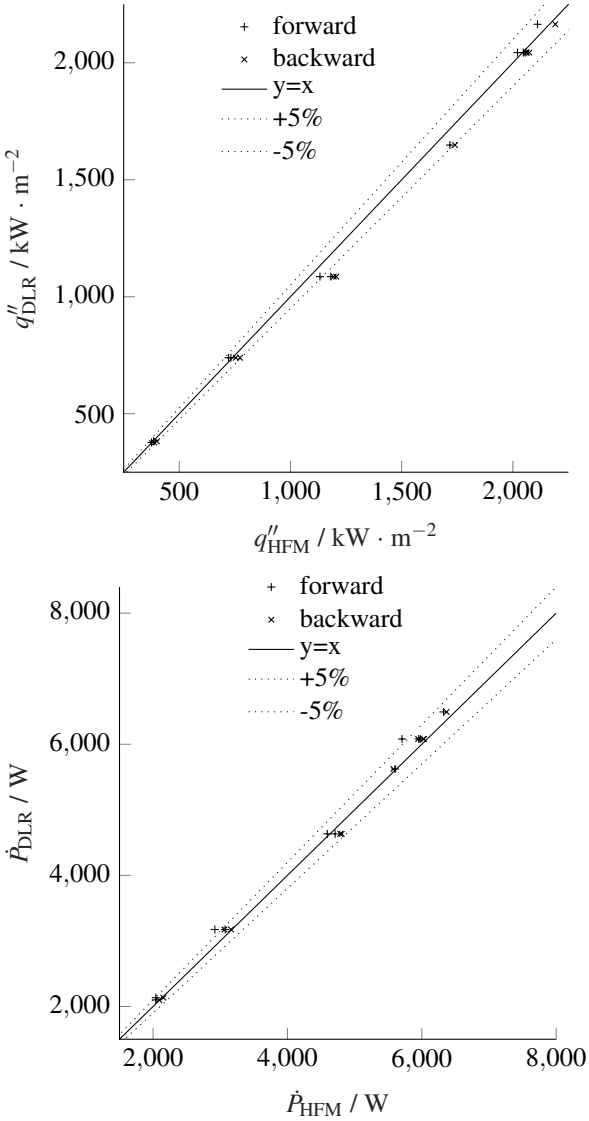

Figure A.9: Measured values for total power and peak flux density against their reference values.

The measured values with the manually identified calibration function (A.6) agree very well with the reference. The scattered only slightly crosses the $\pm 5\%$ margins. The powers and fluxes measured during forward drive are systematically slightly smaller than during backward drive as they are shifted to the left.

Based on these data, what is the measurement uncertainty for additional data points?

If all HFM measurements exactly equaled the reference values they would directly inherit the reference's uncertainty of 3% as reported by DLR. However, due to the scatter around the reference values additional uncertainty is present. This additional uncertainty results from all sources mentioned in the previous paragraphs.

According to GUM 2008 [71] the uncertainty of FMAS should be interpreted as a type B uncertainty, that is, it is not based on statistical information but on an experience.

In such case, where no information on the probability distribution is provided it shall be assumed that the real value may occur with constant probability in the entire interval of plus and minus a around the measured value, where from DLR it is reported that $a = 3\,\%$ for both, flux density and total power.

From this rectangular probability distribution the equivalent relative variance and standard deviation of a normal distribution of probability for, in this case the flux density q'' can be calculated according to GUM section 4.3.7. [71], respectively:

$$\frac{u^2(q''_{\mathrm{DLR}})}{q''^2_{\mathrm{DLR}}} = a^2/3 = 0.0003, \tag{A.7}$$

$$\frac{u(q''_{\mathrm{DLR}})}{q''_{\mathrm{DLR}}} = \sqrt{\frac{u^2(q''_{\mathrm{DLR}})}{q''^2_{\mathrm{DLR}}}} = 0.017, \tag{A.8}$$

and in the same manner for the total power.

In order to quantify the uncertainty of a FHM measurement that is additional to that of FMAS, a linear function b:

$$b(q''_{\mathrm{HFM}}) = y_1 + y_2 q''_{\mathrm{HFM}}, \tag{A.9}$$

shall be derived by a least square fit to the $N = 11$ independently measured offsets between HFM measurement and reference value,

$$b_k(q''_{k,\mathrm{HFM}}) = q''_{k,\mathrm{DLR}} - q''_{k,\mathrm{HFM}}. \tag{A.10}$$

By propagation of error, when Equation (A.10) is rearranged to isolate q''_{HFM}, the uncertainty in q''_{HFM} can be calculated according to:

$$u_c^2(q''_{\mathrm{HFM}}) = \left(\frac{\partial q''_{\mathrm{HFM}}}{\partial q''_{\mathrm{DLR}}}\right)^2 \cdot u^2(q''_{\mathrm{DLR}}) + \left(\frac{\partial q''_{\mathrm{HFM}}}{\partial b(q''_{\mathrm{HFM}})}\right)^2 \cdot u^2\left[b(q''_{\mathrm{HFM}})\right], \tag{A.11}$$

$$= u^2(q''_{\mathrm{DLR}}) + u^2\left[b(q''_{\mathrm{HFM}})\right]. \tag{A.12}$$

Since according to Equation (A.7), $u^2(q''_{\mathrm{DLR}})$ is known, it needs to be discussed how the uncertainty of the correction $u^2\left[b(q''_{\mathrm{HFM}})\right]$ can be determined from the scattered data.

The method of least squares fitting determines the parameters y_1 and y_2 of Equation (A.9) that minimize the function S:

$$S = \sum_{k=1}^{N} \left[b_k - y_1 - y_2 q''_k\right]^2, \tag{A.13}$$

where b_k is the difference between the DLR's reference value and the value as measured with the HFM.

The GUM 2008 [71] provides analytic equations for the determination of both parameters y_1 and y_2, the observed experimental variances $s^2(y_1)$ and $s^2(y_2)$, and finally a value for the coefficient of correlation $r(y_1, y_2)$ when applying a least square fit:

$$y_1 = \frac{\sum b_k \sum q_k''^2 - \sum b_k q_k'' \sum q_k''}{D}, \tag{A.14}$$

$$y_2 = \frac{N \sum b_k q_k'' - \sum b_k \sum q_k''}{D}, \tag{A.15}$$

$$s^2(y_1) = \frac{s^2 \sum q_k''^2}{D}, \tag{A.16}$$

$$s^2(y_2) = N \frac{s^2}{D}, \tag{A.17}$$

$$r(y_1, y_2) = - \frac{\sum q_k''}{\sqrt{N \sum q_k''^2}}, \tag{A.18}$$

$$s^2 = \frac{\sum \left[b_k - b(q_k'') \right]^2}{N-2}, \tag{A.19}$$

$$D = N \sum q_k''^2 - \left(\sum q_k'' \right)^2. \tag{A.20}$$

In these equations all sums are from 1 to N. Further, in the expression $\left[b_k - b(q_k'') \right]$ the parameter b_k is the difference between the two measured values and $b(q_k'')$ the correction as calculated according to Equation (A.9).

The parameters resulting from the application of these equations to the $N = 11$ samples are presented in Table A.4 grouped by forward and backward motion direction, and peak flux and total power values.

The uncertainty of parameter y_1 in the table, $s(y_1)$ is written in the following as $u(y_1)$ and that of y_2 , $u(y_2)$ as $s(y_2)$. These are propagated into the

Table A.4: Parameters of least-square fits to data. (Units omitted in order to allow compact formatting)

parameter	forward		backward	
	q''	$\dot{P}$	q''	$\dot{P}$
D	53 610 333.56	296 235 161.6	54 504 608.9	294 164 139.6
s^2	2036.97	15882.5	1857	10998.25
s	45.13	126.03	43.1	104.87
y_1	18.3	-73.3	40.1	45.2
y_2	-0.0051	-0.0095	0.003	-0.0139
$r(y_1, y_2)$	-0.893	-0.943	-0.895	-0.945
$s^2(y_1)$	909.5	13113	851	9499
$s^2(y_2)$	0.000418	0.00059	0.000375	0.000411
$s(y_1)$	30.16	114.51	29.17	97.46
$s(y_2)$	0.02	0.024	0.019	0.02

value of the combined standard uncertainty (that is, the standard deviation of the mean) of the predicted correction according to:

$$u^2\left[b(q'')\right] = u^2(y_1) + q''^2 u^2(y_2) + y_2^2 u^2(q'') + 2q'' u(y_1) u(_2) r(y_1, y_2) \tag{A.21}$$

where the last term expresses the covariance.

The equation contains one term with the standard uncertainty in the measured value of the heat flux, $u^2(q'')$ as measured by the HFM device, which is currently undetermined.

However, even under the assumption that $u^2(q'')$ is equally large as the uncertainty of the reference, this term contributes only marginally to the combined uncertainty of b. Therefore it is set to zero in this equation so

that $u_c^2\,[b(q'')]$ contains only the variance from the scatter observed in the N measurements.

Mathematically, all uncertainty present in the data is thus accumulated in the uncertainties of the correction function's parameters and consequently in the uncertainty of the resulting correction summand. This correction must then be added to measured values in order to obtain values that can be expected according to the calibration:

$$q''_{k,\mathrm{exp}} = q''_{k,\mathrm{HFM}} + b(q''_{\mathrm{HFM}}). \tag{A.22}$$

By assumption, all observable scatter is assumed to originate only from the uncertainty on the HFM measurement, and not from the FMAS reference. The variance of FMAS is already known and has to be added to the variance of the correction function.

As such the variance of a HFM heat flux measurement is accounted for.

The uncertainty $u(b)$ associated with the correction value, however, describes only the confidence limit for the location of its *mean* $s(\bar{b})$. However, in practice the prediction limit for a *single* value $s(b)$ is required because for each new measurement with the HFM device only one single flux value is aimed for. That uncertainty can be calculated according to Pardoe [84]:

$$s(b) = \sqrt{s^2 + s^2(\bar{b})}, \tag{A.23}$$

where the remaining variance s^2 from Table A.4, which cannot be explained with the linear equation, is added and taken into account.

Then, the combined uncertainty of a single HFM measurement according to Equation (A.12) can be calculated, that is, the uncertainty of the correc-

tion function added to the uncertainty of FMAS. Accordingly, the average uncertainty in the N measurements of HFM is:

$$s_c^2(q'') = 0.0003 \cdot q''^2_{\mathrm{DLR}} + s_c^2\left[b(q''_{\mathrm{HFM}})\right], \tag{A.24}$$

$$s_c(q'') = \sqrt{s_c^2(q'')}. \tag{A.25}$$

The uncertainty of a predicted new value based on a measurement from the HFM device will be calculated using the measured value and the corresponding correction added to it, that is:

$$s_c^2(q'') = 0.0003 \cdot (q''_{\mathrm{HFM}} + b(q''_{\mathrm{HFM}}))^2 + s_c^2\left[b(q''_{\mathrm{HFM}})\right] \tag{A.26}$$

$$s_c(q'') = \sqrt{s_c^2(q'')}. \tag{A.27}$$

This value of experimental standard deviation is based on a relatively small number of $N = 11$ samples and therefore is subject to uncertainty itself. According to GUM [71], section E4, table E.1 the uncertainty for a standard deviation calculated from 11 observations is about 23% and accordingly, this uncertainty is applied to the combined standard deviation resulting from the previous analysis in order to obtain the total uncertainty according to:

$$u_{\mathrm{c,t}}(q''_{\mathrm{HFM}}) = 1.23 \cdot \left(\sqrt{u_{\mathrm{c}}^2(q''_{\mathrm{HFM}})}\right). \tag{A.28}$$

A.2.6 Example calculation of uncertainty

The uncertainty for a single measurement of the peak flux value of $q''_{\mathrm{HFM}} = 2000\,\mathrm{kW\,m^{-2}}$ is calculated as an example, according to the previously specified approach. First, in forward direction, the correction and the standard uncertainty (that is, of the predicted average) can be calculated with the

parameters from Table A.4 and equations (A.10) and equation (A.12) respectively:

$$\begin{aligned} b(q'' = 2000\,\mathrm{kW\,m^{-2}}) =& 18.3\,\mathrm{kW\,m^{-2}} - 0.0051 \cdot 2000\,\mathrm{kW\,m^{-2}}, \\ =& 8\,\mathrm{kW\,m^{-2}}. \end{aligned} \tag{A.29}$$

$$\begin{aligned} u\left[b(q'' = 2000\,\mathrm{kW\,m^{-2}})\right] =& 909.5\,\mathrm{kW\,m^{-2}} \\ &+ (2000\,\mathrm{kW\,m^{-2}})^2 \cdot 0.000418\,\mathrm{m^2\,kW^{-1}} \\ &+ (2 \cdot 30.16 \cdot 0.02 \cdot -0.893)\mathrm{kW\,m^{-2}}, \\ =& 19.5\,\mathrm{kW\,m^{-2}}. \end{aligned} \tag{A.30}$$

The corresponding relative standard deviation at that flux density is $u_c/q'' = 0.975\,\%$.

The combined uncertainty, that is, including the uncertainty of the reference and the remaining variance s^2, for this prediction is $s_c(q'') = 60.14\,\mathrm{W\,m^{-2}}$, and respectively the relative deviation $u_c(q''_{\mathrm{HFM}})/q''_{\mathrm{HFM}} = 3\%$.

The final, total combined uncertainty, including the uncertainty resulting from the small sample size for the measurement with the FHM sensor of a heat flux density of $2000\,\mathrm{kW\,m^{-2}}$ is $u_{\mathrm{c,t}}(q''_{\mathrm{HFM}}) = 3.67\,\%$.

The predicted uncertainty is for the reference power of $10\,000\,\mathrm{W}$ $s_{\mathrm{c,t}}(\dot{P}) = 3.14\,\%$ in forward direction and $s_{\mathrm{c,t}}(\dot{P}) = 3.15\,\%$ in backward direction.

A.2.7 Uncertainty of the flux scanner

The measured data without and with correction as well as the confidence bounds of the correction function are plotted in Figures A.10 and A.11.

The fact that the confidence bounds remain approximately at a constant distance from the bisecting line leads to larger relative uncertainties for smaller values.

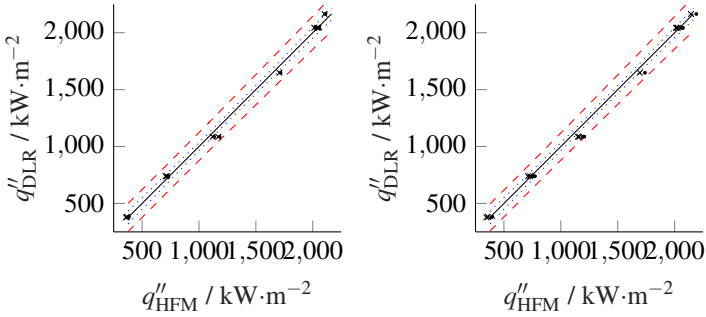

Figure A.10: Measured and corrected data of forward (left) and backward (right) motion (dot and x, respectively). Also shown are the 95% confidence bounds (dotted) and the combined 95% prediction bounds (dashed) around the corrected correlation (solid).

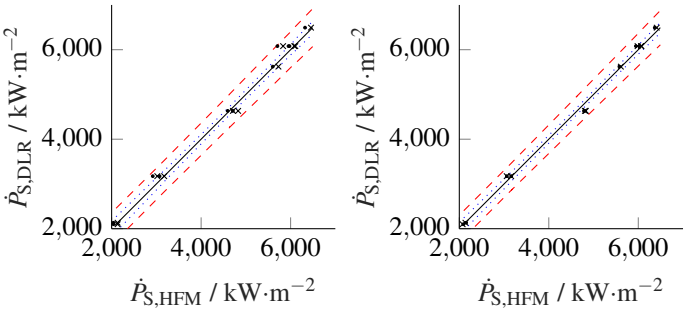

Figure A.11: Measured and corrected data of forward (left) and backward (right) motion (dot and x, respectively). Also shown are the 95% confidence bounds (dotted) and the combined 95% prediction bounds (dashed) around the corrected correlation (solid).

These experiments were conducted with Vatell's amplifier set to a gain of 100, which introduces more error than the available alternative setting of a gain of 1. Therefore 0.9% more uncertainty in the HFS and RTS signal than necessary have been generated that are potentially contained in the scatter of the measured data. When operating with a gain of 1 therefore even slightly higher accuracy of the assembly can be obtained.

A.2.8 Comparison with HFM's off-the-shelf calibration

Vatell calibrates the HFM sensor and provides a calibration function

$$q'' = \frac{U_{\mathrm{HFS}}}{g \cdot T + h}, \tag{A.31}$$

$$T = c \cdot R + d, \tag{A.32}$$

$$R = \frac{U_{\mathrm{RTS}}}{I_{\mathrm{RTS}}} + R_a, \tag{A.33}$$

$$R_a = e \cdot T_{\mathrm{a}} + f, \tag{A.34}$$

and calibration parameters a through h. In this set of equations R_a are the thermal sensor's resistance at ambient temperature T_{a}, R the thermal sensor's total resistance and T the thermal sensor's temperature corresponding with the respective resistance. In order to validate the findings of Yorgev et al. [82] the sensor was during the calibration campaign exposed to constant flux over an extended period of time without motion. Indeed, as shown in Figure A.12, the response quickly approaches a peak value and drops then continuously. The flux has been limited to $624\,\mathrm{kW\,m^{-2}}$ for this test in order to not damage the sensor. This value represents, however, nearly twice the intensity used in the factory calibration applied at Vatell. At higher fluxes the slope of the reading will probably higher, that is in agreement with Yorgev's

reporting. As suggested by Yorgev et al., a higher order polynomial for the temperature correction,

$$q'' = \frac{U_{\mathrm{HFS}}}{g \cdot T^2 + h \cdot T + k}, \tag{A.35}$$

can be fit to the data in order to obtain a constant reading. The response to the same data, however, with the adjusted temperature correction (solid line line) is also shown in Figure A.12. The measured value then indeed remains constant at the value of the reference, which itself is indicated by a dotted line. Although this solution appears good at a first glance it was found that the parameters obtained from fitting to a constant reference flux value are only valid at this flux value. For example, when this fit is applied for a scan of flux distribution # 47 (refer to Table A.3 in forward direction, instead of the reference power of 6493 W and the reference peak flux of 2164.7 $\mathrm{kW\,m^{-2}}$ the device detects only 5586 W and 1869 $\mathrm{kW\,m^{-2}}$, which is a much larger error (nearly 14 % for both) than what Vatell's original calibration and the one resulting from the surface fit generate.

Thus, although the calibration based on a surface fit as presented above cannot yield a constant reading under constant exposure to flux it is capable of measuring with satisfactory accuracy at all power levels obtained during calibration.

Because of the visible trend under extended exposure, Vatell's original calibration was expected to give bad results in the current application. However, although HFM readings under high fluxes have been observed to 'run away', when used in rotation the readings are more precise than expected. The two plots in Figure A.13 show the relative errors of the measured power of both calibrations in forward and inward direction, respectively. A very similar result is observed for the determination of the peak flux. The system shows a systematic proportional offset, when Vatell's original calibration is applied. However, especially towards larger powers, the deviation is quite

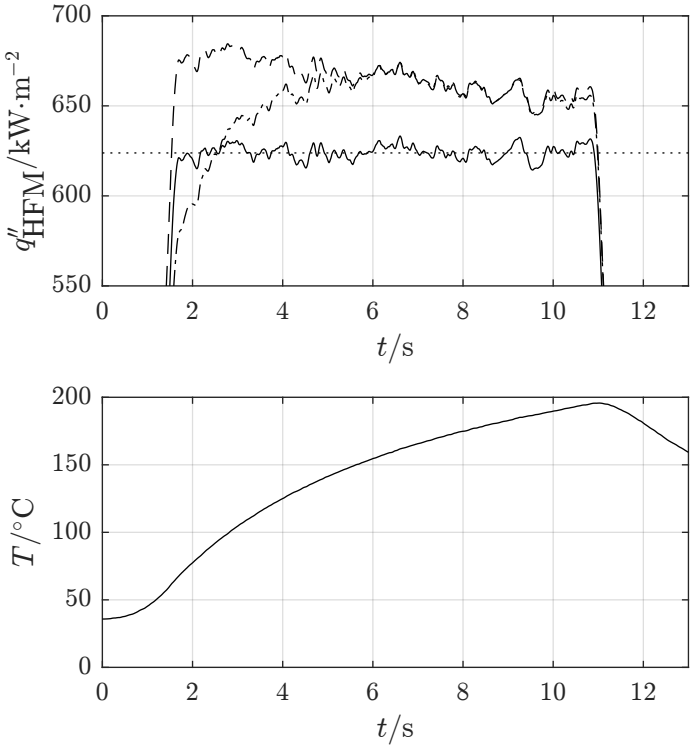

Figure A.12: Top graph: Heat flux as measured by the HFM sensor with original calibration by Vatell (dashed line), with a higher order polynomial applied for the temperature correction (solid line) and with the final calibration (dash-dotted line), compared to the reference heat flux (dotted line). Bottom graph: sensor temperature as detected from the RTS sensor.

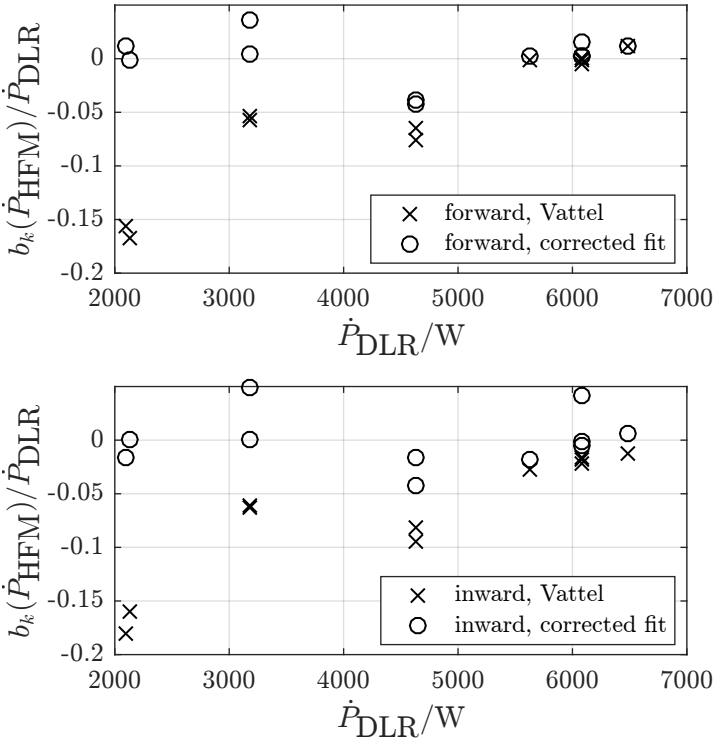

Figure A.13: Top graph: forward direction, bottom graph: inward direction. Both show the relative error in the power measurement for both, measurements with the original Vatell's calibration (crosses) and the new calibration including the correction (circles).

small. For lower powers, however, more than 15% offset is observable and potentially, the offset grows for higher fluxes. Reliable readings, therefore, require a calibration such as the one performed in Cologne.

A.2.9 Practical experiences

During the project, Vatell HFM sensors one sensor was damaged during calibration, most likely from unnoticed overheating in the focal point for a few seconds without rotation, which caused the solder of the connected signal wires of the resistance thermal sensor to liquify. A large offset in the resistance value and strange hystereses in the measured temperature remained afterwards. However, this could also have been caused by vibration. Further operation experience is required in order to finally conclude this type of sensor's suitability for such application. For example, on the new sensor, the Pyromark coating on the just mentioned solder bead flaked off after a few weeks of operation under full power. Luckily, as this occurred outside the sensitive region of the sensor, the measurement is not affected.

Vatell's amplifier's casing should be separately grounded in order to reduce signal noise. It also appears to not be equipped with a filter for noise from its power supply.

In general it turned out that for the high fluxes obtained in SOMMER no signal amplification would be required and manual zeroing of the reading on the amp could just as well be performed on the measured data during post-processing. Nevertheless, if required, signal amplification could probably be performed with calibrated micro-voltage amplifiers of brands other than Vatell. Potentially, this would reduce the investment costs if the excitation current can be generated elsewhere.

Vatell owns a de-facto monopoly for this kind of sensor with a resulting very low price transparency combined with a very coarse vendor network

across the globe. Sensors are produced and calibrated on demand, resulting in lead times of several weeks.

New and improved micro-scale approaches for this sensor type have been reported in literature ([85]), however, without yet stating an applicable temperature range. This generates hope for more players in the market in the future, potential competition for price models and maybe a more mechanically robust design.

A.2.10 Summary of system components

A list of major parts used for the system's assembly are listed in Table A.5.

A.3 The thermal Receiver

For the design of the thermal receiver un-scaled and scaled sections of the large-scale reference receiver have been considered. Finally, the significant dissimilarity of heat flux distribution diminished the option of strictly scaling the reference down.

In the following paragraphs the implications of both approaches on the loop design are nevertheless discussed.

A.3.1 A life-scale model receiver design

If an un-scaled element of the reference shall be used in the SOMMER experiment the following reference parameters have to be maintained in the model:

- Tube diameter and wall thickness
- Mass flow rate

Table A.5: Components used for the assembly of the solar flux density measurement device.

component	manufacturer	model	price EUR
HFM	Vatell	HFM-6D/H	5810
amplifier	Vatell	AMP-10	3750
angular encoder	WayCon	A36-H-6,35-L-3600-KR	140
linear encoder	ELGO	LMIX2-000-01.5-1-11	113
magnetic tape	ELGO	MB20.50	37
rot. motor	Sumitomo	RNYMS004-07-5/F50L/4	439
frequency inverter	Siemens		$\sim$ 300
linear motor	LINAK	365A11+82250225	–
data acq.	NI	NI PCIe-6341	965
cable	NI	SHC68-68-EPM	156
connector block	NI	SCB-68A	370
24 V power source			$\sim$ 50
PC			$\tilde{7}$00
bearings	SKS		18
belt drive			$\sim$ 50
gliders			$\sim$ 50
parts & fabrication			$\sim$ 150
		Total	$\sim$ 13073

- Temperature level

A hypothetical receiver design with the least possible number of three tubes is shown as a draft in the right image of Figure 4.17 with a black square indicating the patch taken from a reference panel as shown in the left image. Due to the small available flux zone in SOMMER the aperture is limited to a square.

Three tubes each with an outer diameter of 21 mm will fill an area that is 6.3 cm wide. On such an area the solar furnace projects a thermal power of approximately 7.69 kW at 800 $\mathrm{W\,m^{-2}}$ DNI, according to preliminary ray-tracing simulations. A value of 7 kW and three parallel tubes was used as a further design basis.

At this power and a Reynolds number larger than 112 000 a temperature increase along the receiver of only 8 K can be obtained for an outlet temperature of 600 °C. The minimum temperature increase may therefore only just be obtained.

The mass flow rate required in the life-scale approach receiver is 6.22 $\mathrm{kg\,s^{-1}}$ for a temperature increase of 8 K at the thermal power provided by the solar furnace. With this temperature rise an inlet temperature of 592 °C had to be provided by the loop in order to reach the goal of 600 °C to be obtained at the receiver's outlet.

During the design phase it was assumed that a temperature limitation for the pump would be at about 450 °C similar to pumps already in operation in existing loops of our laboratory. At the given mass flow rate therefore quite a significant amount of non-solar thermal power is required to raise the temperature of the flow from 450 °C at the outlet of the pump to this desired inlet temperature.

Two different system layouts were assessed that aimed to fulfill this requirement:

- Electric heating between pump and receiver and heat removal in a cooler
- A recuperating heat exchanger with electric support heating and a cooler

For case one, additionally the effect of an optional bypass was assessed, carrying 60% of the total mass flow for mixing hot fluid from the receiver outlet with cold fluid in order to reduce the fluid temperature before entering the cooler.

Figure A.14 shows this scenario under full-load operation. A very high electrical heating power of 112.3 kW is required in addition to the power from the sun of 10 kW to heat up LBE to the required inlet temperature of the receiver. The heater accomplishing this task must be build to endure very high temperatures at its outlet. The mixing with the bypass is effective as it generates moderate temperatures before the fluid enters the cooler where all power added to the system is then removed and lost in the cooler before the fluid reaches the pump. If a pump were to be found that can operate at temperatures higher than 450 °C, less additional thermal power would be required to bring the LBE to operating temperature. However, even then the additional power requirement would be very large compared to the power provided by the sun. Much of the electric heating power can be saved by recuperating the energy between the receiver outlet and the receiver inlet. This case is shown in Figure A.15 under steady-state conditions.

In this configuration the loop is separated in a 'high temperature' section and a 'low temperature section', the former being heated by a low-power electric heater which delivers in the situation on display 1.4 kW, all of which is then removed from the system in the cooler. This solution reduces the required amount of heating but a large recuperator is required instead. The magnitude of heat to be recuperated of 118 kW is significant. It was expected that the loop control would have become significantly more difficult to implement with such a recuperator.

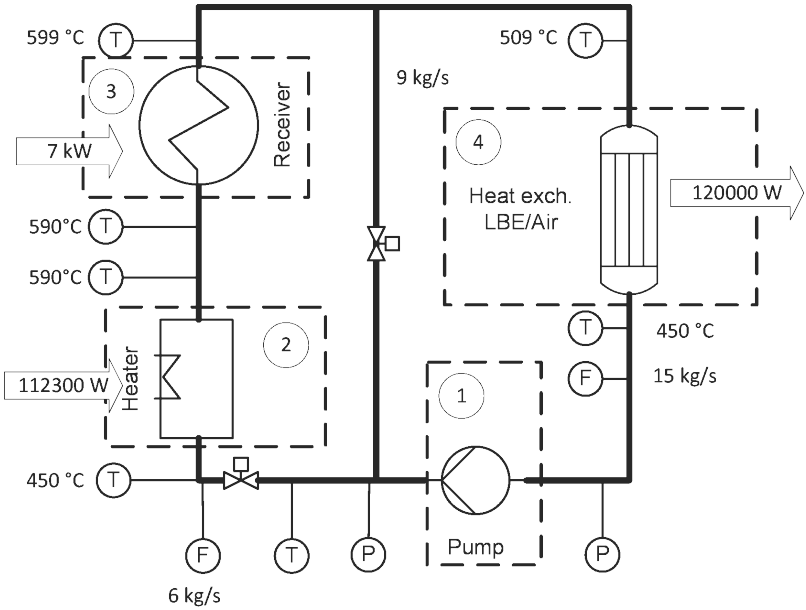

Figure A.14: Loop for the life scale approach receiver with 60% bypass

For the life scale receiver therefore only the moderate operating temperatures were likely to be achieved in order to avoid this massive demand for electric power or very powerful recuperating heat exchanger. Therefore, the selection of this receiver design would have allowed the demonstration of a receiver with real life dimensions and Reynolds number but not the operation at high temperatures. High temperatures were, however, desired in order to demonstrate the liquid metals' high-temperature suitability in STE facilities.

By reducing the mass flow rate and thereby increasing the temperature increase the Reynolds number will drop below the desired value of 10^5.

Due to maintaining the reference tube diameters and due to the available area of 10 cm by 10 cm at most four and, if that constrained is slightly re-

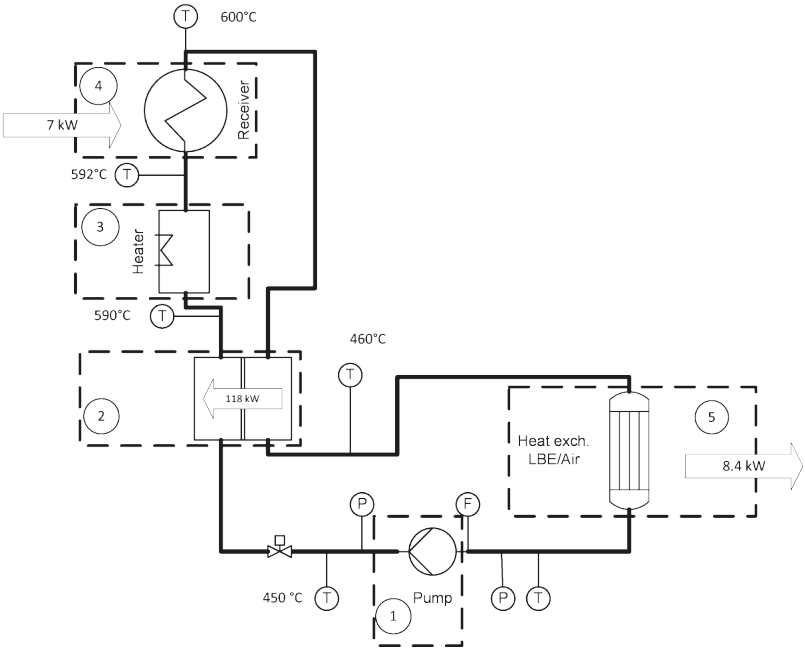

Figure A.15: Loop with recuperator.

laxed, even five parallel tubes could be fit into the available space. However, the additional gain in absorbed thermal power would come at the costs of a reduction of flow rate in all tubes and consequently at reduced Reynolds number to values below the targeted 10^5.

The un-scaled design is therefore badly suited.

It is furthermore uncertain whether a technical solution can be found that generates identical mass flow rates in all three parallel tubes. This would introduce uncertainty in the individual tube flow conditions and make it difficult to draw conclusions from measured tube surface temperatures. That uncertainty will consequently be added to the energy balance and to the value of thermal efficiency of the receiver.

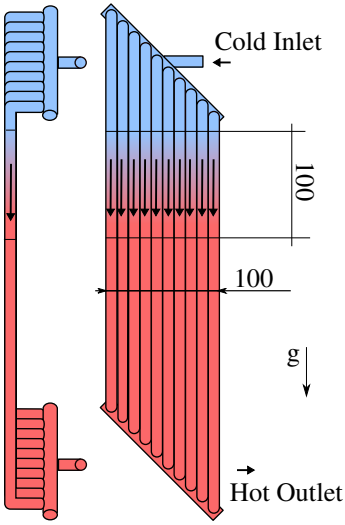

Figure A.16: Scaled model receiver concept.

A.3.2 A down-scaled model receiver design

Larger elements of the reference receiver can be taken from the reference and scaled down as depicted in Figure A.16. Accordingly, a larger patch of the reference receiver area can be examined in the limited irradiated space provided by the SOMMER loop. In a first thought experiment one could try to scale a larger section of the receiver such as in the previously discussed case. A set of parallel tubes but with reduced diameters is placed in the focal point of SOMMER. It turns out that also for the scaled case no solution exists for the receiver at a desired ΔT of 10 K, $\dot{Q} = 10000\,\mathrm{W}$ and a Reynolds number greater than 10^5 in such a parallel flow arrangement. The same problems in the loop design as discussed in the previous section would have been touched.

Therefore, due to the limited available solar power a strict scaling of reference elements was found to be not suitable. Such approach would become

possible at higher available solar powers, such as in DLR's solar furnace in Cologne or DLR's solar simulator in Jülich.

From a practical point of view it is furthermore for both preceding concepts not straight-forward to fabricate these receivers. The ends of the tubes have to be welded to diverters and collectors while no gaps between individual tubes are allowed and identical mass flow rates are required in each individual tube.

The depicted diagonal, pipe-organ-like concept arrangements in Figures A.16 and 4.17 serve the purpose of generating welding space between joints of tube and diverter/collector. However, this leads then to differently well developed hydraulic flow conditions in each tube – yet another dissimilarity between reference and model.

A.3.3 Receiver construction

Figure 4.26 on page 130 shows the large copper shield surrounding the receiver absorber area. Under nominal condition the focal point resides in the geometrical absorber center, where active cooling is provided by the liquid metal flow. The heliostat mirror compensates the earth's rotation and prevents the focal point from leaving the absorber area. The copper shield covers a layer of stainless steel sheet of low thermal conductivity which contains the thermal insulation material beneath. Without the copper shield misdirected concentrated solar radiation would immediately result in intolerably high temperatures on this steel surface, potentially leading to its melting. Copper is used to distribute all intercepted solar energy evenly in its volume, and re-radiating it from its large surface area and thus preventing the surroundings of the absorber from local temperature peaks. This shield is mounted in front of the receiver, however, without physical contact with the coil's mounting.

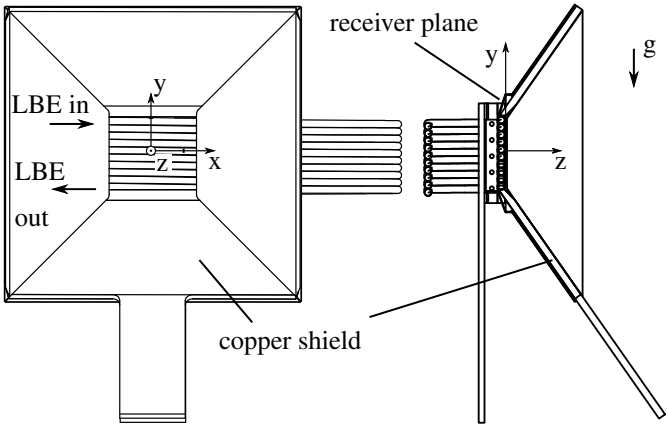

Figure A.17: Left: Frontal view of thermal receiver, Right: Cut vertical through aperture center.

On the right image in Figure A.17 the mounting of the coil is schematically shown. For mounting the coil two 1 mm stainless-steel L-profiles were laid flat against each other to form a T profile which was positioned vertically and flat on the absorber tubes' rear side, that is, on the coil's inner wall. The T-profile's respective two edges touching the rear 'crowns' of each of the coil's tubes were then spot-welded to the absorber tubes, a procedure which required significant care in order not to pierce the 0.5 mm strong wall of the tubes. The T-profiles' remaining, protuding plate was then clamped with screws between two stainless steel blocks. These were then screwed to the main support.

Left and right of the absorber area brass clamps enforce the tubes' thermal expansion to occur only in the tubes' axial direction while preserving their parallel, gap-less arrangement. The entire receiver is mounted to a vertical copper support, which protudes from the thermal insulation and which is mounted to the loop's aluminum construction elements.

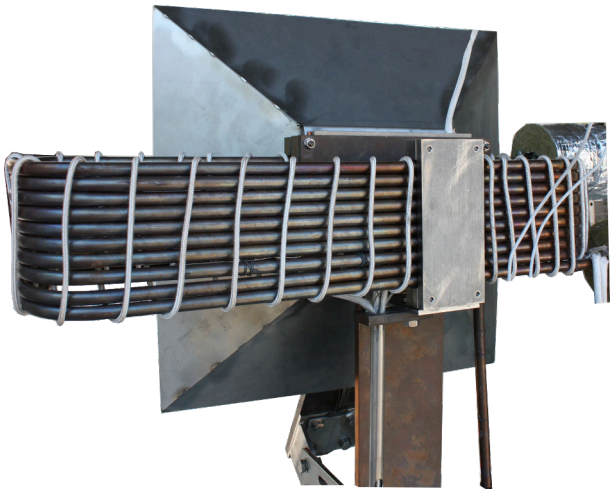

Figure A.18: Rear view of receiver with trace heating elements and without insulation. Frank Fellmoser 2018

The weight of the coil's rear tubes is significant when filled with LBE given the thin tube walls. Therefore, a stainless steel clamp holds together the coil and rests loosely on a horizontal plate to support the coil's weight. This clamp and the copper main support are clearly visible in Figure A.18, which shows the final receiver prior to the application of thermal insulation. A layer of thermal insulation board has been inserted between all interfaces of support elements that are in direct contact with the absorber tubes.

The entire coil is equipped with heater wires in order to prevent LBE from freezing during stand-by. The gap behind the absorber tubes is filled out with an electric heating element as well.

The receiver as described is intended to serve as a prototype. It is made of 1.4571 stainless steel, which is commonly used in LBE loops for temperatures of up to 550 °C. A second receiver coil has been already fabricated, however, without any means of fixation applied, yet. This coil is made of 1.4828 stainless steel which, according to its data sheet is intended for op-

eration of up to temperatures of 800 °C and is expected to be more resistive against corrosion attack from LBE due to its increased Si content compared with 1.4571.

This second coil is ready to be assembled into a receiver once operation experience from the prototype has been obtained.

A.4 Receiver control

This section provides a brief summary of control algorithms applied in the Solar Two project and in the SSPS project. Then, in a similar fashion, a control algorithm of the SOMMER loop is designed, using simple, dynamic models of loop components.

A.4.1 Reference control algorithms

The Solar Two power plant accomplished a constant outlet temperature by regulating the mass flow rate [86]. The control algorithm was developed with the help of a simulation model ('T-BRD'), including valves, pumps, tanks and controls. For example, one single ordinary differential equation was applied for the energy conservation in the control volume of an entire receiver panel (a bundle of 32 tubes).

Simulations resulted in the second evolution step of the development process of a control algorithm that featured feedforward control based on the measurements of solar flux gauges and feedback control based on the outlet temperature of the receiver.

The algorithm was specified to secure all panels from overheating by applying full clear-sky mass flow in situations where individual panels would receive very different fluxes than others which could occur when clouds would cover some sections of the heliostat field. The occurrence of this

situation was determined by eight photometers that measured the amount of light reflected from the panels. Also during moments with a completely covered sun, this high mass flow rate was maintained. This provided good cooling for the moment when the sun re-appeared and the power quickly rose, generating the risk of overheating the tubes. This stand-by operation was triggered when less than 25% of nominal flux was measured on any of the panels or if the outlet temperature dropped below 510 °C.

Adaptive gains for the PI controllers were implemented that depended on the mass flow rate. One PI controller was acting upon the outlet temperature set point difference, a second PI controller upon the error in mass flow rate and feed-forward setpoint value.

This in general quite simple scheme was used successfully during the project lifetime.

In the SSPS control scheme the mass flow rate was limited to a minimum rate during cloud stand-by and raised to maximum flow at the end of the passage [26]. This caused undesirable dropping outlet temperatures prior to reestablishment of the set point outlet temperature. The authors claim that improved irradiation measurement at the receiver and better adaptation of the mass flow to the measured condition reduced this problem.

A fast inner feedforward loop manipulated the flow rate based on input from a heat flux measurement reading. A second, intermediate speed feedback loop with PD controller (adaptive gains) acted upon variations between in- and outlet temperature differences of all panels. A slow, outer feedback loop with adaptive integrating gain (I) controller acted upon outlet temperature variation.

This algorithm used input from ten photometers distributed across the heliostat field as feedforward input to the mass flow regulation. In one example situation, where irradiance drops by more than 50% the outlet temperature drop of the receiver is limited to 10K by this algorithm.

Also in case of the SSPS receiver a coarse model (for example, taking wind speed into account but no gusts) of the dynamics was established and compared to the measured response. Differences are mainly due to errors in the assumed flux distribution compared to the one present during the experiments. Nevertheless the response times are met quite accurately. Due to the non-linear character of the response three sets of time constants and gains were determined for different modes of operation.

The authors report a quick response behavior of the receiver, which theoretically is capable of being heated 'from 270 to 530 °C in less than three minutes [26] at noon'.

This following discussion is limited to cases where the DNI changes by up to 30% of the maximum value (full load). At the time of writing the loop operation was performed manually to record step responses of the heater but no further experience, for example with solar input, has been obtained. Such experience is necessary in order to define operation limits for the loop and to develop the control algorithm further.

The model based simulations herein have been used in order to evaluate whether the designs of loop components would result in a responsive system. Thus, the ability to control the final loop has been taken into account during the design phase. Therefore, this section is limited to approaches of linear control theory.

For more advanced approaches of loop control the following works can be referred to: For fundamentals of model-predictive control [87] and [88], for its application in solar thermal plants [89], [90], [91] and [92].

A.4.2 Heater: A non-linear model

The heater (section 4.2.2) is used in the loop to increase the flow temperature from 380 °C at the pump outlet to 530 °C at the receiver inlet at full

load. It consists of a cylindrical vessel containing 6 heater rods. The outlet temperature$T_o(t)$ shall be controlled.

For the design of a controller first a simplified analytical, non-linear, dynamic model of the heater is generated. Its dynamic output will then compared to experimental step responses of the real heater to validate the model's accuracy. If a satisfactory accuracy is obtained a linearized model is deduced from the validated, non-linear model and linear control theory will be applied to identify suitable parameters for a basic controller. It will be attempted to also design a compensation for the effects of measurable disturbances from changes in the mass flow rate and inlet temperature. The identified compensators and the controller will finally be tested on the original model in order to assess their expected performance.

This model assumes a constant heat capacity, independent from temperature for both, heater rods and metal flow as well as a constant heat transfer coefficient, independent from the mass flow rate. For the applied heater design a Nusselt number of 5.8 is obtained which corresponds to a convective heat transfer coefficient of $h = 7300\,\mathrm{W\,m^{-2}\,K^{-1}}$. The impact of the variation of these parameters on the outlet temperature is small compared to the variation of the mass flow rate, the variation of inlet temperature and the variation of heating power which justifies this simplification.

The vessel wall is expected to have the smallest impact on the dynamic behavior versus heater rods and liquid volume flow. As an additional simplification therefore the mass of the device is roughly estimated to equal the mass of the heating rods (neglecting the vessel wall) in order to avoid the definition of an extra control volume and a corresponding coupled balance equation in the model.

For simplicity the rods and the fluid volume are accounted for by a single control volume each. No further axial or radial discretization of these volumes is applied. This model is depicted in Figure A.19.

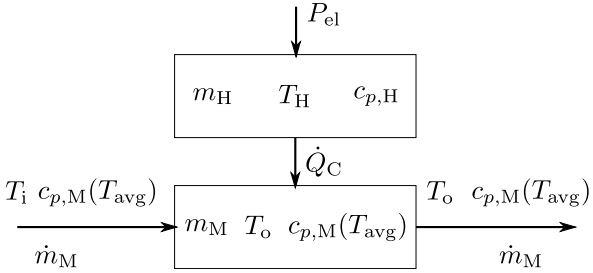

Figure A.19: Schematics of the heater model

The balance equation around the heater rods (index H) is as follows:

$$\frac{dQ_{\mathrm{H}}(t)}{dt} = \dot{P}_{\mathrm{el}}(t) - hA \cdot (T_{\mathrm{H}}(t) - T_{\mathrm{o}}(t)) \tag{A.36}$$

with $\dot{P}_{\mathrm{el}}(t)$ the time dependent electric power used for heating and A the combined surface area of all rods.

The fluid volume balance is

$$\frac{dQ_{\mathrm{M}}(t)}{dt} = hA \cdot (T_{\mathrm{H}}(t) - T_{\mathrm{o}}(t)) + \dot{m}(t) c_{p,\mathrm{M}} \cdot (T_{\mathrm{in}}(t) - T_{\mathrm{out}}(t)). \tag{A.37}$$

As final simplifications the convective heat transfer between the rods and the flow is modeled by applying a mean temperature to the heater rods, T_H and using the heater's outlet temperature value T_o, instead of, for example, a logarithmic mean temperature between in- and outlet for the flow. Also the enthalpy contained in the liquid metal's control volume is defined as $Q_{\mathrm{M}} = m_{\mathrm{M}} c_{p,\mathrm{M}} T_{\mathrm{o}}$ (the outlet temperature is used for the calculation) and the enthalpy of the rod is defined as $Q_{\mathrm{H}} = m_{\mathrm{H}} c_{p,\mathrm{H}} T_{\mathrm{H}}$. Thus, the rate of heat transfer to the metal flow is systematically under-estimated and the actual energy capacity of the liquid volume is over-estimated for the sake of simple

equations, leading, however, to slower dynamics than to be expected in the real application.

These balances are re-arranged for the heater rod temperature and heater outlet temperature: to get:

$$\frac{dT_{\mathrm{out}}(t)}{dt} = \frac{(\dot{m}(t)c_{p,\mathrm{M}} - hA)T_{\mathrm{out}}(t) + \dot{m}(t)c_{p,\mathrm{M}}T_{\mathrm{in}}(t) + hAT_{\mathrm{H}}(t)}{m_{\mathrm{M}}c_{p,\mathrm{M}}}, \quad \text{(A.38)}$$

$$\frac{dT_{\mathrm{H}}}{dt} = \frac{\dot{P}_{\mathrm{el}}(t) - hA(T_{\mathrm{H}}(t) - T_{\mathrm{out}}(t))}{m_{\mathrm{H}}c_{p,\mathrm{H}}}. \quad \text{(A.39)}$$

The thermal inertia of the vessel's wall is artificially introduced by assuming the heater's central displacement body as a seventh solid heater rod.

These equations are solved in Matlab by their implementation in Simulink as a block diagram and the `ode45` solver with a variable time step size (standard) is used.

The parameters in these equations are calculated as follows, with n_{R} being the number of rods:

$$m_{\mathrm{M}} = \left(\frac{\pi}{4}d_{\mathrm{HV}}^2 L_{\mathrm{HV}} - n_{\mathrm{R}}\frac{\pi}{4}d_{\mathrm{H}}^2 L_{\mathrm{H}}\right)\cdot\rho_{\mathrm{M}}, \quad \text{(A.40)}$$

$$m_{\mathrm{H}} = \left(n_{\mathrm{R}}\frac{\pi}{4}d_{\mathrm{H}}^2 L_{\mathrm{H}}\right)\cdot\rho_{\mathrm{H}}, \quad \text{(A.41)}$$

$$A = n_{\mathrm{R}}\pi d_{\mathrm{H}} L_{\mathrm{H}}. \quad \text{(A.42)}$$

The values of these model parameters used throughout this thesis are listed in Table A.6. Physical properties of LBE are calculated at T_{avg} according to correlations from Ref. [32].

Table A.6: Parameters for the heater model

parameter	symbol	unit	value
diameter of rod shell	d_{H}	m	0.022
length of rod shell	L_{H}	m	0.4
inner length of vessel	L_{HV}	m	0.445
inner diameter of vessel	d_{HV}	m	0.078
convective heat transfer coefficient	h_H	$\mathrm{W\,m^{-2}\,K^{-1}}$	7600
heat capacity of rod	$c_{p,\mathrm{H}}$	$\mathrm{J\,kg^{-1}\,K^{-1}}$	500
density of rod	ρ_{H}	$\mathrm{kg\,m^{-3}}$	5000
average temeperature	T_{avg}	K	453.258
design mass flow rate	$\dot{m}$	$\mathrm{kg\,s^{-1}}$	1

A.4.3 Heater: Experimental step responses

This system of differential equations has been implemented as a Matlab Simulink model.

The heater outlet temperature is the output to be adjusted by the heating power. The dynamic behavior of that outlet temperature is examined via the experimental response to steps in heating power and mass flow rate.

Negative steps of 10 %, 20 % and 30 % of a reference heating power of 19 500 W are generated at two different mass flow rates of $1\,\mathrm{kg\,s^{-1}}$ and $0.5\,\mathrm{kg\,s^{-1}}$ and two different inlet temperatures of 200 °C and 300 °C. The resulting responses are compared with the predicted responses from the dynamic model.

The responses to steps in the heating power are shown in Figure A.20.

The dotted lines represent the step response of the model. The step responses of the heater outlet temperature are proportional to the steps in heat-

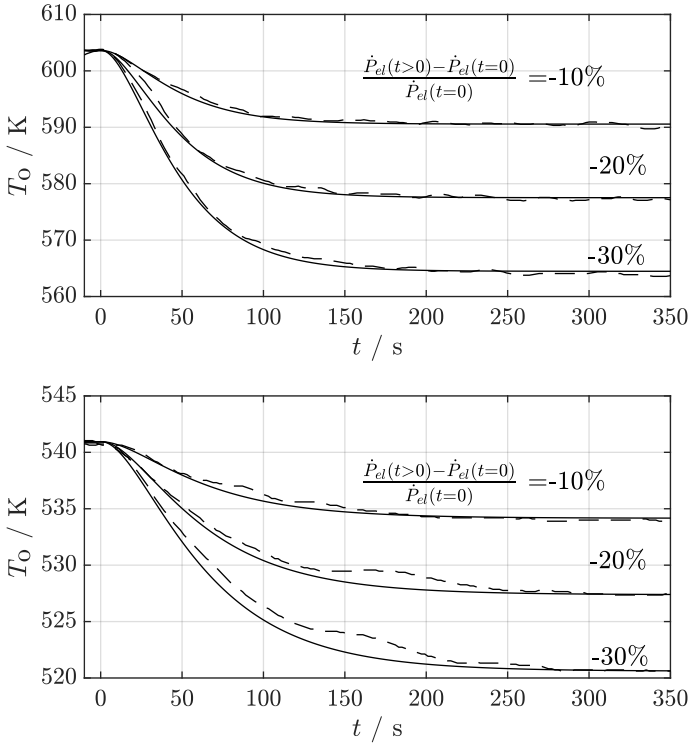

Figure A.20: Outlet temperature response of the heater to negative steps at $t = 0\,\mathrm{s}$ of the heater power, both experimental (dashed lines) and simulated (solid lines) for an inlet temperature of 200 °C. Top graph: a mass flow rate of $1\,\mathrm{kg\,s^{-1}}$ and an initial power of 19 500 W. Bottom graph: a mass flow rate of $0.6\,\mathrm{kg\,s^{-1}}$ and an initial power of 6000 W.

Table A.7: Outlet temperature response of heater upon steps in heating power (left) and mass flow rate (right).

$\frac{\Delta \dot{P}_{el}}{\dot{P}_{el,0}}$	$\frac{(T_{o,0}-T_{i,0})-(T_{o,\infty}-T_{i,\infty})}{(T_{o,0}-T_{i,0})}$	$\frac{\Delta \dot{m}}{\dot{m}_0}$	$\frac{(T_{o,0}-T_{i,0})-(T_{o,\infty}-T_{i,\infty})}{(T_{o,0}-T_{i,0})}$
-10 %	-9.9 %	+10 %	-9.2 %
-20 %	-20.3 %	+20 %	-16.8 %
-30 %	-30.3 %	+30 %	-22.9 %

ing power. However, the dynamics of the physical device is much slower than that of the simplified model.

This difference could be removed by adding an additional PT_1 delay behind the step function of the heater power with a time constant of $T_7 = 20\,s$. With this additional delay the simulation fits the measured data. (The 'bumps' in the bottom graph result from a slight increase of the inlet temperature during this experiment as no perfect steady-state conditions were present.) The model then well represents the response times of the experiment.

There remains a slight difference between experimental data and model immediately after the step, likely due to the model not being discretized in flow direction but modeled as a single volume with perfectly mixed fluid. Thus an earlier response is observed from the model whereas in fact hot fluid near the outlet of the heater continues to leave the heater even after the step.

The response to positive steps in the mass flow rate is shown in Figure A.21. The response in the outlet temperature is inversely proportional to the step size, which is expressed by the numbers provided the second colum of Table A.7.

In this case the model dynamics match the experimental data well enough without the introduction of an additional delay.

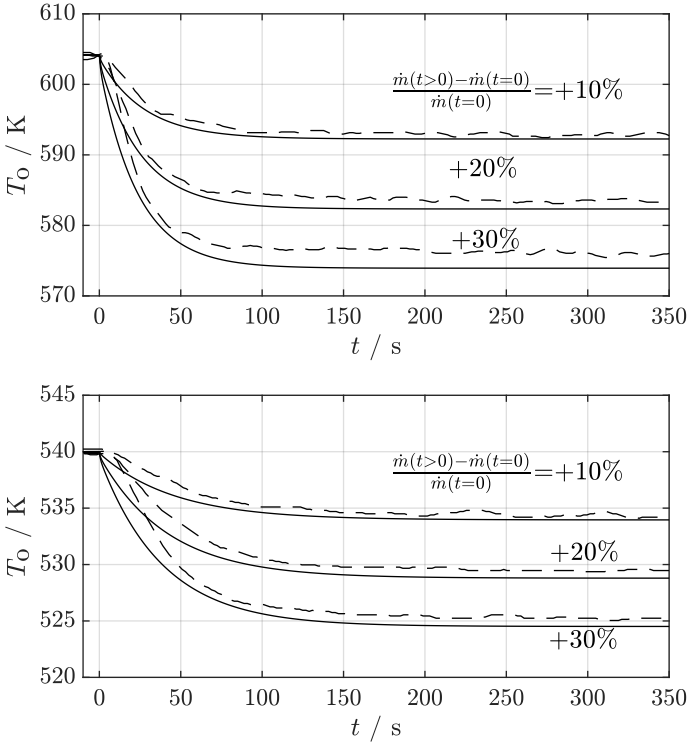

Figure A.21: Step responses of the heater with experimental (dashed line) and simulated (solid line) data for an inlet temperature of 200 °C. Shown here are temperature responses of positive steps at $t = 0$ s of the mass flow rate of 10 %, 20 % and 30 %. Top graph: , an initial power of 19 500 W and an initial mass flow rate of 1 kg s^{-1}. Bottom graph: a power of 6000 W and an initial mass flow rate of 0.6 kg s^{-1}.

Due to feedback effects in the loop, where no controllers are active the measured inlet temperature in these examples increased after the step. This causes an offset of the measured steady-state temperatures and the simulation and is true for two different initial values of the mass flow rates and heating powers.

The model simplifications neglect a slight delay visible in the experimental data . The assumption of a constant heat transfer coefficient in spite of the changes in flow velocity and turbulence does, however, potentially lead to only a slight steady-state temperature offset, which, however is small enough to be corrected by controllers later on. .

With the introduction of the extra delay for changes in heating power the model is considered to be sufficiently well representing the heater's dynamics and can be used for controller design.

A.4.4 Heater: A linearized model

The non-linear differential equations are linearized under steady-state conditions (index s) by first-order Taylor expansion:

$$\begin{aligned}
&\frac{\partial(T_{\mathrm{o,s}}+\zeta_{T_\mathrm{o}}(t))}{\partial t} = \frac{\partial \zeta_{T_\mathrm{o}}(t)}{\partial t}\dots,\\
&\dots = \underbrace{f(T_{\mathrm{o,s}},\dot{m}_\mathrm{s},T_{\mathrm{i,s}},T_{\mathrm{H,s}})}_{=0} + f(\zeta_{T_\mathrm{o}}(t),\zeta_{\dot{m}}(t),\zeta_{T_\mathrm{i}}(t),\zeta_{T_\mathrm{H}}(t))\dots\\
&\dots \approx 0 + \left.\frac{\partial f(T_\mathrm{out}(t),\dot{m}(t),T_\mathrm{in}(t),T_\mathrm{H}(t))}{\partial T_\mathrm{out}(t)}\right|_{(\dot{m}_\mathrm{s},T_{\mathrm{i,s}},T_{\mathrm{H,s}})} \zeta_{T_\mathrm{o}}(t)\dots\\
&\dots + \left.\frac{\partial f(\dots)}{\partial T_\mathrm{in}(t)}\right|_{(\dot{m}_\mathrm{s},T_{\mathrm{o,s}},T_{\mathrm{H,s}})} \zeta_{T_\mathrm{i}}(t) + \left.\frac{\partial f(\dots)}{\partial \dot{m}(t)}\right|_{(T_{\mathrm{i,s}},T_{\mathrm{o,s}},T_{\mathrm{H,s}})} \zeta_{\dot{m}}(t)\dots\\
&\dots + \left.\frac{\partial f(\dots)}{\partial, T_\mathrm{H}(t)}\right|_{(\dot{m}_\mathrm{s},T_{\mathrm{o,s}},T_{\mathrm{i,s}})} \zeta_{T_\mathrm{H}}(t)\dots,\\
&\dots = -\frac{hA+\dot{m}c_{p,\mathrm{m}}}{m_\mathrm{M}c_{p,\mathrm{m}}}\zeta_{T_\mathrm{o}}(t) + \frac{c_{p,\mathrm{m}}(T_{\mathrm{i,s}}-T_{\mathrm{o,s}})}{m_\mathrm{M}c_{p,\mathrm{m}}}\zeta_{\dot{m}}(t) + \frac{\dot{m}c_{p,\mathrm{m}}}{m_\mathrm{M}c_{p,\mathrm{m}}}\zeta_{T_\mathrm{i}}(t)\dots\\
&\dots + \frac{hA}{m_\mathrm{M}c_{p,\mathrm{m}}}\zeta_{T_\mathrm{H}}(t). \qquad \text{(A.43)}
\end{aligned}$$

and alike for the balance equation of the heater rods:

$$\frac{\partial \zeta_{T_\mathrm{H}}(t)}{\partial t} \approx \frac{1}{m_\mathrm{H}c_{p,\mathrm{H}}}\zeta_{\dot{P}_\mathrm{el}}(t) - \frac{hA}{m_\mathrm{H}c_{p,\mathrm{H}}}\zeta_{T_\mathrm{H}}(t) + \frac{hA}{m_\mathrm{H}c_{p,\mathrm{H}}}\zeta_{T_\mathrm{o}}(t). \qquad \text{(A.44)}$$

The values of the dynamic parameters $T_o(t)$ and $T_H(t)$ under steady-state conditions are determined by setting the left hand side of both initial non-linear differential equations to zero, then setting all remaining, independent design process parameters to their desired values and solving the equation system for the heater rod temperature and the metal outlet temperature.

Groups of constant parameters occurring in these equations are substituted by the following constants:

$$K_1 = \frac{1}{hA}, \tag{A.45}$$

$$K_2 = \frac{hA}{hA + \dot{m}_\mathrm{s} c_{p,\mathrm{M}}}, \tag{A.46}$$

$$K_3 = \frac{(T_\mathrm{i,s} - T_\mathrm{o,s}) c_{p,\mathrm{M}}}{hA + \dot{m}_\mathrm{s} c_{p,\mathrm{M}}}, \tag{A.47}$$

$$K_4 = \frac{\dot{m}_\mathrm{s} c_{p,\mathrm{M}}}{hA + \dot{m} c_{p,\mathrm{M}}}, \tag{A.48}$$

$$T_1 = \frac{m_\mathrm{H} c_{p,\mathrm{H}}}{hA}, \tag{A.49}$$

$$T_2 = \frac{m_\mathrm{M} c_{p,\mathrm{M}}}{hA + \dot{m}_\mathrm{s} c_{p,\mathrm{M}}}. \tag{A.50}$$

The steady state solutions are then:

$$T_\mathrm{H,s} = \dot{P}_\mathrm{s} \frac{K_1}{K_4} + T_\mathrm{i,s}, \tag{A.51}$$

$$T_\mathrm{o,s} = \dot{P}_\mathrm{s} \frac{K_1 K_2}{K_4} + T_\mathrm{i,s}. \tag{A.52}$$

When the Laplace transform is applied to the linearized equations and when the dependent variables are isolated in the resulting algebraic equations the linear model of the heater results in:

$$T_{\mathrm{H}}(s) = \frac{K_1(T_2 s+1)}{(T_2 s+1)(T_1 s+1)-K_2}\dot{P}_{\mathrm{el}}(s) + \frac{K_3}{(T_2 s+1)(T_1 s+1)-K_2}\dot{m}(s)\ldots \tag{A.53}$$

$$\cdots + \frac{K_4}{(T_2 s+1)(T_1 s+1)-K_2}T_{\mathrm{i}}(s) \tag{A.54}$$

$$T_{\mathrm{o}}(s) = \underbrace{\frac{K_1 K_2}{(T_2 s+1)(T_1 s+1)-K_2}}_{G_S(s)}\dot{P}_{\mathrm{el}}(s) + \underbrace{\frac{K_3(T_1 s+1)}{(T_2 s+1)(T_1 s+1)-K_2}}_{G_{SZ1}(s)}\dot{m}(s)\ldots \tag{A.55}$$

$$\cdots + \underbrace{\frac{K_4(T_1 s+1)}{(T_2 s+1)(T_1 s+1)-K_2}}_{G_{SZ2}(s)}T_{\mathrm{i}}(s) \tag{A.56}$$

The linearized model features a PT_2 characteristic for the heater's outlet temperature regarding changes in the heater power and a PDT_2 characteristic regarding disturbances and changes in the mass flow rate and inlet temperature.

Since an additional first order delay towards a change in heater power has been identified in the experimental step response, the respective factor is added to the model of $G_S(s)$:

$$G_S(s) = \frac{K_1 K_2}{((T_2 s+1)(T_1 s+1)-K_2)\,(T_7 s+1))} \tag{A.57}$$

with $T_7 = 20\,\mathrm{s}$.

A.4.5 Heater: The model step response

Both, the non-linear system of differential equations and the linearized equation for the outlet temperature have been implemented in Simulink.

For steps in heating power both, linearized and nonlinear system behave identical in the top graph in Figure A.22. The bottom graph shows the system's response to a step disturbance of the mass flow rate of 10, 20 and 30% increase.

In the bottom graph the difference between linearized model and nonlinear model is visible. Here the linearization causes significant divergence for large disturbances; for only a 10 % step the linearization still very well approximates the system dynamics. This is due to the initial steady-state mass flow rates in the constant parameters K_3 and K_2 which are mainained even after the step has occurred. The error grows, however, for increasing steps in the mass flow rate.

In order to have the linearized model better predict the behavior, sets of constants can be provided among which a suitable one is selected by the control system depending on the current mass flow rate, a method also called 'gain scheduling'. Nevertheless, for brevity the controller design is continued with only a single set of constants. The capability of the resulting controller will then be assessed in the end and a decision will be made whether or not the linearization leads to problems.

A.4.6 Heater: Controller design

The heater shows individual dynamic response to changes in mass flow rate, inlet temperature and heater power. The former two can be regarded as measurable disturbances $Z_1(s)$ and $Z_2(s)$ according to the signal flow chart in Figure A.23 while the heater power is used as actuator ($U(s)$) for the control of the outlet temperature. A main feed-back controller is designed

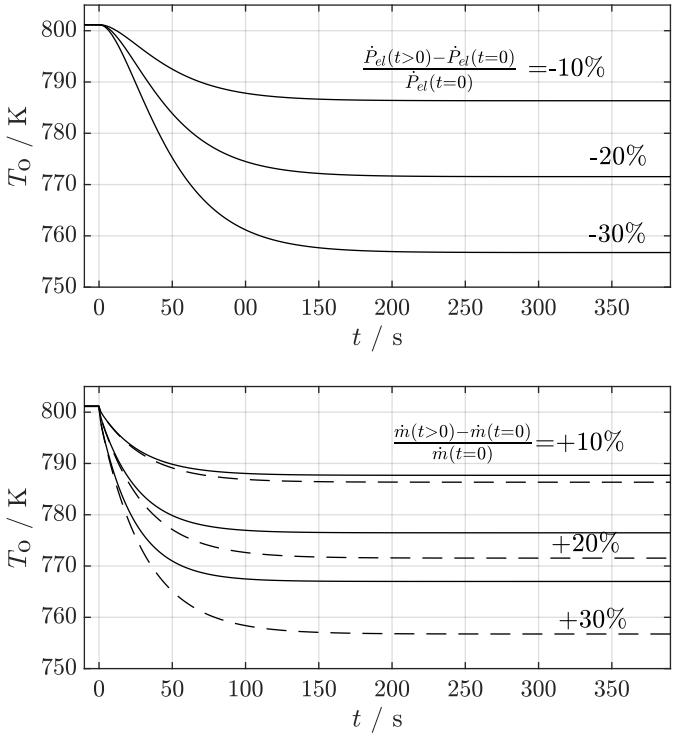

Figure A.22: System response for negative steps at $t = 10\,\mathrm{s}$ in, top graph, heater power of 10, 20 and 30% relative to reference power of $P = 19.5\,\mathrm{kW}$and, bottom graph, positive steps in mass flow rate of 10, 20, 30% relative to reference mass flow rate of $1\,\mathrm{kg\,s^{-1}}$.

that takes care of all non-measured disturbances and of the compliance with the reference variable.

It is the objective of the control algorithm to maintain a constant outlet temperature of the heater in order to keep the inlet temperature to the receiver constant and also in order not to violate temperature limitations of the structural material of the heater.

As changes in mass flow rate and inlet temperature are measurable this information can be fed to the control system according to Figure A.23 indicated as $Z_1(s)$ and $Z_2(s)$, respectively and the disturbances can be compensated by the actuator before their effects become measurable at the outlet of the heater. The dynamics of the outlet temperature with respect to the

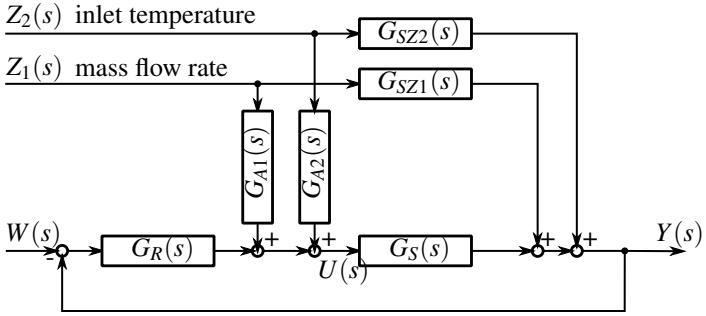

Figure A.23: Control block diagram for the heater.

disturbances and their compensation are, according to the flow chart:

$$Y(s) = Z_1(s)\frac{G_{SZ1}(s) + G_{A1}(s)G_S(s)}{1 + G_R(s)G_S(s)} + Z_2(s)\frac{G_{SZ2}(s) + G_{A2}(s)G_S(s)}{1 + G_R(s)G_S(s)} + W(s)\frac{G_R(s)G_S(s)}{1 + G_R(s)G_S(s)}. \quad \text{(A.58)}$$

It is demanded that the compensation A_1 completely cancels out the effect of disturbance $Z_1(s)$ (a change in mass flow rate). The required characteristic

of the compensation is therefore determined by setting the response of the transfer function for Z to zero:

$$G_{SZ1}(s) + G_{A1}(s)G_S(s) \stackrel{!}{=} 0 \tag{A.59}$$

$$\Leftrightarrow G_{A1}(s) = -\frac{G_{SZ1}(s)}{G_S(s)} \tag{A.60}$$

and alike for the second disturbance. Both, the transfer function for a change in heating power G_S and in the mass flow rate G_{SZ_1} have been determined in Section A.4.4, so that the compensation would ideally have the follwoing transfer function:

$$G_{A1} = -\frac{K_3}{K_1 K_2}(T_1 s + 1)(T_7 s + 1), \tag{A.61}$$

which, however, presents the requirement of non-causal behavior indicated by the higher order of the de-nominator in s than the nominator which can not be attained practically.

Only through the formal introduction of delays $1/(T_1 s + 1)$, $1/(T_2 s + 1)$ and $1/(T_7 s + 1)$, which eliminate the dynamics this compensation can be implemented at the cost of slower dynamic response with regard to disturbances:

$$G_{A1} = -\frac{K_3}{K_1 K_2}, \tag{A.62}$$

$$G_{A2} = -\frac{K_4}{K_1 K_2}. \tag{A.63}$$

The main controller can be determined independent from the compensations. It shall act upon deviations of the outlet temperature from its set point by adjusting the heating power, i.e. the available actuator. The heater transfer function upon changes in the heating power G_S has beendetermined with PT_3 characteristics. According to linear control theory it is possible to de-

mand PT_3 characteristic for the closed loop. When re-arranged the transfer function for the main controller is obtained:

$$\frac{G_R G_S}{1 - G_R G_S} = \frac{1}{(T_3 s + 1)(T_4 s + 1)}, \tag{A.64}$$

$$\Leftrightarrow G_R = \frac{((T_1 s + 1)(T_2 s + 1) - K2)\,(T_7 s + 1)}{K_1 K_2\,((T_3 s + 1)(T_4 s + 1) - 1)}. \tag{A.65}$$

The resulting order of s in the denominator is larger than that of the nominator. By designing the controller without the factor $(T_7 s + 1)$ the causality is restored at the cost of speed in the closed-loop.

For $T_3 = 30$ and $T_4 = 30$ it was found that the response time is acceptable without exceeding the actuator's capacity.

For the controller design properties of the liquid metal at arithmetic mean temperature (between in- and outlet) have been applied. The geometry parameters of the heater mechanical design are maintained for this section. The values of the applied parameters are listed in Table A.6.

The performance of the main controller and the compensation is shown in Figure A.24 when applied to the linearized model (top graph) and to the non-linear model (bottom graph) with the values of the constants as listed in Table A.8.

The top graph shows for a 30% step in the mass flow rate the response of the lineratized model for different cases from bottom to top line: with neither control nor compensation (bottom line) with only the main controller active in a closed loop (second lowest line), with only the compensation active in an open loop (second line from top) and when both, controller and compensation are active (top line). It can be observed that the compensation enables the system to very well maintain the desired outlet temperature. It reduces the maximum resulting deviation from the set point to about 1 K.

The predicted actuator power for the compensation of the disturbance peaks at about 6.5 kW in addition to the initial steady-state power of 21 kW

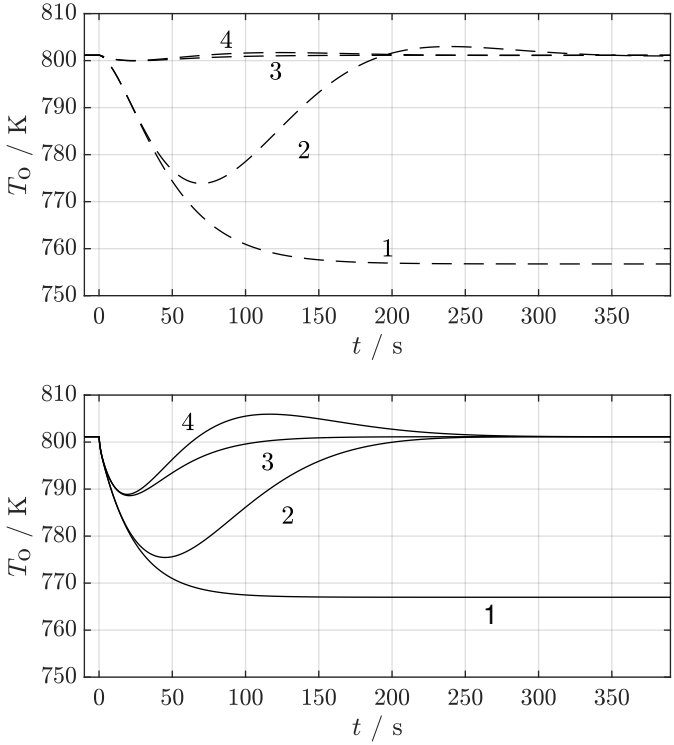

Figure A.24: Open loop step response of the heater to a positive step in the mass flow rate of 30% at $t = 0$ s when applied to the linearized model (top graph, dashed lines) and the non-linear model (bottom graph, solid lines) All plots shown with initial conditions of the reference operation. The curves represent, from bottom to top, the response of the open loop without controller (1), with only the main controller active (2), with only the compensation active (3) and with both, controller and compensation active (4).

Table A.8: controller constants derived for full load operation

parameter	value
K_1	0.000 68
K_2	0.912
K_3	−13.022
K_4	0.088
T_1	1.8092
T_2	0.9464
T_3	30
T_4	30

for the 30 %-step and thus resides below the power design constraint of 30 kW.

The bottom graph shows the system response when the identified compensation and controller are applied to the non-linear system model which allows a more likely prediction of the real system's behavior with the compensation and controller applied. The distortion cannot be compensated as well; it is however limited to about 12 K when the compensation is active versus 25 K with the main controller alone.

The performance of controller and compensation as specified based on design (full load) steady-state conditions is also tested at reduced mass flow rates of 0.5 $\mathrm{kg\,s^{-1}}$, as shown in Figure A.25 with positive step in the mass flow rate of 30 % for the non-linear model with the solid line in the top graph. The maximum disturbance from the set point is smaller than at design conditions, however, the time before steady-state conditions are achieved is increased. It is less stable than at design conditions. If a controller and compensation is applied that are specified based on steady-state parameters

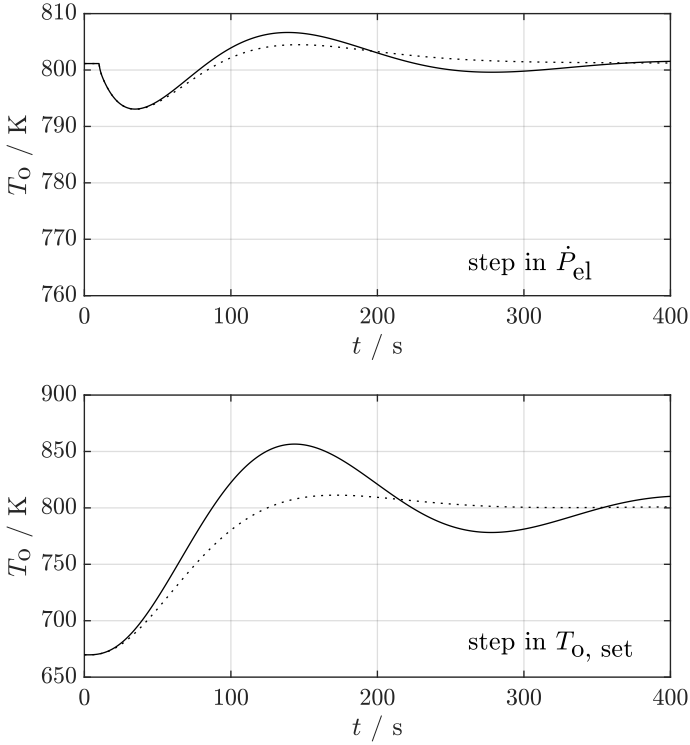

Figure A.25: System responses to steps of the heater outlet temperature from initial steady state conditions of $\dot{m}_0 = 0.5\,\mathrm{kg\,s^{-1}}$ and $\dot{P}_{el} = 10\,500\,\mathrm{W}$. Solid line: controller design based on full load steady state operation parameters; dotted line: controller design based on part load steady-state operation parameters as present before step. Top: Step response to change in mass flow rate of +30% at $t = 0\,\mathrm{s}$ with controller and compensation active. Bottom: Step response to a change of the outlet temperature set point from initially 400 °C to 530 °C.

from part load operation the stability is improved. This, again, points to the option of providing a set of control parameters that are assigned by the control system to the actuators based on the operation state.

In the bottom graph a step in the set point of the outlet temperature is shown from 400 °C to 530 °C (at $t = 0$). With compensation and controller designed for initial conditions an overshoot of the outlet temperature can be avoided.

A.4.7 Receiver: Single tube thermal model

The thermal receiver consists of a steel tube which is bend to form a spiral. The tube does, however, not follow a constant curvature. Instead, straight pieces alternate with 180° bends of a 100 mm diameter. The tubes are exposed to concentrated solar radiation along a portion of the straight tube sections. The heated section is 100 mm wide. After having passed this section the tube goes on for approximately 1020 mm before re-entering the heated zone again. The thermal model of the receiver is therefore composed of sequential sections of a heated straight tube, connected by isothermal tube sections. When exposed to a step signal, these passive sections delay the propagation of the signal to the inlet of the consecutive heated tube section.

The receiver tube is modeled including the tube wall and the flowing fluid that fills the tube section's volume. Disturbances of the system from steady-state occur due to fluctuations of the solar radiation power $I''_{\mathrm{S}}(t)$, changes in the fluid's mass flow rate $\dot{m}_{\mathrm{M}}(t)$ and variation of the inlet temperature $T_{\mathrm{in}}(t)$. The model consists of two control volumes, one for the tube wall energy balance and one for the energy balance of the fluid element. Only one fluid element is refined per irradiated tube section to keep the model simple. Both control spaces exchange heat via convective heat transfer $\dot{Q}_T$. The thermal insulation of tube sections outside the exposed area is neglected, thus, no losses are assumed and also no thermal capacity of the insulation material.

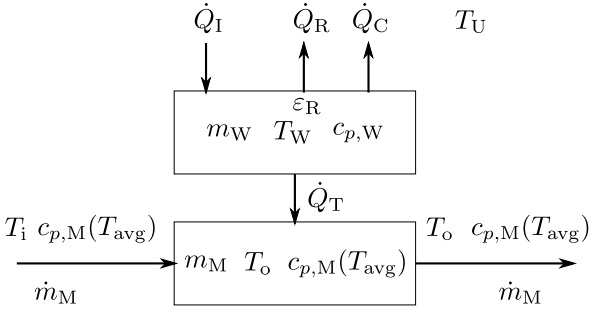

Figure A.26: Schematics of the model of a single receiver tube

No temperature gradients are modeled: each volume has an average temperature, $T_\mathrm{W}(t)$ being the wall temperature, $T_\mathrm{M}(t)$ being the bulk temperature of the metal which is assumed to be the adiabatic mixing temperature of the fluid element. The schematic for this model is shown in Figure A.26. The energy balance for the tube wall is:

$$\frac{dQ_\mathrm{W}(t)}{dt} = \dot{Q}_I - \dot{Q}_R - \dot{Q}_C - \dot{Q}_T, \tag{A.66}$$

with $\dot{Q}_I$ being the incident solar thermal power, $\dot{Q}_R$ radiative thermal losses to the ambient, $\dot{Q}_C$ convective losses to the ambient and $\dot{Q}_T$ convective heat transfer to the bulk fluid. The energy balance of the fluid is:

$$\frac{dQ_\mathrm{M}(t)}{dt} = \dot{Q}_T + \dot{Q}_\mathrm{i} - \dot{Q}_\mathrm{M}, \tag{A.67}$$

with $\dot{Q}_\mathrm{i}$ and $\dot{Q}_\mathrm{M}$ being the incoming and exiting enthalpy rates of the metal flow.

The individual heat fluxes are defined as follows. Note, that the tubes are exposed to flux only from one side:

$$\dot{Q}_I = A_\mathrm{o} \cdot \varepsilon_I \cdot I''_\mathrm{S}(t), \tag{A.68}$$

with $A_\mathrm{o} = \pi \cdot d_\mathrm{o} \cdot L_\mathrm{T}$ and ε_I an absorptance value for solar radiation I''_S.

$$\dot{Q}_R = A_\mathrm{o} \cdot \varepsilon_\mathrm{R} \cdot \sigma \cdot (T_\mathrm{W}(t)^4 - T_\mathrm{U}^4), \tag{A.69}$$

with σ being the Stefan-Boltzman constant and T_U the ambient temperature which is assumed to be constant in this model.

$$\dot{Q}_C = A_\mathrm{o} \cdot h_\mathrm{o}(T_\mathrm{W}(t) - T_\mathrm{U}), \tag{A.70}$$

with h_o being a constant convective heat transfer coefficient accounting for natural and forced convection. Due to fact that the actively controlled temperature of the tubes will not change significantly and low exposure to wind, the assumption of a constant value may be acceptable. The convective heat exchange is modeled according to the following equation:

$$\dot{Q}_\mathrm{T} = A_\mathrm{i} \cdot h_\mathrm{i} \cdot (T_\mathrm{W}(t) - T_\mathrm{out}(t)), \tag{A.71}$$

with $A_\mathrm{i} = \pi \cdot d_\mathrm{i} \cdot L_\mathrm{T}$ and $h_\mathrm{i} = \mathrm{Nu} \cdot k_\mathrm{M}/d_\mathrm{i}$. For the Nusselt number, a correlation by Lubarsky and Kaufmann [49] for turbulent forced convective flow under constant heat flux boundary condition is used:

$$\mathrm{Nu} = 0.625 \cdot \mathrm{Pe}^{0.4} = 0.625 \cdot \left(\frac{v(t) d_\mathrm{i} \rho_\mathrm{M}}{\eta_\mathrm{M}} \frac{\eta_\mathrm{M} c_{p,\mathrm{M}}}{k_\mathrm{M}} \right)^{0.4}. \tag{A.72}$$

All constants are summarized so that h_i can be expressed as:

$$h_\mathrm{i} = C \cdot v^{0.4} \tag{A.73}$$

with $C = 0.625 \cdot (\frac{v(t) d_\mathrm{i} \rho_\mathrm{M}}{\eta_\mathrm{M}} \frac{\eta_\mathrm{M} c_{p,\mathrm{M}}}{k_\mathrm{M}})^{0.4} \cdot k_\mathrm{M}/d_\mathrm{i}$:

$$\dot{Q}_\mathrm{i} = \frac{\pi}{4} d_\mathrm{i}^2 \cdot v \cdot \rho_\mathrm{M} \cdot c_{p,\mathrm{M}} \cdot T_\mathrm{in}(t), \tag{A.74}$$

and likewise for $\dot{Q}_{\mathrm{M}}$.

Eventually the outlet temperature is of interest. Therefore, the equations are rearranged for the temperatures:

$$\frac{dQ_{\mathrm{W}}(t)}{dt} = \frac{\pi}{4} \cdot (d_{\mathrm{o}}^2 - d_{\mathrm{i}}^2) \cdot L_{\mathrm{T}} \cdot \rho_{\mathrm{W}} \cdot c_{p,\mathrm{W}} \cdot \frac{dT_{\mathrm{W}}(t)}{dt}. \tag{A.75}$$

All physical properties are held constant for simplicity. For LBE, values at 560°C are used:

$$\frac{dQ_{\mathrm{M}}(t)}{dt} = \frac{\pi}{4} \cdot d_{\mathrm{i}}^2 \cdot L_{\mathrm{T}} \cdot \rho_{\mathrm{M}} \cdot c_{p,\mathrm{M}} \cdot \frac{dT_{\mathrm{out}}(t)}{dt}. \tag{A.76}$$

With all constants summarized, the system of differential equations is the following:

$$\begin{aligned}\frac{dT_{\mathrm{W}}(t)}{dt} = {} & P \cdot I_{\mathrm{S}}(t) - Q \cdot v^{0.4}(t) \cdot (T_{\mathrm{W}}(t) - T_{\mathrm{out}}(t)) \\ & - R \cdot (T_{\mathrm{W}}(t) - T_{\mathrm{U}}) - S \cdot (T_{\mathrm{W}}(t)^4 - T_{\mathrm{U}}^4),\end{aligned} \tag{A.77}$$

and

$$\frac{dT_{\mathrm{out}}(t)}{dt} = T \cdot v(t) \cdot (T_{\mathrm{in}}(t) - T_{\mathrm{out}}(t)) + U \cdot v^{0.4}(t) \cdot (T_{\mathrm{W}}(t) - T_{\mathrm{out}}(t)). \tag{A.78}$$

A first-order system of non-linear differential equations due to the thermal radiation losses and the variable flow velocity is obtained. Thermal radiation losses are, however, a main contribution to the overall loss and cannot be neglected a-priori.

The constants are:

$$A = \frac{2}{(d_{\mathrm{o}}^2 - d_{\mathrm{i}}^2) \cdot \rho_{\mathrm{W}} \cdot c_{p,\mathrm{W}}}, \tag{A.79}$$

$$B = \frac{2}{d_{\mathrm{i}}^2 \cdot \rho_{\mathrm{W}} \cdot c_{p,\mathrm{W}} \cdot L_{\mathrm{T}}}, \tag{A.80}$$

$$P = A \cdot \varepsilon_I \cdot d_{\mathrm{o}}, \tag{A.81}$$

$$Q = A \cdot d_{\mathrm{i}} \cdot C, \tag{A.82}$$

$$R = A \cdot d_{\mathrm{o}} \cdot h_{\mathrm{o}}, \tag{A.83}$$

$$S = A \cdot d_{\mathrm{o}} \cdot \varepsilon_{\mathrm{R}} \sigma, \tag{A.84}$$

$$T = \frac{B}{2} \cdot d_{\mathrm{i}}^2 \rho_{\mathrm{M}} \cdot c_{p,\mathrm{M}}, \tag{A.85}$$

$$U = B \cdot d_{\mathrm{i}} \cdot L_{\mathrm{T}} \cdot C. \tag{A.86}$$

For this system the following design conditions are set, with thermophysical properties evalueated at the arithmetic mean temperature between receiver in- and outlet of $T_{\mathrm{avg}} = 565\,^{\circ}\mathrm{C}$:

A.4.8 Receiver: Single tube steady state solution

The steady-state solution of this system has been calculated with MATLAB's fsolve function, after setting the left hand sides of the equations to 0. The system (during the passage of only one of ten passes through the focal point) is at equilibrium at the following two temperatures:

Table A.9: Parameters for model

parameter	unit	value
I_S	W/m^2	1 100 000
v	m/s	1.57
T_i	K	803.15
ρ_M	kg/m^3	9982
ρ_W	kg/m^3	7000
$c_{p,M}$	J/(kg K)	139.9
$c_{p,W}$	J/(kg K)	500
k_M	W/(m K)	15.22
d_i	m	0.009
d_o	m	0.01
L_T	m	0.1
h_o	W/(m^2 K)	600
σ	W/(m^2 K^4)	5.67E-8
ε_I	–	0.92
ε_R	–	0.95
T_U	K	300

Note, that the value of h_o has been simply guessed in order to achieve a reasonable outlet temperature, that is one thenth of the overall temperature gain of the flow through the entire receiver at design conditions of 70 K.

A.4.9 Receiver: Single tube step response

The system of differential equations has been implemented as a MATLAB SIMULINK model. The step response to a change in the flow velocity is

Table A.10: Steady-stage temperature solution at equilibrium for the receiver at reference conditions.

parameter	unit	value
$T_{\mathrm{W,s}}$	K	849.6
$T_{\mathrm{o,s}}$	K	810.5

shown in Fig. A.27 for different step sizes. The flow velocity has been reduced by 0.3, 0.6 and 0.9 m/s. In a linear system, the resulting response equilibrium values is linear with respect to the input step size. This is not expected in this system, as the wall temperature contributes with radiation at a power of four and the flow velocity with a power of 0.4, due to momentum transport.

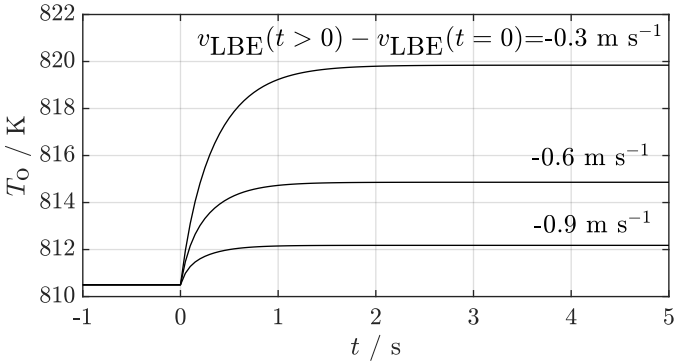

Figure A.27: Temperature response for different reductions in the flow velocity.

Around this operating point the temperature response is not linear with the reduction in flow velocity.

When steps of 100 000, 200 000 and 300 000 W m^{-2} are applied to the referenceflux density, the responses shown in Fig. A.27 are obtained.

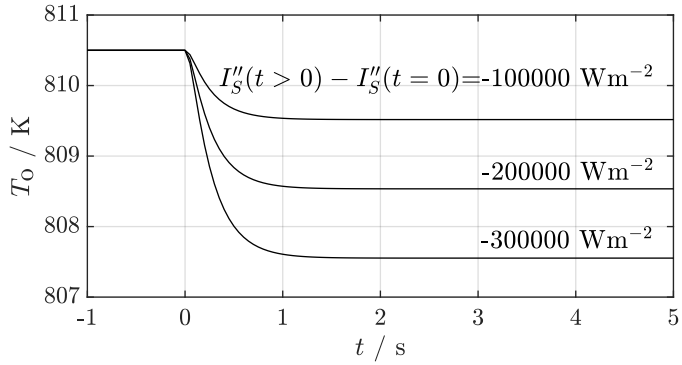

Figure A.28: Temperature response for different steps in the solar flux density.

With respect to the flux density the system can be considered a linear system. In fact, the contribution of thermal radiation of the SOMMER receiver is low: Under the assumption of 92% emissivity and a surface temperature of 900K,

$$\dot{Q}_R = \sigma \cdot A_{\text{Receiver}} \cdot \varepsilon_R \cdot (T_{\text{M}}^4 - T_{\text{U}}^4) = 5.67 \times 10^{-8}\,\text{W}\,\text{m}^{-2}\,\text{K}^{-4} \cdot 0.01\,\text{m}^2 \cdot 0.92 \cdot ((900\,\text{K})^4 - (300\,\text{K})^4) = 338.023\,\text{W}. \quad \text{(A.87)}$$

At a thermal power rating of the receiver of 10000 W this makes up for 3.4 %. The radiation heat losses are therefore significant for the thermal efficiency but don't play a major role in the receiver control.

The flow velocity is kept constant, so no delay of the response is observed.

A.4.10Receiver: The complete non-linear model

In order to obtain a model for the complete receiver, ten instances of the single tube model are connected in series. In-between each block for a single

tube, a transport delay block is added to account for the fluid transport in the non-heated tube sections that connect the heated sections. These non-heated sections have a length of 1.02 m. As a simplification compared to the real receiver the model assumes a homogeneous flux distribution across the receiver so that each pipe segment absorbs the same power. This is a significant deviation from reality, however, it is assumed to be appropriate in order to estimate the dynamic behavior of the receiver with respect to changes in mass flow and overall power input. The system's response to positive steps in the flow velocity of 0.3, 0.6 and 0.9 $\mathrm{m\,s^{-1}}$ compared to the steady-state-situation at reference conditions (as listed in Table A.9) are shown in Figure A.29. The step is initiated at t=0 s. Due to the transport delay at steady-state conditions, which depends on the flow rate, the response is faster for higher flow rates. Nevertheless, even for low flow velocity the response is very fast compared to that of the heater. For this reason, in the context of this loop the impact of the receiver model's simplifications on the loop dynamics become negligible compared to those of the heater.

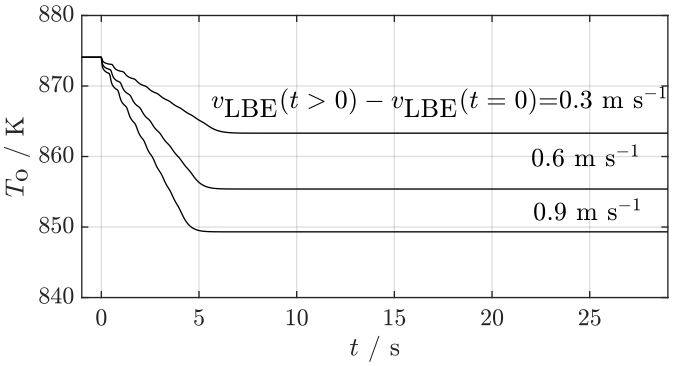

Figure A.29: Temperature response for different steps in the metal flow velocity.

The ribbles to be observed in the negative ramp of the response arise from the indiviually modeled tube segments that are configured serially, each ap-

plying a dampening effect to their respective output. For negative steps in flux density of 100 000 W/m^2, 200 000 W/m^2 and 300 000 W/m^2 the responses are shown in Figure A.30. With regard to the flux density at a constant flow velocity this system is linear.

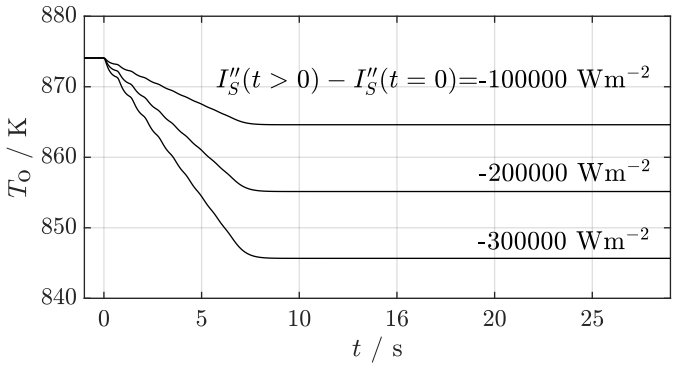

Figure A.30: Temperature response for different steps in the solar flux density and a constant flow velocity.

Both responses have a ramp-like shape, which does not fall into the categories of basic linear control theory. It will therefore be attempted to implement a PID controller for the outlet temperature with parameters determined by trial and error!

A.4.11Control of the thermal receiver and heater

It is desired to keep the outlet temperature of the receiver at a constant value of 600°C (873K). This objective is challenged by the fluctuating nature of the intensity of solar radiation, which is, for example, affected by the passage of clouds or simply by the fact that the sun rises and falls throughout the day.

The control of the thermal receiver can be accomplished by either adjusting the inlet temperature or affecting the mass flow rate to compensate

changes in the solar power supply. The actor is then either the heater or the pump, respectively. In large scale applications there is usually no heater. To keep a degree of similarity between the large scale application and the experiment, the receiver outlet temperature shall be controlled by adjustment of the mass flow rate.

An adjustment of the mass flow rate, however, will not only influence the outlet temperature of the thermal receiver, but also the outlet temperature of the heater. It is therefore required to also adjust the power of the heater to maintain a constant outlet temperature of the heater when the flow rate has been adjusted to maintain a constant receiver outlet temperature.

In principle such task requires a fast feed back control loop for the heater outlet temperature and a slower feed-back control loop for the receiver outlet temperature. Unfortunately, the dynamics of the heater are one order of magnitude slower than those of the thermal receiver.

The control task can thus not be accomplished this way. The feed-back control is difficult to implement for a second reason, being quite long transport delays in the tubular system.

Fortunately the major disturbance to the system – being the solar power – is constantly measured. The live value of the solar power can be used to facilitate the control scheme. Therefore, the system can act before a change in the outlet temperature can be detected by a sensor.

If a deviation $\Delta I''$ of the nominal solar power occurs, a reaction by the pump will lead to a required $\Delta\dot{m}$ and a reaction by the heater will lead to a required $\Delta\dot{P}_{\mathrm{el}}$. From the energy balances around both sections,

$$\Delta I''_{\mathrm{S}} = \dot{m} \cdot c_{p,\mathrm{M}} \cdot (T_{\mathrm{o,R}} - T_{\mathrm{i,R}}), \tag{A.88}$$

and,

$$\dot{Q}_{\mathrm{H}} = \dot{m} \cdot c_{p,\mathrm{M}} \cdot (T_{\mathrm{i,R}} - T_{\mathrm{i,H}}), \tag{A.89}$$

it can be deducted that on occurrence of a $\Delta I''_{\mathrm{S}}$,

$$\Delta \dot{m} = \frac{\Delta I''_{\mathrm{S}}}{c_{p,\mathrm{M}}(T_{\mathrm{o,R}} - T_{i,R})}, \tag{A.90}$$

and,

$$\Delta \dot{Q}_{\mathrm{H}} = \Delta I''_{\mathrm{S}} \cdot \frac{(T_{\mathrm{i,R}} - T_{\mathrm{i,H}})}{(T_{\mathrm{o,R}} - T_{\mathrm{i,R}})}, \tag{A.91}$$

have to be applied to keep the temperature difference $(T_{\mathrm{i,R}} - T_{\mathrm{i,H}})$ constant. The latter equation is already implemented in the heater control based on a change in mass flow rate. The thermal losses to ambient can be neglected in this case because they depend on the surface temperature which remains constant if $(T_{\mathrm{o,R}} - T_{\mathrm{i,H}})$ remains constant. This neglects the effect of a lesser overheat of the tube surfaces because of reduced sun intensity. However, for the overall energy balance this effect is negligible.

The resulting scheme is shown in Figure A.31. The slow, inner control loop is indicated with a dashed frame. A feed-forward compensation based on changes in the mass flow for quick reaction and a controller are contained in this section. The faster acting outer loop contains a feed-forward controller based on a measurement of the DNI value and a controller to compensate a remaining deviation from the desired outlet temperature.

However, because the response of the thermal receiver to a change in the set point of the mass flow rate is faster than the response of the heater to a change in the set point of the heating power it is likely that a temperature fluctuation will occur at the outlet of the thermal receiver. A rise of the receiver outlet temperature much above of 600°C is not allowable due to

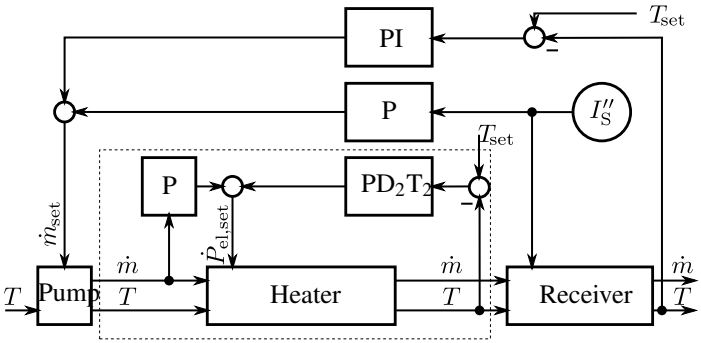

Figure A.31: Control scheme of SOMMER receiver and heater.

material constraints. Therefore the adjustment of the mass flow rate should be applied with a variable factor to make sure that temperature limit is not exceeded as long as the heater needs to find the new operating point.

The response of the combined system of heater and receiver is shown in Figure A.32 at design conditions.

The dotted lines show the response of the system when no action is taken to maintain the desired outlet temperature. The dashed lines show the effect of adjusting the mass flow rate in a feed-forward fashion upon a change in the measured insolation value for three different steps. The solid line, finally, for a step in 300000 W/m^2, shows the active feed-forward compensation and a slow PID controller combined. For the PID-controller for the receiver's outlet temperature good performance was found for P = 0.007 and I = 0.0004. Both are in combination able to limit the fluctuations in the response, even though an overshoot up to nearly 880 K occurs. This is, however, tolerable.

In the response of the receiver the disturbance of the heater arrives with a delay of approximately 15 seconds due to transport delay.

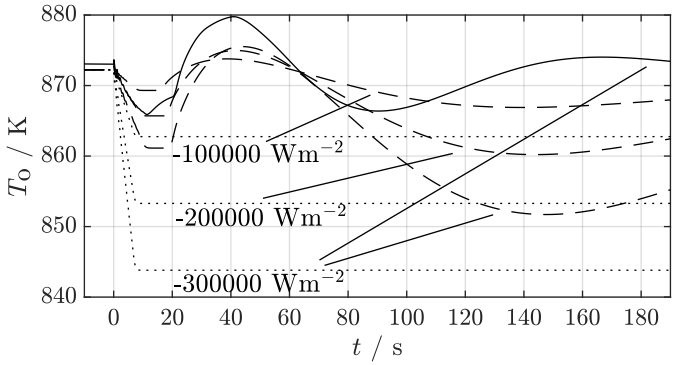

Figure A.32: Response of the receiver's outlet temperature for negative steps of 100 000, 200 000 and 300 000 W m^{-2} in flux density. Dotted lines: all controllers switched off. Dashed lines: compensations active, solid line: compensations and PI controller active (for the case of a negative step of 300 000 W m^{-2}.

The heater-receiver system is non-linear. Therefore the parameters used in this operating point will likely not work as well if the step in solar power is larger.

In that case it will be necessary to generate a table with gain values for different operating points. If the loop acts at a point between entries in that table, values have to be interpolated.

A.4.12Conclusions

Within this chapter the implementation of a control algorithm has been demonstrated which operates on the receiver outlet temperature in a comparable manner as in reference solar facilites. The main difference between these facilities and the SOMMER loop is the heater, which is usually not present in solar power facilities. Additionally its thermal inertia are significant and inhibit fast response to fast dynamics of the solar incidence. This

makes the control more difficult. Nevertheless the principles used in the reference facilities can be applied to the demonstration loop and will be able to maintain the outlet temperature of the receiver within reasonable bounds.

Note that in the presented approach two separate units have been treated individually, one of which is the receiver, in order to obtain a similarity to reference plants where the receiver is controlled separately as well. Of course for the sole purpose of maintaining a constant receiver outlet temperature this is not the easiest approach to use in this demonstration loop. For example, the power of the heater could be directly controlled in proportion to a feed-forward signal from the DNI measurement, whereas it is now controlled in feed-forward fashion based on the change of the mass flow rate, instead. Changes in the mass flow rate are now generated by the receiver's control loop based on the DNI value. This introduces the response time of the pump before the heater power begins to adjust.

This demonstration of a 'complicated'approach is intended to show that the use of liquid metals does not influence the way loop control can be implemented compared to conventional coolants.

A.5 The heater design

Coaxial flow configuration

As the heat source cylindrical electrical resistance heating rods made by Waltow have been selected that have been fit into the lid of the heater's pressure vessel. These rods have a standard diameter of 19 mm (3/4") and 400 V 3-phase power supply at maximum power of 5000 W each. Using a multiple of three rods allows for a simple electrical installation. Thus an arrangement of six rods with maximum power is the straight-forward selection. These are arranged on the lid on a circle surrounding the central axis of the heater vessel. In the center the flow inlet is located. The flow is

radially displaced from the central axis toward he six heater rods by a central, passive (non-heated), hollow cylindrical body and re-unites once that body is passed before outlet. The heater rods which are made of Incoloy 800 steel are protected against corrosion by sheaths made of 1.4571 stainless steel tubes with 22 mm outer diameter. Into these the rods are inserted after the completion of the vessel and from these they can be removed again if necessary. The flow is directed in parallel flow to the rod axes in order to achieve a symmetrical flow distribution as in a nuclear rod bundle. With this arrangement the heat transfer between the rods and the fluid is estimated based on Nusselt number correlations developed for the cooling of nuclear rod bundles with liquid metals. These bundles are often arranged in such a hexagonal manner, however, with the central body typically being an additional actively heated rod. While the velocity profile in the heater will be valid for the application Nusselt number correlation higher heat transfer coefficients than predicted by the correlation will result due to that passive central rod.

A co-axial flow inlet provides a symmetrical flow development zone prior to the heated section of the rods and helps to prevent local stagnant zones which could be induced by radially configured flow inlets.

Heater rod and sheath configuration

In order to provide reasonably developed flow conditions for the applicability of the Nusselt number correlation a 50 mm long non-heated section of the rods is specified at the flow inlet. Also the sheath length is specified such that the rods still extend from the vessel lid when fully inserted in order to provide enough grip for their removal. Accordingly, the non-heated section is selected to have a length of 15 cm.

For the requirement of their insertion after the fabrication the smallest reasonable fit between the inner sheath diameter and the outer heater rods

diameter to be fabricated with reasonable effort has been found to be 0.1 mm for a tube length of approximately 0.5 m. And indeed, even with potentially present camber in the rods the insertion poses no problem – even without lubricant.

The required length of the heaters results from the allowable power density on the sheath of the rod that prevents overheating of the heater core during operation. Watlow provides a graph for the maximum power allowable depending on the actual fit and the desired operating temperature. Based on the steady-state maximum fluid outlet temperature of 530 °C and a radial temperature difference from heat transfer through the wall of the protective tube of about 10 K and about 50 K from wall-to-bulk heat transfer in the flow at maximum design power a design temperature of 590 °C is defined for the rod. The graph in the data sheet recommends a maximum power of about 20 W cm^{-2} for this case.

From this allowable power results a heated length of 0.4 m at the maximum power of 5000 W and the standard diameter of the rod.

The rods have been ordered with a total length of 550 mm so that in addition to the active length of 400 mm and the passive section a large enough portion of the rods extends from the vessel. The specification is summarized in Table A.11.

For the welding the protective steel shells to the lid of the heater vessel a distance between two shells and between a shell and the vessel wall of $d_{R;R} = 3$ mm has been found to be sufficient given the capabilities of the local fabrication shop at KIT. This results in a pitch-to-pin ratio of 1.13. With these parameters, the required inner diameter of the vessel is:

$$d_{V,i} = 3 \cdot d_R + 4 \cdot d_{R,R} = 78\text{mm}. \tag{A.92}$$

Table A.11: Heater rod configuration. Abbrevations: T/C = thermocouple

parameter	value
diameter	0.746” ± 0.002”
diameter	18.9484 mm± 0.0508 mm
length	21.65”
length	549.9 mm
voltage	400 V
power	5 kW
leads	FIREROD HT
lead length	12”
lead length	304.8 mm
sheath material	Incoloy 800
instrumentation	Type K T/C in tip
price per piece	170 EUR

Mechanical design

The vessel has an inner length of 445 mm and an outer wall thickness of 2 mm. The central, non-heated tube (closed on both ends and indicated by ‘2’ in Figure 4.14) is held in place by conical tube pieces with large cut-outs to provide a passage for the LBE flow. The shells for the heater rods are welded to the inlet flange and are welded shut on their opposite end while being attached to a pin to hold the ends in place. This final design holds approximately 1.1 L of volume. The assembled device is shown in Figure A.33 (including the name plate) with a long tube section welded to the inlet flange and a short tube welded to the outlet flange with a Swagelock fitting attached.

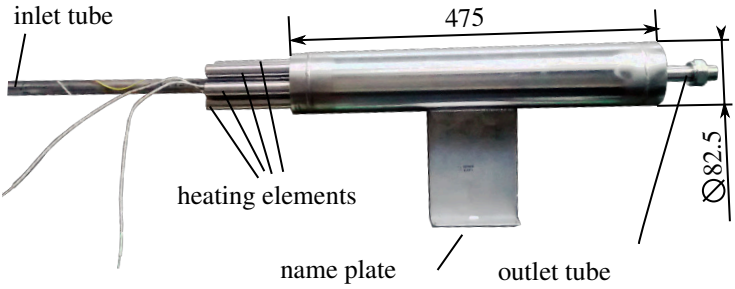

Figure A.33: heater of the SOMMER LBE-loop

Thermo-hydraulics

A Nusselt number correlation for hexagonally spaced rods and co-axial flow according to Ref. [93] is applied[5], valid in a range of Peclét numbers of $1 \leq \mathrm{Pe} \leq 4000$.

That correlation is applied for a pitch-to-pin ratio of $P/D = 1.136$, and a parameter ε for the 'azimutal variation in the heat flux on a single rod' of $\varepsilon = 0.4$ at a Peclét number of Pe=50.9. The Peclét number is the product of the Prandtl and the Reynolds number, both obtained with the hydraulic diameter d_h of the heater,

$$d_h = 4A_C/U_w, \tag{A.93}$$

with A_C being the cross section for the flow between the rods and U_w the wetted perimeter.

Table A.12 (page 276) lists the obtained hydraulic parameters of the underlying geometry for thermo-physical properties evaluated at the highest

[5] This correlation is featured in the 2015 LBE-Handbook [32]. A plot is therein provided for the determination of the Nusselt number with the Peclét number and pitch-to-pin ratio as parameters. The values in that plot are, however, different from those to be obtained from the provided correlation. Furthermore, the provided correlation differs from the originally referenced source (Ushakov [93]; The sign in front of the square root is opposite; the handbook has a negative sign.) For the determination of the heater's thermal hydraulics the correlation from the original source is used.

expected film temperature on the heater rods of 565 °C (design outlet temperature plus wall-to-bulk temperature difference estimate of 35K). At lower temperatures a lower heat transfer coefficient and larger Richardson number are obtained.

The resulting Peclét number of Pe = 50 is within the validity range of Ushakov's correlation.

A heat flux density on the outside of the protective tubes q''_o of 180.8 kW m^{-2} is calculated. With the conservative value of the convective heat transfer coefficient of the flow results a wall-to-bulk temperature difference ΔT_{rad} of 29 K. The protective metal shells for the rods have been fabricated with a final wall thickness of 1.45 mm which results in a radial temperature difference due to conduction at the given heat flux density of slightly below 15 K.

Both thermal resistances generate a summed up temperature difference of less than 45 K which is less than the estimated margin of 60 K during the selection of the heater rods. Accordingly, an additional safety temperature margin remains for this specification.

The sheath's wall thickness is also sufficient to resist the design pressure of 17 bar.

A.6 The air cooler design

The cooler of the SOMMER facility has been designed by Michael Kant during his master's thesis as air cooler for a cooling power of 10 kW in two different temperature ranges, namely 300 °C to 200 °C at an LBE mass flow rate of 0.262 m^3 h^{-1} (approx. 0.74 kg s^{-1}) and between 550 °C and 350 °C at 0.131 m^3 h^{-1} (approx. 0.37 kg s^{-1}).

On the air side during the design process a flow rate of 210 m^3 h^{-1} has been selected with an outlet temperature of 260 °C. For the lower temper-

ature case a much larger air flow rate of $820\,m^3\,h^{-1}$ has been selected with an approximated air outlet temperature of 75 °C.

The heater's pressure drop on the air side has been tested by Kant in a test bench after having been connected to a blower via air an rectangular air channel before and a rectangular reduction section ending in a circular tube after the cooler. A characteristic quadratic curve for the pressure drop as a function of the air flow has been measured up to nearly $350\,m^3\,h^{-1}$, however, including the effects of a flow straightener, and the channel and reduction pieces.

During the detailed design of the SOMMER loop the requirements for the heater changed significantly. Maximum thermal power of up to 40 kW could momentarily arise at LBE temperatures of 600 °C at the inlet of the cooler which had to be cooled down to 380 °C. Conservatively, at these conditions at the four-fold thermal power to be removed in the cooler the four-fold air flow was required, leading to a 16-fold estimated pressure loss in the cooler than expected during its design.

It was estimated that existing hardware could cope with the changed requirements given a sufficiently strong blower.

In the final design the heat exchanger was placed between a diffusor and a reducer piece and at the respective in- and outlet automatic wing flaps were installed. These can be shut during idle mode and close the air volume which is then trace heated to temperatures sufficiently high to prevent LBE in the heat exchanger tubes from freezing. The final assembly is shown in Figure A.34.

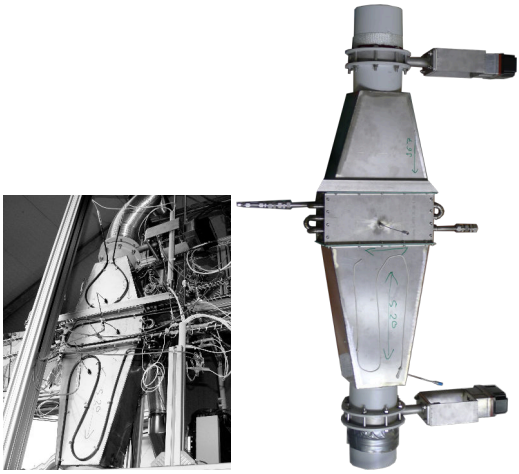

Figure A.34: Air cooler withouth thermal insulation. The air inlet diffusor is located at the bottom (above the inlet wing flap outside the picture frame) and outlet reducer at the top, followed by automatic wing flap. The casing is equipped with trace heating elements.

Table A.12: Hydraulic and geometry parameters of the heater

parameter	symbol	unit	value
rod diameter	D	m	0.022
rod pitch (center to center)	P	m	0.025
pitch to pin ratio	P/D	–	1.1364
vessel inner diameter	D_{V}	m	0.078
free crosssection	A_{c}	m^2	0.0021
wetted perimeter	U_w	m	0.7288
hydraulic diameter	D_h	m	0.0116
density LBE (565°C)	ρ_{LBE}	$\mathrm{kg/m}^3$	10000
heat capacity LBE (565°C)	$c_{p,LBE}$	J/(kg K)	140
dynamic viscosity LBE (565°C)	μ_{LBE}	Pa s	1.2E-3
thermal conductivity LBE (565°C)	k_{LBE}	W/(m K)	15.1
mass flow rate LBE	$\dot{m}_{LBE}$	kg/s	1
volume flow rate LBE	$\dot{V}_{LBE}$	m^3/s	0.0001
flow velocity LBE	v_{LBE}	m/s	0.047
Reynolds number	Re	–	4574
Prandtl number	Pr	–	0.0111
Peclét number	Pe	–	50.88
Nusselt number	Nu	–	5.8
avg. convective heat transfer coefficient	h	$\mathrm{W/(m}^2\ \mathrm{K)}$	7580
20% reduced h (safety margin)	h_S	$\mathrm{W/(m}^2\ \mathrm{K)}$	6066
Grashof number	Gr	–	6×10^7
Richardson number	Ri	–	2.86
vessel inner length	L_V	m	0.445
liquid volume	V_{LBE}	m^3	0.0011
residence time	t_{res}	s	10.85